THERMO-HYDROLOGICAL-MECHANICAL ANALYSIS OF A CLAY BARRIER FOR RADIOACTIVE WASTE ISOLATION: PROBABILISTIC CALIBRATION AND ADVANCED MODELING

A Thesis

by

LAKSHMAN KUMAR DONTHA

Submitted to the Office of Graduate Studies of
Texas A&M University
in partial fulfillment of the requirements for the degree of

MASTER OF SCIENCE

May 2012

Major Subject: Civil Engineering

Thermo-Hydrological-Mechanical Analysis of a Clay Barrier for Radioactive Waste Isolation: Probabilistic Calibration and Advanced Modeling

THERMO-HYDROLOGICAL-MECHANICAL ANALYSIS OF A CLAY BARRIER FOR RADIOACTIVE WASTE ISOLATION: PROBABILISTIC CALIBRATION AND ADVANCED MODELING

A Thesis

by

LAKSHMAN KUMAR DONTHA

Submitted to the Office of Graduate Studies of
Texas A&M University
in partial fulfillment of the requirements for the degree of

MASTER OF SCIENCE

Approved by:

Co-Chairs of Committee,	Marcelo Sanchez
	Zenon Medina-Cetina
Committee Member,	Frederick Chester
Head of Department,	John Niedzwecki

May 2012

Major Subject: Civil Engineering

ABSTRACT

Thermo-Hydrological-Mechanical Analysis of a Clay Barrier for Radioactive Waste Isolation: Probabilistic Calibration and Advanced Modeling.

(May 2012)

Lakshman Kumar Dontha, B.Tech, Banaras Hindu University

Co-Chairs of Advisory Committee, Dr. Marcelo Sanchez
Dr. Zenon Medina-Cetina

The engineered barrier system is a basic element in the design of repository to isolate high level radioactive waste (HLW). It plays a prominent role in conducting the heat generated from the waste; reducing the flow of pore water, and maintaining the structural stability of the waste canister. During the life time of the repository, the barrier will undergo different coupled thermal, hydrological and mechanical (THM) phenomena due to heating (from the heat-emitting nuclear waste) and hydration (from the saturated host rock). The design of nuclear repository requires the prediction of the long term barrier behavior (i.e. hundred or thousand years), so numerical modeling is a basic component of the design. The numerical analyses are performed using a mathematical THM formulation and the associated numerical code, where constitutive models are an essential part. Those constitutive models represent the intrinsic behavior of the material for the individual physical phenomenon (i.e. thermal, hydraulic and mechanical). Although,

deterministic analyses have demonstrated potential to describe the physical behavior of barrier system, to study the effect of the inherent uncertainties associated with the constitutive models on the global behavior of the isolation system a probabilistic approach is required.

The first part of the thesis is related to application of recent probabilistic methods to understand and assess the impact of uncertainties on the global THM model response. Experimental data associated with the FEBEX project has been adopted for the case study and a fully coupled THM finite element program, CODE_BRIGHT, is used to perform the numerical analysis.

The second part of thesis focuses on the complex mechanical behavior observed in a barrier material subjected (during 5 years) to heating and hydration under actual repository conditions The studied experiment is the (ongoing) full scale in-situ FEBEX test at Grimsel test site, Switzerland. The clay underwent both elastic and plastic volumetric deformations at different suction and temperature levels with changes in the pre-consolidation pressure and voids ratio that are difficult to explain with conventional models and thus a double structure elasto plastic model is proposed. The study shows that the double structure model explains satisfactorily the observed changes in the mechanical behavior of the clay material.

DEDICATION

In the memory of my grandfather, the late Shri. Srishailam Dontha

ACKNOWLEDGEMENTS

I would like to take this opportunity to gratefully acknowledge the support of my advisors, Dr. Marcelo Sanchez and Dr. Zenon Medina-Cetina for their sustained support, guidance and encouragement throughout the course of my graduate studies and for the enormous time he dedicated for my masters research. I would like to thank Dr.Medina for offering the cluster required to perform the rigorous calculations involved in the research, without which it would have been impossible to complete this research. I would also like to thank Dr. Frederick Chester for kindly consenting to be a member of my committee and helping me revise this document. I would also like to acknowledge Dr. M.V. Villar for providing me the oedometric data required for the research.

I wish to thank the entire faculty of the Department of Civil Engineering at Texas A&M University for providing me with the tools and knowledge required for this work. I must also acknowledge the effort and time given by my friend, Ajay Shastri. I also thank him for cooperating with initial computations in the present work.

Finally, my deepest gratitude is due to my parents, my brother and my sister for their constant love and support.

TABLE OF CONTENTS

Page

Page

LIST OF FIGURES

FIGURE Page

FIGURE Page

FIGURE Page

FIGURE Page

FIGURE Page

FIGURE Page

FIGURE Page

LIST OF TABLES

1. INTRODUCTION

1.1 Background

The high level radioactive wastes (HLW) are isolated by nuclear waste repository in deep geologic media. The design of repository includes construction of an engineered barrier between the waste canister and geological host rock. For effective isolation of nuclear wastes, the barrier should have the ability to restrict the flow of groundwater from host rock and thus retard migration of radio nuclides, dissipate the heat generated from the canister, and should maintain structural integrity, withstanding mechanical stress from the rock and sealing cracks (Pusch, 1982). Bentonite has been one of common sealing material in most disposal concepts because of its low permeability, swelling capacity and retention properties, among other features. The barrier initially unsaturated is subjected to complex thermo-hydro-mechanical (THM) actions at all stages of disposal (Tsang et al., 2000) due to simultaneous heating (generated due to the radioactive waste) and hydration (due to inflow of water from the surrounding rock). Understanding and analyzing this behavior of the barrier on the long term basis is necessary for the successful and safe design of the repository.

Efforts have been made by a number of researchers to characterize the behavior of the engineered barrier by conducting various experiments at different scales including some postmortem tests (Villar, 2002; Villar et al., 2008). Theoretical models have been proposed to reproduce THM phenomena using fundamental governing equations.

This thesis follows the style of *Géotechnique.*

Olivella et al. (1994) have proposed a coupled thermo-hydro-mechanical framework based on which a finite element code CODE_BRIGHT was proposed (Olivella et al., 1996). The parameters used in the constitutive and balance equations in those numerical analyses were obtained deterministically from the experimental observations. However the results of the experiments conducted on bentonite clay showed that there were uncertainties involved while determining these parameters. The present work is an effort to characterize the uncertainty in parameters; and to quantify and compare uncertainty in the model response output due the different parameter sources.

Expansive clays in compacted form like the compacted bentonite, in unsaturated state are often used as sealing material in high-level radioactive waste repositories for their swelling and self-healing capabilities (Pusch, 1980; Delage, 2010). Analyzing the behavior of barrier thus highlights the understanding of mechanical behavior of the clay material under similar thermal-hydraulic-mechanical conditions. A model describing the stress-strain behavior of unsaturated soils was proposed by Alonso et al. (1990) with respect to thermal and suction changes. This further extended to the expansive soils by Gens & Alonso (1992) based on the distinction within the material of a micro structural level, where the basic swelling takes place and a macro structural level, which is responsible for major structural rearrangements. The present work also focus is placed on implementation of this double structure model to better understand mechanical behavior of the bentonite clay. In particular, an effort has been made to numerically model the structural changes due to heating and hydration during the disposal process.

1.1.1 Purpose of Uncertainty Treatment

In the past few years, the subject of uncertainty has received increasing amount of attention in a variety of engineering disciplines, especially those involving complex physics. In such complex fields, mathematical models can only serve as simplified and reduced representations of true physics and there exists a significant amount of uncertainty associated with parameter values, boundary and initial conditions, constitutive laws etc. The behavior of clay barrier used in HLW repository is one such complex phenomenon that involves coupled thermal-hydraulic-mechanical (THM) processes. And building its conceptual modeling consists, basically, the assembling of all the constitutive and balance equations which describe physics individually.

The parameters of constitutive equation, incorporating physical phenomenon of the material, are obtained deterministically based on laboratory and representative experiments. Use of such experiments to measure parameters associated with a given phenomenon without proper treatment of other phenomena that may be taking place simultaneously, leads to assumption of parametric value which may not be applicable under conditions of interest. Under the complex field conditions and mutual interaction between multi-physics, the soil properties may vary in space and time. The experiments also assume that the material is isotropic, ignoring the local effects. Further, measurement of data often exhibit significant scatter across a site due to spatial variability of soil properties and the variable parameters are replaced with either a lumped parameter or a deterministic value. In addition to all above factor, there is

always some measurement error in the parameters due to various reasons like error in equipment, human error etc. This parametric uncertainty and heterogeneity, affect the constitutive models significantly in quantifying the actual response of material making the THM characterization uncertain. Therefore, it is very important to assess the parametric uncertainty and their effects on uncertainty in the output response to improve barrier characterization and decision making.

The measure of uncertainty enforces a complete examination of the experimental procedure, including the potential sources of troubles and errors. It helps to identify beforehand, the desired accuracy of the experiments and minimizes instrument cost for a given output accuracy. It provide appropriate basis for deciding whether computations agree with data or lie outside the acceptable limits. It provide a check against unknowingly taking data in some odd corner where uncertainties become very large and advise when more accurate experiments must be provided to further 'calibrate' approximate theory. But, the uncertainty analysis is not a replacement for calibrations, cross-checks, closures using governing equations and for sound technique. It is not a substitute for understanding the problem and the physics underlying the mensuration techniques. It only provides a framework inside which the cross-checks are made effectively and ensuring requisite accuracy with minimum cost and time (Kline, 1985). Overestimation of the uncertainty intervals makes it difficult to spot real differences and allows bad data to stay unchallenged while underestimation provokes unnecessary

arguments. Hence, the uncertainty should be within some confidence limits that should always be explicitly noted (Moffat, 1988).

1.1.2 Mechanical Behavior of Bentonite Barrier

During its lifetime the barrier experience volume changes when they are subjected to heating and hydration. For instance, under high temperature, the normally consolidated soil contracts and over-consolidated soil dilates before contraction (Cui et al., 2000). Under drying conditions the swelling soils shrink due to increasing suction, while during wetting conditions they swell which may reduce permeability (Cui et al., 2001). The constant volume condition within the barrier restricts the swelling which further alter the soil water retention characteristics (Cui et al., 2008). Due these various effects, particularly, in thermo-hydraulic-mechanical phenomena, it is essential to understand the mechanical behavior of unsaturated expansive soils under a wide range of testing conditions including the influence of micro scale mechanics.

The volumetric behavior of saturated clays was first analyzed and modeled using Cam-clay (Roscoe et al., 1963) and modified cam-clay model (Roscoe and Burland, 1968). The model is applied with modifications to unsaturated soils by Alonso et al. (1990), and is commonly called Barcelona Basic Model (BBM), which remained as a general framework for many other elasto-plastic models later developed (Josa et al., 1992; Kohgo et al., 1993; Wheeler & Shivakumar, 1995; Cui et al., 1995; Wheeler, 2003). This framework is then extended to unsaturated expansive clays by Gens and Alonso (1992)

on the distinction within the material of a micro structural level, where the basic swelling takes place and a macro structural level, which is responsible for major structural rearrangements. The double structure model has been further applied in various different problems (Romero, 1999; Cui et al., 2002; Lloret et al., 2003; Sanchez, 2004).

According to elasto-plastic BBM model, the material behaves elastically as long as the stress state is inside the yield surface. But, the clay undergoes some amount of irrecoverable deformations upon reloading (Lubliner, 1991). It lags to explain the plastic deformations that occur within the yield surface. These deformations are attributed to the swelling of micro pores and its intrusion into macro pores. The elasto-plastic model framework is proposed by Gens and Alonso (1992) considers this interaction mechanism between micro and macro structures. Sanchez et al. (2005) formulated and effectively applied the framework to materials to explain the irrecoverable deformations upon reloading and behavior of soils under cyclic loading. This framework gave a better understanding of plastic behaviour of clay and hence applied in the case of barrier in nuclear waste disposal.

1.2 Scope and Objective

The work presented here has two objectives: the uncertainty quantification with regards to parametric uncertainty and the advanced mechanical modeling of the swelling clay using double structure framework.

1.2.1 Uncertainty Quantification

Uncertainty is assessed by the quantification of model outputs and the use of basic statistics like expected value (mean), variance, range and distribution. Additionally, the quantification of model outputs can be compared to measurements as reference data. Monte Carlo analysis is used to estimate the uncertainty in the parameters and their influence on model output response.

In the present study, the uncertainty analysis is performed using the thermal and hydraulic properties in terms of thermal conductivity; soil water interaction (retention) curve and the hydraulic conductivity respectively. Probability Distribution Functions (PDF) of sample parameters are generated and THM response is evaluated for each element of the input parameter sample, using CODE_BRIGHT, a finite element program. And the output is analyzed in terms of dry density, temperature and water content. The cumulative distribution functions (CDF) of output are obtained for different combinations of parameter variations and compared the parametric contribution to uncertainty in model response. Finally, a stochastic model is built by establishing the correlation between the output responses with input parameters.

1.2.2 Advanced Mechanical Modeling of Swelling Clay

A brief discussion is made on the mechanical behavior at the micro and macro structure levels and their interaction between them and the stress strain relationships including the interaction functions between micro and macro structures are defined from the

formulations developed by Sanchez et al. (2005). In this way, it is possible to achieve a more complete understanding of the mechanisms that underlie observed behaviour and irreversible plastic deformations of the clay soil.

The double structure plasticity model is applied to explain mechanical behavior of compacted bentonite barrier used in full scale in situ test, carried out as a part of in the FEBEX project. It is then numerically modeled using CODE_BRIGHT, the finite element program. The changes in the barrier are captured in term of micro and macro void ratio and apparent pre-consolidation pressure. The samples are then collected for modeling odometer tests, which were originally conducted under controlled suction. The results from in situ modeling and odometer tests are then compared with the experimental results.

1.3 Methodology

Broadly, four tasks were accomplished to meet the objectives as outlined in section 1.2. The tasks accomplished were as follows:

Task 1: Parametric Uncertainty

The material properties, which are the interest of study, are identified for their values and defining constitutive law from the experiment data (taken from Villar et al., 2008) and from them, the model parameters are determined deterministically. To define the probability distribution functions (PDF) of the parameters, their entire set of possible

values are required. So, large set of parameters (termed as 'sample realizations') are generated from the limited available experimental data using Bayesian approach (Medina-Cetina, 2006). Integration of the posterior function formed by updating a prior function which is the a-priory knowledge of parameters, with the likelihood function, obtained from the experimental observations, is performed using Monte Carlo integration method which uses the rules of Markov Chains (MCMC) and Metropolis-Hastings (M-H) algorithm (Gilks et al., 1996).

Task 2: Uncertainty Quantification

The generated sample sets are propagated into a finite element code, CODE_BRIGHT, to perform THM analysis. The sets are propagated individually and in combinations and the output response from the model is statistically analyzed between different sources of possible uncertainty. The uncertainty in the response variables is estimated in terms of their mean, variance, and distributive functions, spatially and temporally. Cumulative distribution functions (CDF) are also used to provide probability estimates, i.e. the range and distribution of possible outcome, at different levels of performance. The correlation functions are developed between input parameter and the responses; auto and cross correlation of their THM response.

Task 3: Mechanical Behavior of Bentonite Clay

Then the barrier is numerically modeled using CODE_BRIGHT, the finite element program. The in situ test setup consisting of canister heaters, bentonite barrier and the

host rock, is modeled using 1-D axis symmetric mesh with linear elements. The macro and micro structure properties of the bentonite are used as calculated by in Lloret et al. (2003) respectively. The boundary conditions and the sequence of the program is followed in the stage by stage and time by time as that followed in the in situ test. After the analysis, the THM responses of the material are obtained and are compared to the actual response from the site and the BBM model response from the Gens et al. (2009). Then, the model is analyzed for mechanical behavior in terms of the void ratio and pre-consolidation pressure.

Task 4: Odometer Tests

These odometer tests are again modeled using CODE_BRIGHT with the double structure approach. The results from the task 3 are used to prepare samples for the odometer test analysis. That is, the samples are collected at collected at various distances from the heater. The samples is loaded and observed for their load deformation curves. The boundary conditions in the model are followed same as that of the post-mortem experiments performed on the bentonite blocks retrieved after dismantling the first section of the FEBEX in situ test (Villar and Lloret, 2007).The pre consolidation pressures obtained from model results are then compared with that obtained from the experimental observations.

1.5 Layout of the Thesis

The first part of Chapter 2 contains the description of FEBEX project and the experimental work for the study of near field for HLW repository. Later, theoretical background with all the governing equations and concepts related to thermo-hydrological-mechanical (THM) phenomena of porous media are discussed. In Chapter 3, Monte Carlo simulation method for probabilistic calibration of THM parameters is explained. This method is then applied to calibrate variability in thermal and hydraulic parameters and to quantify the parametric uncertainty of THM response in Chapter 4. A laboratory experiment, conducted as supplementary tests to characterize the THM behavior, is modeled using simple BBM for this purpose. The uncertainties in temperature, dry density and water content are obtained and then studied for their sensitivity. In chapter 5, two of elasto-plastic models: Barcelona basic model and double structure models are discussed in detail with their mathematical formulations. And then, these are then applied to reproduce the behavior of bentonite clay in the FEBEX in situ heating test. In chapter 6, following the in situ test the oedometer tests conducted as part of postmortem analysis is modeled numerically and the results are checked with the experimental observations. Finally, in Chapter 7 summary and conclusions from the research done as well as proposed plan for future work have been presented.

2. NUCLEAR WASTE DISPOSAL

2.1 Disposal of High Level Nuclear Waste

Disposal of high level radioactive wastes, from both domestic and military sources, is a major concern in the recent years in view that the life of most nuclear plants reaching their age limit and vigorous development of new plants. United States itself produces about 2000 metric tons of heavy metal (uranium, plutonium etc.) and stands current greatest producer of high-activity waste (NRC, 2010). The disposal can be done in two ways: reprocessing/destruction and isolation, dilution being not acceptable due to high activity of wastes. Destruction/reprocessing is a costly and extensive process other than the fact that not all radio nuclides can be destroyed. Moreover, recent data show that reprocessing increases the total volume of radioactive waste (DOE, 2008). This leaves the isolation in deep geological repositories the only alternative. According to IAEA Guidelines, the acceptable option for disposal of High Level Radioactive Waste is that of deep geological disposal.

The concept of deep geologic disposal has gained international consensus as the preferred option disposal of high level nuclear waste. Almost all deep geologic disposals are based on four basic concepts: (1) steep holes with two or more canisters, called as Very Deep Hole (VDH). The large holes are drilled to a substantial depth and thereafter filled with buffer and canisters in a stack extending from 2 km depth and downward (Harrison, 2000); (2) wide rooms or vaults with depositional holes with single canisters.

One such is the Canadian concept, where the nuclear waste is isolated with a series of barriers situated in a deep (500-1000m) underground vault, built in a stable geological formation such as granitic rocks of Canadian Shield (AECB 1985); (3) vertical/inclined depositional holes with single canisters (like KBS-3V and KBS-3i concepts). Here, the waste canisters with are inserted in vertical holes, backfilling the corridor with pre-compacted blocks and the pellet filling; (4) very long holes (like KBS-3H, Swiss and Spanish concepts). Swiss concept consists of placing of HLW in horizontal galleries and surrounded by an engineered barrier made up of a heavily compacted mixture of sand and bentonite (Thomas et al., 2008; Delage, 2010). An alternative to these is injection of the HLW directly into the host rock at depth if suitable rock formations exist, but the method is not in use and requires further research.

2.2 FEBEX Project

To study the behaviour of components in the near field for a high-level radioactive waste (HLW) repository in crystalline, FEBEX (Full-scale Engineered Barriers Experiment) project was performed. The project is based on the Spanish reference concept for disposal of radioactive waste in crystalline rock (AGP Granito): the waste canisters are placed horizontally in drifts and surrounded by a clay barrier constructed from highly-compacted bentonite blocks (ENRESA, 2006).

The experimental work consists of three main parts: (1) an in situ test, under natural conditions and at full scale, performed at the Grimsel Test Site (GTS, Switzerland); (2) a

mock-up test, at almost full scale, performed at CIEMAT facilities (Madrid); and (3) a series of laboratory tests to complement the information from the two large-scale tests. In the two large-scale tests, the thermal effect of the wastes is simulated by means of heaters, whereas hydration is natural in the in situ test and controlled in the one performed on the mock-up. The clay barrier is built of various types of blocks, obtained through uniaxial compaction, are arranged in vertical slices. The blocks are monitored, for the evolution of the temperature, total pressure, water content, water pressure, displacements and other parameters continuously in different parts of the barrier and the host rock.

To supplement the performance of large-scale in situ, laboratory tests at different scales in which the conditions of bentonite in an engineered barrier for HLW disposal are simulated. A series of infiltration tests are performed in cells in which the compacted bentonite is subjected to simultaneously to heating and hydration, in opposite directions in order to better understand the hydration process (Villar et al. 2005, 2008).

2.3 Thermo-Hydrological-Mechanical Formulation

The general framework formulation proposed by Olivella et al. (1994) is considered to analyze coupled THM behavior of the clay. The formulation uses multi-phase, multi-species approach in the context of the continuum theory for porous media. The liquid phase may contain water and dissolved air; and the gas phase may be a mixture of dry air and water vapour. Air is considered as a single species regardless of mixture of several

gases. Given the mineral type, solution/precipitation of solids is not considered and local equilibrium is assumed throughout the experiment. The framework constitutes three main parts (i) governing laws (ii) constitutive laws (iii) equilibrium conditions.

2.3.1 Governing Laws/Equations

Mass Balance Equation

The conservation of mass of species can be illustrated as either conservation of mass each species or mass in each phase. The current framework establishes the conservation of mass of each species.

The mass balance for the solid mass in the media is given as

$$\frac{\partial}{\partial t}\left(\rho_s(1-\phi)\right)+\nabla.\left(\rho_s(1-\phi)\dot{u}\right)=0 \tag{2.1}$$

where, ρ_s is the mass of solid per unit volume of solid

Φ is the porosity

$\dot{u}$ is solid mass flow rate at time t

∇ is divergence operator

The fluid species can be in two different forms i.e. water can be mixed in air as vapour form or air may be mixed in the water. In such cases, there is possibility of advective fluxes within the phase. Hence, conserving the fluid in all phases and different flows, the mass balance equation of fluids i.e. water and the dry air is given by

$$\frac{\partial}{\partial t}\left(\theta_l^{\alpha}S_l\phi+\theta_g^{\alpha}S_g\phi\right)+\nabla.\left(\mathbf{j}_l^{\alpha}+\mathbf{j}_g^{\alpha}\right)=f^{\alpha};\ \alpha=\text{water, air} \tag{2.2}$$

where, θ_l^{α} and θ_g^{α} are the masses of fluid per unit volume in liquid and gas phases respectively

$\mathbf{j}_l^{\alpha}$ and $\mathbf{j}_g^{\alpha}$ are the total mass fluxes of fluids in liquid and gas phases

f^{α} denotes the external supply of fluid

Energy Balance Equation

It is assumed that all the phases are in thermal equilibrium at any time which means, they will be at same temperature at any time and the time to obtain thermal equilibrium is neglected. Thus the energy supplied externally is equal to sum of internal energy of each phase in the medium given as:

$$\frac{\partial}{\partial t}\left(E_s\rho_s(1-\phi)+E_l\rho_{lp}S_l\phi+E_g\rho_g S_g\phi)\right)++\nabla.\left(\mathbf{i_c}+\mathbf{j}_{Es}+\mathbf{j}_{El}+\mathbf{j}_{Eg}\right)=f^E \qquad (2.3)$$

where, E_s, E_l, E_g are specific internal energies of solid, liquid and gas phase respectively,

ρ_s, ρ_l, ρ_g are solid density, liquid and gas phase densities respectively,

$\mathbf{i}_c$ is conductive heat flux

$\boldsymbol{j}_{Es}$, $\boldsymbol{j}_{El}$, $\boldsymbol{j}_{Eg}$ are advective energy flux of solid phase, liquid and gas phases respectively

f^E is the energy supply per unit volume in medium

Momentum Balance Equation

The total momentum in the porous medium is expressed in terms of the stresses as:

$$\nabla\cdot\boldsymbol{\sigma} + \mathbf{b}=0 \qquad (2.4)$$

where, $\boldsymbol{\sigma}$ is the stress tensor

$\mathbf{b}$ is vector of body forces

2.3.2 Constitutive Laws

The constitutive law is the relation between two physical quantities that is specific to a material or substance, and approximates the response of that material to external forces. They define the dependent variable response with the independent material variable and explain the behavior of the material when it is subjected to different conditions. A few of such basic laws taken in the framework are given as follows:

Thermal Laws

The heat produced by the disposed waste package as a result of its radioactive decay has to be dissipated through the buffer and backfill into the host rock. This process of heat transfer through the buffer causes moisture diffusion and produces desiccation and shrinkage cracking of the buffer near the heat the heat source (canister). Thus, a buffer material having a good thermal conductivity over a wide range of moisture content is preferred (Radhakrishna and Chan, 1989). Thermal conductivity of an unsaturated soil is the progressive combination of the matter that constitutes the soil and they are determined using conductive flux of heat.

Fourier's Law:

Fourier's law is the basic constitutive law defining the thermal behavior of any media. As it can be seen from the Eq.2.6, the thermal conductivity of the compacted bentonite is combination of the thermal conductivity of solid particles (bentonite), and of fluids (i.e. water and air). How the pore space is filled by the fluid phases is dictated by the phase

degree of saturation (i.e. Sl or Sg). The conductive flux of heat is defined by the Fourier's law which states that rate of heat transfer ($\boldsymbol{i}_c$) through a material is proportional to the negative gradient temperature (ΔT) between the ends the heat passes.

$$\mathbf{i}_c = -\lambda \nabla T \tag{2.5}$$

Where, λ is thermal conductivity.

The thermal conductivity of the clay soil depends on the hydration state of the clay and also the components in the soil (i.e. soil, water, air) given as:

$$\lambda = \lambda_{sat}^{S_e} \lambda_{dry}^{(1-S_e)} \tag{2.6}$$

$$\lambda_{dry} = \lambda_{solid}^{(1-\phi)} \lambda_{gas}^{\phi} \; ; \; \lambda_{sat} = \lambda_{solid}^{(1-\phi)} \lambda_{liq}^{\phi}$$

Where, λ_{dry} – thermal conductivity of dry soil,

λ_{sat} – thermal conductivity of saturated soil,

λ_{solid} – thermal conductivity of bentonite clay,

λ_{liq} – thermal conductivity of liquid entrapped in saturated porous clay,

λ_{gas} – thermal conductivity of gas entrapped in porous clay.

Hydraulic Laws

The engineered barriers are progressively saturated by the pore water coming from the host rock, which infiltrates the barrier at a very low rate owing to its low permeability. This infiltration is initially considered to obey standard unsaturated soils water transfer rules, but indeed the conditions of impeded swelling that are imposed to the engineered barriers present some specifics that make the infiltration process somewhat different (Delage, 2010).

Darcy's Law:

Darcy's law is the basic constitutive law defining the flow of liquid through a saturated porous medium, but can be extended for advective flow in unsaturated soils through relative permeability. The permeability of the medium plays critical role in its hydraulic behavior and depends on the intrinsic permeability (***k***) of the medium and the relative permeability ($k_{r\alpha}$; α=l,g) of the respective fluids. The relative permeability is the ratio of the permeability under the actual (partial saturation) condition to that under saturated condition. Different relative permeability models have been proposed (like van Genuchten, 1980, Gardner, 1958), here the well-known power law in terms of liquid degree of saturation has been adopted. The flow of fluid between two points through a porous media is proportional to the pressure gradient between them.

$$\mathbf{q}_\alpha = -\mathbf{K}_\alpha\left(\nabla \mathbf{P}_\alpha - \rho_\alpha \mathbf{g}\right);\ \alpha = l,g \qquad (2.7)$$

Where, P_l and P_g are liquid and gas pressure respectively,

ρ_l is liquid density,

$\boldsymbol{g}$ is gravity,

$\boldsymbol{K}_\alpha$ is permeability tensor of alpha phase (*l, g*) given as:

$$K_\alpha = k\,\frac{k_{r,\alpha}}{\mu_\alpha};\ \alpha = l,g \qquad (2.8)$$

$\boldsymbol{k}$ is the intrinsic permeability tensor, depends on pore structure of medium

k_{rl} is the relative permeability controlling permeability in the unsaturated regime

μ_α is the dynamic viscosity

Relative Permeability:

The flow of one of the fluids at a point will be reduced due to presence of another fluid present in the pore space in the vicinity of that point. Thus, the permeability of the porous medium would be reduced with respect to the fluid considered. Relative permeability takes into account this reduced pore space of the porous medium for the fluid in question. In an unsaturated soil, the air filled pores are non-conductive channels to the flow of water and therefore can be considered as behaving similar to the solid phase, and the soil can be treated as saturated soil having a reduced liquid degree of saturation. Figure 2.1 shows that k_{rl} approaches 1 soil becomes fully saturated at the same time k_{rg} approaches 0 and vice versa as liquid degree of saturation approaches 0.

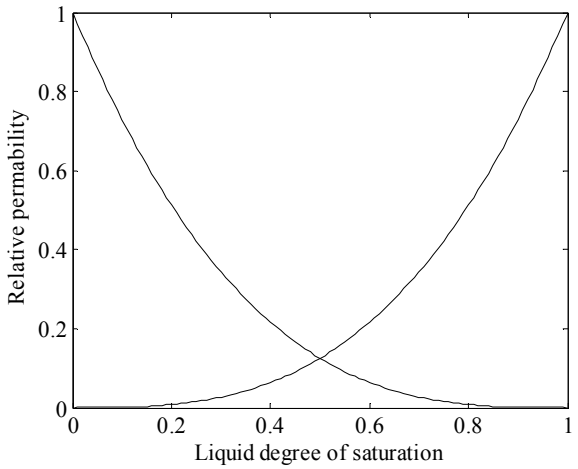

Figure 2.1. Relative permeability of liquid and gas at liquid degree of saturation.

The relative permeability of liquid (k_{rl}) is made dependent on effective liquid degree of saturation (S_e) by the power law as:

$$k_{rl}=S_e^n; \tag{2.9}$$

$$S_e = \frac{S_l - S_{lr}}{S_{ls} - S_{lr}} \tag{2.10}$$

where, S_l is liquid degree of saturation,

S_{lr} and S_{ls} are residual and maximum degree of saturation, respectively,

n is material parameter (n=1,2,3).

Kozeny's Law:

The intrinsic permeability is associated with the soil porous structure (i.e. it is independent of the flowing fluid). The Kozeny's law relates the intrinsic permeability with porosity. In the present study, a modified Kozeny's law is used to relate saturated permeability of deionised water $\boldsymbol{k}$ with porosity is obtained from the measurement of the permeability of FEBEX bentonite compacted at different dry densities and is given as:

$$\mathbf{k} = k_0 \frac{\phi^3}{(1-\phi)^2} \frac{(1-\phi_0)^2}{\phi_0^3}\ \mathbf{I} \tag{2.11}$$

Where, k_0 is the intrinsic permeability corresponding to reference porosity (ϕ_0)

Soil-Water Retention Law:

The soil water retention curve, also known as soil-water characteristic curve, defines the relationship between soil suction and degree of saturation. The knowledge of the curve is of great interest in unsaturated soil, as suction changes are generally related to significance changes in volumetric strain, effective stress, strength and other flow properties. In an unsaturated soil, when the liquid surface is subjected to an air pressure u_a, greater than the water pressure u_w. The pressure difference (u_a - u_w) is referred to as

the matric suction (or capillary pressure, s). The pressure difference causes the liquid surface to curve according to the equation:

$$(u_a - u_w) = s = \frac{2\,T_s}{R_s} \tag{2.12}$$

where, T_s is surface tension,

R_s is radius of curvature of the contractile skin.

The connected soil pores can be considered as rough and twisted capillary tubes allowing the water to rise. The suction (s) varies with mean curvature of the (microscopic) menisci within the pores. As the curvature varies with saturation the suction is also a function of liquid degree of saturation (S_l). A conceptual retention relation can be derived from the soil pore structure (Hassanizadeh & Gray, 1993). There are other empirical retention laws proposed by various researchers (Brooks and Corey, 1966; van Genuchten, 1980; Russo, 1988). A modified van genuchten law has been used to define the retention curve for FEBEX bentonite and is given as:

$$S_e = \left[1 + \left(\frac{s}{P_0}\right)^{\frac{1}{1-\lambda_0}}\right]^{-\lambda_0} f_d \; ; \quad f_d = \left(1 - \frac{s}{P_d}\right)^{\lambda_d} \tag{2.13}$$

where, s (=P_g - P_l) is suction,

P_0 is Air Entry Value,

λ_0 is parameter controlling shape of the curve,

f_d is function included to obtain more suitable values at high suctions

P_d is parameter related with suction at zero degree of saturation

λ_d is model parameter

The value P_d is maximum suction value that can be obtained which is associated with the least possible liquid degree of saturation (S_l). By convention it is assumed that a sample has a S_l =0, after drying it 24 hours in an oven (ASTM D4643 - 08). According to Fredlund and Xing (1994) the maximum suction in these oven conditions is 1,000 MPa. Other researchers assume the value around 1100MPa (Gens et al., 2009, Sanchez et al., 2011). In this work we assumed the same. Thus uncertainties related to P_d have been neglected and a constant value is assumed.

Non-Advective Flow Law:

In unsaturated conditions water is also present in the gas phase as vapor. The vapor transfer in the gas phase is due to the gradient of vapor concentration and the transfer of trapped air in the liquid phase is due to the gradient of concentration of air in liquid phase, both can be calculated using the Fick's law. So, the molecular diffusion of water vapour in gas phase is given as:

$$\mathbf{i}_{\mathbf{g}}^{w}=-D_g^w\nabla\omega_g^w=-\left(\phi\rho_g S_g\tau D_m^w\mathbf{I}+\rho_g D'_g\right)\nabla\omega_g^w \qquad (2.14)$$

Where $\mathbf{i}_{\mathbf{g}}^{w}$ is non-advective mass flux of water in gas,

D_g^w is dispersion tensor, D'_g is mechanical dispersion tensor,

ω_g^w is mass fraction of water in gas,

τ is tortuosity

D_m^w is molecular diffusion coefficient of vapour in gas

Mechanical Law

The maintenance of structural integrity of the barrier during its lifetime is the most important characteristics of the bentonite clay. The stress developed inside the barrier influence its volumetric behavior in terms of its elastic and plastic deformations.

Barcelona Basic Model:

To define mechanical behavior of the clay soil, a constitutive model BBM (Barcelona Basic Model) given by Alonso et al. (1990) and Gens (1995) has been adopted. The model is elasto-plastic strain hardening model, where a yield surface forming the limit of elastic strains is defined as function of suction and temperature. As the stress path of a material cross over, this yield zone expands thus hardening the soil. The model is explained in detail in Chapter 5 and the related equations are summarized as following:

$$\dot{\epsilon}_v^e = \frac{k_i}{(1+e)}\frac{\dot{p}}{p} + \frac{k_s}{(1+e)}\frac{\dot{s}}{(s+0.1)} + (\alpha_0 + \alpha_2 \Delta T)\dot{T}\ ; \qquad \dot{\epsilon}_s^e = \frac{\dot{j}}{G} \tag{2.15}$$

$$k_i = k_i(1+\alpha_s S); \tag{2.16}$$

$$k_s = k_{s0}(1+\alpha_s \ln p/p_{ref}) \tag{2.17}$$

$$G = \frac{E}{2(1+\nu)} \tag{2.18}$$

2.3.3 Equilibrium Restrictions

Finally, some equilibrium restrictions are assumed to take care of any unknown parameters. These restrictions link the state variables with the amount of species in the phase and any changes in the phase in equilibrium of the medium. In general, the phase

changes are considered to be instant and thus a local equilibrium is considered. For instance, the chemical equilibrium is assumed for both dry gas and vapour in both liquid and gas phases since chemical processes are much faster compared to transport process. The concentration of water vapour in gas phase is given by psychrometric law and solubility of dry gas in water is given by Henry's law.

Psychometric Law

The vapor concentration in the gaseous phase (θ_g^w) is governed by the psychometric law, which can be expressed as:

$$\theta_g^w=(\theta_g^w)^0 \exp(-\frac{s\, M_w}{R\,(273.15+T)\rho_l}) \tag{2.19}$$

where, $(\theta_g^w)^0$ is the vapour concentration in gas phase in equilibrium with liquid,

$$(\theta_g^w)^0=\frac{M_w P_{v(T)}}{R\,(273.15+T)};\ \text{where } P_{v(T)}=136075 \exp(-\frac{5239.7}{273.15+T})$$

s is the suction at temperature T,

M_w is the molecular mass of water (0.018 kg/mol),

R the gas constant (8.314 J/mol/ºK),

ρ_l is the liquid density.

Henry's Law

Henry's law is adopted to define the amount of air dissolved in water. This law expresses a linear relationship between the concentration of air in dissolution and the partial pressure of air (P_a) in the gaseous phase:

$$\theta_g^a = w_a^i \rho_l = \frac{P_a}{H}\frac{M_a}{M_w} \tag{2.20}$$

where, M_a is the molecular mass of the air (0.02895 kg/mol),

H is Henry's constant (1000 MPa).

2.4 FEBEX Bentonite

The compacted bentonite used in the FEBEX Project is called FEBEX bentonite, which was selected by ENRESA (the Spanish Agency for Radioactive Waste Management) as a suitable material to backfill and seal HLW repositories. The FEBEX bentonite was extracted from the Cortijo de Archidona deposit (Almeria, Spain) and processed as follows: disaggregation and gently grinding, drying at 60 8C and sieving by 5 mm. It is made up of a montmorillonite–illite mixed layer, with 10%–15% of illite layers. Likewise it contains variable quantities of quartz (2F1%), plagioclase (2F1%), K-felspar, calcite and opal-CT (cristobalite-trydymite, 2F1%).

The bentonite blocks are manufactured in shape of 12.5-cm thick circular crown sectors were arranged in vertical slices giving place to the geometry of the barrier. It is uniaxially compacted at about 14% water content giving dry density of about 1.7 g/cm^3 (ENRESA, 2006). The physico-chemical properties of the FEBEX bentonite, as well as its most relevant thermo-hydro-mechanical and geochemical characteristics are summarised in the final reports of the project (ENRESA, 2006).

The liquid limit of the bentonite is 102 ± 4%, the plastic limit is 53 ± 3%, the specific gravity 2.70 ± 0.04, and 67 ± 3% of particles are smaller than 2lm. The hygroscopic water content in equilibrium with the laboratory atmosphere is 13.7 ± 1.3%. The external specific surface area, using the BET technique, is 32 ± 3 m^2/g and the total specific surface area, using the hygroscopicity method, is about 725 m^2/g. The analysis of the mercury intrusion data reveals that the intra-aggregate pores (smaller than 0.006lm) represents the 73–78% of total pore volume when the bentonite is compacted at a dry density of 1.7 g/cm^3.

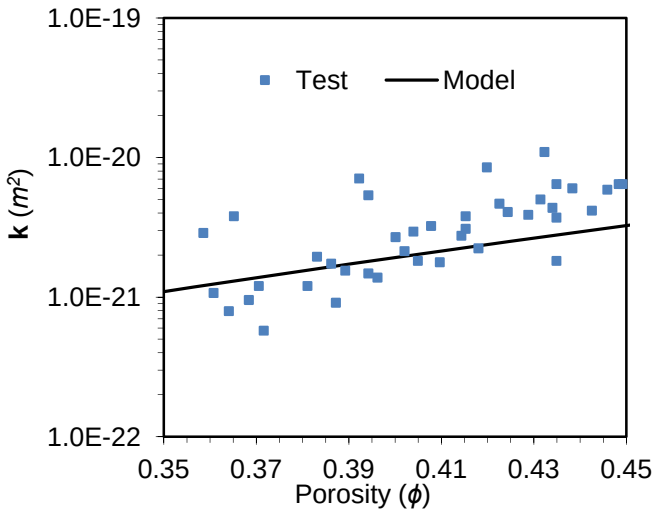

Figure 2.2. Experimental data and adopted model for intrinsic permeability of FEBEX bentonite (Source: Villar et al., 2008)

Figure 2.2 shows the experimental observations of the saturated permeability to deionised water **k** (Eq.2.11), of samples of untreated FEBEX bentonite compacted at

different dry densities. It can be related with porosity through a modified Kozeny's law by Eq.2.11, where, k_0 of 1.9 x 10^{-19} m^2 is observed at reference porosity (ϕ_0) of 0.40.

The retention curve of the bentonite was determined in samples compacted to different dry densities (Lloret et al., 2004). The volume of the samples remained constant during the determinations, since they were confined in constant volume cells. To impose the different relative humidity the cells were placed in desiccators with sulphuric acid solutions of various concentrations. A modified van Genuchten law (Eq.2.13) with P_0 = 28 MPa, λ_0 = 0.18, P_d = 1100 MPa, λ_d = 1.1 and η = 0.7 has been adopted to model the dependence of the degree of saturation on suction (Figure 2.3).

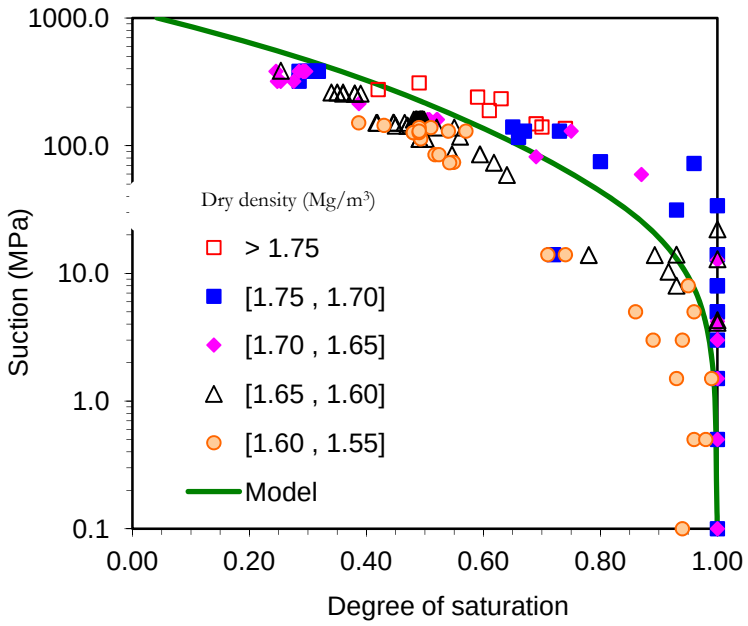

Figure 2.3. Retention curve adopted in the analyses, the experimental data for FEBEX bentonite (Source: villar et al., 2008)

The parameters of relative permeability law for the bentonite were determined from back-calculation of hydration test carried out in small cell (Pintado et al., 2002) and given as: S_{lr} = 0.01; S_{ls} = 0.01 ; n = 3. And for the vapour diffusion law, a tortuisity τ = 0.8. The viscosity for liquid and gas are given as:

$$\mu_l = 2.1 \times 10^{-12} e^{\left(\frac{1808.5}{273.15+T}\right)} \tag{2.21}$$

$$\mu_g = \frac{1.48 \times 10^{-12} e^{\left(\frac{1808.5}{273.15+T}\right)}}{\left(1+\frac{119.4}{273+T}\right)} \tag{2.22}$$

The thermal conductivity λ, of the compacted bentonite at laboratory temperature is related to the degree of saturation S_e (Eq.2.6). Figure 2.4 presents the experimental values obtained for the FEBEX bentonite together with the assumed model with λ_{dry} equal to 0.47 and λ_{sat} 1.15.

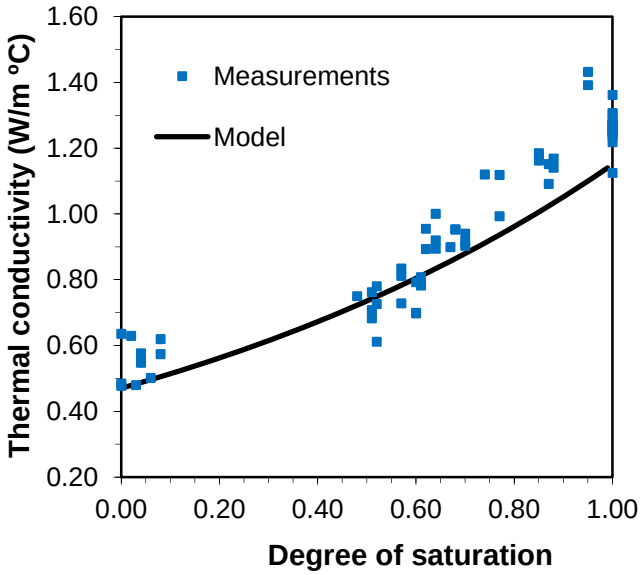

Figure 2.4. Thermal conductivity of FEBEX bentonite experimental measurements and the fitting model (Source: Villar et al., 2008)

The specific energy of the solid phase of bentonite is (E_s/T) is 1091 J/kg°C. The thermal expansion coefficient of the bentonite (α_o) is derived as 1.5×10^{-4} °C^{-1}.

Finally, the parameters of the mechanical model have been determined from back-calculation of swelling pressure tests performed by Villar (2002) and are tabulated as below:

Table 2.1. Parameters of the mechanical constitutive model (Gens et al, 2009).

Elastic Parameters		Plastic Parameters	
κ_o	0.05	$\lambda_{(0)}$	0.15
κ_s	0.25	r	0.925
μ	0.40	ζ	0.10
α_s	-0.003 MPa	ρ	0.20 °C^{-1}
α_{sp}	-0.161	K	0.10
p_{ref}	0.01	p_c	0.50 MPa
α_0	1.5 x 10^{-4} °C^{-1}	M	1.00
α_2	0 °C^{-2}	α	0.53
		P_o*	12.0 MPa

3. PROBABILISTIC CALIBRATION

3.1 Uncertainty Analysis

The term ‘uncertainty’ means the randomness of a parameter with respect to its true value. It is an appropriate expressing of variability of the parameter during its measurement. The uncertainty is a possible value that the parameter might take over a range (Kline, 1985) and is a statistical variable. And uncertainty analysis is the estimate of uncertainty in a system’s performance resulting from the uncertainty of one or more factors associated with the system. Such an analysis requires definition of a system, description of the uncertainties in the factors that are to be investigated and the characteristics of the system that is to be observed.

The success of a mathematical model lies in its capability to capture every possible response of the material behavior taking into account the physical description of its parameters with regards to its actual behavior. But, often, their results may not be in good agreement with experimental observations. The reason could be of two types: (1) there may be some error in recording the true experimental observations which could be due to variations in to measuring devices, or handling errors by the operator or both, (2) there could be an error in finding out the material properties, which when used to ascertain the parameter values. In both cases, there exists uncertainty in form of data uncertainty in formal case and parametric uncertainty in later case.

Most models are often insufficient in describing physical interpretation of the parameters and their variation, due to which unexpected errors and misleading conclusions are obtained. For instance, in geotechnical engineering, when a model is applied deterministically to a soil condition for which it is not calibrated, the uncertainty in some measured parameters may become negligible, while some unidentifiable parameters may become sensitive. And when we extend an identified local scale model built in laboratory to a larger scale of in-situ, the resulting spatial variability must be explicitly accounted for since variability at the local scale is normally much smaller than the scale of the system concerned (Kueper and McWhorter, 1992). Thus there is huge amount of uncertainty in the material properties itself, which is further propagated to model response. Hence, calibration of the parametric uncertainty within the constitutive model is a key process for accurate predictions.

3.2 Methodology

The techniques for quantifying parametric uncertainty in the performance assessment of radioactive waste disposal were proposed and reviewed long before in early 90's (Tiktinsky, 1988; Zimmerman, 1990; Helton, 1993). These include Monte Carlo simulations, differential analysis, etc. In the present work, probabilistic calibration method proposed by Medina-Cetina (2006) is followed to quantify the THM response of bentonite clay used as material in nuclear waste repository, using the probability distributions of thermal and hydraulic parameters as input. The technique basically involves repeated evaluation of the model, so that the output response is estimated in the

form of probability distribution. In the first step, the input parameters, which are the interest of study, are identified for their values and defining constitutive law through various sources including experiments and previous study. Their distribution of observations with the constitutive law is selected. The sample observations and the distribution are used in any sampling techniques, to generate a large set of parameters called 'sample realizations'. Then, this set of parameters is used to evaluate the model and the obtained output response is then statistically analyzed for uncertainty analysis. The uncertainty can be expressed in terms of mean, variance, and distribution functions. Often, cumulative distribution functions (CDF) are used by providing probability estimates for different levels of performance. The steps involved are further explained below in detail.

3.3 Probabilistic Calibration Method

3.3.1 Parameter Estimation

Conventionally, the parameters of a constitutive model are estimated from the data obtained by performing the limited number of available experiments on the phenomena of interest (*e.g.* Villar et al. 2008). The experiment is repeated at under similar conditions, so that the material property is measured for entire population set of control variables. But, it is practically impossible to observe entire target population, that is, the samples representative of entire population cannot be collected. In general practice, the model formed from few collected samples is generalized over entire population.

So, for accurate representation of entire population, samples are to be generated from the limited observations in the form of random variables leading to random parameters. The randomness of the parameters along with their uncertainty, due to various other reasons explained before, is captured by probabilistic formulation using Bayesian inference. The possible range and distribution of constitutive parameter values are expressed in form of probability density function (PDF) using their prior distribution, obtained from previous knowledge or experience, and the likelihood, obtained from the predicted model performance with respect to the experimental observations. By updating the prior with likelihood of model performance we get a joint PDF called posterior, and when integrating the posterior yields the probability of occurrence of the parameters in the possible range. The various elements and method involving the Bayesian inference are explained in the following section. The variation in parameters is expressed in terms of mean, standard deviation, and covariance.

Bayesian Inference

Bayesians represent uncertainty about unknown parameter values by probability distributions and proceed as if parameters were random quantities (Gilks et al., 1996). If a set 'ε' of represent the observed experimental values x_1, $x_2 \ldots x_n$, and θ represent the model parameters, then their joint probability distribution over all random quantities is given by:

$$P(\mathcal{E},\theta)=\pi(\theta)P(\mathcal{E}|\theta) \tag{3.1}$$

The term $P(\mathcal{E}|\theta)$ is called likelihood also denoted as $L(\theta)$; and is expressed as:

$$L(\theta)=P(\ .\mathcal{E}|\theta)=\prod_{i=1}^{n} f_x(x_i|\theta) \tag{3.2}$$

The term $\pi(\theta)$ is called prior; it is distribution of the parameters 'θ', either assumed with prior knowledge and experience with parameter or obtained from any previous study. Using Bayes' theorem, when we update the prior distribution of the parameter with the knowledge of present experiments in terms of likelihood, we get a posterior density function which is expressed as:

$$f''(\theta|x_i)=\frac{[\ \prod_{i=1}^{n} f_x(x_i|\theta)dx\ ]\pi(\theta)}{\int_{-\infty}^{\infty}[\ \prod_{i=1}^{n} f_x(x_i|\theta)dx\ ]\pi(\theta)d\theta} \tag{3.3}$$

Since the denominator is independent of θ and is considered as a normalizing constant, the posterior is proportional to prior ($\pi(\theta)$) times the likelihood ($L(\theta)$).

Prior

The prior is the first of two sources of information used to obtain the posterior distribution of variable. It gives the distribution of constitutive parameters as found from the theoretical and experimental sources. The prior information can be distinguished into four groups: Non-informative prior, conjugate prior, posterior updated prior and engineering judgmental prior. The prior could assume any form of distribution depending on parameter nature obtained from theoretical and experimental knowledge. In the absence of any a-prior information on the nature of parameters, a non-informative prior which is generally uniform distribution prior is used. When the likelihood has a special form, conjugate prior validated with experimental observations can be assumed yielding the posterior which has the distribution same as that of the likelihood function.

Furthermore, if there are multiple parameters influencing as per a constitutive law, a multivariate prior can also be assumed. This multivariate prior distribution is obtained from the joint probability distribution of all the parameters defining the constitutive law and could assume any standard form like uniform, Gaussian or lognormal. The common Gaussian and log-normal prior distributions are given as:

$$\pi(\theta)=\prod_{i=1}^{n}\frac{1}{(2\pi)^{n/2}\sqrt{\det \dot{C}}}\exp\left[-\frac{1}{2}\left(\dot{\theta}-\theta_{prior}\right)^{T}\dot{C}^{-1}\left(\dot{\theta}-\overline{\theta_{prior}}\right)\right] \quad (3.4)$$

$$\pi(\theta)=\prod_{i=1}^{n}\frac{1}{(2\pi)^{n/2}\sqrt{\det \ddot{C}}}\exp\left[-\frac{1}{2}\left(\ln\left(\ddot{\theta}\right)-\theta_{prior}\right)^{T}\ddot{C}^{-1}\left(\ln\left(\ddot{\theta}\right)-\theta_{prior}\right)\right] \quad (3.5)$$

where, θ_{prior} represent the prior parameter vector,

$\overline{\dot{\theta}}$ and $\dot{C}$ are parameter mean vector and covariance matrix respectively,

$\overline{\ddot{\theta}}$ and $\ddot{C}$ are parameter mean vector and covariance matrix of underlying log-normal parameters respectively

The covariance matrix defines the cross correlation between the observed parameters themselves. Since parameter samples are generated as random variables, it is important to consider the correlation within the parameters when defining prior, to avoid inaccurate physical relationship between the parameter values and making the generated samples have no physical sense. This is very particular in the case where the parameters are naturally correlated in space. For instance, permeability of unsaturated porous media can be calculated either from the liquid flow or gas flow. It would seem that the flows with respect to liquid and gas are independent, but they may be correlated with porosity or

relative permeability. In another example, the shape of retention curve depends on its parameters – P_0, λ_0 and λ_d and their values are assumed in such a way that the retention curve represent or fit the experimental observations. The parameters air entry value P_0 and pore size distribution index λ_0 are correlated in such a way that if one increases, the other should decrease.

Likelihood

Likelihood is the second source of information required to obtain posterior distribution. It is also a measure of predictive model performance given the observational data. If 'ε' represents the set of experimental data observations (x_1, $x_2 \ldots x_n$) and θ represents the set of parameter values obtained from them, then the probability of ε given θ is given by f(ε|θ) which is also called the likelihood of θ given ε. That is, the likelihood is the probability of observing the experimental data set 'ε' from the random sample of population *X,* with probability density function $f_X(x)$ and parameter distribution of θ; and could assume as proportional to the PDF of observed experimental values (x_1, $x_2 \ldots x_n$). Assuming that the observed values are independent to each other as they are obtained by independent experiments, the likelihood of model is obtained from the joint probability distribution of each observation which the product of probability of occurrence of each experimental observation. It is denoted as $L(\theta|x_i)$ or $L(\theta)$ and is expressed as:

$$L(\theta|x_i)=f(x_1;\theta)f(x_2;\theta)\ldots f(x_n;\theta)= \prod_{i=1}^{n} f_x(x_i|\theta) \qquad (3.6)$$

Similar to prior, the likelihood could assume any distribution like Gaussian or log-normal depending on the difference between observations and predictions of

experimental data set 'ε'. The common Gaussian and log-normal likelihoods are given as below

$$L(\theta)=\prod_{i=1}^{n}\frac{1}{\sqrt{2\pi}\sigma}\exp\left[-\frac{1}{2}\left(\frac{x_i-\mu}{\sigma}\right)^2\right] \tag{3.7}$$

$$L(\theta)=\prod_{i=1}^{n}\frac{1}{\sqrt{2\pi}\zeta x_i}\exp\left[-\frac{1}{2}\left(\frac{\ln(x_i)-\lambda}{\zeta}\right)^2\right] \tag{3.8}$$

Where, x_i represent the experimental observations,

μ and σ are mean and standard deviation of Gaussian experimental response,

λ and ζ are mean and standard deviation of log-normal experimental response.

Normally, it is assumed that the observations are independent as they recorded by repeatedly conducting the experiments which have no influence and thus independent to each other.

Posterior

The posterior is the joint probability function of the prior of the parameters and the likelihood function. From the equation, we can observe that the posterior is a conditional distribution for model parameters given the observed data. Integrating the posterior will yield the distribution of parameters updated with the current experimental observations. But, when the posterior is of non-standard distribution or if it is a multivariate distribution, then performing integration becomes very difficult, sometime impossible, as there are a number of parameters to integrate over (Martinez and Martinez, 2001). To avoid this situation, Monte Carlo integration is adopted for integration of posterior using the rules of Markov Chains (MCMC) and Metropolis-Hastings (M-H).

The Monte Carlo integration estimates the integral by obtaining the samples X_t from the prior distribution and then calculating the expected posterior value. The samples obtained from prior do not have to be independent as long as they are obtained from entire domain of prior and in correct proportions. This is done by constructing a Markov chain that has posterior as its stationary distribution.

Markov Chains

In generating the sample variables, the occurrence of a given event in one trial may affect the occurrence of same event in next trial i.e. the probability of value random variable in given sequence may depend on the previous sequence which leads to conditional probability. Thus the realizations of this sequence of random variables such that next state X_{t+1} is distributed by $P(X_{t+1} \mid X_t)$ is called as Markov chain. As the sequence increases, the chain will forget its initial state and will converge to a stationary distribution and sample points X_t become dependent sample from that distribution, also known as target distribution.

Metropolis-Hastings Algorithm

The Metropolis-Hastings method is generalization of the Metropolis technique of Metropolis et al. (1953). A chain of random variables is created to produce the stationary target distribution using Metropolis-Hastings algorithm. The state of the chain at $t+1$ is sampled as a candidate point Y from a proposal distribution $P(.| X_t)$. And then this candidate point is accepted as the next state of chain with the probability $\alpha (X_t, Y)$ given

as below. If the point *Y* is not accepted, the chain does not move ($X_{t+1} = X_t$) and another value of *Y* is taken from the proposal distribution and so on (Medina-Cetina, 2006). The starting value of the chain is the deterministic value provided by Villar et al., 2008.

$$\alpha(X_t,Y)=\min\left\{1,\frac{\pi(Y)P(X_t|Y)}{\pi(X_t)P(Y|X_t)}\right\} \quad (3.9)$$

The algorithm of Metropolis-Hastings is generalized as:

1. Initialize the chain to X_0 and set t = 0,
2. Generate a candidate point *Y* from P (.|X_t).
3. Generate 'U' from a uniform (0, 1) distribution.
4. If $U \leq \alpha (\boldsymbol{X}_t, Y)$ then set $\boldsymbol{X}_{t+1} = Y$, else set $\boldsymbol{X}_{t+1} = \boldsymbol{X}_t$
5. Set t = t+1 and repeat steps 2 through 5.

When implementing the Metropolis-Hastings algorithm, the scale of proposal distribution affects the efficiency of MH algorithm. If small steps are taken, then acceptance probability (α) will be high, yielding a higher rate of acceptance but the chain will take longer time to get stationary distribution. On the other hand, if large steps are taken, the chain may take less time, but the chain may go to range tails resulting in low acceptance probability. So, the step size should be taken of enough size to balance the time taken to reach stationary distribution and with optimum acceptance probability.

One issue that needs addressing is how long the chain has to be run. When the chain has been run for '*m*' iterations such that further iterations yielding the sample points X_t, t = *m*+1 … n, which form the stationary distribution, then we can discard the first *m*

iterations and use the remaining *n-m* samples as the target samples with particular distribution. The number of samples that are discarded *m* is called the burn-in samples and the size of the burn-in samples can be varied in various methods. One such common method is to estimate the expected value of the chain and where the variation between two consecutive trials is less than a minimum value δ, until then chain is burnt and further samples are taken as target samples.

3.3.2 Performance of Conceptual Model

The conceptual model simplifies the real system into a mathematical model, which in turn can be solved using analytical or numerical techniques. Limited capability to formulate important processes and their associated couplings; insufficient data to such process may lead model uncertainty. Other contributing factors include the boundary conditions, spatial and temporal scales of assumed process, extension of the model to situations different from those on which it is built. Hence, it is necessary to take into consideration the model uncertainty in uncertainty quantification.

3.3.3 Quantification of Model Response

Next step is to propagate the distribution parameters into the model and observe its output response. The model is run repeatedly by taking each set of parameters from their stable target distribution, obtained from previous section 3.3.1. Again, the number of times that the model has to be run depends on the statistical variation of its output data. It should be taken care that the vector of the values of each parameter, passed into the

model, should have the same statistics (mean and variance) as that of their parent set i.e. the target distribution, so as to take the entire range of the parameter. The response output from the model is assembled and analyzed for spatial-temporal statistics.

First Order Statistics

The first order statistics which includes mean (expected value), standard deviation (variance) are the classical method to express the uncertainty of a variable. The mean value or expected value gives a good approximation of expected pattern of the response variable both spatially and temporally; and the standard deviation gives the deviation relative to the mean value and gives the measure of variable dispersion - lower the value, more certain is the variable. If X is a continuous random variable with PDF, $f_x(x)$, then the expected value and variance are given by:

$$E(X)= \int_{-\infty}^{\infty} x f_x(x)dx = \mu_x \tag{3.10}$$

$$Var(X)= \int_{-\infty}^{\infty} (x-\mu_x) f_x(x)dx \tag{3.11}$$

Further, the unbiased mean and standard deviation of sample variables are given by:

$$\bar{x}= \frac{\sum_{i=1}^{n} x_i}{n} \tag{3.12}$$

$$s^2= \frac{\sum_{i=1}^{n} (x_i-\bar{x})}{n-1} \tag{3.13}$$

Second Order Correlation Statistics

The responses of the material are directly or indirectly related to the material properties by different laws and corresponding equations. But, sometimes, defining a direct relation of the uncertainty in corresponding response with variation of the input properties and becomes difficult especially when there is non-linear statistical relationship. So, they can be related statistically by the covariance of those random variables. The covariance is the measure of degree of linear relationship between two random variables.

A joint second moment of the random variables X and Y is defined as:

$$E(X\,Y)= \iint_{-\infty}^{\infty} x\,y\,f_{X,Y}(x,y)dx\,dy \tag{3.14}$$

If the variables are statistically independent (i.e. whether one of them occurs makes it neither more probable nor less probable that the other occurs), then this becomes

$$E(XY)= \iint_{-\infty}^{\infty} xy\,f_{X,Y}(x,y)dx\,dy = \int_{-\infty}^{\infty} xf_X(x)dx \int_{-\infty}^{\infty} yf_Y(y)dy = E(X)E(Y) \tag{3.15}$$

And the covariance which is the joint central moment of X and Y is given by

$$Cov(X,\,Y)= E\left[\left(X-\mu_X\right)\left(Y-\mu_Y\right)=E(X\,Y)-E(X)E(Y)\right] \tag{3.16}$$

The physical significance of covariance may be inferred from the above equation (Eq. 3.16). If the Cov(X,Y) is large and positive, the values of X and Y tend to be both large or both small relative to their respective means, whereas if Cov(X,Y) is large and negative, the values of X tend to be large when the values of Y are small and vice versa, relative to their respective means. If the Cov(X,Y) is small or zero, then there is weak or no (linear) relationship between the values of X and Y; or the relationship may be non-linear. For practical purposes, the covariance is normalized and is expressed as correlation coefficient, which is defined as:

$$\rho = \frac{Cov(X,Y)}{\sigma_X \sigma_Y} \tag{3.17}$$

The correlation coefficient is dimensionless and varies between -1.0 and +1.0. If the correlation coefficient is equal to $\pm$ 1.0, then the variables *X*, *Y* are said to be linearly related. If it is zero, they are randomly related and intermediate values means their distribution is scattered.

It is proposed to estimate the covariance and correlation coefficient of within the response output themselves and with each of their possible combination with their spatial and temporal reference. The correlation coefficient between any two variables gives the effect of spatial and temporal variations of one variable over the other. The correlation of output response with the input parameter in spatial-temporal space will give the impact of input parameter on the output response. It also gives us the estimate of local variability of material properties depending on the actual observations at given time and location. Autocorrelation, referring to the correlation to itself at different locations and duration, gives the variation of the response variable with its own past and future values at different locations. For instance, the positive autocorrelation might be considered a specific form of "persistence", a tendency for a system to remain in the same state from one observation to the next. Similarly, cross correlation refers to correlation between two different responses. It gives us an estimate variation of one unknown response at particular time and space, when other response is known at any other time or at location.

4. UNCERTAINTY QUANTIFICATION OF THM BEHAVIOR

4.1 Problem Description

4.1.1 Experimental Setup

The behavior of a HLW repository is characterized by the changes that may occur in thermal, hydraulic, mechanical properties as a result of the combined effects of heat generated by the radioactive decay and of the water supplied by the surrounding rock. Similar environment is simulated in a series of tests performed with cylindrical cells of length 60 cm, diameter 7 cm (Villar et al., 2005) as shown in Figure 4.1. Inside the cells, six blocks of FEBEX bentonite compacted to dry density 1.65 g/cm^3 were piled up similar to compacted bentonite blocks used in the HLW repository in crystalline rock (ENRESA, 2006).

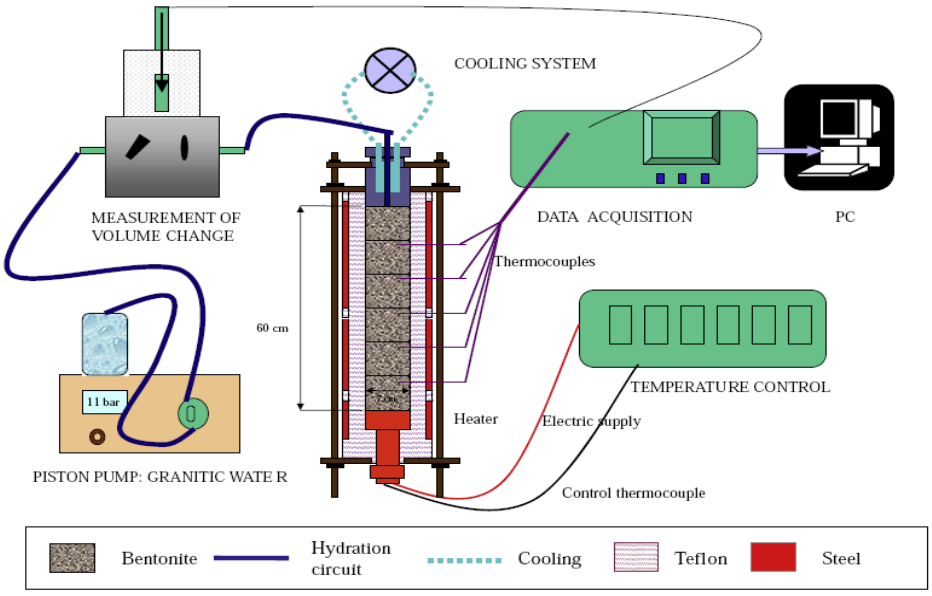

Figure 4.1. Experimental setup for the infiltration tests (Villar et al., 2008).

The bottom surface of the material was heated at 100°C and the top surface was injected with granitic water. A series of seven such tests were performed for different periods of time (two of 0.5 year duration, two of 1 year duration, two of 2 years duration and one of 7.6 years duration).

Initial Conditions

The actual average initial water content of the bentonite in the seven tests performed was 13.6%, and the average initial dry density was 1.66 g/cm^3. The bottom part of the cell was a flat stainless steel heater set during the tests at a temperature of 100°C, which is the temperature expected on the surface of the waste container in the Spanish concept. Over the upper lid of the cell there was a deposit in which water circulated at room temperature (20 - 30°C). Hydration with granitic water (salinity 0.02%) took place through the upper surface under an injection pressure of 1.2 MPa. The number of thermocouples in each cell was 2, 3 or 5. Only the 7.6-year duration test was not instrumented with thermocouples.

4.1.2 Finite Element Model Formulation

In the experimental setup, the flow of fluid and heat transfer is observed to be in one dimension, heating from one end and hydrating from other. Hence a 1D finite element mesh with 50 linear elements is created to represent the one dimensional cell. These elements are assigned the properties of compacted bentonite used in the experiment. The boundary conditions of heating to 100°C at one end and hydrating to the liquid pressure

of 0.1 MPa are maintained at either ends. A fully coupled thermo-hydro-mechanical (THM) analysis was performed using a finite element program, CODE_BRIGHT.

4.2 Calibration of THM Parameters

In the present case, the uncertainty is assessed using the thermal and hydraulic properties in terms of thermal conductivity, retention curve and hydraulic conductivity respectively. The sample realizations are generated from the experimental data (Section 2.4) using the procedure mentioned in Section 3.3.1. From the generated samples sets, equal numbers of realizations are collected from each set. The collected sample sets of realizations have the same distribution as that of their original distribution i.e. the target distributions. In our case, 60,000 realizations are collected from each set. Each set of realization is then passed to the THM model to simulate the multi-physics analysis The output response corresponding to each input are collected which are used as the to get the probability distribution of output response.

4.2.1 Thermal Conductivity

Figure 2.4 presents thermal conductivity experiments conducted on FEBEX compacted bentonite at various degree of saturation. The model proposed by Villar et al. (2008) is adopted as our model to generate a number of realizations. The adopted model has the value of thermal conductivity of dry sample λ_{dry0} as 0.47 W/m°C and the value of thermal conductivity of saturated sample λ_{sat0} as 1.15 W/m°C.

From the experimental values of thermal conductivity of bentonite from previous studies, the prior of each parameter is assumed as its reciprocal values. Thus the joint prior of dry and saturated thermal conductivities is given as:

$$\pi(\lambda)=\frac{1}{\lambda_{dry}\lambda_{sat}} \tag{4.1}$$

From the Figure 2.4, the values tend to be distributed equally on both sides of the model and the pattern is same as that of Gaussian distribution. Thus a multivariate Gaussian likelihood of the observation values is assumed and is given as:

$$f(\lambda|\lambda_{dry},\lambda_{sat})=\prod_{i=1}^{n}\frac{1}{\sqrt{2\pi}\sigma}\exp\left[-\frac{1}{2}\left(\frac{\lambda_i-\lambda_{sat}^{S_{ei}}\lambda_{dry}^{(1-S_{ei})}}{\sigma}\right)^2\right] \tag{4.2}$$

Where, λ_i represents each independent observed conductivity value from experiments

S_{ei} is degree of liquid saturation at which the conductivity is observed

σ is the standard deviation of the observed values

n is number of experimental observations, here n=78.

$\lambda_{sat}^{S_{ei}}\lambda_{dry}^{(1-S_{ei})}$ is the mean of the conductivity at given saturation (our assumed model)

Therefore, the posterior of the random sample (λ_{dry}, λ_{sat}) which is proportional to prior times the likelihood is given as:

$$f(\lambda_{dry},\lambda_{sat}|\,\lambda_{obs})\propto\frac{1}{\lambda_{dry}\lambda_{sat}}\ X\ \exp\left[-\frac{1}{2}\sum_{i=1}^{n}\left(\frac{\lambda_i-\lambda_{sat}^{S_{ei}}\lambda_{dry}^{(1-S_{ei})}}{\sigma}\right)^2\right] \tag{4.3}$$

Following the Metropolis-Hastings method, a candidate point λ_u is selected from a proposal multivariate normal distribution $q(.|\lambda_l)$ with the adopted model as initial mean

and constant standard deviation given as product of mean and assumed covariance. The covariance matrix is assumed to be a diagonal matrix with covariance of 0.001. The mean is then updated to the accepted candidate point as the chain is created. The initial mean and standard deviation are given as:

$$q_{\mu_0}=[\lambda_{sat_0} \quad \lambda_{dry_0}] \tag{4.4}$$

$$q_{\sigma}=q_{\mu_0}\begin{bmatrix}0.001 & 0\\ 0 & 0.001\end{bmatrix} \text{ and } q_{\sigma_0}=\begin{bmatrix}0.00115 & 0\\ 0 & 0.00047\end{bmatrix} \tag{4.5}$$

A chain of realization sets of λ_{sat} and λ_{dry} was created and after burning some realizations, 300,000 realizations are taken. These realizations formed a stable distribution and the correlation between the parameters is shown in Figure 4.2. The relative frequency of these 300,000 realizations and their distribution are shown in Figure 4.3 and Figure 4.4. It should be observed that the distributions are very near to the Gaussian distribution with very slight difference.

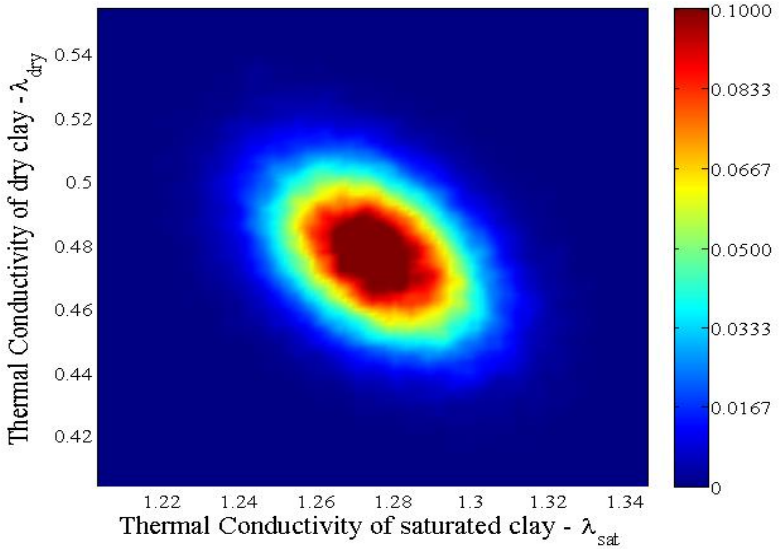

Figure 4.2. Correlation between the thermal conductivities of dry and saturated soil.

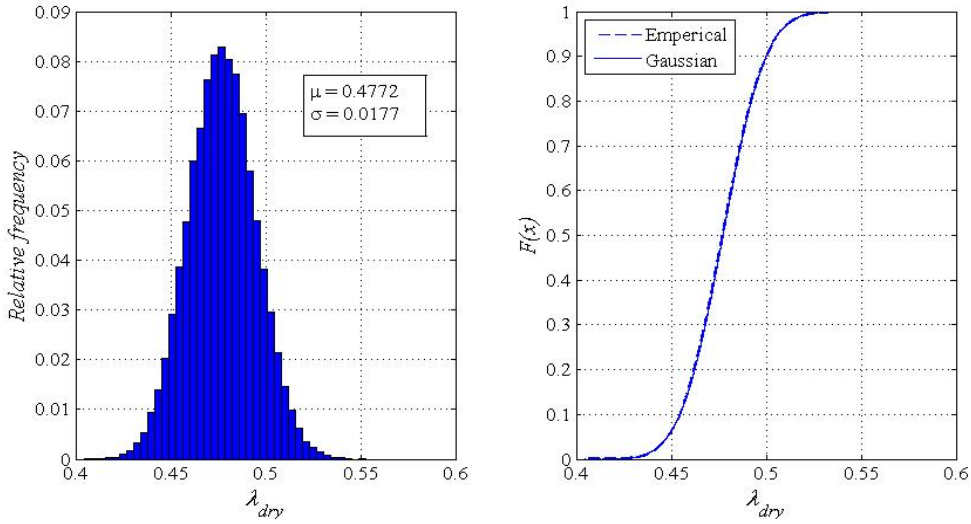

Figure 4.3. Relative frequency distribution and CDF of λ_{dry}.

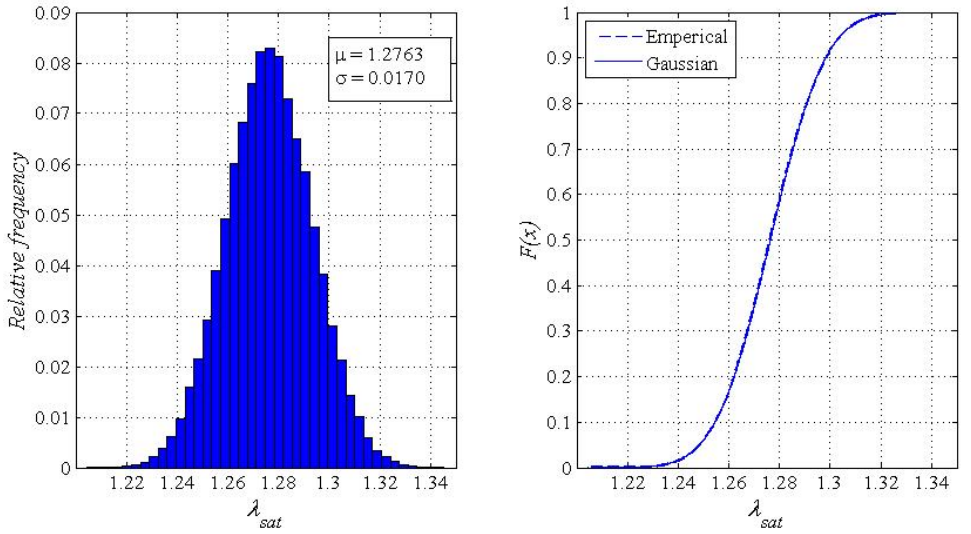

Figure 4.4. Relative frequency distribution and CDF of the λ_{sat}.

The convergences of estimated thermal conductivities are found from the generated samples and are shown in Figure 4.5. From 300,000 realizations, 40,000 forming same the stable distribution, are taken for the purpose of our study.

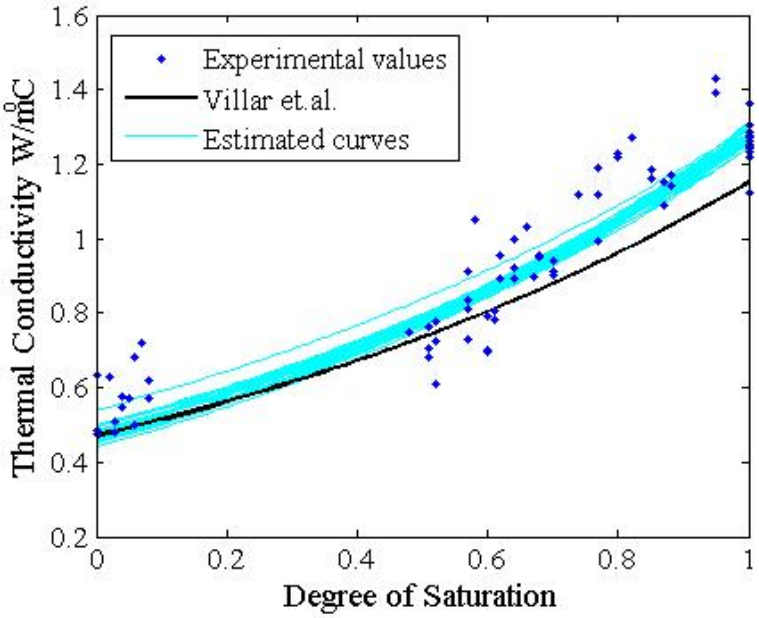

Figure 4.5. Thermal conductivity values estimated from generated sample.

4.2.2 Soil-Water Retention Curve

Figure 2.3 presents the experimental observations of water retention tests performed bentonite alongside the model proposed by Villar et al. (2005). The model adopted has the parameter values: P_0 = 28 MPa, λ_0 = 0.18, λ_d = 1.1. The water retention behavior of soils is a complex phenomenon and the relationship between degree of liquid saturation and suction is highly nonlinear. Therefore, it is difficult to allot any kind of prior distribution to them and an uniform prior is assumed for all three parameters between 0 - 200 MPa for P_0, 0 - 1 for λ_0 and 0 - 5 for λ_d = 1.1. Thus the joint prior distribution of the parameters is given as

$$\pi(P_0,\lambda_0,\lambda_d)=\frac{1}{(b_1-a_1)(b_2-a_2)(b_3-a_3)} \tag{4.6}$$

where, a_1=0, b_1=200, limits of P_0,

$a_2=0$, $b_2=1$, limits of λ_0,

$a_3=0$, $b_3=5$, limits of λ_d

The observation values are distributed equally on both sides of the model in semi-log plot and the pattern is same as that of log-normal distribution (Figure 2.3). Thus a multivariate log-normal likelihood of the observation values is assumed and is given as:

$$f(s_{ei}, S_{ei}|P_0,\lambda_0,\lambda_d)= \prod_{i=1}^{n} \frac{1}{\sqrt{2\pi}\zeta} \exp\left[-\frac{1}{2}\left(\frac{\ln(s_i)-\lambda}{\zeta}\right)^2\right] \quad (4.7)$$

where, s_{ei} represent each independent observed suction value from experiments at effective degree of saturation (S_{ei})

λ is the mean of log of suction values at particular effective degree of saturation (S_{ei}) (basically our adopted model)

ζ is the standard deviation of the logarithmic values of suction

n is the number of experimental observations, here n=145.

Therefore, the posterior of the random sample (P_0,λ_0,λ_d) which is proportional to prior times the likelihood is given as:

$$f(P_0,\lambda_0,\lambda_d|\ s_{ei}, S_{ei}) \propto \exp\left[-\frac{1}{2}\sum_{i=1}^{n}\left(\frac{\ln(s_i)-\lambda}{\zeta}\right)^2\right] \quad (4.8)$$

Following the Metropolis-Hastings method, a candidate point $\varepsilon_u(P_0,\lambda_0,\lambda_d)$ is selected from a proposal multivariate normal distribution $q\ (.|\varepsilon_t)$ with the adopted model as initial mean and constant standard deviation given as product of mean and assumed covariance. The covariance matrix is assumed to be a diagonal matrix with covariance of 0.01. The

mean is then updated to the accepted candidate point as the chain is created. The initial mean and standard deviation are given as:

$$q_{\mu_0}=[P_0 \quad \lambda_0 \quad \lambda_d] \tag{4.9}$$

$$q_{\sigma}=q_{\mu_0}\begin{bmatrix}0.01 & 0 & 0\\ 0 & 0.01 & 0\\ 0 & 0 & 0.01\end{bmatrix} \text{ and } q_{\sigma_0}=\begin{bmatrix}0.28 & 0 & 0\\ 0 & 0.0018 & 0\\ 0 & 0 & 0.011\end{bmatrix} \tag{4.10}$$

A chain of 5,450,000 realization set of P_0, λ_0 and λ_d were created and after burning (3,200,000 realizations), 2,250,000 realizations are observed to form a stable distribution. The correlation between the parameters is shown in Figure 4.6, Figure 4.7 and Figure 4.8. Of these 2,250,000 realizations, 60,000 realizations were taken with the same distribution for the purpose of our study. The relative frequency distribution and cumulative distribution of the realizations are shown in Figure 4.9, Figure 4.10 and Figure 4.11. The convergence of estimated retention curve is found from the generated samples and is shown in Figure 4.12.

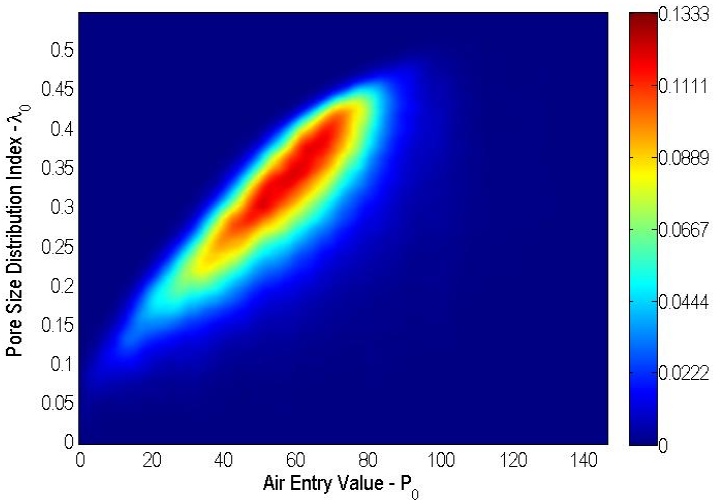

Figure 4.6. Correlation between the air entry value (P_0) and Pore size distribution index (λ_0).

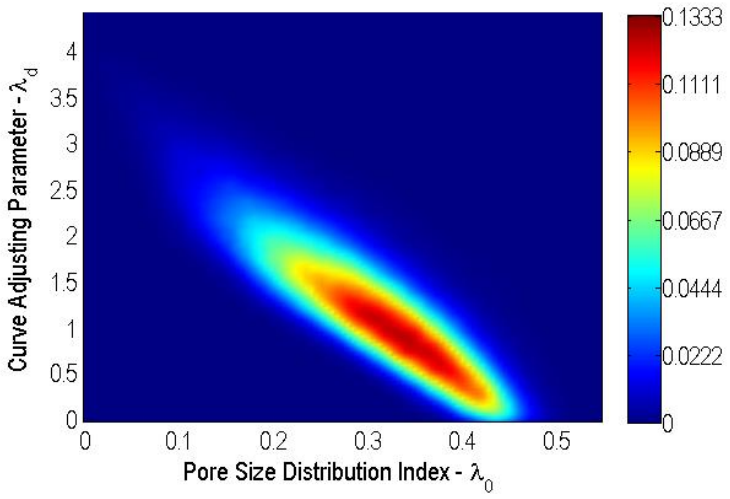

Figure 4.7. Correlation between pore size distribution index (λ_0) and curve factor (λ_d).

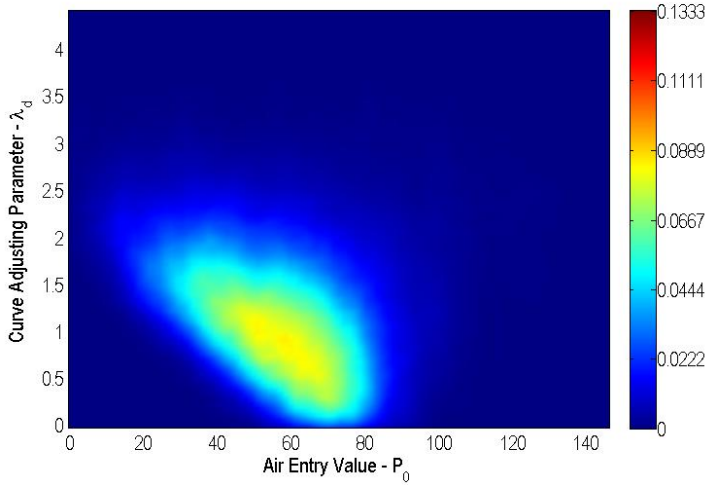

Figure 4.8. Correlation between the air entry value (P_0) and curve factor (λ_d).

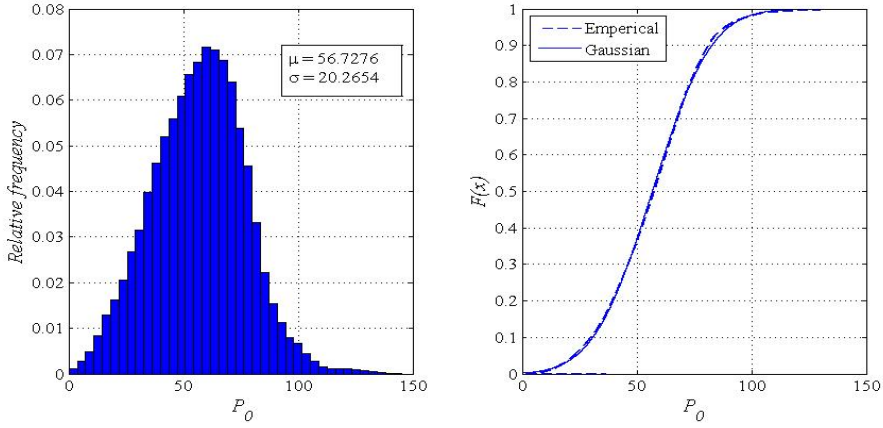

Figure 4.9. (a) Relative frequency distribution and (b) CDF of air entry value (P_0).

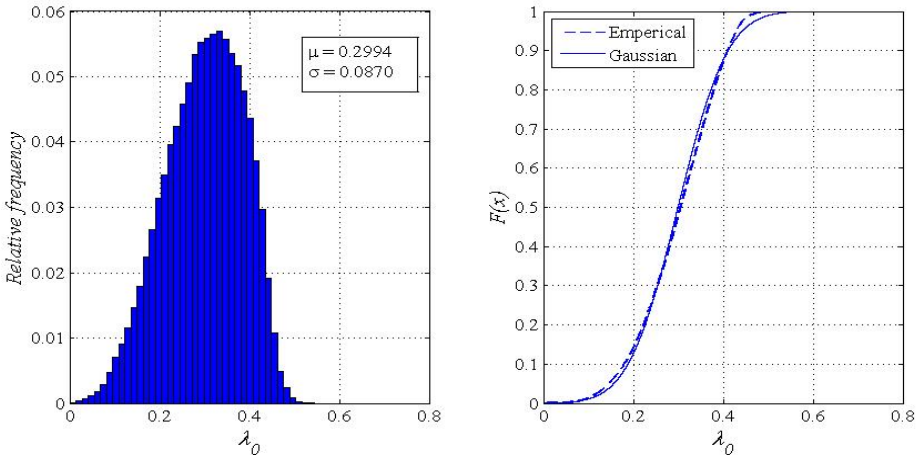

Figure 4.10. (a) Relative frequency distribution and (b) CDF of the pore size distribution index (λ_0).

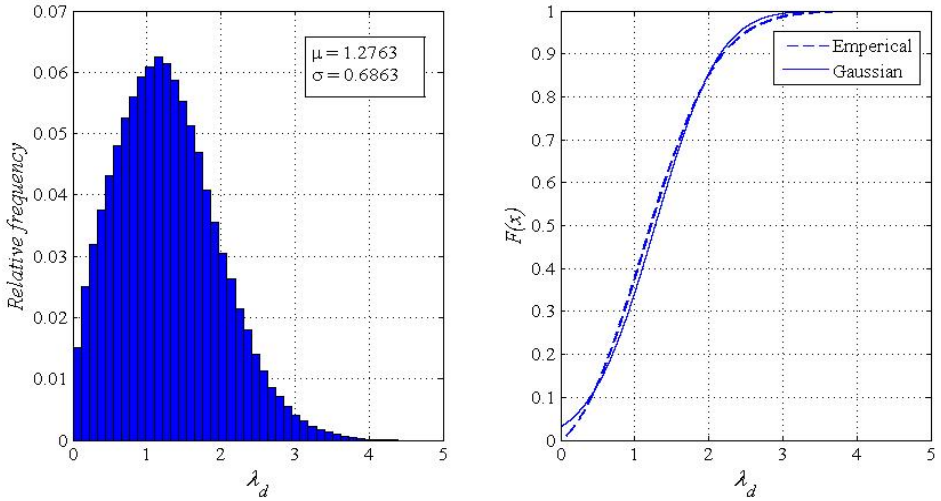

Figure 4.11. (a) Relative frequency distribution and (b) CDF of the curve adjusting factor (λ_d).

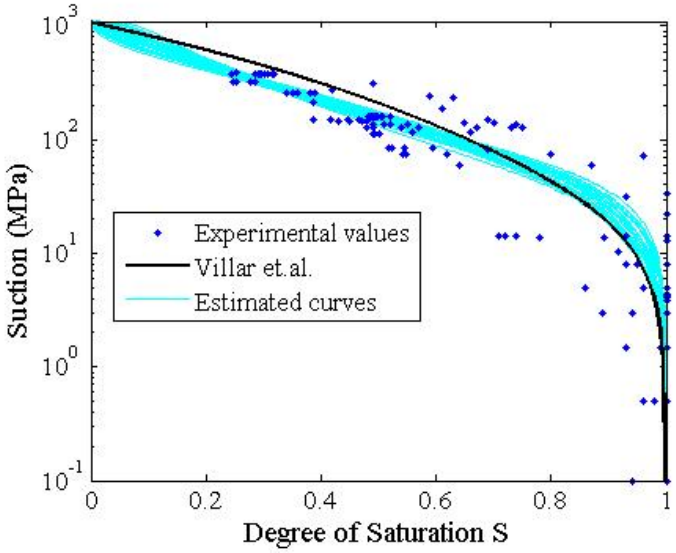

Figure 4.12. Convergence of retention curve estimated from generated sample.

4.2.3 Hydraulic Permeability

The observations from experiments conducted on samples of FEBEX compacted bentonite at different densities are presented in Figure 2.2. A model best fit of the experimental values is adopted as our model to generate more number of realizations. The adopted model has the intrinsic permeability (k_0) of 1.9×10^{-21} m^2 at reference porosity (ϕ_0) of 0.40 (Villar et al., 2008).

A uniform prior is assumed for the parameters between 1×10^{-22} – $1 \times 10^{-19} m^2$. Thus the prior of the parameter is given as

$$\pi(k_0) = \frac{1}{(b-a)} \tag{4.11}$$

where, $a = 1 \times 10^{-22}$, $b = 1 \times 10^{-19}$, limits of k_0

From the Figure 2.2, the observation values are distributed equally on both sides of the model in semi-log plot and the pattern is the same as that of log-normal distribution.

Thus a multivariate log-normal likelihood of the observation values is assumed and is given as:

$$f(k \mid k_0) = \prod_{i=1}^{n} \frac{1}{\sqrt{2\pi}\zeta} \exp\left[-\frac{1}{2}\left(\frac{\ln(k_{0i})-\lambda}{\zeta}\right)^2\right] \quad (4.12)$$

where, k_{0i} represent each independent observed intrinsic permeability value from experiments at reference porosity (ϕ_0) of 0.40

λ is the mean of the logarithmic values of intrinsic permeability values at reference porosity (ϕ_0) of 0.40 (basically our adopted model)

ζ is the standard deviation of the logarithmic values of k_0

n is the number of experimental observations, here n=67.

Therefore, the posterior of the random parameter (k_0) which is proportional to prior times the likelihood is given by:

$$f(k_0 \mid k) \propto \exp\left[-\frac{1}{2}\sum_{i=1}^{n}\left(\frac{\ln(k_{0i})-\lambda}{\zeta}\right)^2\right] \quad (4.13)$$

Following the Metropolis-Hastings method, a candidate point $\varepsilon_u(k)$ is selected from a proposal normal distribution $q(.|\varepsilon_t)$ with the adopted model as initial mean and constant standard deviation given as product of mean and assumed covariance. The covariance matrix is assumed to a diagonal matrix with covariance of 0.01. The mean is then

updated to the accepted candidate point as the chain is created. The initial mean and standard deviation are given as:

$$q_{\mu_0} = k_0 \tag{4.14}$$

$$q_{\sigma} = q_{\mu_0}\,[0.01] \text{ and } q_{\sigma_0} = \left[1.9 \times 10^{-21}\right] \tag{4.15}$$

A chain of 3,650,000 realizations of k_0 were created and after burning (1,650,000 realizations), 2,000,000 realizations are observed to form a stable distribution. Of these 2,000,000 realizations, 60,000 were taken with the same distribution for the purpose of this study. The relative frequency distribution and cumulative distribution of the realizations are shown in Figure 4.13. The convergence of estimated retention curve is found from the generated samples and is shown in Figure 4.14.

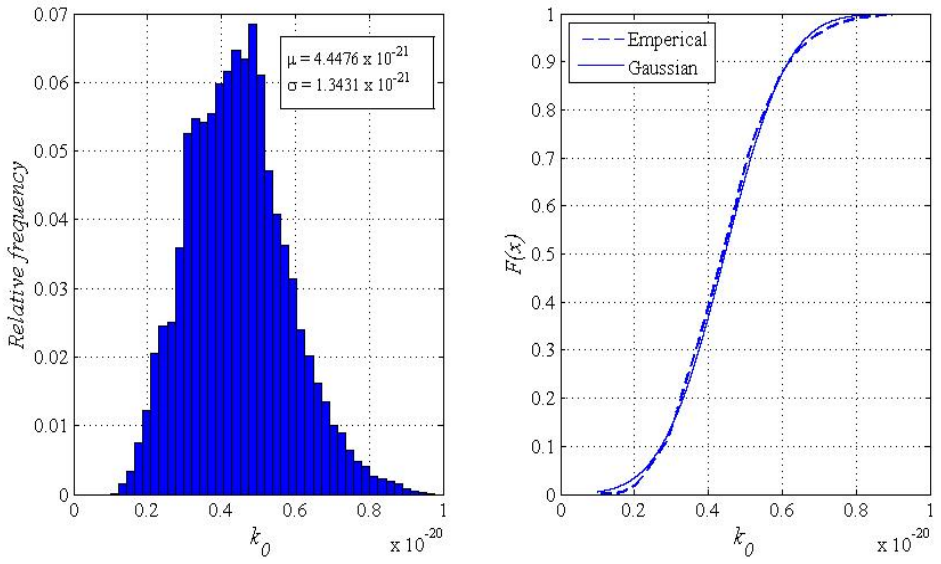

Figure 4.13. (a) Relative frequency distribution and (b) CDF of intrinsic permeability.

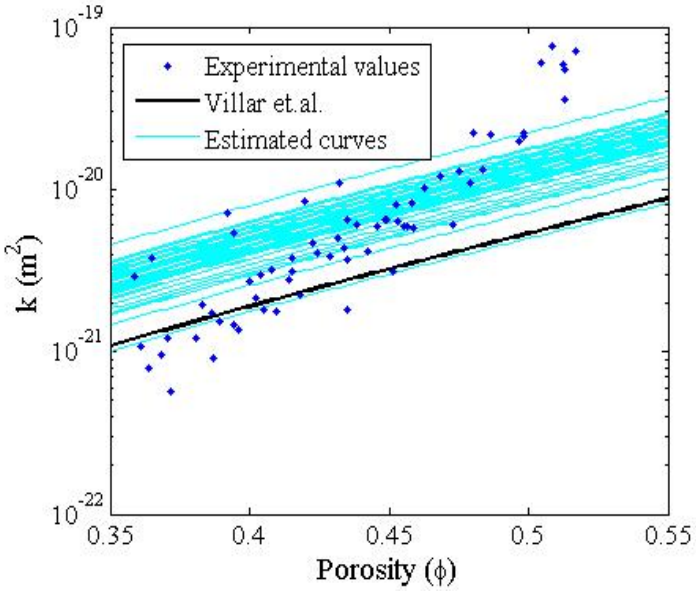

Figure 4.14. Convergence of intrinsic permeability estimated from generated sample.

4.3 Assessment of Parametric Uncertainty

Five sets of parametric variations were used to better understand the influence of each parameter on the overall THM behavior of bentonite clay, as follows

Case 1: Thermal properties,

Case 2: Retention curve parameters of hydraulic property,

Case 3: Permeability parameters of hydraulic property,

Case 4: Both of hydraulic properties,

Case 5: Both of thermal and hydraulic properties.

4.3.1 Case 1: Thermal Conductivity Parameters

From the stable distribution of the thermal conductivities under dry and saturated conditions (i.e. λ_{dry} and λ_{sat}) generated by Monte Carlo simulations with 300,000 realizations, about 44,000 realizations were sampled and analyzed for running the corresponding THM simulations. The mean and standard deviation are as follows

- λ_{dry} - 0.4772 W/m°C and 0.0177 W/m°C respectively,
- λ_{sat} - 1.2763 W/m°C and 0.0170 W/m°C respectively.

For numerical analysis, the size of realizations should be large enough for the output responses to converge and thus be independent of size of the realizations. That is, the number of parameter samples should be large such that the mean output response doesn't vary any further. The considered 44,000 realizations are observed to be sufficiently large for the convergence of output response and hence minimize the influence of the size. The frequency distribution and cumulative distribution of the resultant responses by varying the thermal conductivities at different locations A, B, C (which are at distance of 10cm, 30cm, and 50cm, respectively from heater) at different duration (at 6, 12, 24, 92 months) are shown in Figure 4.15, Figure 4.16 and Figure 4.17. It can be observed that variation of the output responses i.e. dry density, temperature, and water content values is very less with respect to thermal conductivities. The dry densities vary at range of $\pm$0.01gm/cc, temperature at $\pm$1°C and water content at $\pm$0.5%. This can also be seen from the standard deviation values of each parameter at different positions (Figure A-1, Figure A-2 and Figure A-3).

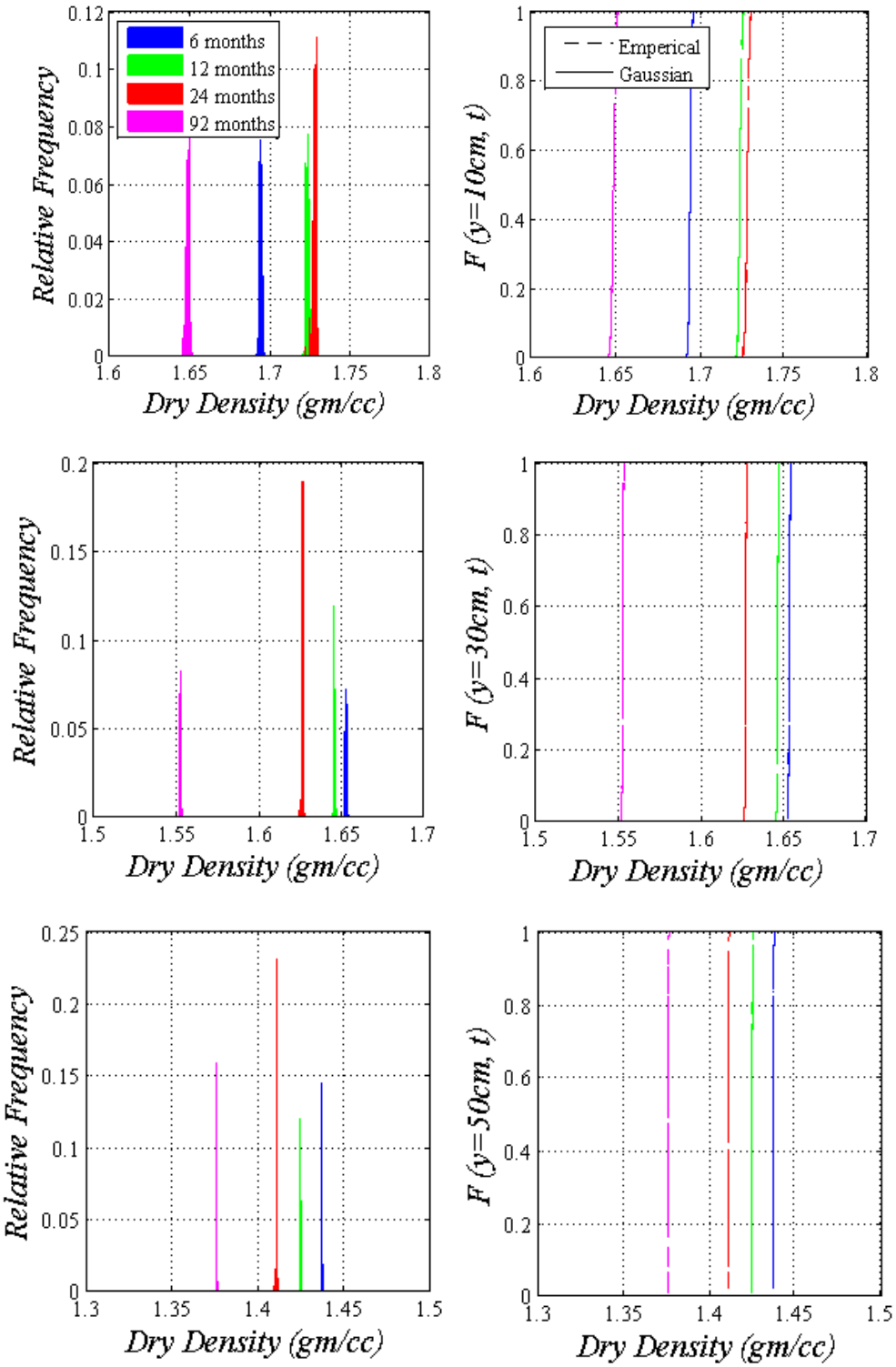

Figure 4.15. Relative frequency distribution and CDF of dry density at A, B, C (10cm, 20cm, 30cm from heater, respectively).

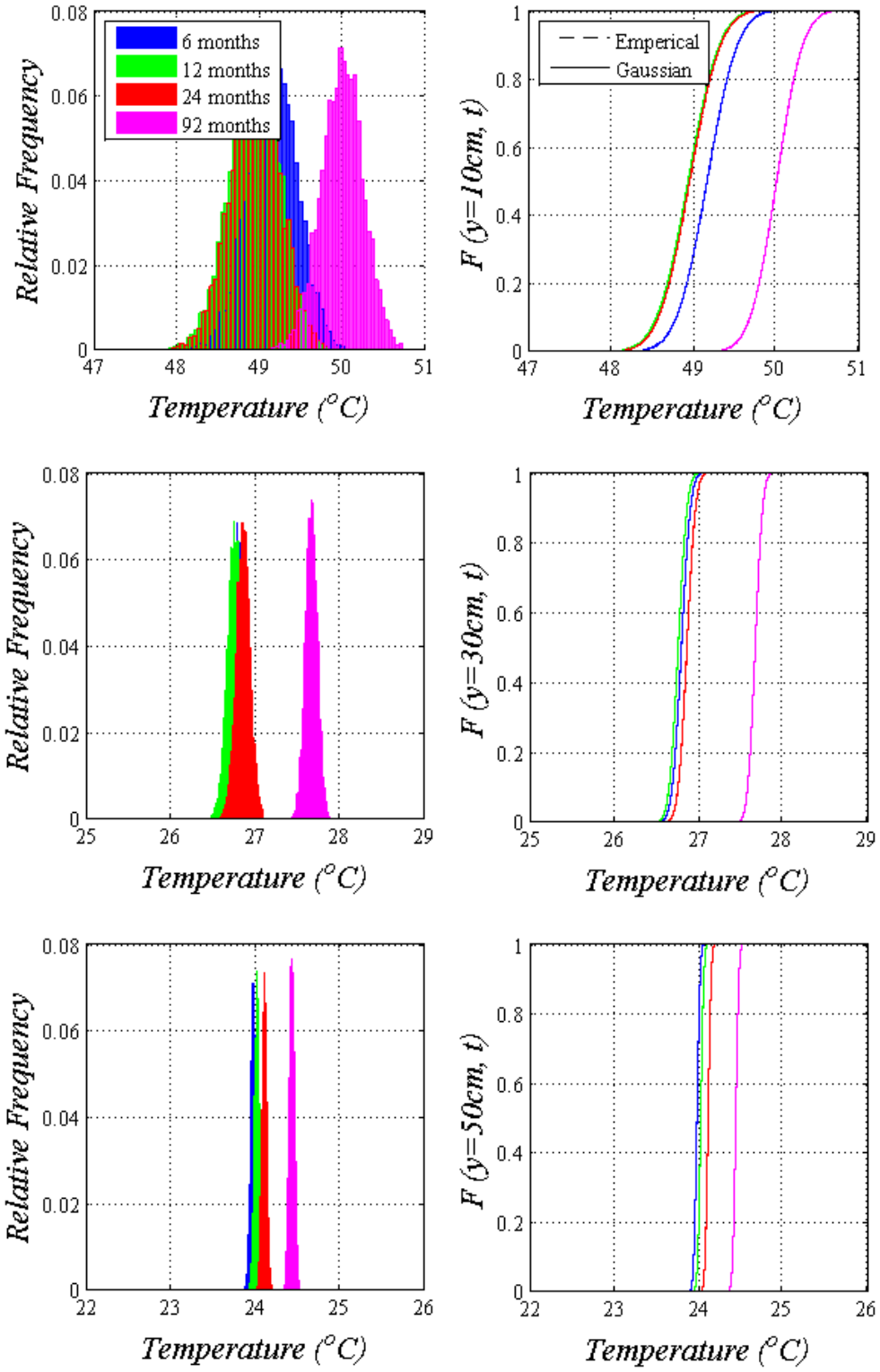

Figure 4.16. Relative frequency distribution and CDF of temperature at A, B, C.

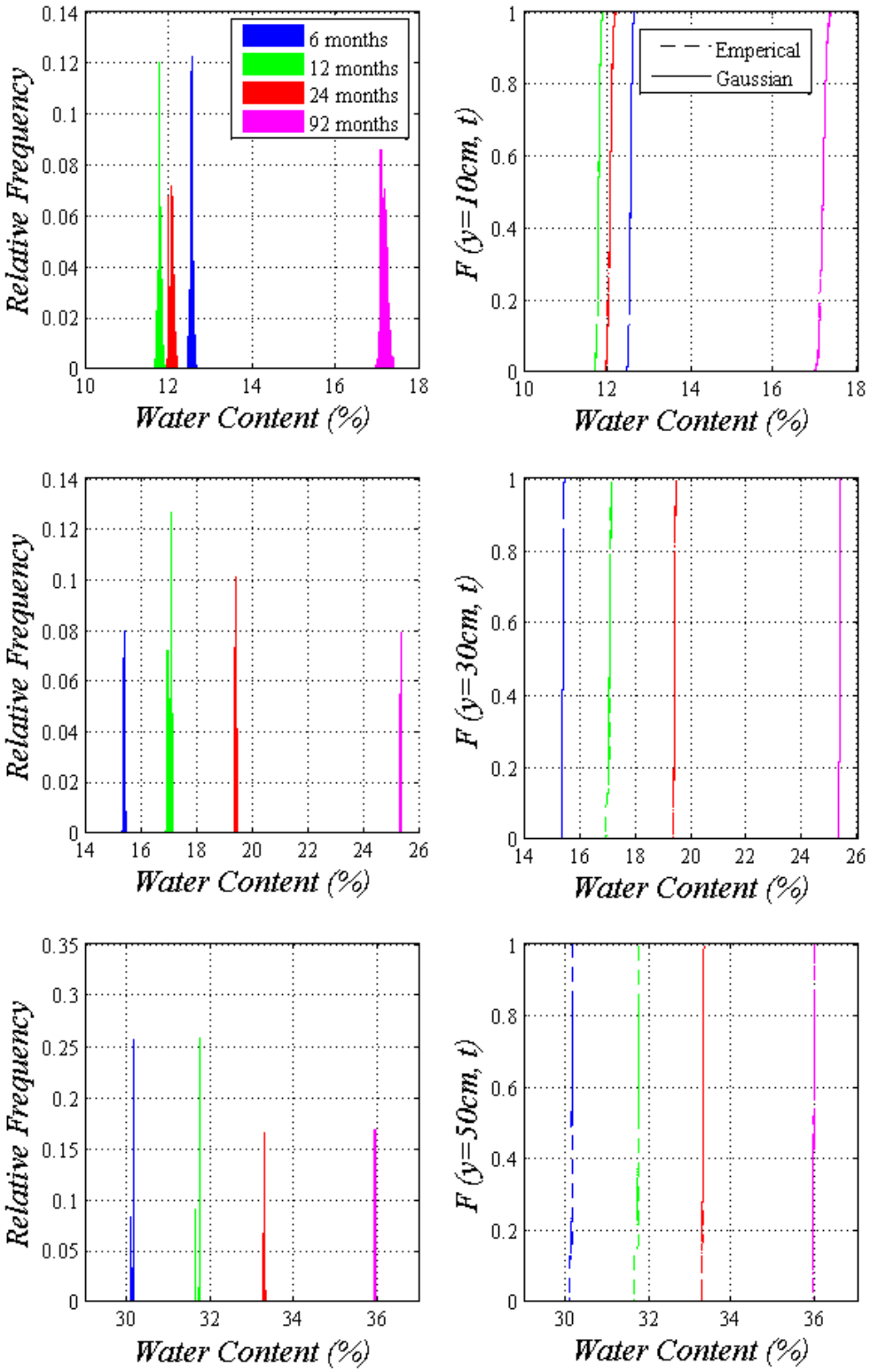

Figure 4.17. Relative frequency distribution and CDF of water content at A, B C.

Furthermore, this variation decreases more when we move away from the heater. For instance, the standard deviation of temperature after 6 months at location A (10cm from heater) is 0.29, at B (30cm from heater) is 0.09 and at C (50cm from heater) is 0.03.

Thus it can be said that the value of the thermal conductivity of the clay has a slight influence on the response of the barrier regardless of temperature and water content values. Furthermore, at low temperatures like that of room temperature, the influence is negligible. Hence, the behavior of the soil is unaffected with the uncertainty in measuring the thermal conductivity.

4.3.2 Case 2: Retention Parameters of Hydraulic Properties

About 60,000 realizations are taken from the generated samples of retention curve parameters (i.e. P_0, λ_0, and λ_d). The mean and standard deviation are as follows:

- P_0 - 56.7246 MPa and 20.2654 MPa respectively,
- λ_0 - 0.2994 and 0.0870 respectively,
- λ_d - 1.2763 and 0.6863 respectively.

The considered size of about 60,000 realizations are observed to be sufficient for the get rid of influence of the size. The frequency distribution and cumulative distribution of the resultant responses by varying the retention curves at locations A, B, C (which are at 10cm, 30cm and 50cm from heater respectively) at different times (at 6, 12, 24, 92 months) are shown in Figure 4.18, Figure 4.19 and Figure 4.20.

It can be observed that there is slight variation of the output responses i.e. dry density, temperature, and water content with respect to retention curve which increases from C (near hydrating end) to A (near the heater) and further, increase with duration. The temperature at A varies between 46°C to 48°C during initial stages of time. But, after 92 months this range increases between 46°C to 50°C. Similar variations can be observed in the case of dry density. While the variation of dry density is very small at B and C, at A it varies widely from 1.6gm/cc to 1.8gm/cc.

The variations are can also be seen significantly in case of water content values. At location A after 92 months, it varies 5% to 25% of water content. This difference in variations can also be evidenced from the standard deviation values of each parameter at different positions (Figure A-14, Figure A-25 and Figure A-36). For instance, the standard deviation of water content after 92 months, at A is 2.05, at B is 0.26 and at C is 0.11.

It can be concluded that the uncertainty of retention curve has some influence on response, though it is small. But, the response variation may increase when the retention curve parameters are combined with uncertainty of other parameters which can observed from case-4 and case-5.

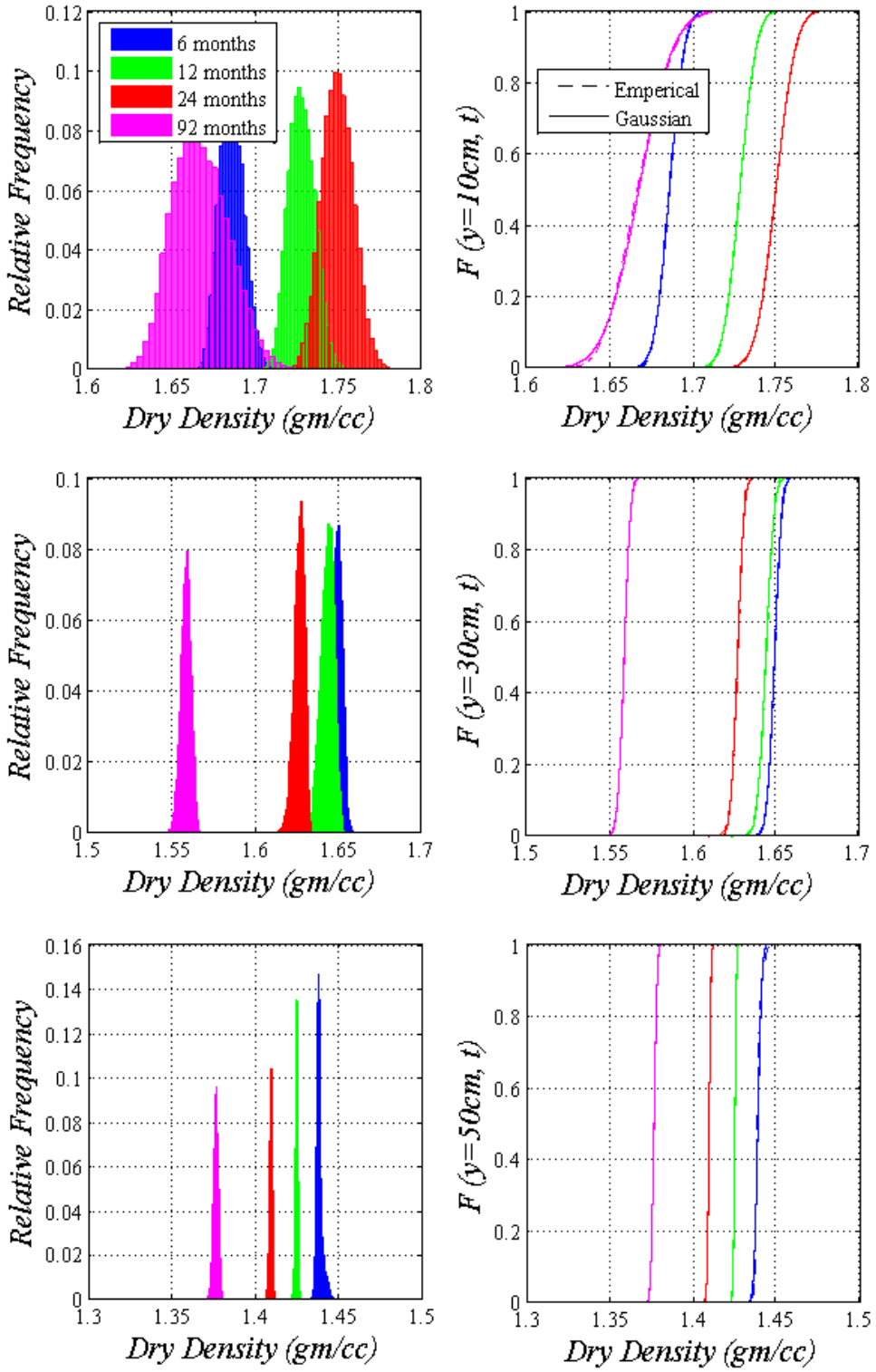

Figure 4.18. Relative frequency distribution and CDF of dry density at A, B, C.

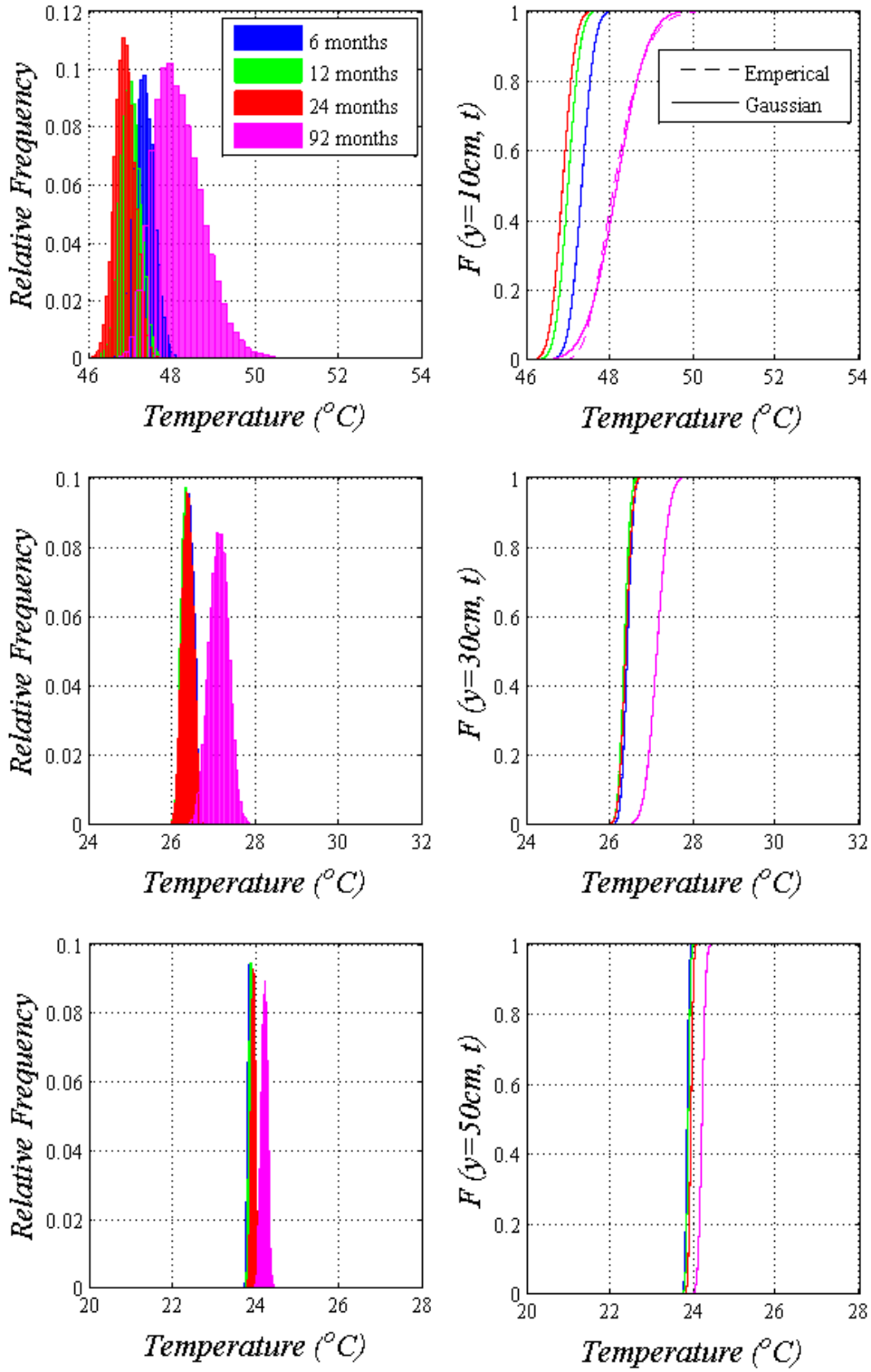

Figure 4.19. Relative frequency distribution and CDF of temperature at A, B, C.

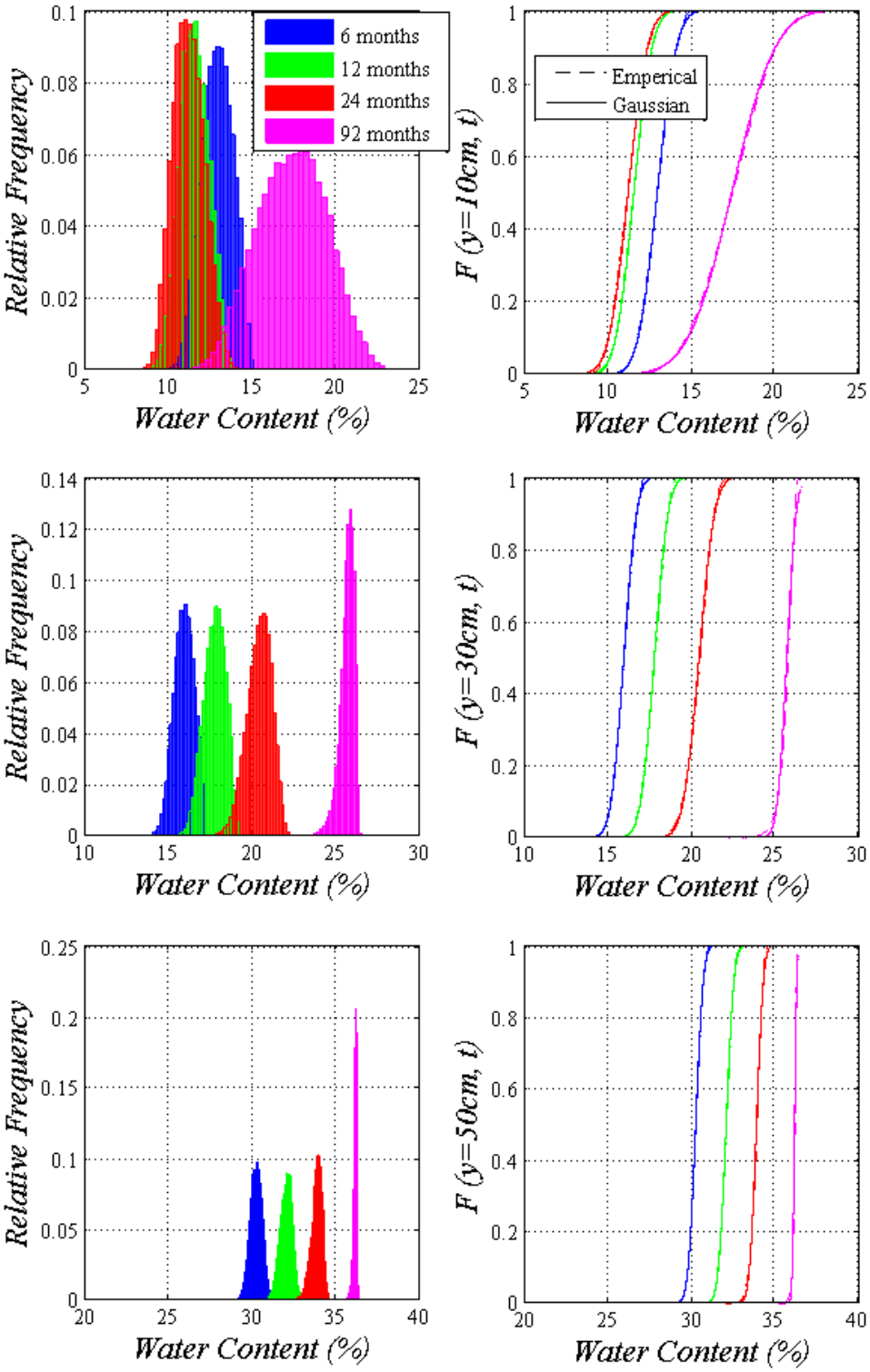

Figure 4.20. Relative frequency distribution and CDF of water content at A, B, C.

4.3.3 Case 3: Soil Permeability

About 60,000 realizations are taken from the samples of permeability (k_0) generated by Monte Carlo simulations (section 3.2.3). Figure 4.13 gives the marginal distribution of the realizations. The mean and standard deviation are given as

- k_0 - 4.448 x 10^{-21} m^2 and 1.343 x 10^{-21} respectively.

The frequency distribution and cumulative distribution of the resultant responses by varying the retention curves parameters at locations A, B, C (which are at 10cm, 30cm and 50cm from heater respectively) at different times (at 6, 12, 24, 92 months) are shown in Figure 4.21, Figure 4.22 and Figure 4.23.

The response variations is similar to that of case 2 where there is slight variation of the output responses which increase from C (near hydrating end) to A (near the heater) and further, increase with duration, except that the variations are little higher with variation in permeability. Although, temperature variation is very less which gradually increase with time, at A it varies between 48°C to 56°C with standard deviation of 1.6. But, the variations are can be seen significantly in case of dry density and water content. This is due to the influence of permeability on the flow of water in the sample, due to which, the dry density and water content without change in temperature. It is also observed that the variation increase with increase of time period which is evident of the time required for transport of fluid. The standard deviations of the material response also show similar results (Figure A-7, Figure A-8 and Figure A-9).

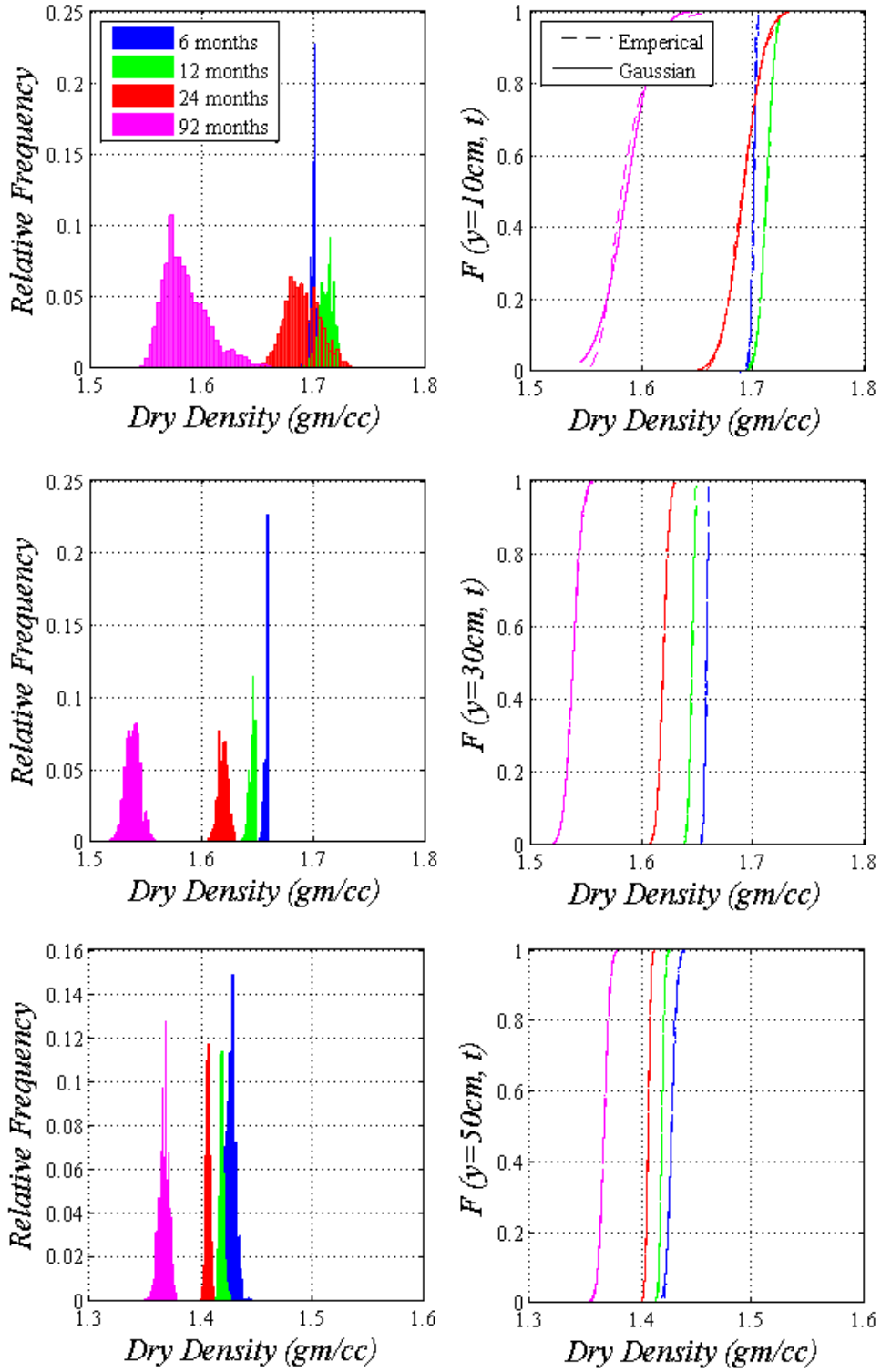

Figure 4.21. Relative frequency distribution and CDF of dry density at A, B, C.

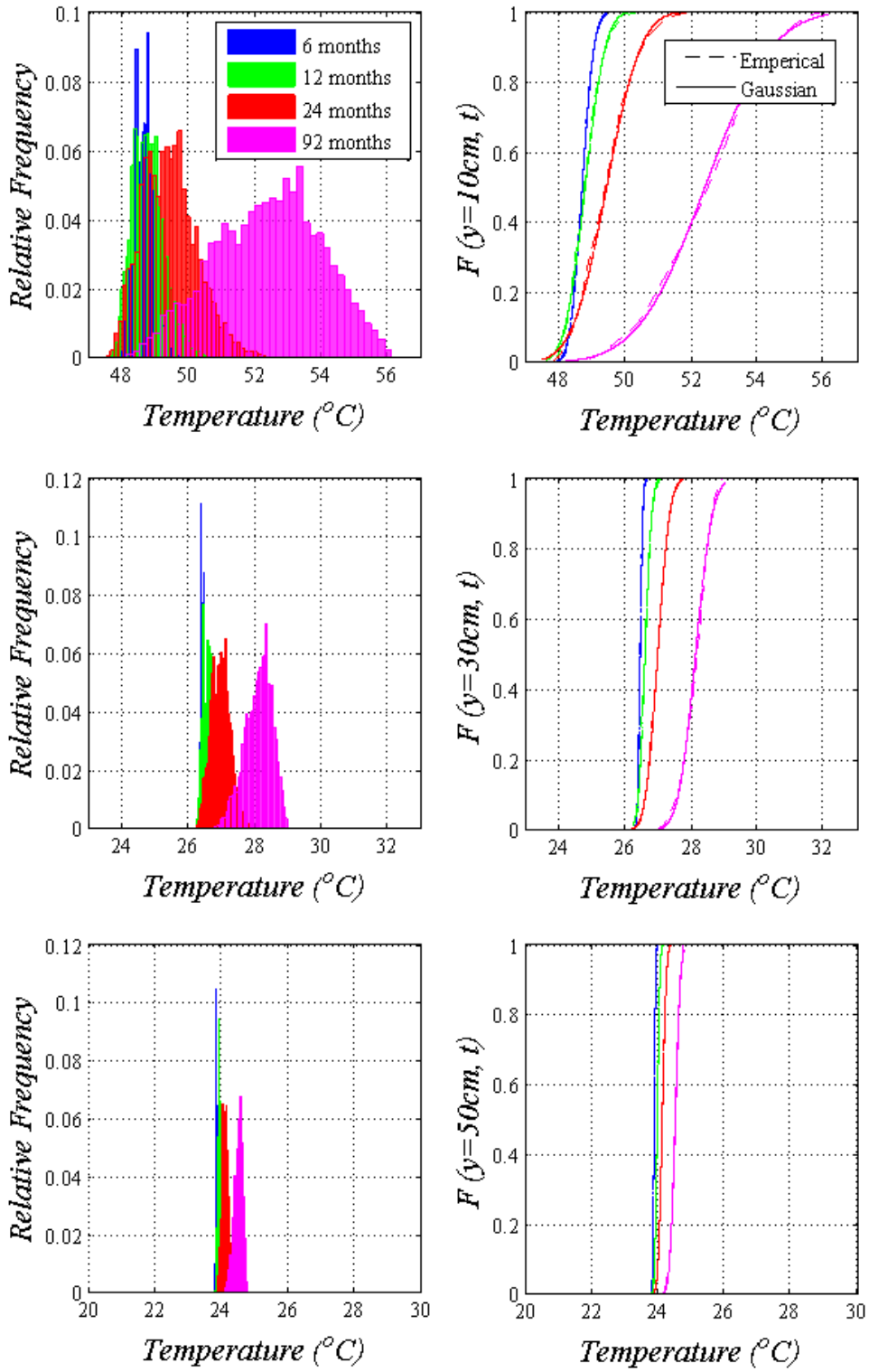

Figure 4.22. Relative frequency distribution and CDF of temperature at A, B, C.

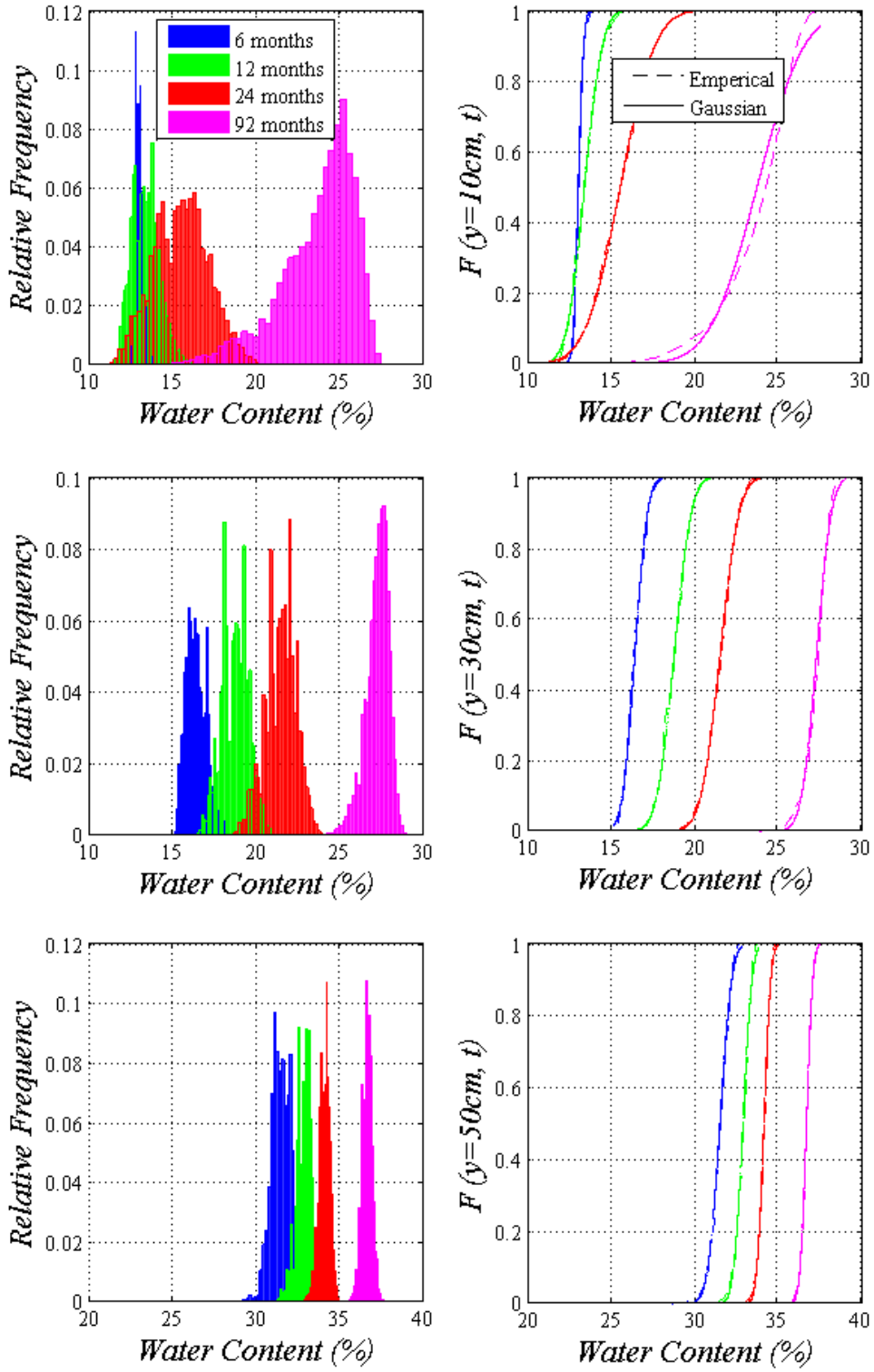

Figure 4.23. Relative frequency distribution and CDF of water content at A, B, C.

It can be concluded that the uncertainty in permeability has significant effect in the material response and this combined with uncertainty of other related parameters is expected to produce higher variation of THM behavior response.

4.3.4 Case 4: Parameters of Both of Hydraulic Properties

In this case, the parametric uncertainty in both retention curve and soil permeability is used to analyze the behavior of soil (i.e. retention curve parameters: P_0, λ_0, λ_d,; and soil permeability: k_0). Since, the material response showed a certain degree of uncertainty when the given parameters are varied individually, their combination may either increase or decrease the variability in material response.

About 60,000 realizations of both retention curve parameters and permeability parameter from the same distributions are taken for the case. The resultant responses from the THM analysis are shown in Figure 4.24, Figure 4.25 and Figure 4.26. It is observed that the response of the materials is similar to that of the behavior when only permeability is varied (i.e. case 3). In fact, the amount of variation is close to that of in case 3 with very slight increase, which means that the permeability has more dominant influence than the soil-water characteristic curve. Hence, it can be said that the permeability measurement plays a key role in assessing a material behavior.

While the pattern of behavior of THM response is similar to that of other cases, there is slight increase in variability in all of the material response. That is, the uncertainty

increases when we move towards the high temperature and also increases for longer durations. For instance, the dry density at A at 92 months varies from 1.55 to 1.73 with range difference of about 0.22; at B it varies from 1.5 to 1.57 with range difference of 0.07 while at C, the range difference further dropped to 0.03 from 1.35 to 1.38. Similarly, at same time, the range difference of temperature decreases from 12°C at A to 3°C at B and to 1°C at C. Similarly, at A, the temperature varies 47°C to 50°C after 6 months, 47°C to 52°C after 12 months, 47°C to 55°C after 24 months, 47°C to 57°C after 92 months. This pattern is also evident from the standard deviation values which increase with decrease in temperature and with duration (Figure A-10, Figure A-11 and Figure A-12).

Further, when compared the cases 2 and 3, where retention curve parameters and permeability are varied individually, the uncertainty has more value. For example, the standard deviation of dry density at A, after 24 months is 0.0207 while the same in case 3 is 0.0154 and in case 2 is 0.0094, the temperature has 1.14, 0,81 and 0.24 respectively in case 4, case 3 and case 2 and water content has 2.22, 1.62, 0.91 respectively.

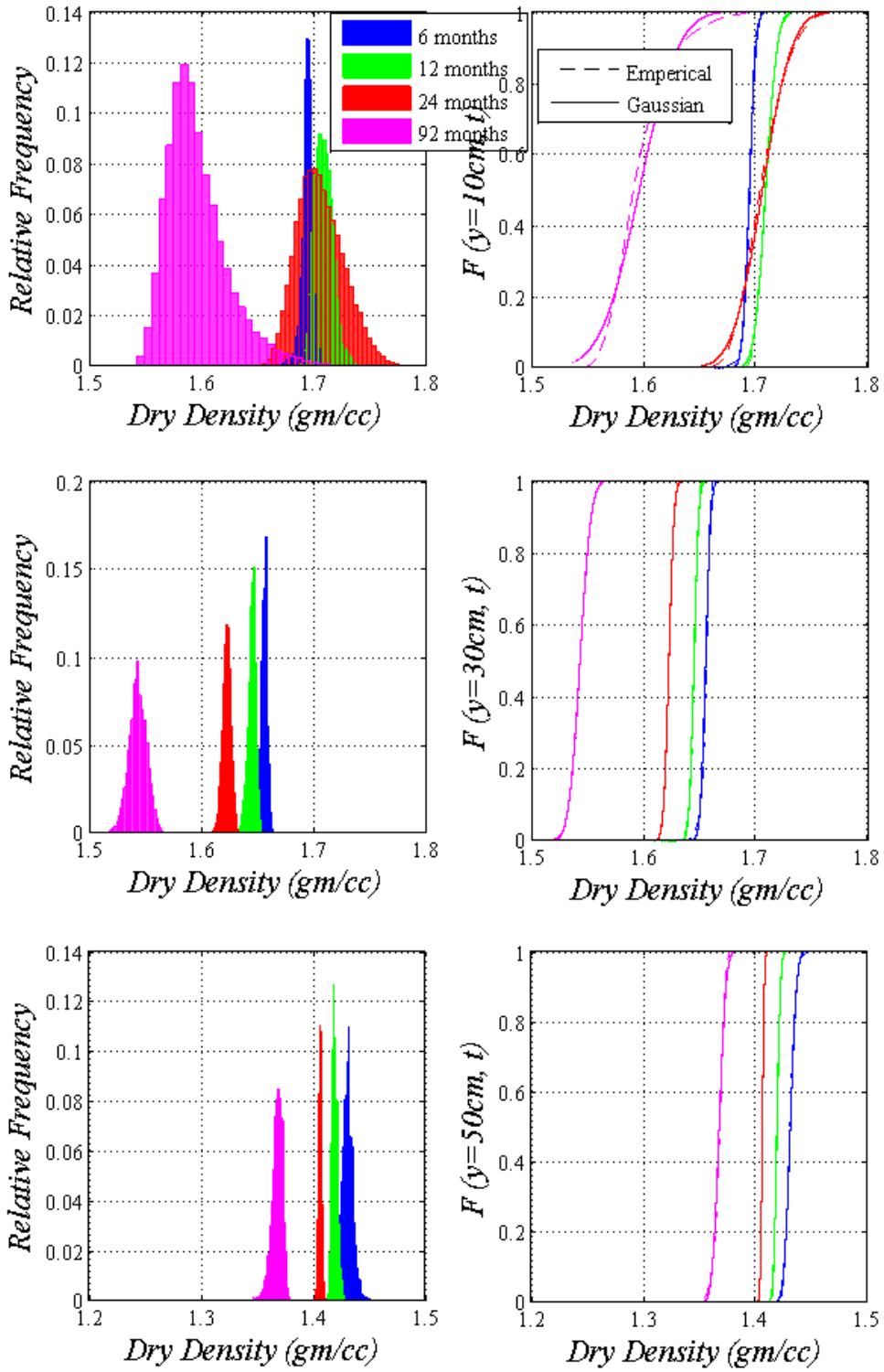

Figure 4.24. Relative frequency distribution and CDF of dry density at A, B, C.

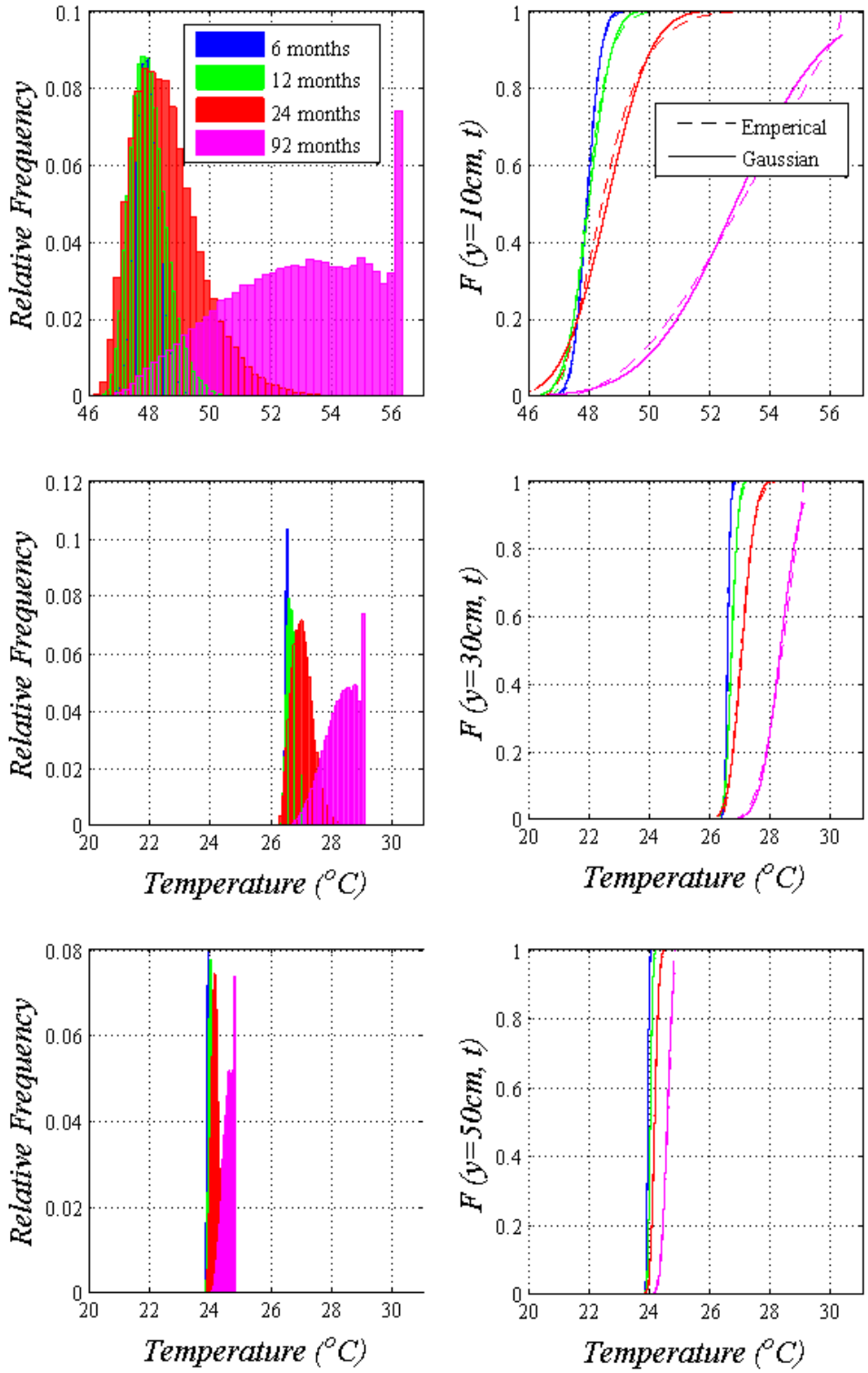

Figure 4.25. Relative frequency distribution and CDF of temperature at A, B, C.

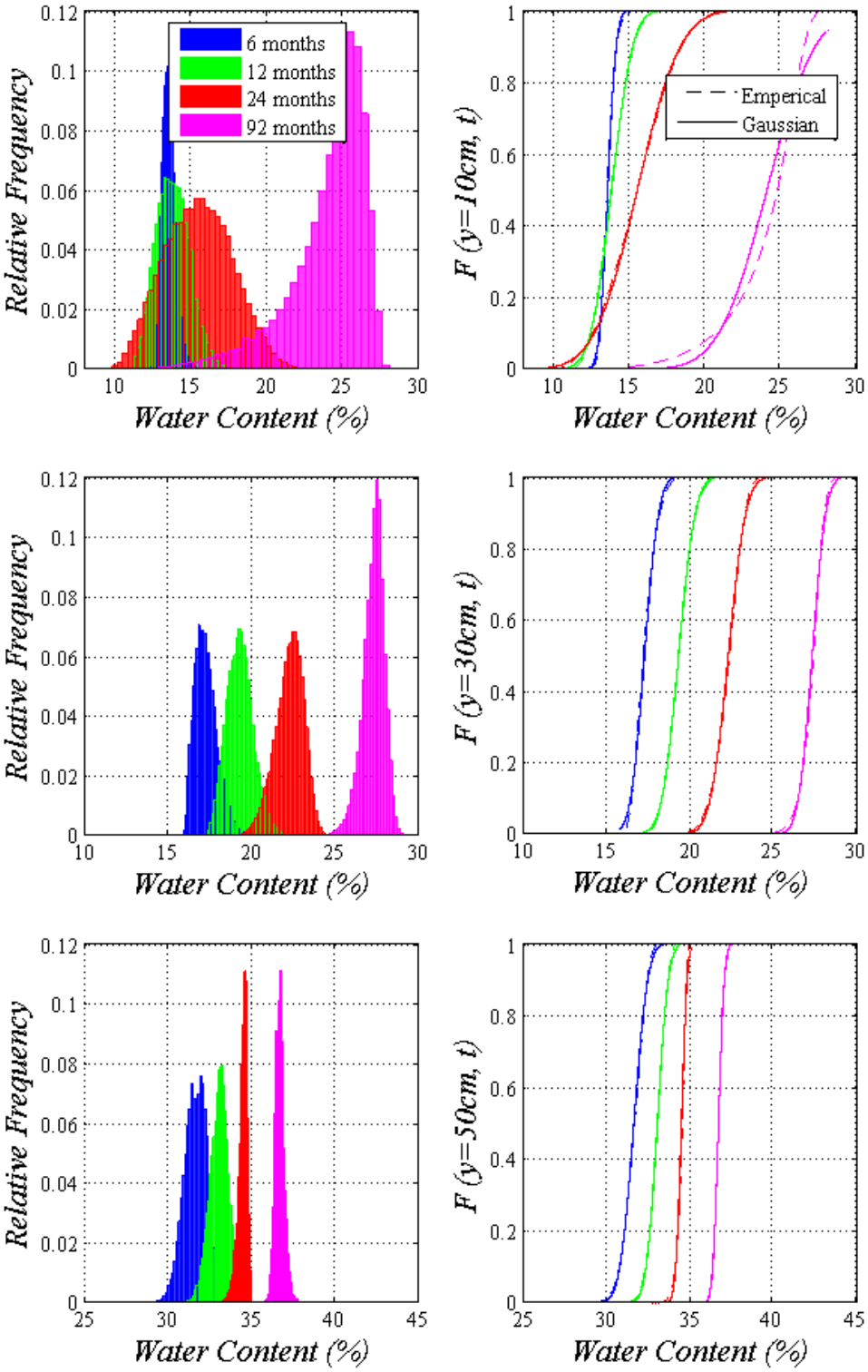

Figure 4.26. Relative frequency distribution and CDF of water content at A, B, C.

4.3.5 Case 5: Parameters of Both of Thermal and Hydraulic Properties

In this case, the parametric uncertainty in both thermal and hydraulic properties is used to analyze the behavior of soil. The frequency distribution and cumulative distribution of resultant responses from the THM analysis are shown in Figure 4.27, Figure 4.28, and Figure 4.29. The mean and standard deviation profiles of dry density, temperature and water content in spatial-temporal space are shown in Figure 4.39, Figure 4.40 and Figure 4.41.

It is observed that there is significant increase in variability response of the materials. The pattern of uncertainty of THM response remained similar to that of other cases. That is, the uncertainty increases when we move towards the high temperature and also increases for longer durations. For instance, the dry density at A, after 92 months varies from 1.45gm/cc to 1.7 gm/cc with range difference of about 0.35, at B it varies from 1.45 gm/cc to 1.52 gm/cc with range difference of 0.07 while at C, the range difference further dropped to 0.03 between 1..32 gm/cc to 1.35 gm/cc. Similarly at same time, the range difference of temperature decreases from 12°C at A to 4°C at B and to 1.5°C at C from heater. Similarly, at A the temperature varies between 47°C -51°C after 6 months, 47°C – 53°C after 12 months, 47°C -55°C after 24 months, and 47°C – 58°C after 92 months. This pattern is also evident from the standard deviation values which increase with decrease in temperature and with duration (Figure A-13, Figure A-14 Figure A-15).

The material response showed a great degree of uncertainty when compared to the cases where the parameters are varied individually. While the thermal conductivity, when varied individually in case-1, has almost negligible effect on the behavior uncertainty; the soil water characteristic curve when varied in case-2, has slight effect and permeability when varied in case-3, has certain effect; their combination has significant effect on the behavior response of the material. For example, the standard deviation of dry density at A, after 24 months in case-1 is 0.0010, in case-2 is 0.0094, in case-3 is 0.0154 and in case-4 is 0.0207 while in case 5, where all parameters are varied it is 0.0269. Similarly, the standard deviation of temperature has 0.30, 0.24, 0.81, 1.14, 1.32 and water content has 0.05, 0.91, 1.62, 2.22, and 2.58 respectively for cases 1 to 5.

This degree of uncertainty increase from low temperature end to high temperature end and also increases for longer duration of time. Hence, any small duration experiments assessing short term effects like that of sudden loading, at lower temperatures cannot detect the influence of the parametric uncertainty, but the experiments assessing the long-term effects like consolidation will be effected by the uncertainty of the input material properties.

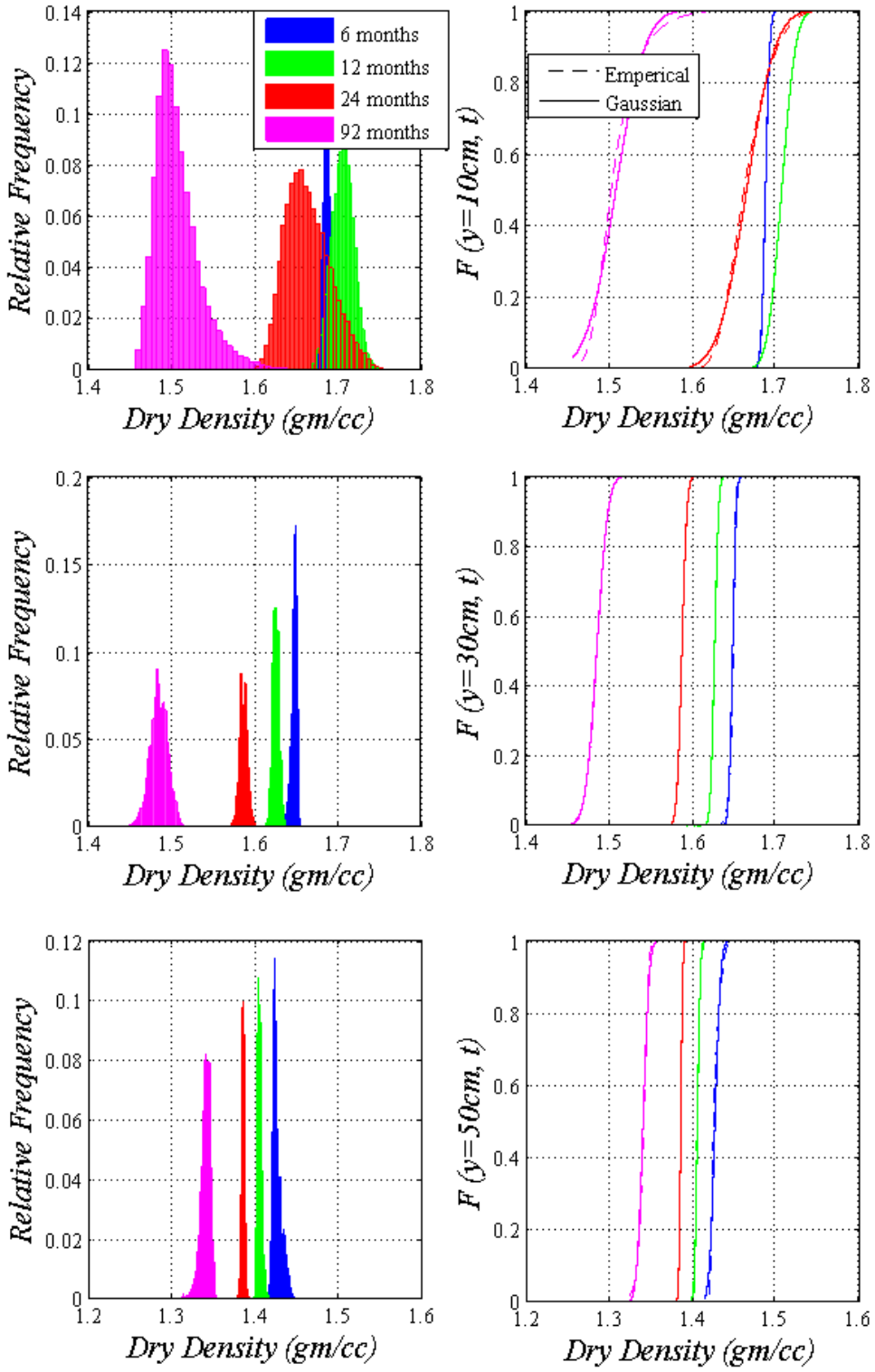

Figure 4.27. Relative frequency distribution and CDF of dry density at A, B, C.

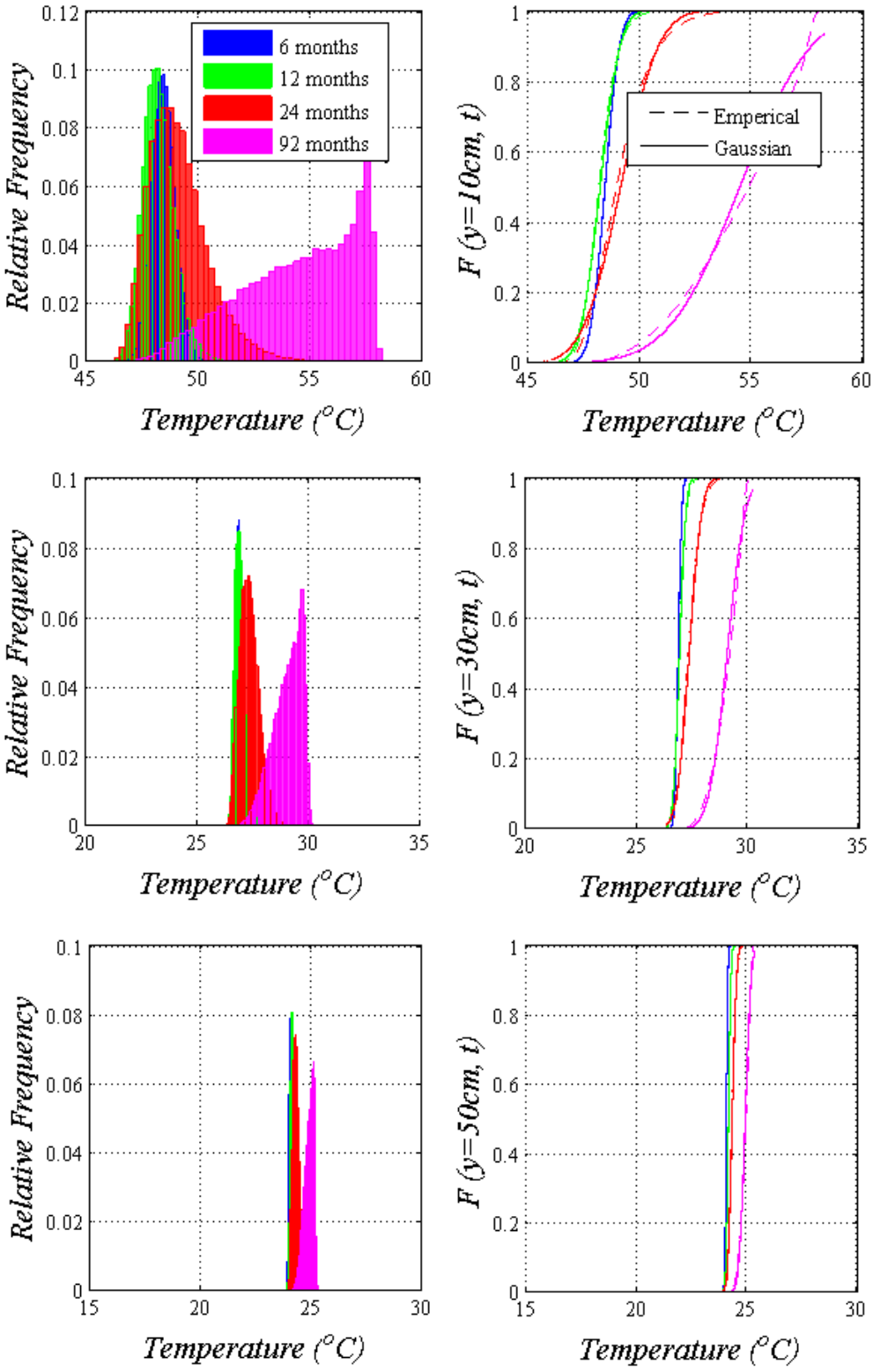

Figure 4.28. Relative frequency distribution and CDF of temperature at A, B, C.

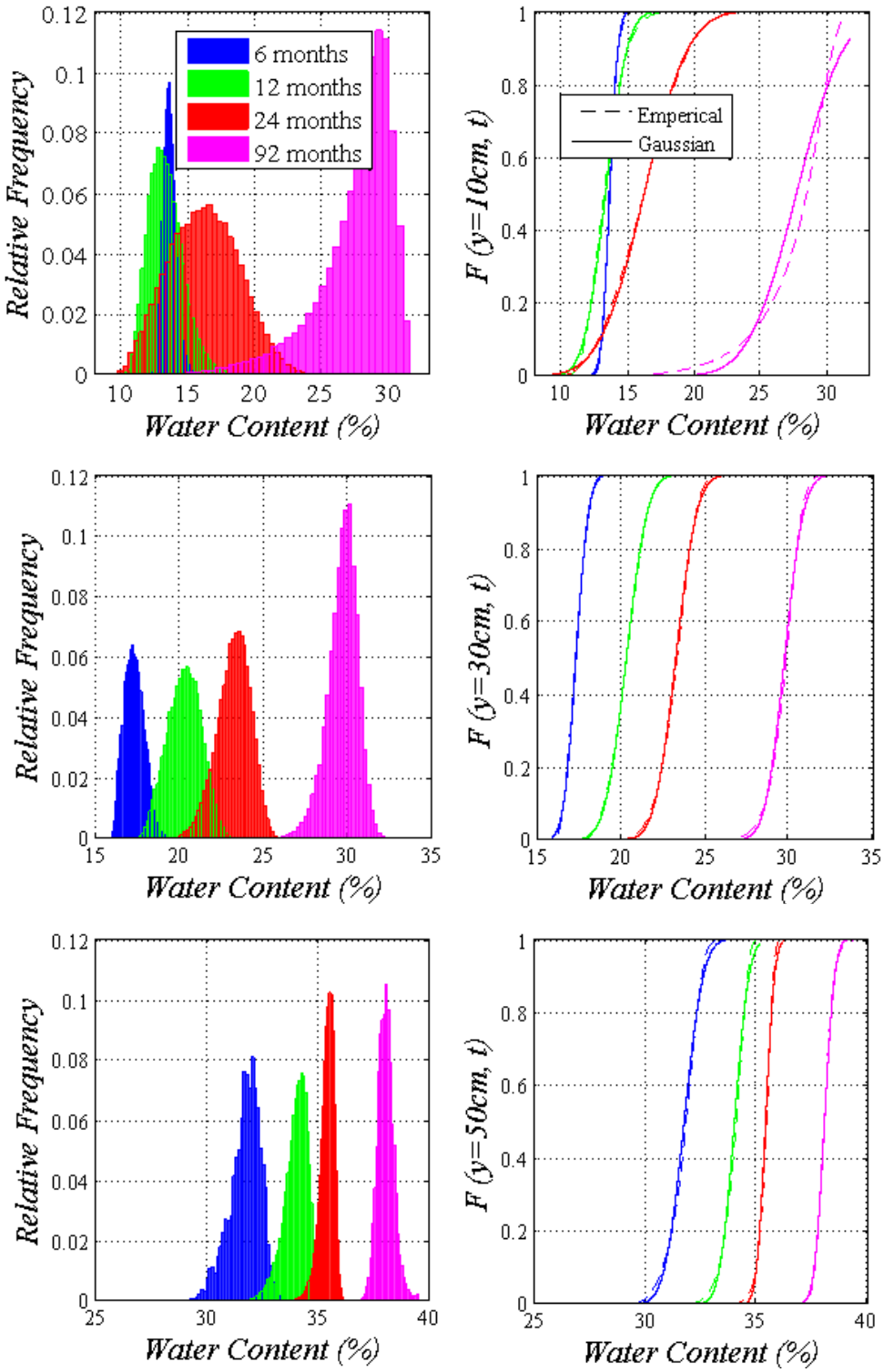

Figure 4.29. Relative frequency distribution and CDF of water content at A, B, C.

4.4 Comparison of Uncertainty in Cases 1 to 5

For better understanding of sources of parametric uncertainty of the THM behavior of material, a comparison is made between the cases 1 to 5. For any discrete random variable X, its probability distribution may be described by the probability mass function (PMF) denoted as $P_X(X=x_i)$, which is simply a function expressing the probability for all x_i. It can also be expressed in terms of Cumulative distribution function CDF given as:

$$F_X(x)=\sum_{\text{all } x_i \le x} P(X=x_i) = \sum_{\text{all } x_i \le x} P_X(x_i) \tag{4.16}$$

The CDF of all the three material response i.e. dry density, temperature and water content for all the cases (1 to 5) at three selected locations and at selected time are computed and are shown in . In each sub-figure, shown are the CDF of dry density at particular location and particular time for the above five cases.

The mean expected values of the responses and the respective standard deviations at different locations (10cm, 20cm, 30cm, 40cm and 50cm from heater) and at different times (6 months, 12 months, 24 months and 92 months) for cases 1 to 5 are summarized in Table 4.1 to Table 4.6. The mean profiles are shown in the Figure 4.30, Figure 4.33, and Figure 4 36.

The standard deviation profiles (Figure 4.31, Figure 4.34, and Figure 4.37) show the decrease of variability of the material response from the high temperature end to the low temperature end. From the standard deviation profile of dry density, it is observed that in the initial stage of time i.e. at 6 months, the standard deviation increased at y=20cm and

at y=40cm from the heater. This indicates that the response variation is not only influenced by the temperature, but also by the water injection from the other end. Hence, in problems involving water flow, the uncertainty of the material properties has significant influence on variability of dry density. But, this influence decrease eventually with increase in time period. Then again, temperature profile (Figure 4.34) shows, the uncertainty increases at higher temperature and the longer duration of time. The water content profile (Figure 4.37) shows a different pattern of variation. The standard deviation during initial stages i.e. at 6 months is more at low temperature end when compared to the high temperature end. But then, this is reversed with time. This can be due to the fact that the water takes time to permeate through the material.

4.3.1 Dry Density

The Figure 4.32 shows the cumulative distributions of dry density horizontally at three selected locations A, B, and C and vertically at four different time intervals t=6 months, t=12 months, t=24 months, t=96 months. As explained in the case studies, other than actual physical changes in the values of the response with respect to position and time, the variability increases from left to right (horizontally) and vertically downwards. That is, the range between which the dry density value changes with the parametric variation increases with time and decreasing distance from heater. The dry density at 10cm from heater varies between 1.667 and 1.711, 1.662 and 1.779, 1.598 and 1.801, 1.458 and 1.717 after 6months, 12 months, 24 months and 92 months respectively for case-5. Similarly, the dry density after 92 months varies between 1.414 and 1.450, 1.612 and

1.659 and 1.667 and 1.711 at 50cm, 30cm and 10cm from heater respectively for the case-5.

The cumulative distributions in all the cases are shown in each of sub-figure. For instance, the CDF of dry density at A (10cm from heater), after 24 months (third row and third column), increases between 1.723 and 1.731, 1.697 and 1.793, 1.649 and 1.740, 1.649 and 1.811 and 1.598 and 1.801 for cases 1 to 5 respectively. As seen from the Figure 4.32, the CDF of dry density in the case 1 increases within short span giving very narrow range of variation (0.008). This span increases to width of 0.096 in case-2 and to 0.091 in case 3. But the span increase tremendously to 0.162 in case-4 and to 0.204 in case-5. The uncertainty in dry density higher in combined variation of both hydraulic properties than, when they are varied individually. Similarly, the thermal parameters which have negligible effect on density when combined with the hydraulic parameter variation produced very high degree of uncertainty.

Thus, it can be said that the uncertainty with respect to dry density is negligible when measured at low temperature and when used for short duration purposes. Whereas, at higher temperatures and for the long duration purpose like that of consolidation, the dry density possess high uncertainty with respect to material properties and thus need to be measured very sensitively. It can also be said that the even if the variability of each single material properties may not influence the uncertainty of output dry density response, but when varied together produce high degree of uncertainty.

Table 4.1. Mean expected value of dry density for cases 1 – 5.

	Time duration	Distance from heater	Varying Parameters				
			λ_{dry}, λ_{sat}	P_0, λ_0, λ_d	k_0	P_0, λ_0, λ_d, k_0	λ_{dry}, λ_{sat}, P_0, λ_0, λ_d, k_0
Mean Dry Density (gm/cc)	6 months	10 cm	1.741	1.686	1.700	1.694	1.687
		20 cm	1.643	1.625	1.662	1.652	1.643
		30 cm	1.624	1.649	1.657	1.655	1.648
		40 cm	1.613	1.642	1.618	1.621	1.617
		50 cm	1.422	1.438	1.428	1.432	1.426
	12 months	10 cm	1.770	1.729	1.711	1.708	1.707
		20 cm	1.666	1.642	1.663	1.653	1.643
		30 cm	1.620	1.644	1.645	1.645	1.627
		40 cm	1.585	1.617	1.597	1.602	1.579
		50 cm	1.408	1.425	1.419	1.420	1.405
	24 months	10 cm	1.772	1.750	1.691	1.705	1.665
		20 cm	1.662	1.648	1.639	1.642	1.605
		30 cm	1.604	1.627	1.619	1.622	1.588
		40 cm	1.559	1.584	1.573	1.574	1.542
		50 cm	1.395	1.409	1.407	1.407	1.385
	92 months	10 cm	1.709	1.668	1.586	1.596	1.509
		20 cm	1.576	1.575	1.548	1.552	1.484
		30 cm	1.529	1.559	1.539	1.543	1.486
		40 cm	1.498	1.523	1.503	1.505	1.458
		50 cm	1.362	1.376	1.368	1.368	1.340

Table 4.2. Standard deviation of dry density for cases 1 to 5.

	Time duration	Distance from heater	Varying Parameters				
			λ_{dry}, λ_{sat}	P_0, λ_0, λ_d	k_0	P_0, λ_0, λ_d, k_0	λ_{dry}, λ_{sat}, P_0, λ_0, λ_d, k_0
Standard Deviation of Dry Density	6 months	10 cm	0.0010	0.0071	0.0024	0.0048	0.0041
		20 cm	0.0008	0.0046	0.0069	0.0105	0.0093
		30 cm	0.0004	0.0035	0.0017	0.0037	0.0036
		40 cm	0.0008	0.0013	0.0089	0.0074	0.0068
		50 cm	0.0004	0.0019	0.0040	0.0045	0.0054
	12 months	10 cm	0.0009	0.0078	0.0062	0.0080	0.0132
		20 cm	0.0008	0.0042	0.0020	0.0069	0.0043
		30 cm	0.0003	0.0040	0.0026	0.0034	0.0039
		40 cm	0.0007	0.0011	0.0064	0.0069	0.0074
		50 cm	0.0003	0.0008	0.0022	0.0025	0.0028
	24 months	10 cm	0.0005	0.0094	0.0154	0.0207	0.0269
		20 cm	0.0006	0.0030	0.0053	0.0040	0.0074
		30 cm	0.0003	0.0032	0.0045	0.0037	0.0048
		40 cm	0.0005	0.0012	0.0056	0.0045	0.0049
		50 cm	0.0002	0.0009	0.0021	0.0014	0.0019
	92 months	10 cm	0.0007	0.0165	0.0209	0.0271	0.0276
		20 cm	0.0005	0.0012	0.0074	0.0088	0.0123
		30 cm	0.0003	0.0031	0.0068	0.0079	0.0107
		40 cm	0.0004	0.0023	0.0093	0.0102	0.0129
		50 cm	0.0002	0.0015	0.0044	0.0048	0.0060

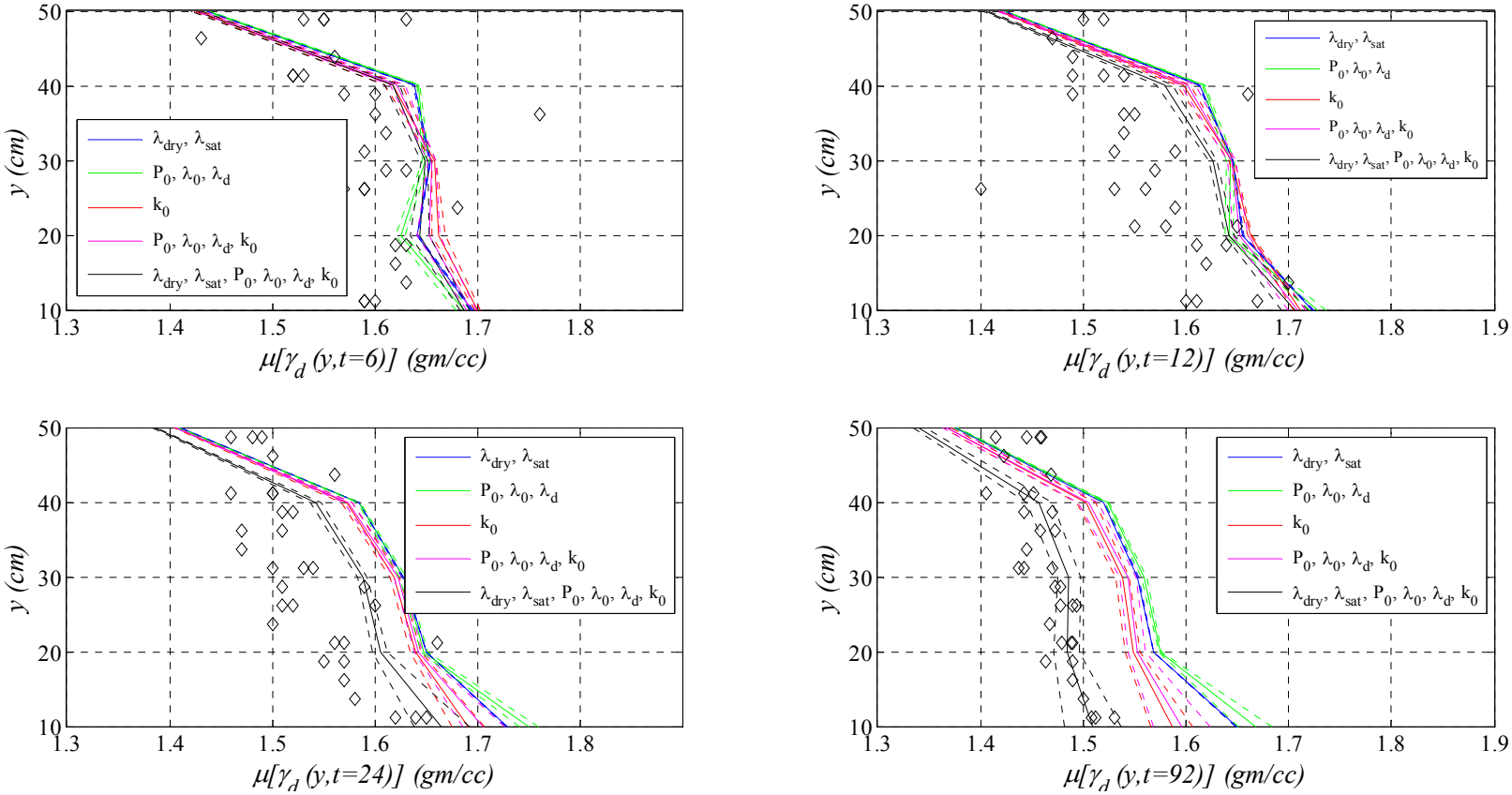

Figure 4.30. Mean profile of dry density in cases 1 to 5.

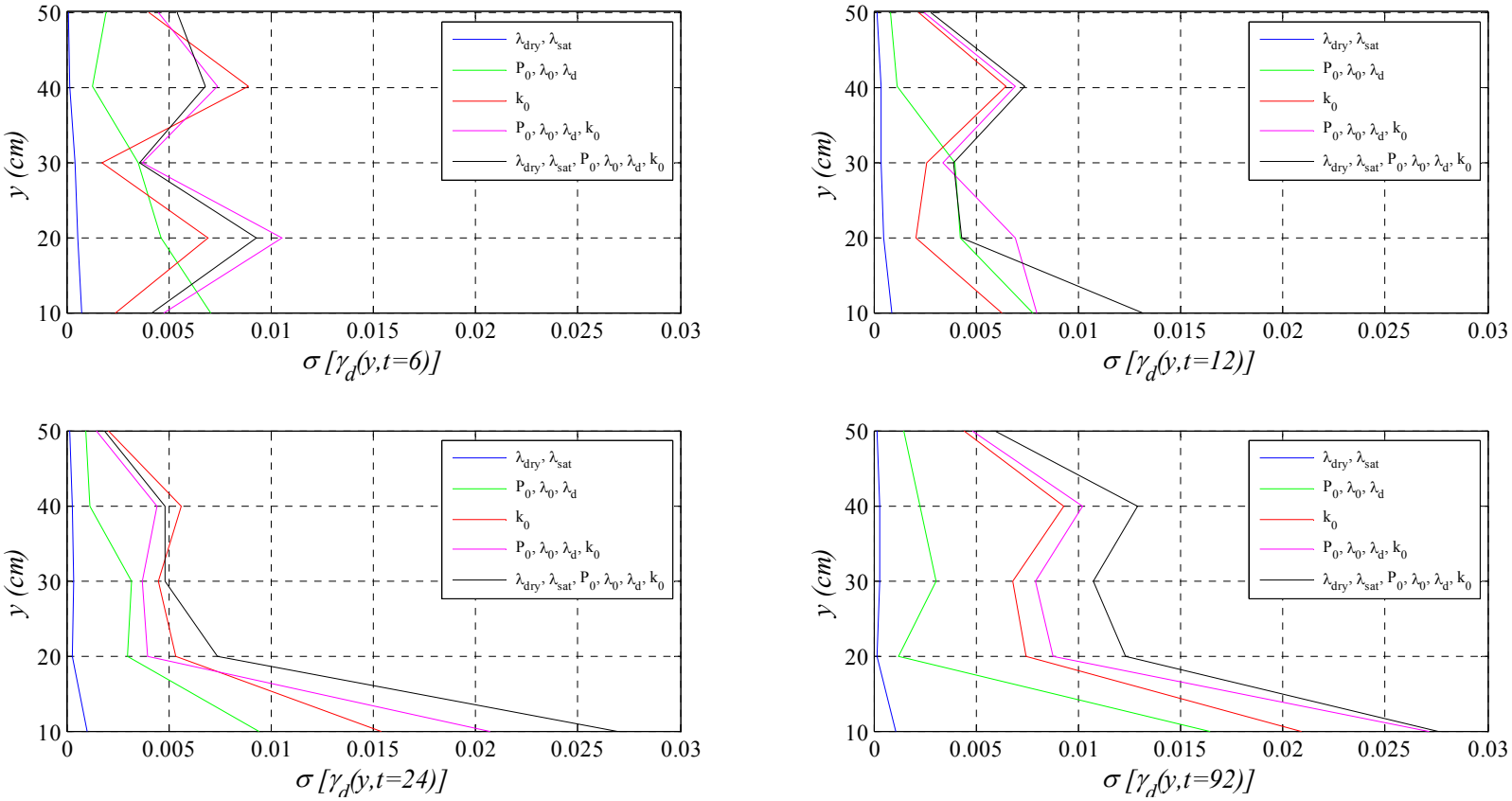

Figure 4.31. Standard deviation profile for dry density in cases 1 to 5.

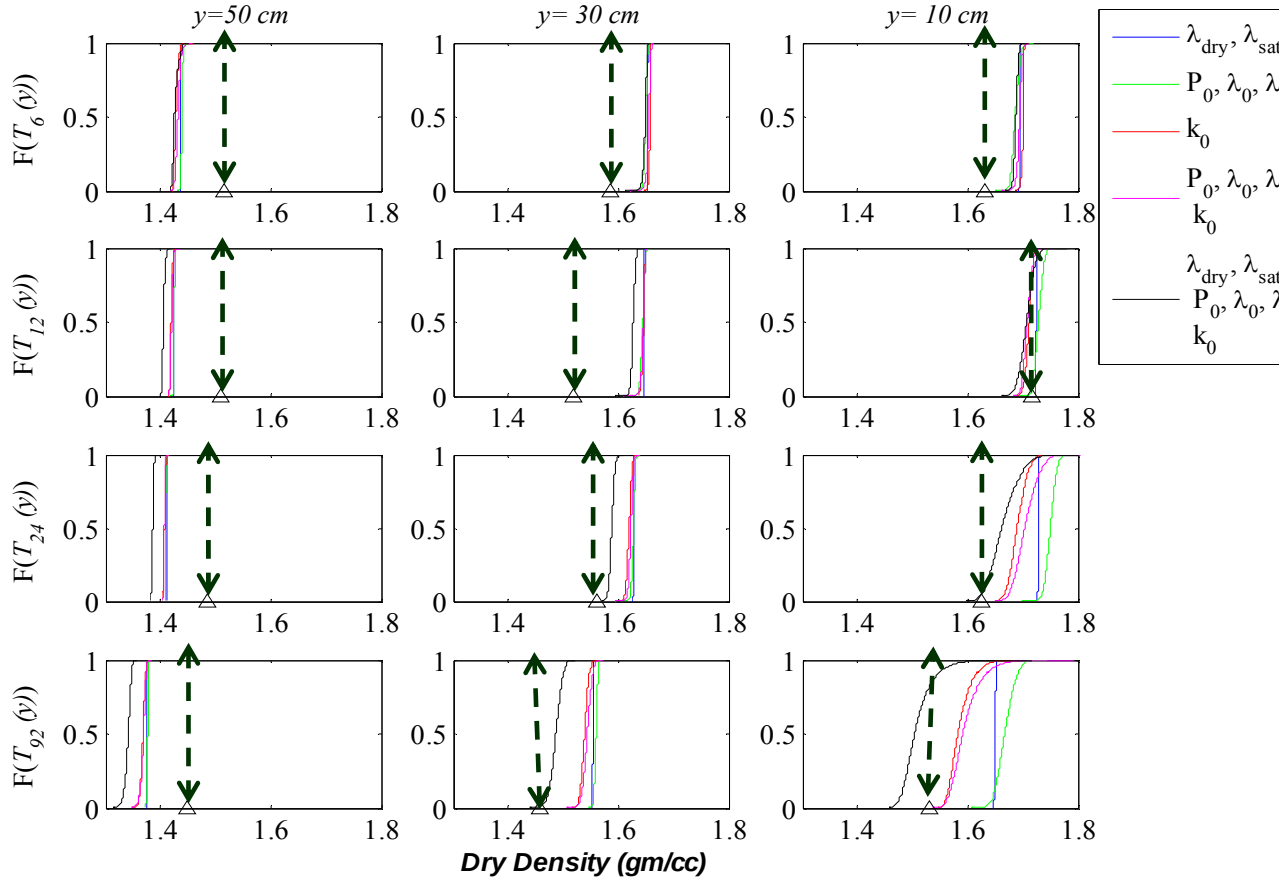

Figure 4.32. Comparison of cumulative distribution functions of dry density at three locations (*y=50cm, y=30cm, y=10cm* from heater – shown horizontally) between cases 1 to 5 at different time intervals (*t=6 months, t=12 months, t=24 months, t=92 months* shown vertically).

4.3.2 Temperature

Figure 4.35 shows the CDF of temperature horizontally at three selected locations: A, B, C (which are at 10cm, 30cm and 50cm from heater respectively) and vertically at four different time intervals t=6 months, t=12 months, t=24 months, t=96 months. Similar to dry density, it can be observed that the variability increases from left to right (horizontally) and vertically downwards. That is, the range between which the temperature value changes with the parametric variation increases with time and decreasing distance from heater. The temperature at A varies between 46.3°C and 51.2°C, 45.8°C and 52.4°C, 45.7°C and 56.3°C, 46.9°C and 58.2°C at 6months, 12 months, 24 months and 92 months respectively for case-5. Similarly, the temperature after 92 months varies between 46.3°C and 51.2°C, 26.4°C and 27.5°C, 23.8°C and 24.3°C at A, B, C respectively for the case-5.

Similarly, the CDF in all the cases are shown in each of sub-figure. For instance, the CDF of temperature at A, after 24 months (third row and third column), increases between 47.78°C and 49.8°C, 45.8°C and 48.5°C, 47.5°C and 52.5°C, 45.9°C and 54.9°C and 45.7°C and 56.3°C for cases 1 to 5 respectively. As seen from the Figure 4.35, the CDF of temperature in the case 1 increases within short span giving very narrow range of variation (2.0°C). This span increases to width of 2.6°C in case-2 and to 5.0°C in case 3. But the span increase tremendously to 9.0°C in case-4 and to 10.6°C in case-5.

The uncertainty in temperature is more in permeability variation than in retention curve variation and higher in combined variation of both hydraulic properties. This is further high when the variability of thermal parameters is included. The thermal parameters have very small effect on uncertainty of temperature even with its combination with hydraulic parameters.

Thus, it can be said that the uncertainty of temperature is negligible when measured at lower temperatures and when used for short duration purposes. Whereas, at higher temperatures and for the long duration purpose like that of consolidation, the temperature possess high uncertainty with respect to material properties and thus need to be measured very sensitively. It can also be said that the even if the variability of each single material properties may not influence the uncertainty of output temperature response, but when varied together produce high degree of uncertainty.

Table 4.3. Mean expected value of temperature for cases 1 – 5.

	Time duration	Distance from heater	Varying Parameters				
			λ_{dry}, λ_{sat}	P_0, λ_0, λ_d	k_0	P_0, λ_0, λ_d, k_0	λ_{dry}, λ_{sat}, P_0, λ_0, λ_d, k_0
Mean Temperature (Celsius)	6 months	10 cm	69.1	47.3	48.7	47.9	48.5
		20 cm	48.7	32.2	32.5	32.5	33.0
		30 cm	36.6	26.4	26.5	26.5	26.9
		40 cm	30.5	24.3	24.4	24.4	24.6
		50 cm	28.4	23.8	23.9	23.9	24.1
	12 months	10 cm	69.4	47.0	48.8	48.0	48.3
		20 cm	49.2	32.0	32.7	32.6	32.9
		30 cm	36.9	26.4	26.6	26.7	26.9
		40 cm	30.4	24.3	24.5	24.5	24.7
		50 cm	28.2	23.9	24.0	24.0	24.2
	24 months	10 cm	69.4	46.9	49.5	48.6	49.2
		20 cm	49.1	31.9	33.3	33.1	33.7
		30 cm	36.5	26.4	27.0	27.0	27.4
		40 cm	29.9	24.4	24.7	24.7	25.0
		50 cm	27.8	23.9	24.1	24.2	24.3
	92 months	10 cm	68.6	48.2	52.4	52.8	54.5
		20 cm	47.2	33.2	35.4	35.6	36.9
		30 cm	34.5	27.1	28.1	28.3	29.1
		40 cm	28.5	24.8	25.3	25.3	25.8
		50 cm	26.8	24.2	24.5	24.6	24.9

Table 4.4. Standard deviation of dry density for cases 1 – 5.

	Time duration	Distance from heater	Varying Parameters				
			λ_{dry}, λ_{sat}	P_0, λ_0, λ_d	k_0	P_0, λ_0, λ_d, k_0	λ_{dry}, λ_{sat}, P_0, λ_0, λ_d, k_0
Standard Deviation of Temperature	6 months	10 cm	0.28	0.24	0.28	0.37	0.51
		20 cm	0.30	0.19	0.14	0.16	0.25
		30 cm	0.21	0.11	0.06	0.08	0.13
		40 cm	0.15	0.06	0.04	0.05	0.07
		50 cm	0.11	0.04	0.03	0.04	0.06
	12 months	10 cm	0.29	0.23	0.48	0.60	0.70
		20 cm	0.31	0.19	0.31	0.34	0.42
		30 cm	0.22	0.11	0.16	0.17	0.23
		40 cm	0.14	0.06	0.09	0.10	0.13
		50 cm	0.10	0.04	0.06	0.07	0.09
	24 months	10 cm	0.29	0.24	0.81	1.14	1.32
		20 cm	0.31	0.21	0.55	0.71	0.85
		30 cm	0.21	0.13	0.29	0.35	0.44
		40 cm	0.12	0.07	0.14	0.17	0.22
		50 cm	0.09	0.05	0.10	0.12	0.15
	92 months	10 cm	0.27	0.58	1.59	2.29	2.50
		20 cm	0.26	0.44	0.86	1.15	1.32
		30 cm	0.15	0.23	0.41	0.52	0.64
		40 cm	0.09	0.11	0.19	0.24	0.31
		50 cm	0.07	0.08	0.13	0.16	0.21

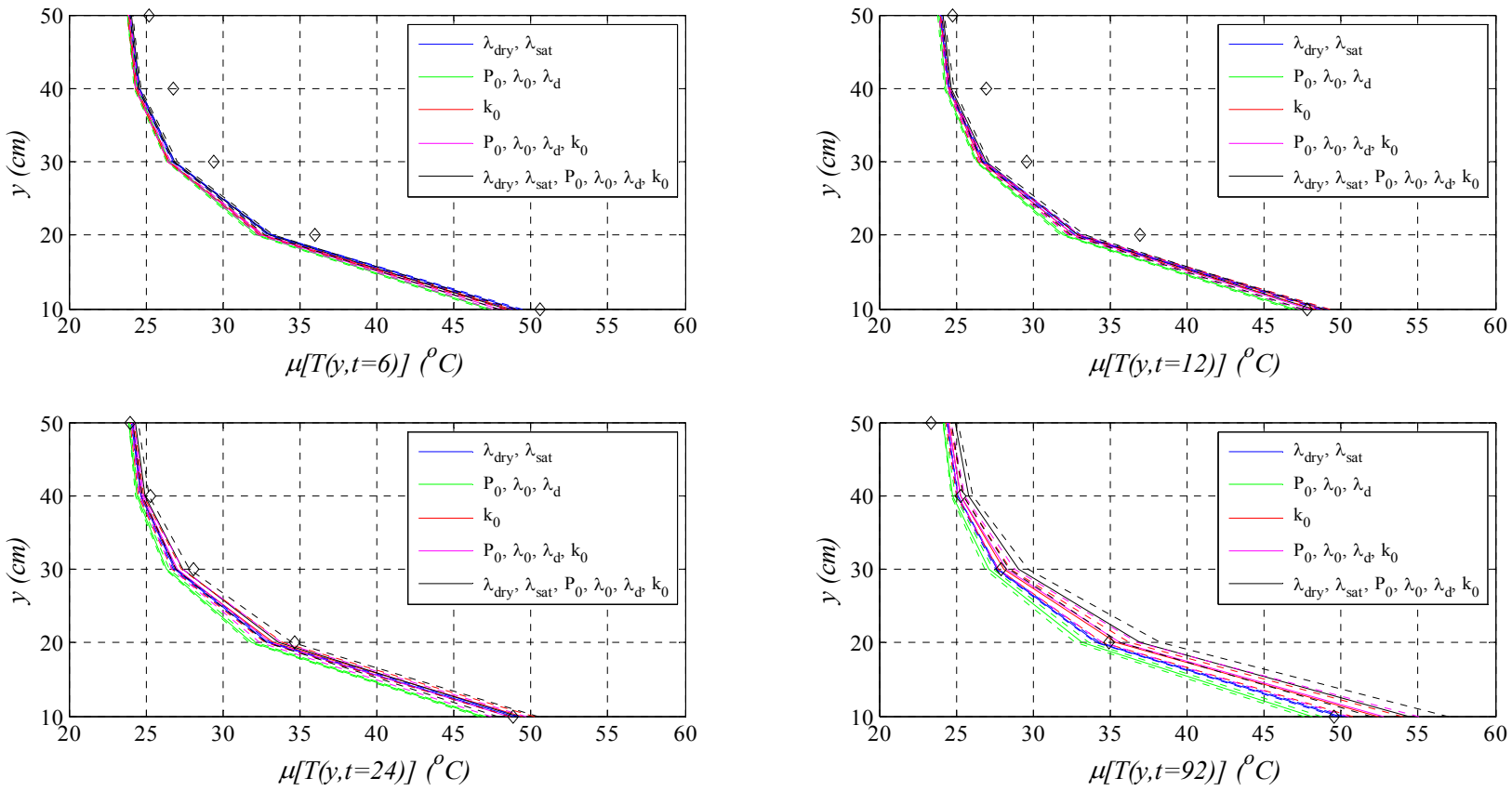

Figure 4.33. Mean profile for temperature in cases 1 to 5.

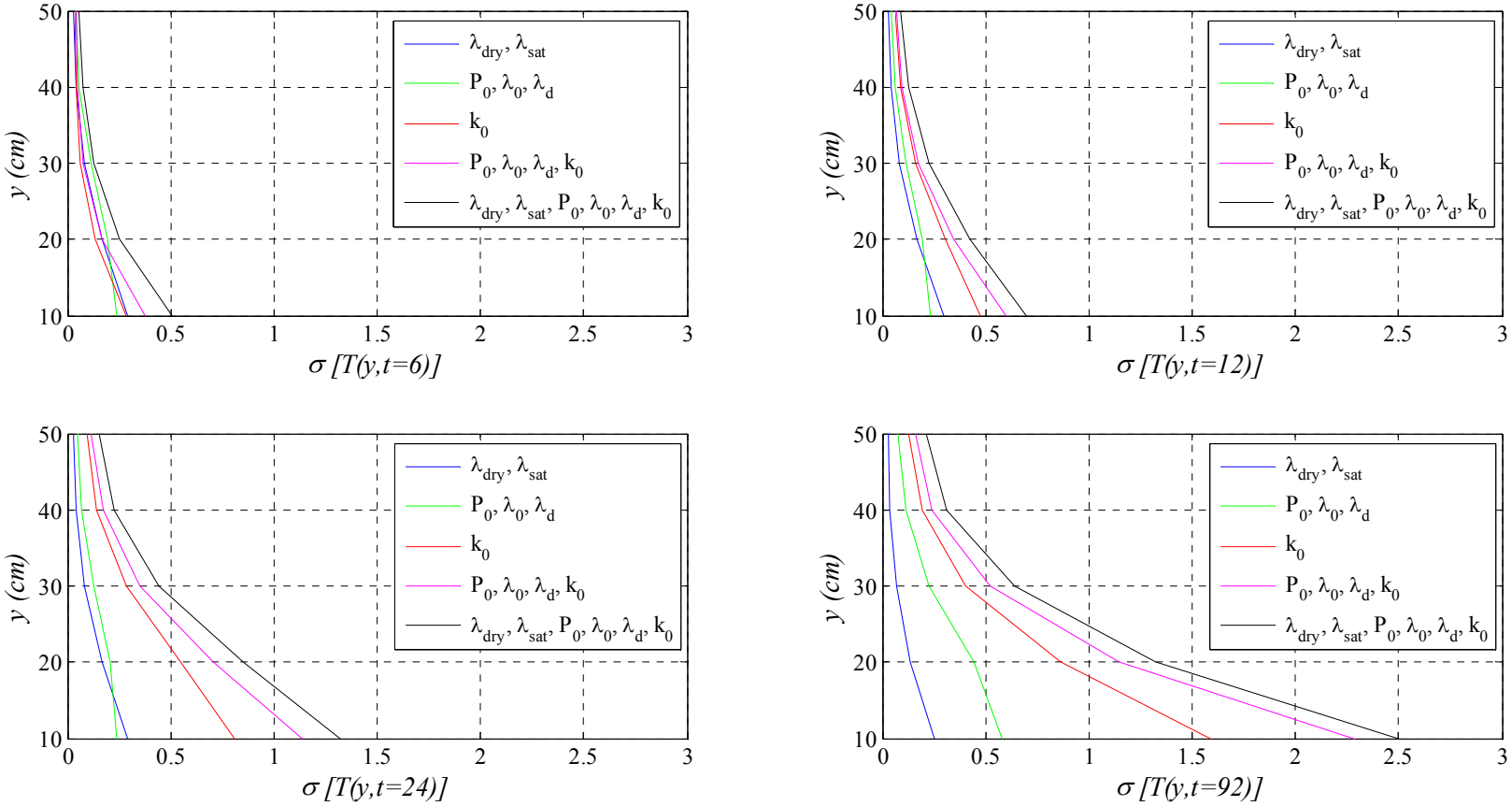

Figure 4.34. Standard deviation profile for temperature in cases 1 to 5.

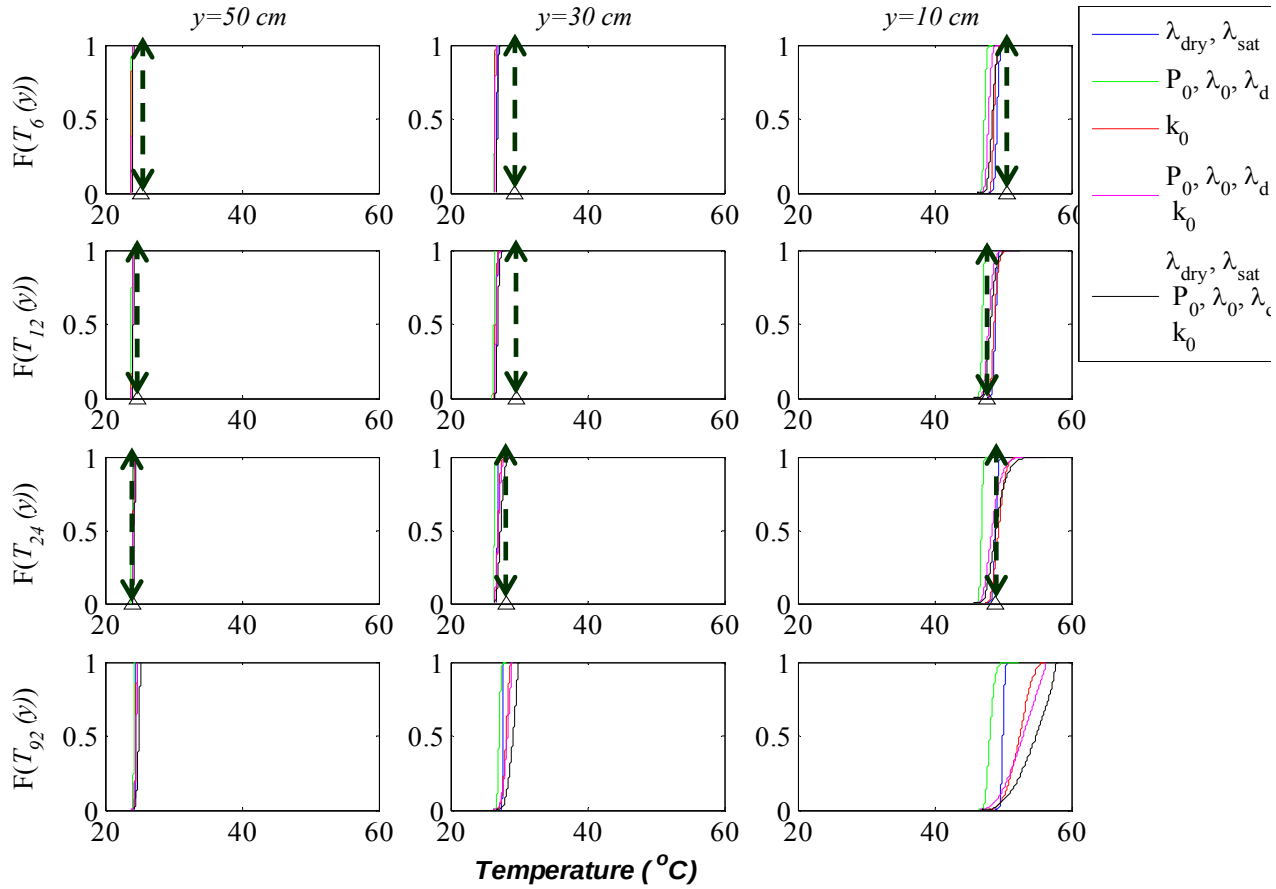

Figure 4.35. Comparison of cumulative distribution functions of temperature at three locations (*y=50cm, y=30cm, y=10cm* from heater – shown horizontally) between cases 1 to 5 at different time intervals (*t=6 months, t=12 months, t=24 months, t=92 months* shown vertically).

4.3.3 Water Content

Figure 4.38 shows the cumulative distributions of water content horizontally at three selected locations A, B, C and vertically at four different time intervals t=6 months, t=12 months, t=24 months, t=96 months. It can be observed that similar to dry density and temperature, the variability of water content also increases from left to right (horizontally) and vertically downwards. That is, the range between which the water content value changes with the parametric variation increases with time and decreasing distance from heater. The water content at A varies between 11.8%-16.1%, 9.8%-19.2%, 9.0%-24.5% and 10.7%-31.5% after 6months, 12 months, 24 months and 92 months respectively for case-5. Similarly, the water content after 92 months varies between 11.8%-16.1%, 15.9%-19.8%, 29.0%-33.8 at A, B, C respectively for the case-5.

Similarly, the CDF in all the cases are shown in each of sub-figure. For instance, the CDF water content at 10cm from heater, after 24 months (third row and third column), increases between 11.9% and 12.2%, 8.2% and 17.9%, 11.0% and 20.4%, 9.2% and 22.7% and 9.0% and 24.5% for cases 1 to 5 respectively. As seen from the Figure 4.38, the CDF of water content in the case 1 increases within short span giving very narrow range of variation (0.3%). This span increases to width of 9.7% in case-2 and to 9.4% in case 3. But the span increase tremendously to 13.5% in case-4 and to 15.5% in case-5.

The uncertainty in water content is more in combined variation of both hydraulic properties than when they are varied individually. This holds true when the variability of

thermal parameters are also included. Similar to the dry density response, the thermal parameters, which when varied individually had negligible effect on water content, when combined with the hydraulic parameter variation produced very high degree of uncertainty.

Thus, it can be said that the uncertainty in measurement of water content is negligible when measured at lower temperatures and when used for short duration purposes. Whereas, at higher temperatures and for the long duration purpose like that of consolidation, the water content possess high uncertainty with respect to material properties and thus need to be measured very sensitively.

It can be said that the even if the variability of each single material properties may not influence the uncertainty of output water content response, but when varied together produce high degree of uncertainty.

Table 4.5. Mean expected value of water content for cases 1 – 5.

	Time duration	Distance from heater	Varying Parameters				
			λ_{dry}, λ_{sat}	P_0, λ_0, λ_d	k_0	P_0, λ_0, λ_d, k_0	λ_{dry}, λ_{sat}, P_0, λ_0, λ_d, k_0
Mean Water Content (w %)	6 months	10 cm	10.3	13.0	13.1	13.6	13.6
		20 cm	15.3	17.3	15.7	16.9	17.1
		30 cm	16.9	16.0	16.4	17.3	17.3
		40 cm	18.0	16.6	19.3	19.8	19.7
		50 cm	31.1	30.2	31.5	31.6	31.8
	12 months	10 cm	9.6	11.6	13.4	13.9	13.3
		20 cm	14.8	17.2	16.9	18.1	18.2
		30 cm	18.4	17.8	18.8	19.3	20.3
		40 cm	21.4	20.0	22.2	22.3	23.9
		50 cm	32.8	32.1	32.9	33.0	34.0
	24 months	10 cm	9.9	11.2	15.5	15.5	16.2
		20 cm	15.7	18.0	19.4	20.3	21.1
		30 cm	20.4	20.4	21.5	22.3	23.3
		40 cm	24.3	23.7	24.7	25.3	26.4
		50 cm	34.2	33.9	34.1	34.5	35.4
	92 months	10 cm	13.2	17.4	23.7	24.1	27.5
		20 cm	22.3	24.0	26.4	26.6	29.4
		30 cm	26.5	25.7	27.3	27.3	29.7
		40 cm	28.8	27.9	29.2	29.2	31.4
		50 cm	36.7	36.1	36.7	36.7	38.0

Table 4.6. Standard deviation of dry density for cases 1 – 5.

	Time duration	Distance from heater	Varying Parameters				
			λ_{dry}, λ_{sat}	P_0, λ_0, λ_d	k_0	P_0, λ_0, λ_d, k_0	λ_{dry}, λ_{sat}, P_0, λ_0, λ_d, k_0
Standard Deviation of Water Content	6 months	10 cm	0.03	0.90	0.25	0.44	0.49
		20 cm	0.03	0.68	0.13	0.21	0.20
		30 cm	0.03	0.60	0.59	0.66	0.58
		40 cm	0.07	0.66	1.17	1.28	1.14
		50 cm	0.04	0.36	0.56	0.66	0.68
	12 months	10 cm	0.02	0.85	0.83	1.09	1.27
		20 cm	0.03	0.76	0.61	0.47	0.71
		30 cm	0.05	0.64	0.81	0.79	0.98
		40 cm	0.09	0.75	1.00	1.19	1.17
		50 cm	0.04	0.36	0.43	0.52	0.52
	24 months	10 cm	0.02	0.91	1.62	2.22	2.58
		20 cm	0.04	0.87	1.10	1.07	1.37
		30 cm	0.03	0.73	0.90	0.83	0.99
		40 cm	0.04	0.69	0.75	0.70	0.75
		50 cm	0.02	0.33	0.33	0.27	0.32
	92 months	10 cm	0.05	2.05	2.22	2.49	2.79
		20 cm	0.05	0.85	1.00	0.97	1.29
		30 cm	0.01	0.44	0.70	0.65	0.89
		40 cm	0.02	0.26	0.64	0.60	0.80
		50 cm	0.01	0.11	0.30	0.28	0.36

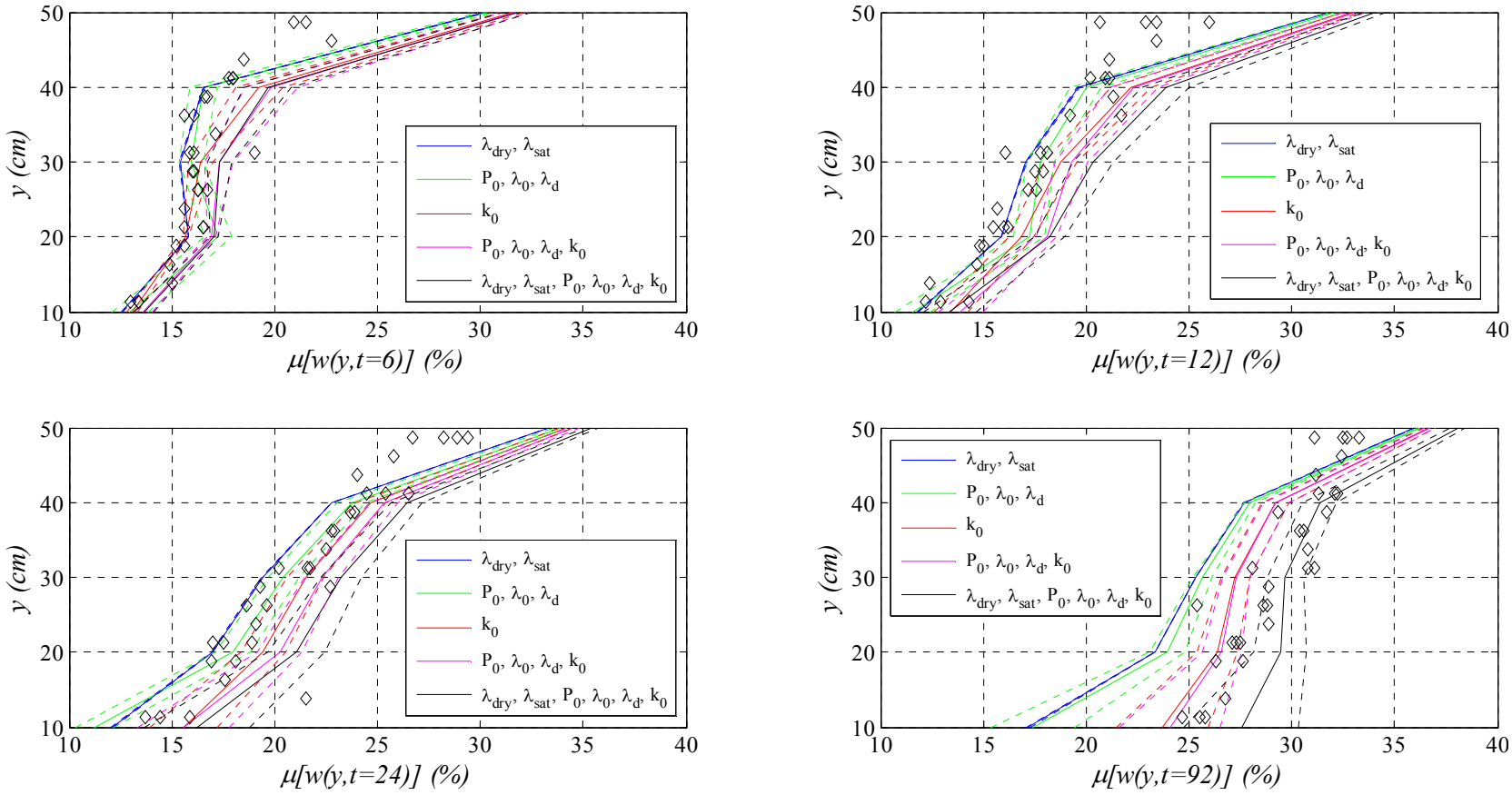

Figure 4 36. Mean profile of water content in cases 1 to 5.

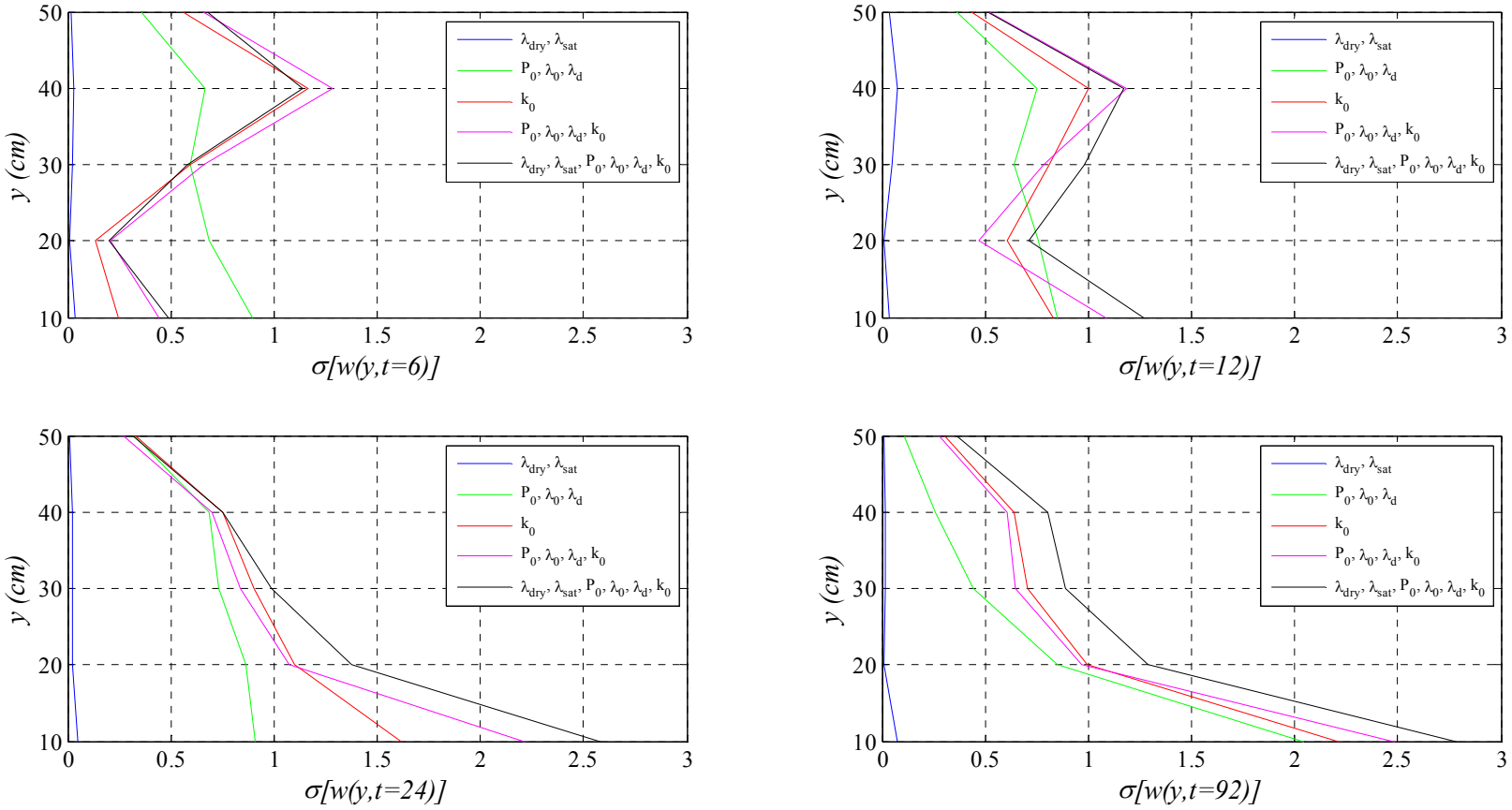

Figure 4.37. Standard deviation profile of water content in cases 1 to 5.

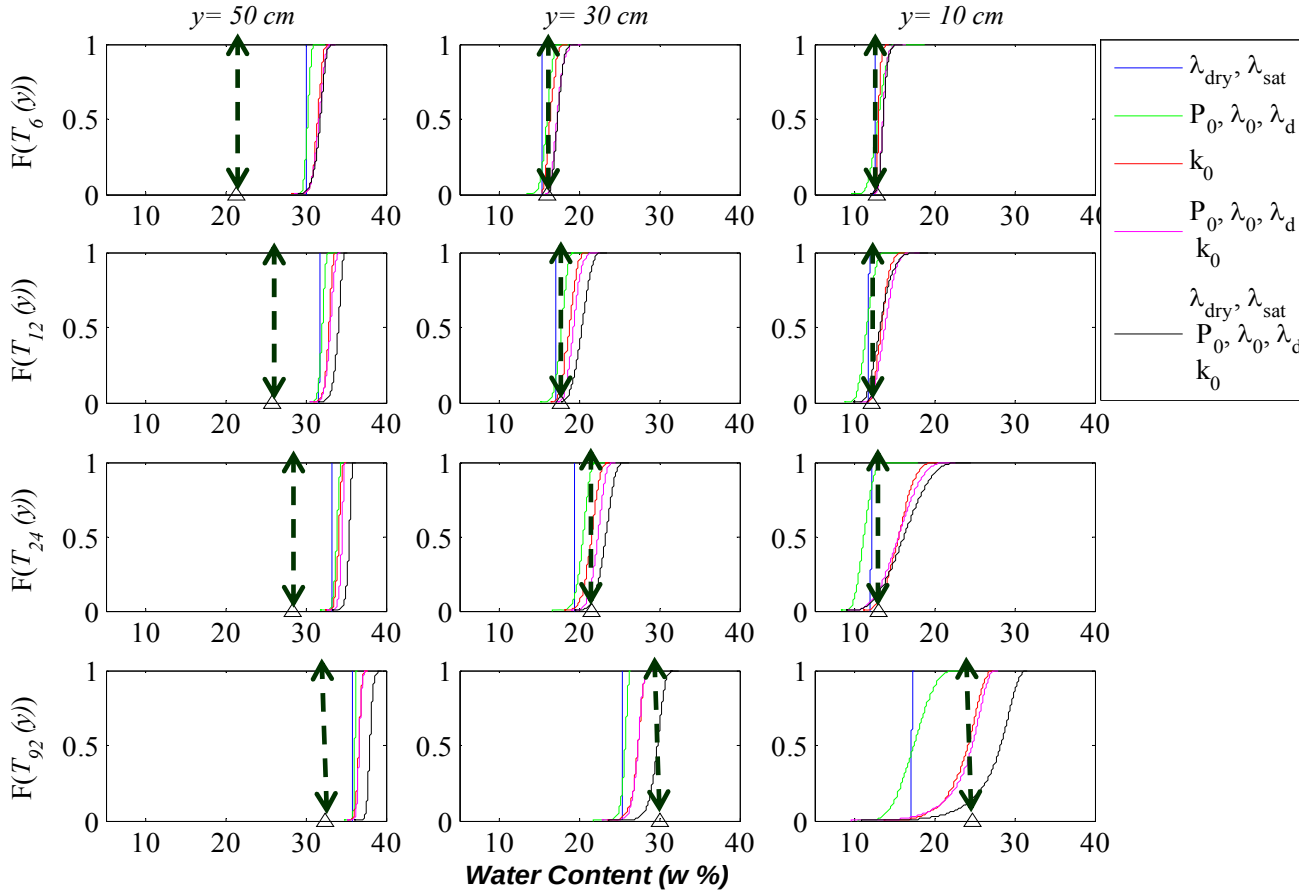

Figure 4.38. Comparison of cumulative distribution functions of water content at three locations (*y=50cm, y=30cm, y=10cm* from heater – shown horizontally) between cases 1 to 5 at different time intervals (*t=6 months, t=12 months, t=24 months, t=92 months* shown vertically).

4.5 Correlation and Covariance of THM Response

A special attention is given to case-5, where both thermal and hydraulic parameters are varied. Correlation is established between the output response and the input parameters. This gives us an idea of how each parameter has its influence on the output response. Figure 4.42, Figure 4.43 and Figure 4.44 shows the correlation coefficient at three positions A, B and C (10cm, 30cm and 50cm from the heater) at different time with respect to all six parameters.

Figure 4.42 shows the dry density correlation with the parameters. It can be observed that effect of both thermal properties has very less influence, where as it is highly negatively correlated with the intrinsic permeability. The retention curve parameters also have negative impact near the heater when compared to near the hydrating end. Figure 4.43 shows the temperature correlation with the parameters. It can be observed that the hydraulic parameters influence the temperature than the thermal parameters which was also observed in previous case studies. Figure 4.44 shows the water content correlation with the parameters. Again, the thermal parameters have no effect on the water content, while the intrinsic permeability has direct impact. Figure 4.45, Figure 4.46 and Figure 4.47 show the same in full scale spatial-temporal space.

The cross correlation between the output response variables both within themselves and with respect to each other are also plotted. To simply the plots, the correlation is plotted

in space lag (τ_y) domain at four different durations (6months, 12 months, 24 months and 92 months). This way it is possible to capture the local variation of the response.

Figure 4.48, Figure 4.49, and Figure 4.50 show the spatial-temporal correlation of dry density, temperature, and water content with themselves, respectively. In each figure, the subplots are plots at different times; For instance, the subplot second row third column has the correlation between the duration t=6months and t=12 months. In this scheme, correlation combinations lying on the diagonal represent the response output autocorrelation with respect to time. Cases off the diagonal are full cross correlations at different time durations. And in each subplot, one unit dimension corresponds to the space lags of 20 cm. The y-axis ranging from 0 to 60 is the location at which we are finding correlation, and the x-axis also ranging from 0 to 60 shows the position with which correlation is found. For example, when y = 0 cm is correlated with y=0, y=20 y=40 and y=60, the correlation coefficients are given at (0, 0), (0, 20), (0, 40) and (0, 60) respectively; when y = 20 cm is correlated with y=0, y=20 y=40 and y=60, the correlation coefficients are given at (20, 0), (20, 20), (20, 40) and (20, 60) respectively; when y = 40 cm is correlated with y=0, y=20 y=40 and y=60, the correlation coefficients are given at (40, 0), (40, 20), (40, 40) and (40, 60) respectively.

Figure 4.51, Figure 4.52, and Figure 4.53 show the cross correlation between one another in the similar fashion. In these figures, the horizontal and vertical subplots correspond to different output response. For instance in Figure 4.51, dry density at

different time is plotted horizontally against temperature on vertically. That is, the subplot in second row and third column give correlation between, temperature at t = 6 months and dry density at t = 12 months, whereas, the subplot in third row and second column give correlation between, temperature at t = 12 months and dry density at t = 6 months.

4.6 Discussion

The individual thermal conductivities show no influence on the THM response, but when combined with the variation in hydrological parameters, its influence increases. Similarly, retention curve parameters and permeability parameters individually show lower variation when compared to the case where their variation is combined with that of other parameters.

The correlation between the response variable and the material parameters show that:

- The dry density is not affected by the variation in thermal conductivities at any time and location, whereas the retention curve parameter significant influence and intrinsic permeability has huge impact during the initial period. But the influence of retention curve parameters decreases gradually and at longer durations, and interestingly, the intrinsic permeability show negative influence.

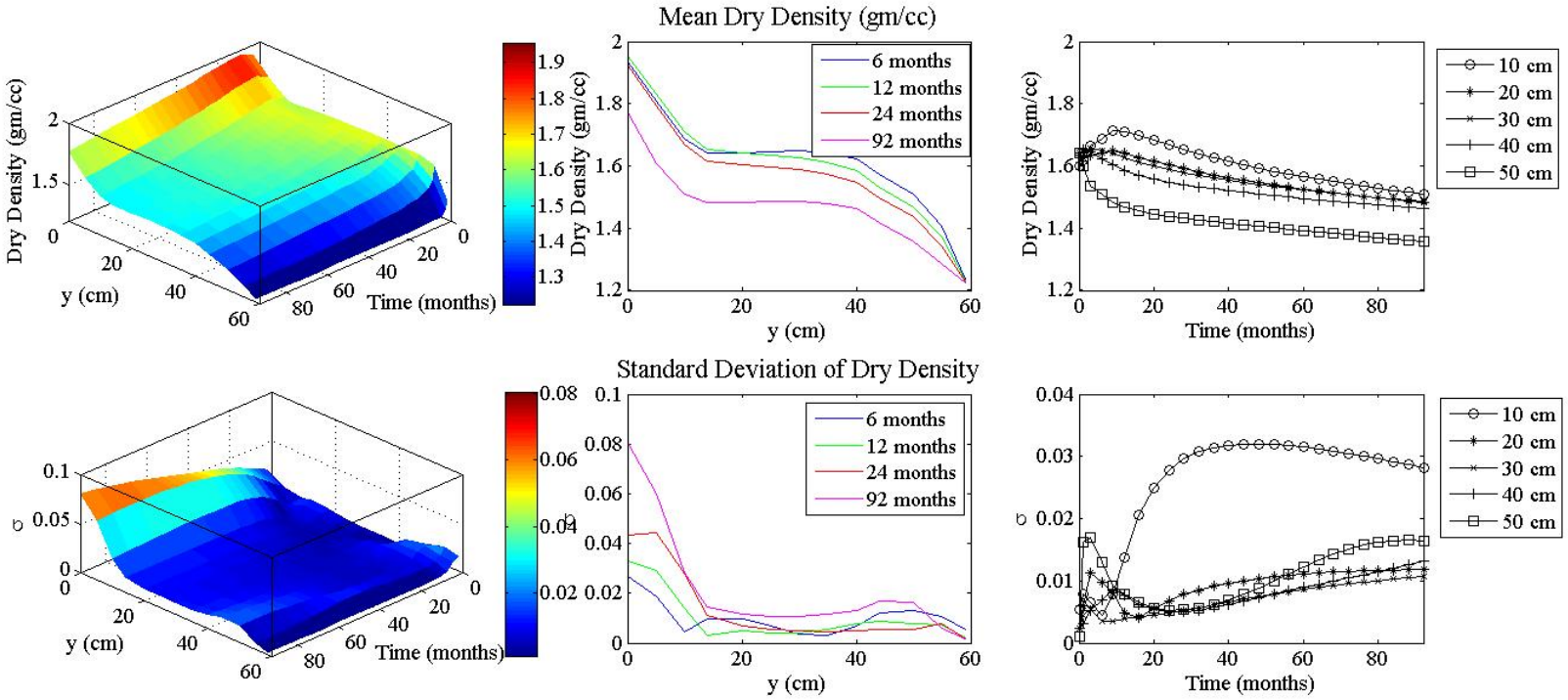

Figure 4.39. Mean and standard deviation of dry density with distance from heater (y) and duration time (t).

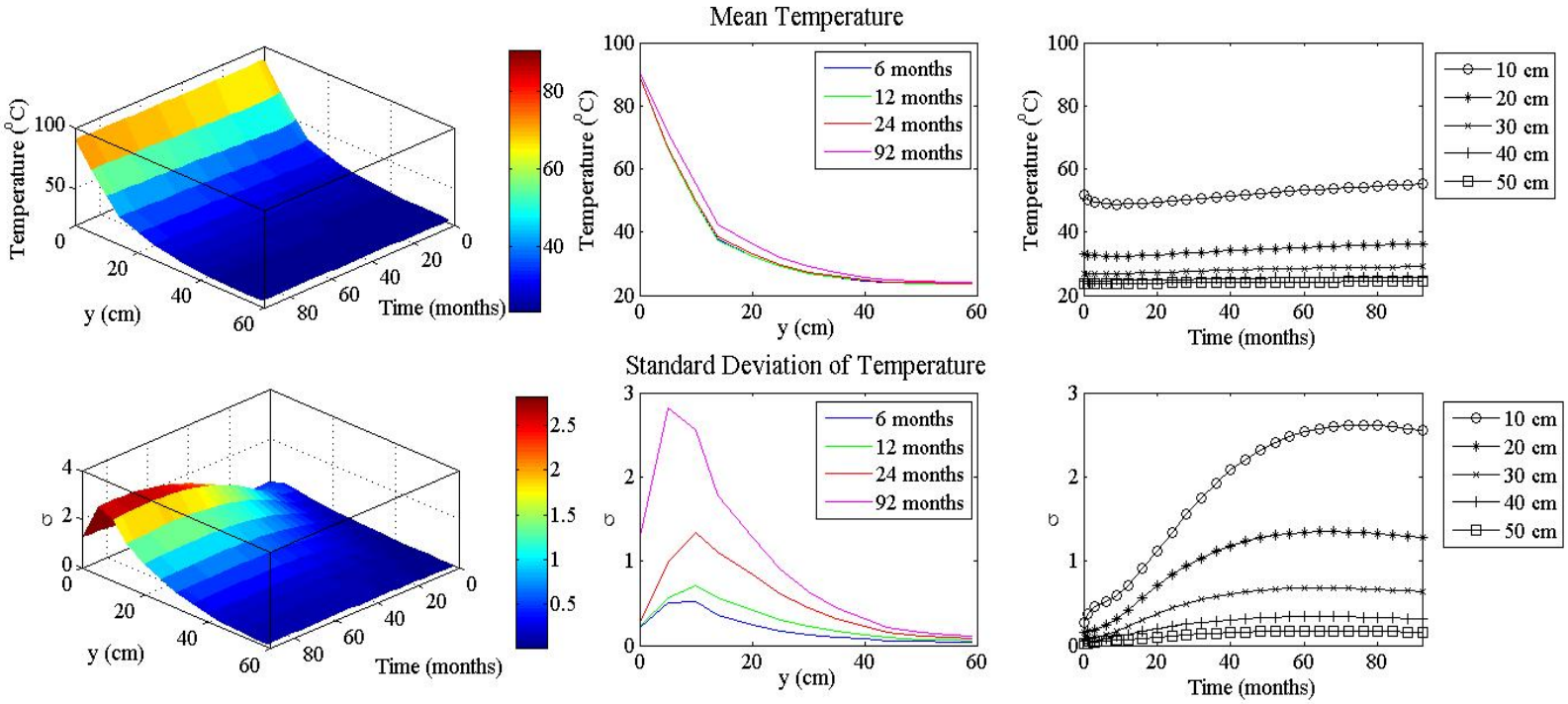

Figure 4.40. Mean and standard deviation of temperature with distance from heater (*y*) and duration time (*t*).

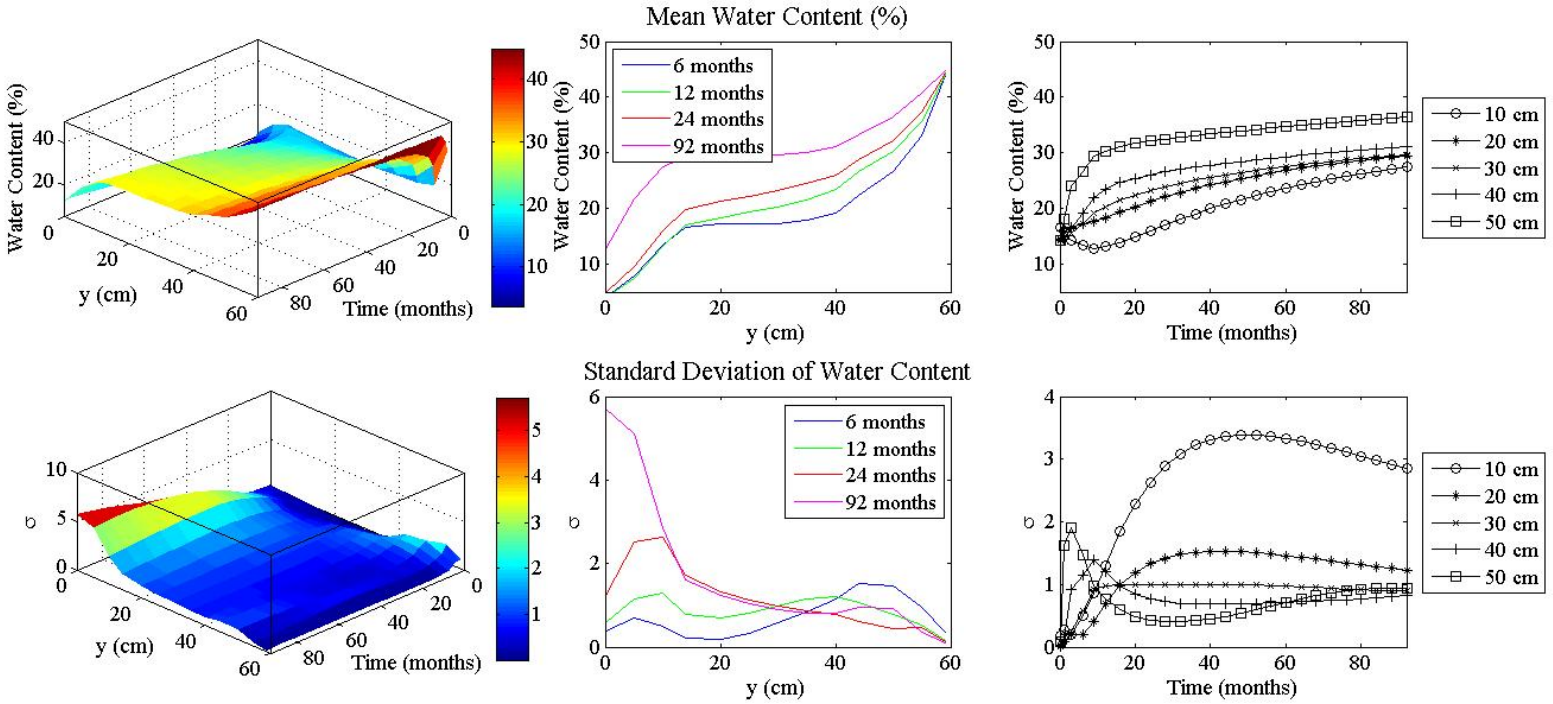

Figure 4.41. Mean and standard deviation of water content with distance from heater (y) and duration time (t).

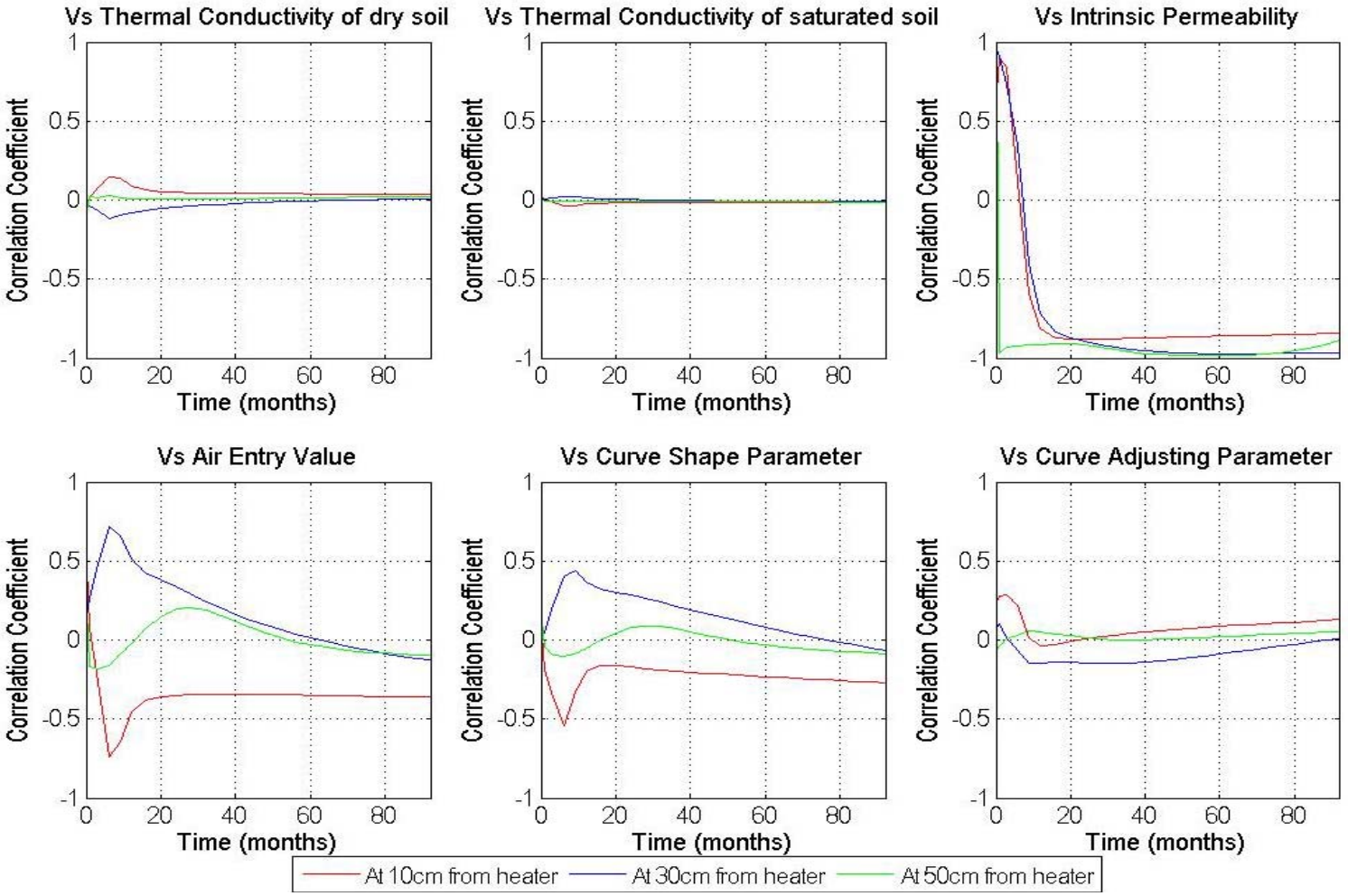

Figure 4.42. Correlation coefficient between dry density and the parameters at three locations (*y=10cm, y=30cm, y=50cm* from heater) with time.

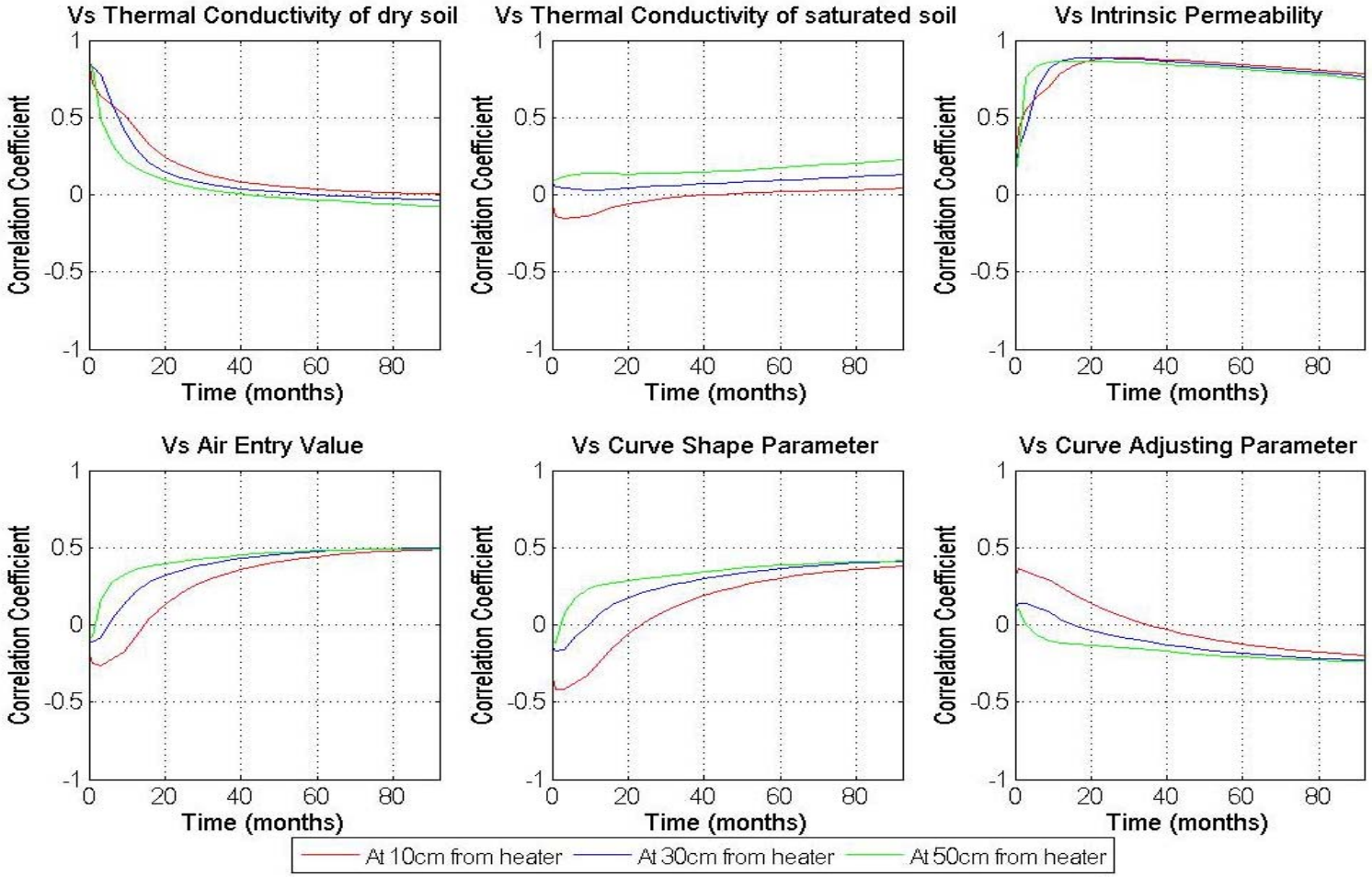

Figure 4.43. Correlation coefficient between temperature and the parameters at three locations (*y=10cm, y=30cm, y=50cm* from heater) with time.

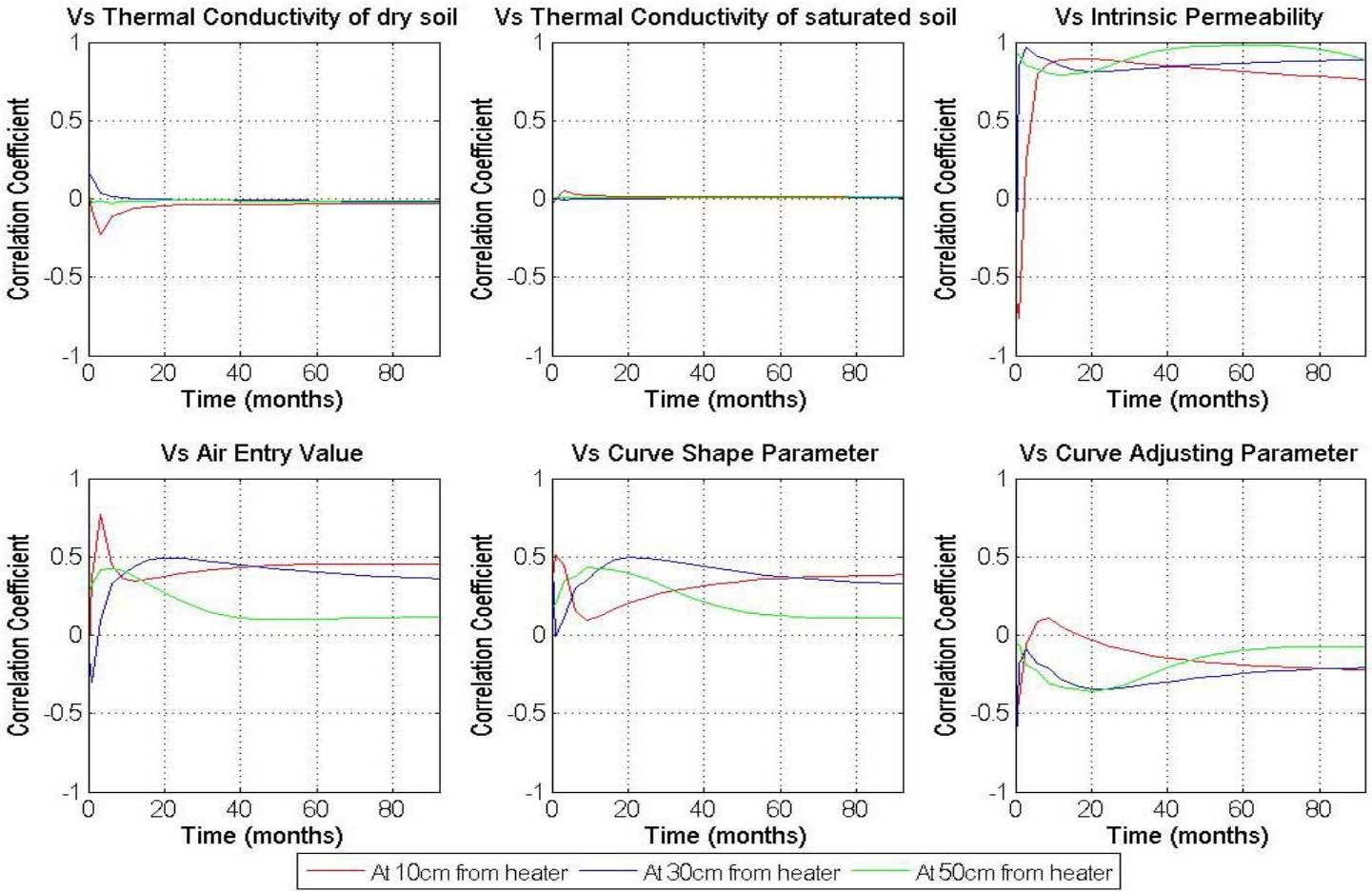

Figure 4.44. Correlation coefficient between water content and the parameters at three locations (*y=10cm, y=30cm, y=50cm* from heater) with time

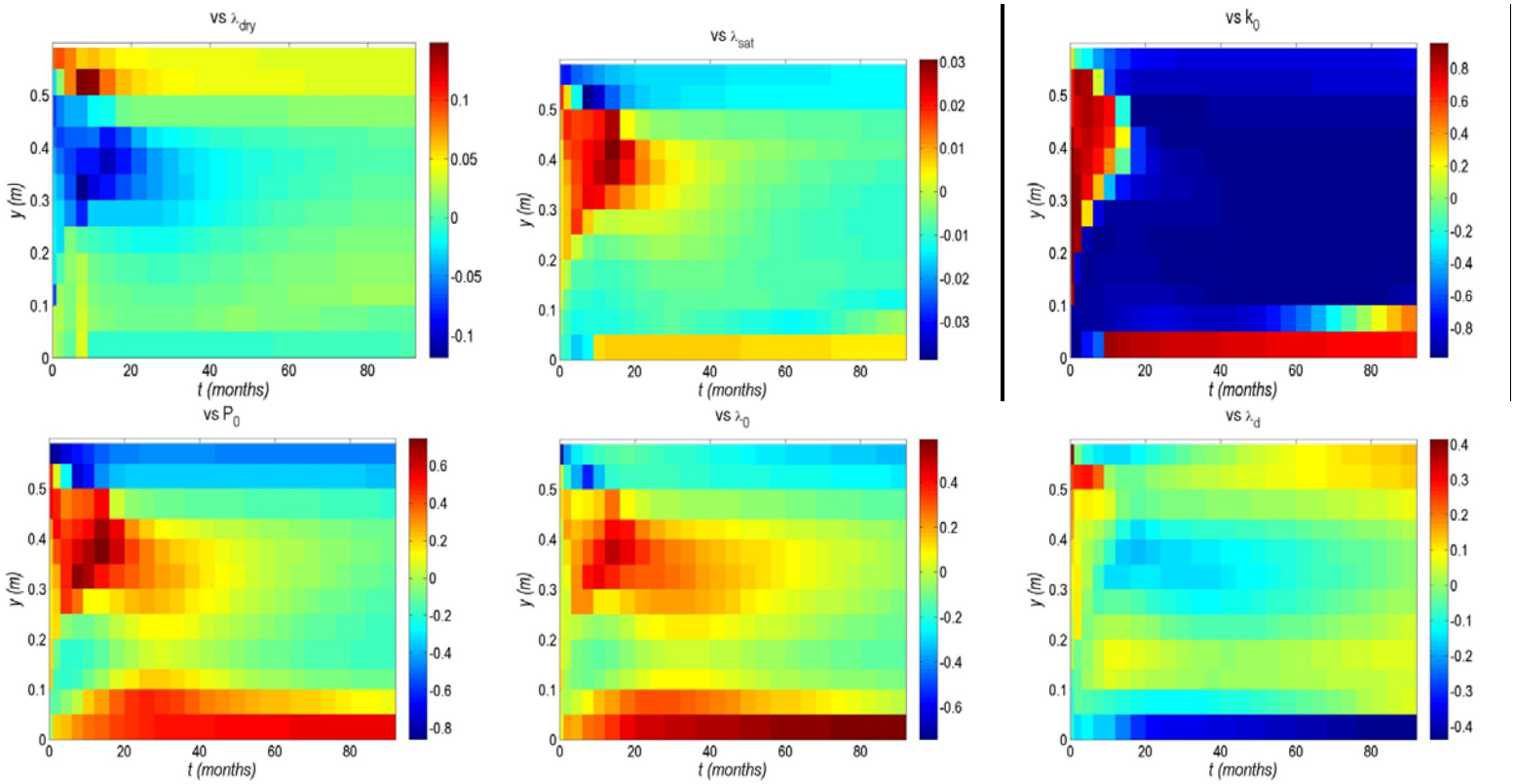

Figure 4.45. Correlation coefficient between dry density and the input parameters in full space and time.

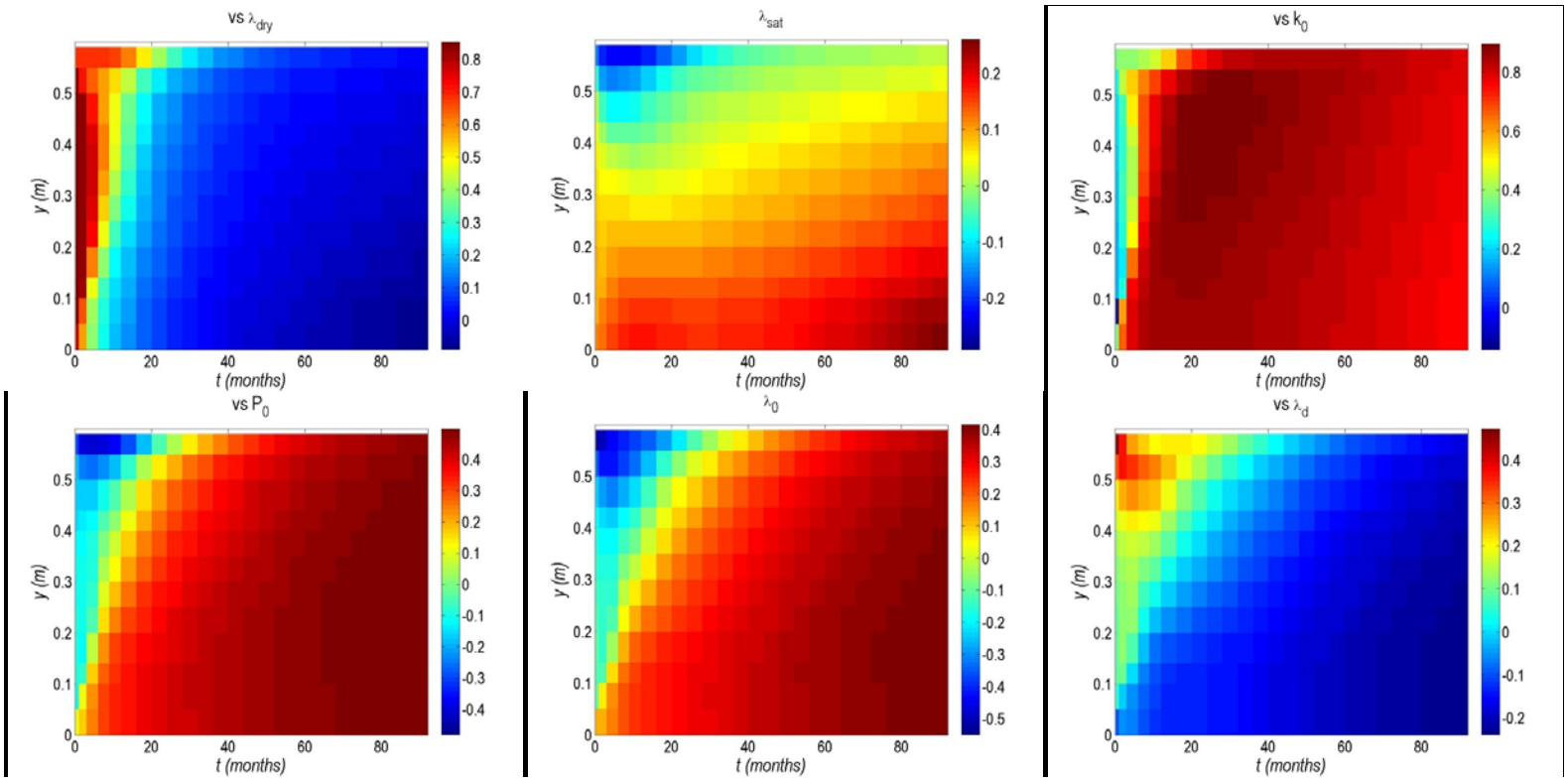

Figure 4.46. Correlation coefficient between temperature and the parameters in space and time.

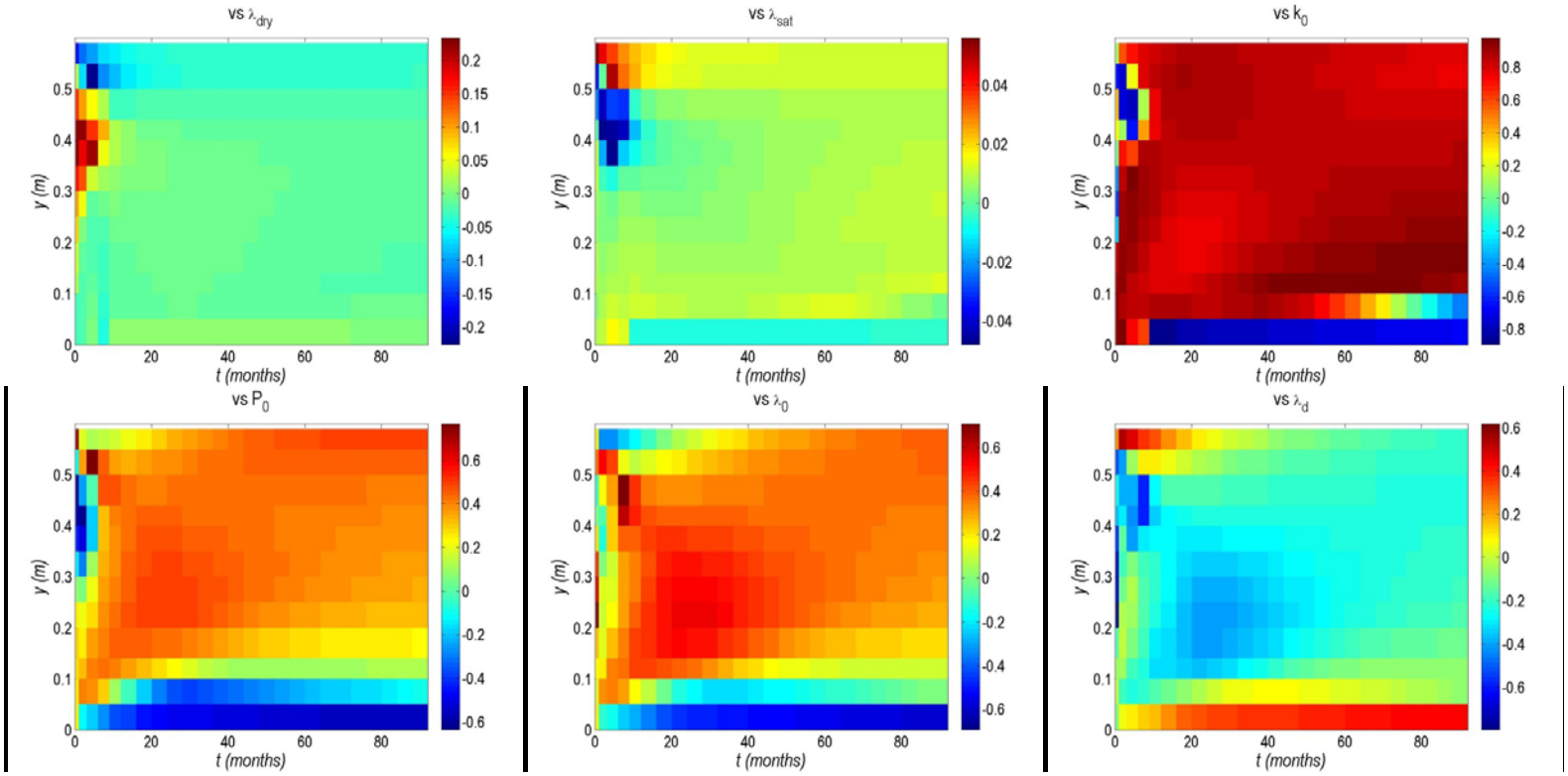

Figure 4.47. Correlation coefficient between water content and the parameters in space and time.

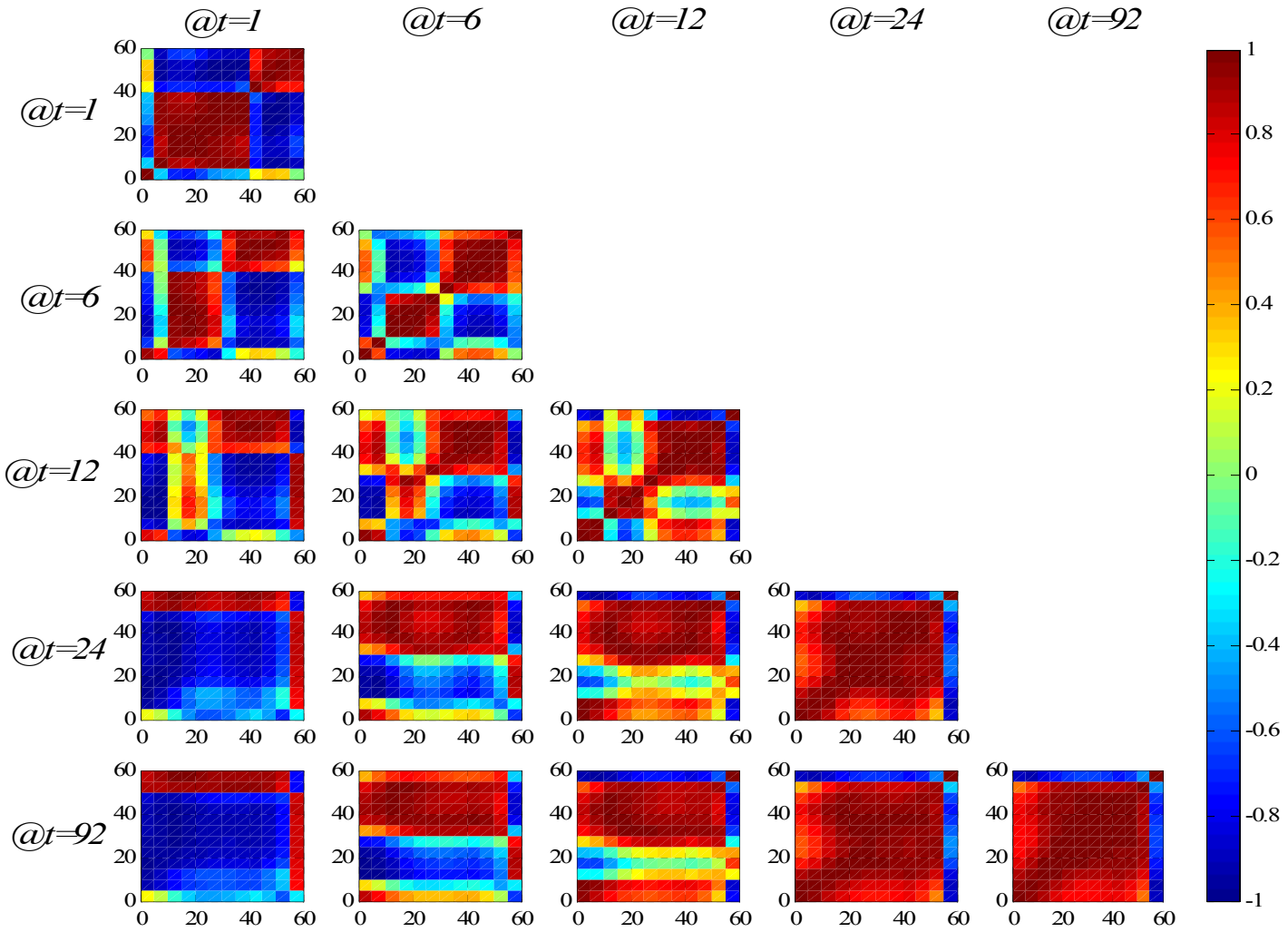

Figure 4.48. Spatial-temporal correlation of dry density.

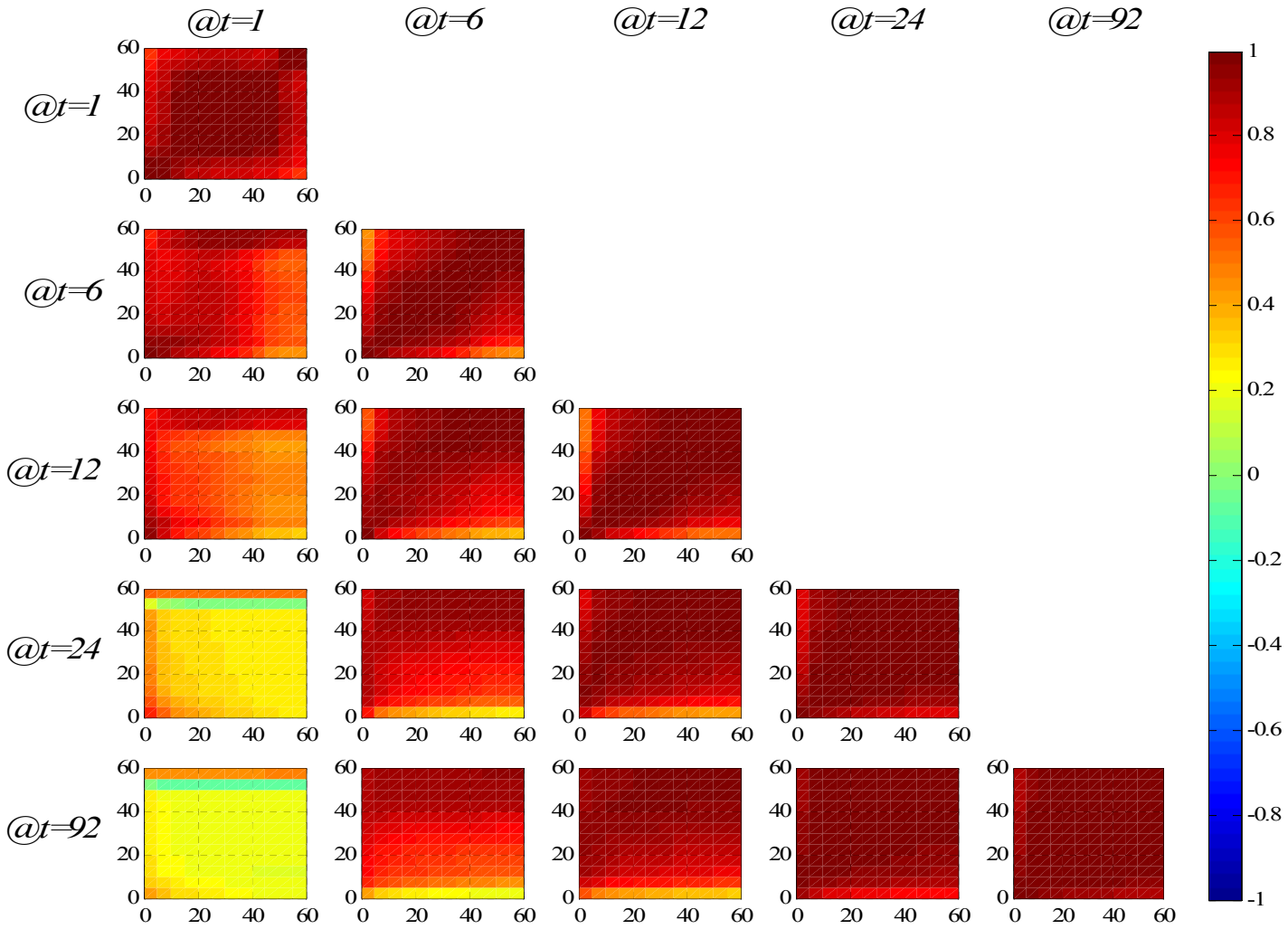

Figure 4.49. Spatial-temporal correlation of temperature.

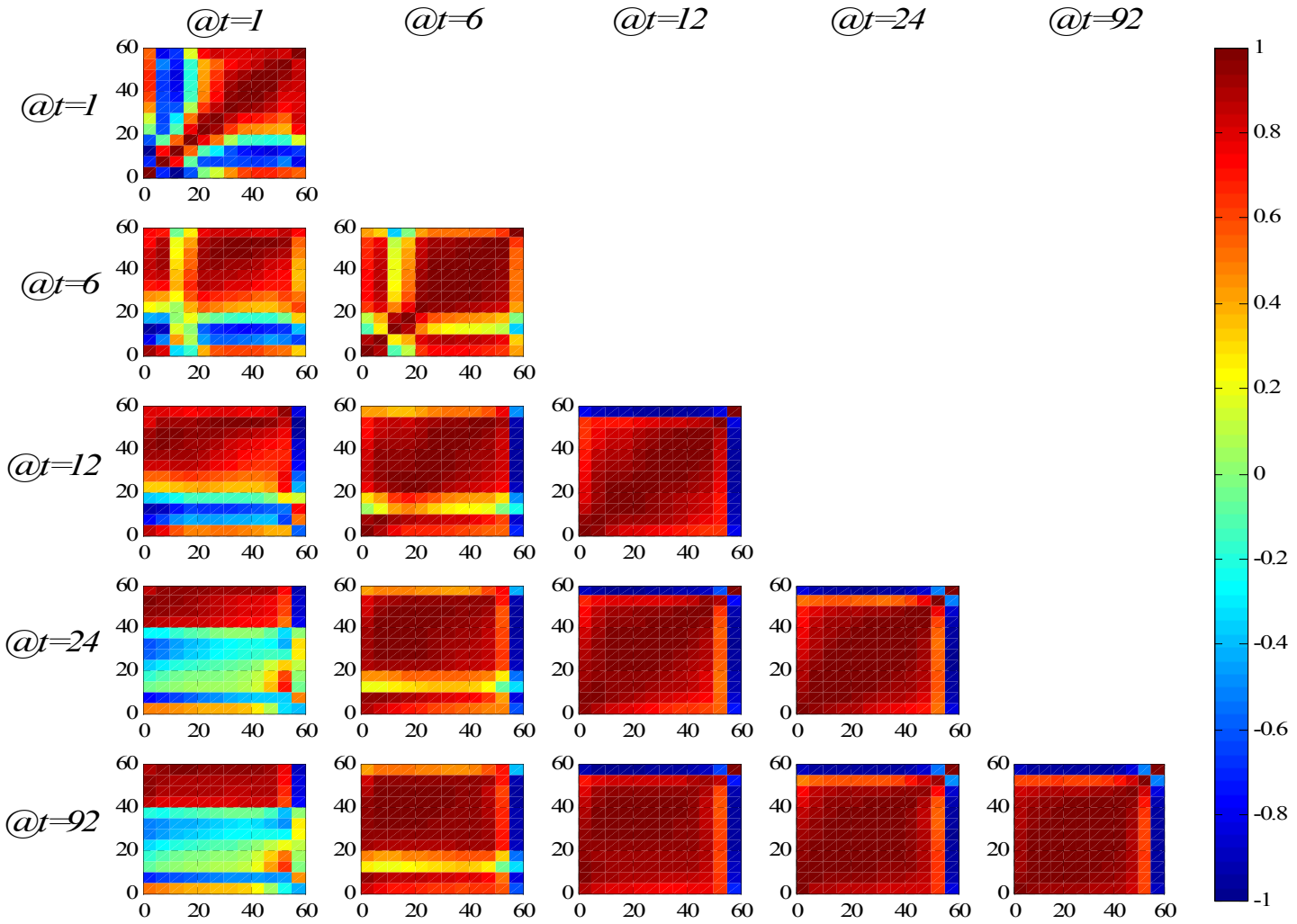

Figure 4.50. Spatial-temporal correlation of water content.

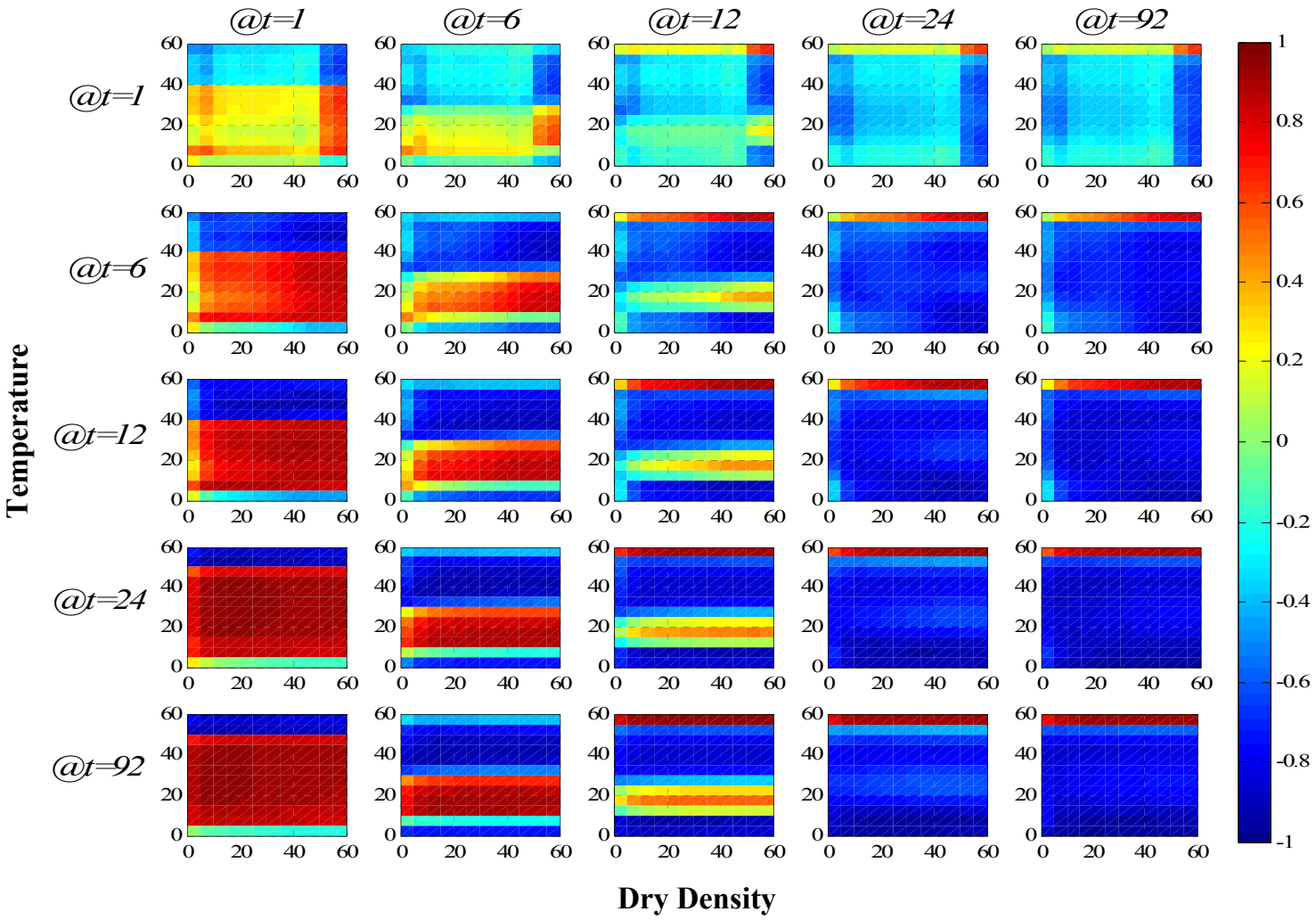

Figure 4.51. Cross correlation between temperature and dry density.

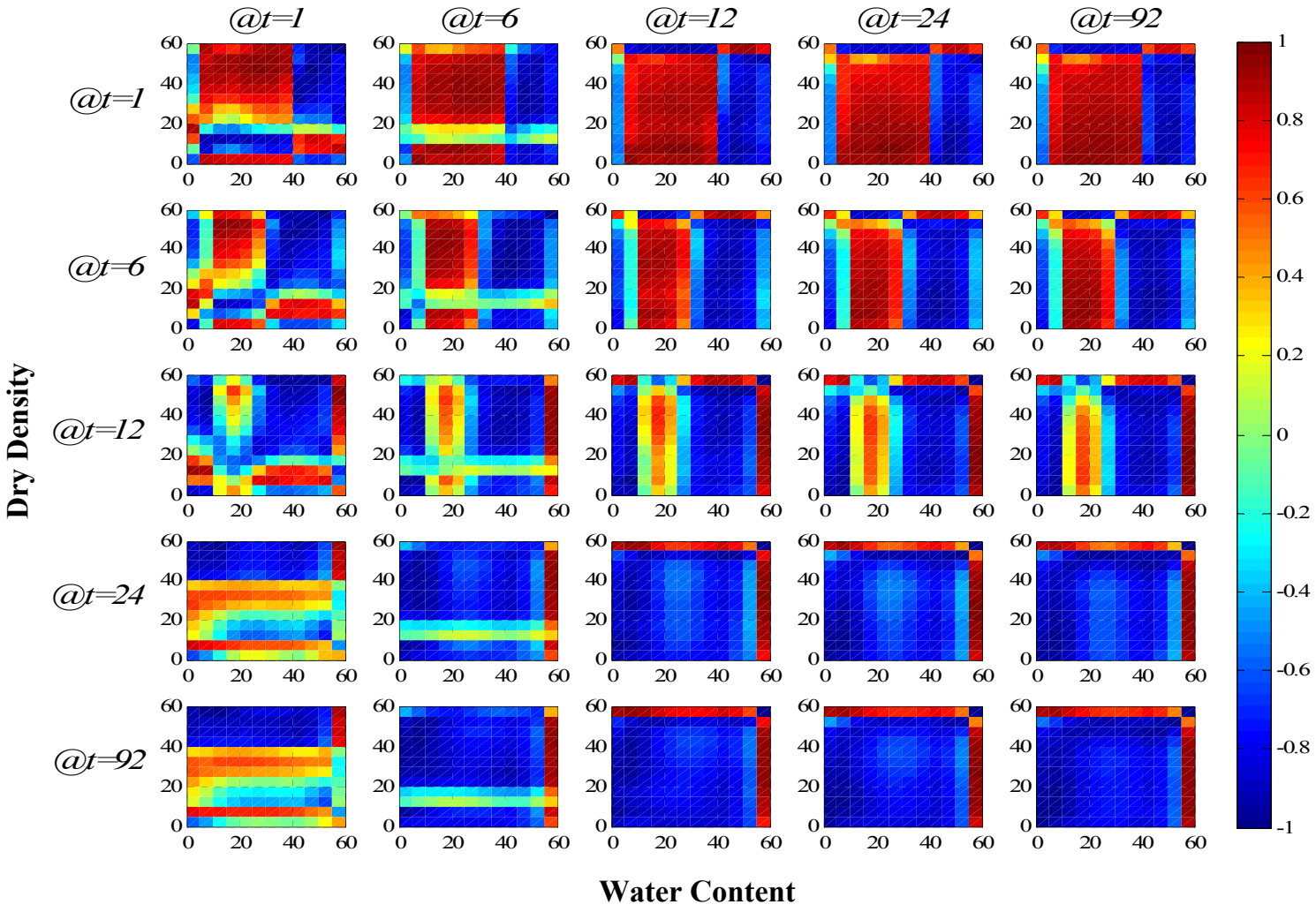

Figure 4.52. Cross correlation between dry density and water content.

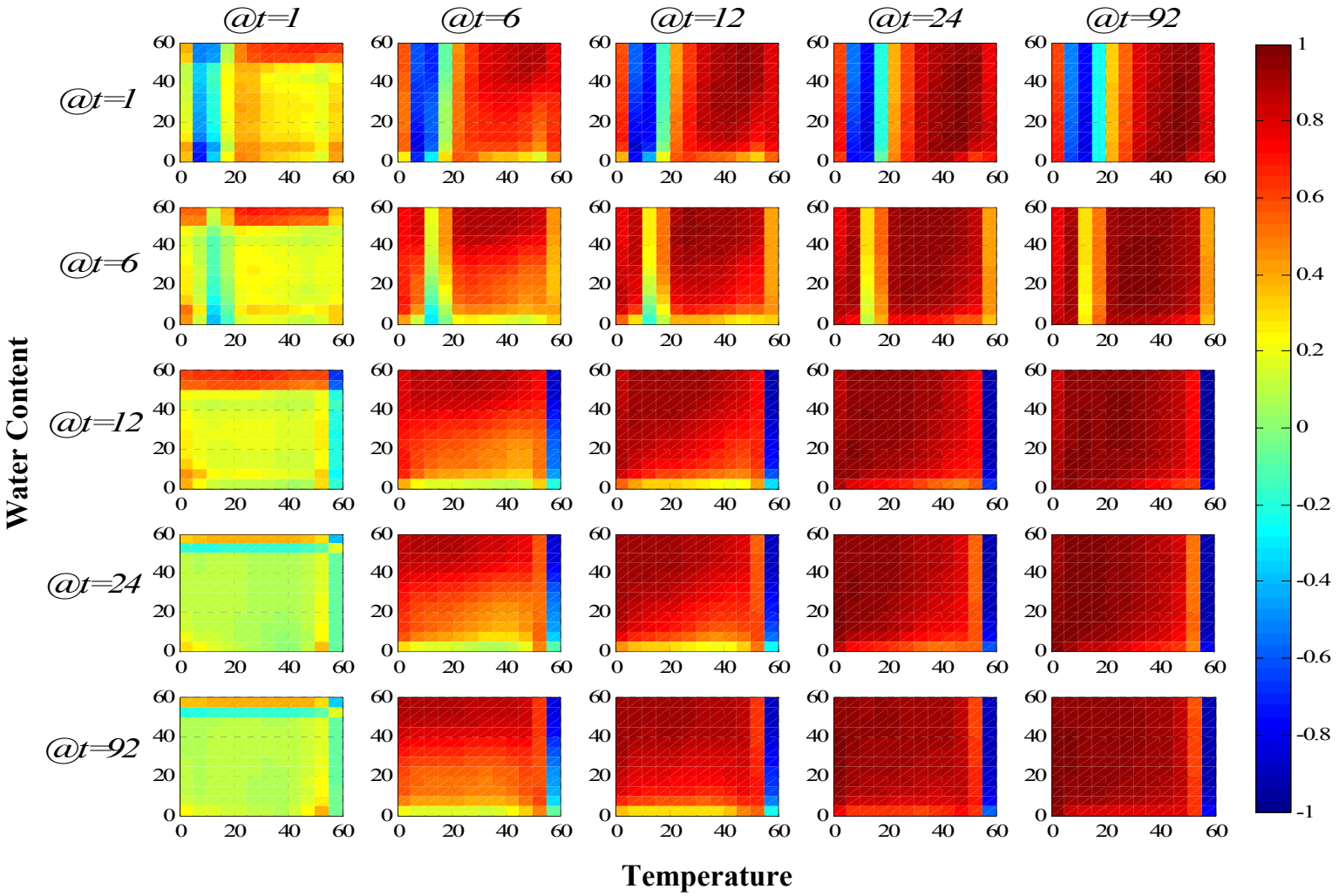

Figure 4.53. Cross correlation between water content and temperature.

- The temperature response is significantly affected by all the input parameters. But, the influence of thermal conductivities decreases with time. While, the hydraulic parameter show same influence throughout the time. It should be noted that the intrinsic permeability shows great influence even after long time.

- The water content shows no dependency on the thermal conductivities at any point of time. But, as expected, the influence of intrinsic permeability is almost the maximum influence ($\rho \sim 1$). Also the retention curve parameters especially the air entry value also have significant influence on the water content response.

From the autocorrelation functions of the THM responses, we can draw following deductions.

- The autocorrelation of dry density shows that as the time gap increase between two response readings, the correlation between them changes from negative effect to positive effect. That means if we measure the reading at smaller interval of time, the correlation is opposite indicating that the correlation changes from time to time. The spatial variability negative as we go closer to the heating end and as we go farther from heater the correlation become positive. This show that, there exists a huge local variation in space and this variation is opposite near the heater.

- The autocorrelation of temperature shows that the time variation is always positive, that is, the as the time duration decrease, the correlation increases and vice versa. Also, the space variability is almost uniform at any given time. This means that

there is no influence of local space variability on the temperature. This helps us in accurate predictions of temperature both in space and time.

- The autocorrelation of water content shows that as the time gap increase between two response readings, the correlation between them changes increases. That means if we measure the reading at smaller interval of time, the correlation is near 1, indicating that the correlation uniform for shorter duration of time. The spatial variability is almost uniform after period of a year. It means that the local variability influence the water content for some period and after the influence diminishes.

In the same manner, from the cross correlation, we can draw following deductions.

- Figure 4.51: When the temperature at any particular period is related to the dry density at different periods, the correlation between them becomes negative as the duration, at which dry density is related, increases. For instance, when the temperature at t=12 months is related to dry density, as we move toward horizontally right (in sense, duration at which dry density is increased), the correlation inverts from +1 to -1. The vice versa is not true, i.e. when temperature is correlated with dry density at early period, the correlation is becomes positive whereas it becomes negative, when temperature is correlated with dry density at later period.

- Figure 4.52: Similar behavior is observed when the temperature above is replaced with water content. It is to be noticed that the correlation becomes almost stable when compared with the water content after 12 months. For instance, the dry density at

t=12months has same correlation matrix with water content at t=12months, at t=24 months, and t=92 months.

- Figure 4.53: The cross correlation between water content and temperature are consistent throughout the time duration. That is, the correlation becomes stable when the water content values are correlated after 12 months. Also, the correlation becomes more positive when the duration, at which temperature is related, increases. That is, when water content at any particular duration, the correlation increases towards +1 when related with temperature at t=6months, t=12months, t=24months and t=92 months.

5. ANALYSIS OF A CLAY BARRIER USING DOUBLE STRUCTURE MODEL

The gap between the waste canister and the host rock is backfilled with the sealing material forming the engineered barrier. This engineered material, apart from filling the gap, also maintains the structural stability of the repository. It forms the first contact of the waste canister for any changes in the stresses, caused either due to different thermo-hydraulic-mechanical processes induced within the barrier or due to stresses from the host rock. Compacted clay like bentonite blocks, in an initially unsaturated state, is commonly chosen barrier material because of its expansive nature.

As mentioned earlier, the barrier is subjected to hydration due to water seepage from the rock and heating from nuclear waste canister. The material undergoes wetting and drying near the host rock and the canister respectively and due to expansive nature of the material, the clay undergoes volumetric changes: expands when wetted and contracts when dried. But gradually, when the heat is transmitted radial outwards while water flows inwards, the amount of heating and saturating is different at different location of the barrier. It results in coupled process and complex deformations, both elastic and plastic. Hence, the mechanical behavior of compacted expansive clays is a key factor impacting the design of barrier.

A constitutive model, called Barcelona Basic Model was proposed for moderately expansive unsaturated soils to represent their plastic behavior by Alonso et al. (1990).

The model considered two independent sets of stress variables (total stress over air pressure and suction) and formulated for the hardening plasticity of the soil. The model is modified for the highly expansive clays by Gens and Alonso (1992), attributing the expansive nature to the mechanical and physical-chemical phenomena occurring at particle micro structural level; and to its contribution to the macro level. Basing on this and with some modifications and developments (Alonso, 1998; Alonso et al., 1999), a generalized double structure theory is proposed and is mathematical framed by Sanchez et al. (2005). An advantage of the double structure model with respect to BBM (or a simple one) is that the double structure is able to reproduce complex features of expansive clays which is not possible to be explained with those simple models. The changes observed in the preconsolidation pressure and void ratio of the in situ analysis presented in the thesis is one of such feature.

The present work is the application of the above theoretical framework with mathematical modeling to the compacted bentonite clay used in the FEBEX in situ experiment. The distinguishing of clay fabric into two structural levels, micro and macro, has been an area of interest in its application to understand the behavior of expansive clay in the nuclear barrier scenario (Pusch, 1982; Young, 1999; Lloret et al., 2003; Delage, 2007). The fabric of the clay soil has been studied and found that the initial micro structure of compacted bentonite is in aggregate form with relatively large inter aggregate voids, showing the presence to two different structural levels. The same

distinction is found for the compacted FEBEX bentonite by mercury intrusion porosimeter tests (Figure 5.1).

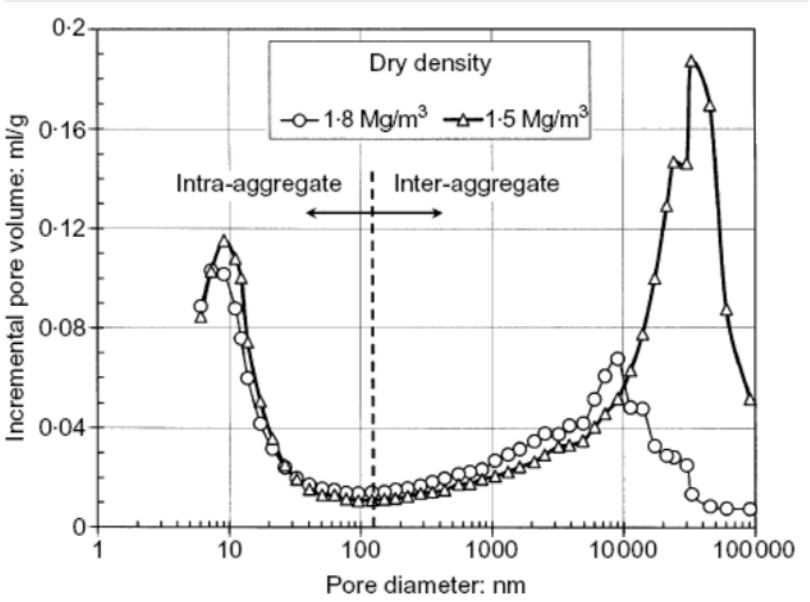

Figure 5.1. Distribution of incremental pore volume for compacted bentonite samples at two different dry density. Mercury Intrusion Porosimeter test (Lloret, 2003).

The behavior of the clay is thus attributed to the deformations at both micro and macro structural levels and their influence on each other. The deformations at micro level are controlled by physicochemical interactions at particle level and are assumed independent of macro-structural effects; whereas, the deformations at macro level are affected not only by the loading and collapsing, but also by its interaction with micro structure. The description of behavior at macro structural level is done using the elasto plastic BBM model, while the behavior of micro structural level, assumed reversible, is described by

simple elastic model. The double structure framework is summarized briefly using the mathematical formulations in further section.

5.1 Macro Structural Model

The deformations at macrostructural level are both elastic and plastic and could be modeled using the Barcelona Basic Model, which explains the mechanical behavior of partially saturated soils. The model is an extension of modified Cam-Clay using two independent stress variables (total stress over gas pressure, $p = \sigma_m - u_a$; and suction, $s = u_w - u_a$). It describes the hardening elasto-plasticity of the soil and is successful in representing the basic features of the behavior of non-expansive unsaturated soils such as soil stiffening with increase of suction; path dependency of volumetric response of the soil; irreversible collapse under wetting; increase of shear strength and irreversible shrinkage at higher suctions. These phenomena are similar to the macrostructural level, where the skeleton of the material is affected. Hence, it is considered to model the macrostructural behavior of the clay. The formal derivation of the model is briefly summarized below taking reference from Alonso et al. (1990).

The main feature of BBM is dependency of yield surface on the suction and temperature. The yield surface is the locus of stress points where irreversible deformations take place when the stress path crosses it. This may be due to reduction of suction (C, collapse strains) or increase of load (L, load strains), which ever, the effect is similar in the movement of yield curve. On reaching complete saturation, the model becomes a critical

state of saturated soils, hence, the full saturation become the boundary conditions for model verification.

In the isotropic loading of a soil sample at given suction *s*, the compression curve defining the void ratio *e* along the virgin state with respect to the load *p* is given by:

$$(1+e)=N(s)-\lambda(s)\ln\frac{p}{p_c} \tag{5.1}$$

Where, p_c is reference stress state for which (1+e) = N(s). The stiffness parameter λ(s) depends on the amount of suction and it decreases as the suction is increased indicating the increase of stiffness with suction. However, the increase in stiffness is limited and hence the λ reaches an asymptotic value as suction is increased. Thus, it is expressed as:

$$\lambda(s)= \lambda(0)[r+(1-r)e^{-\beta S}] \tag{5.2}$$

The elastic unload/reload curve is given by Eq. 5.3, where κ elastic stiffness with respect to stress unloading and is also dependent on suction *s*.

$$de=-\kappa\frac{dp}{p};\qquad \kappa=\kappa_i(1+\alpha_s s) \tag{5.3}$$

Similar to stress unloading, the suction unloading is also assumed as elastic change and reversible swelling is given by Eq. 5.4, where, *v* specific volume (=1+*e*) and κ_s is elastic stiffness with respect to suction unloading, but also depends on current stress state.

$$dv=-\kappa_s\frac{ds}{(s+p_{at})};\qquad \kappa_s=\kappa_{s0}(1+\alpha_{sp}\ln(p/p_{ref}) \tag{5.4}$$

It is proposed that when the soil is dried over a threshold suction value s_o, then irreversible strains begin to occur. This suction value s_o is an analogous to the

preconsolidation pressure with respect to loading, only it is assumed to be independent of current stress state. The specific volume change along the virgin curve with respect to suction increase is given by:

$$dv^p = -\lambda_s \frac{ds}{(s+p_{at})} \tag{5.5}$$

From all the above equations, the compression curve of the sample at suction *s* and at saturated condition (*s* = 0), is shown in the Figure 5.2 (Alonso et al., 1990). The preconsolidation pressure at saturated condition is given by p_o*, while the apparent preconsolidation pressure at suction *s* by p_o. From the figure it can be seen that $\lambda(s) < \lambda(0)$, that is, the stiffness parameter decreases as suction increases indicating the increase of stiffness with suction. The trace of preconsolidation pressure at different suction, in (*p,s*) plane is called LC (loading-collapse) and is shown in Figure 5.3.

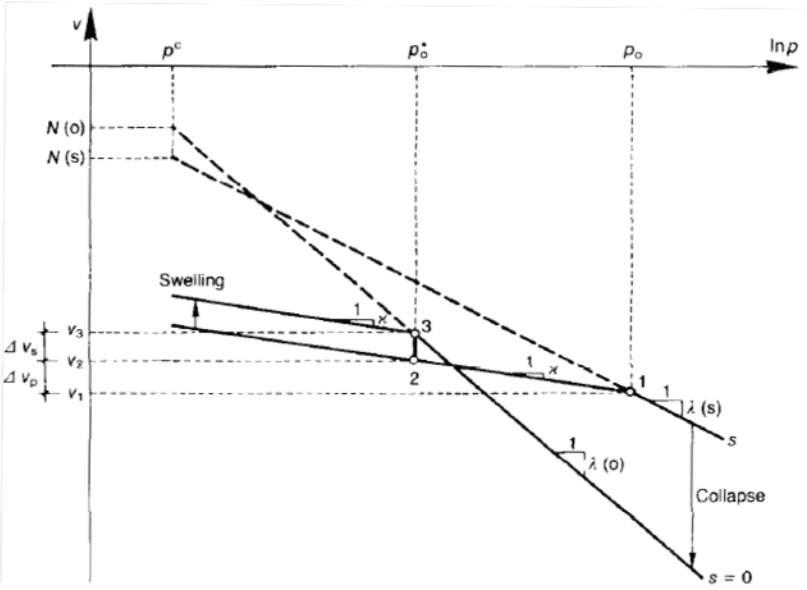

Figure 5.2. Compression curve for saturated and unsaturated soil.

In the same manner, the yield with respect to suction is called SI (suction increase) and shown as a straight line parallel to stress axis. Hence the region enclosed by LC and SI is the elastic zone. Any stress path within this region is considered to be elastic and when the stress path crosses the yield curve, then the yield surface moves along to accommodate the maximum stress level as new yield (Figure 5.4).

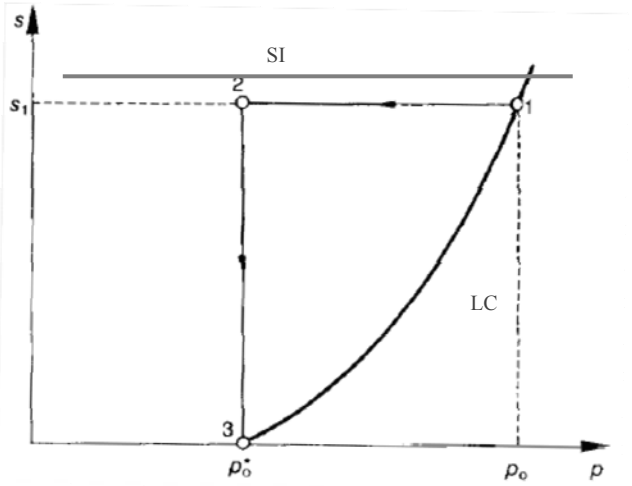

Figure 5.3. Yield curve in (*p,s*) stress plane.

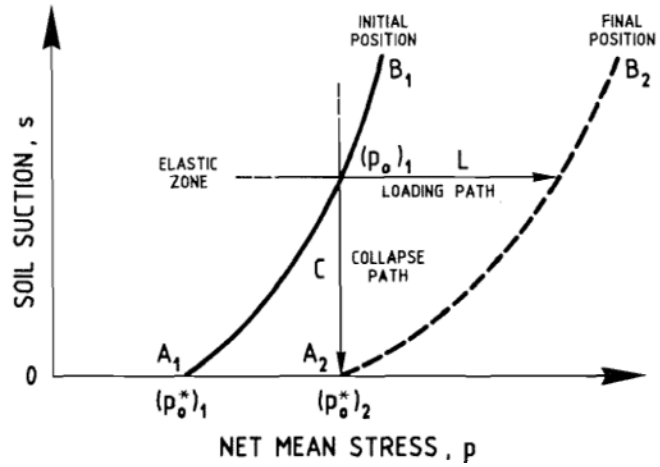

Figure 5.4. Yield curves for load-collapse behavior of an unsaturated soil.

The preconsolidation pressures, p_o and p_o* can be related through the change in void ratio and is given by Eq.5.6. This equation defines the yield value p_o for each associated suction and hence, the family of yield curves (LC) can be represented by specifying single value of preconsolidation stress at full saturation (p_o*).

$$\left(\frac{p_o}{p_c}\right)=\left(\frac{p_o^*}{p_c}\right)^{[\lambda(0)-\kappa]/[\lambda(s)-\kappa]} \tag{5.6}$$

From the Eq.5.3, the volumetric strain in the elastic zone induced by the increasing the load (p) is given by:

$$d\varepsilon_{vp}^{e}=-\frac{dv}{v}=\frac{\kappa}{v}\frac{dp}{p} \tag{5.7}$$

And on reaching the yield surface (p_o), the volumetric strain computed from Eq.5.1 and Figure 5.2 is given by:

$$d\varepsilon_{vp}^{total}=\frac{\lambda(s)}{v}\frac{dp_o}{p_o} \tag{5.8}$$

From Eq.5.7 and Eq.5.8, the net plastic component of volumetric strains is obtained as:

$$d\varepsilon_{vp}^{p}=\frac{\lambda(s)-\kappa}{v}\frac{dp_o}{p_o} \tag{5.9}$$

As mentioned before, the family of yield curve can be represented by p_o* and the hardening law with respect to load increase is obtained from Eq.5.9 as:

$$\frac{dp_o^*}{p_o^*}=\frac{v}{\lambda(0)-\kappa}d\varepsilon_{vp}^{p}=\frac{(1+e)}{\lambda(0)-\kappa}d\varepsilon_{vp}^{p} \tag{5.10}$$

And from Eq.5.4 and Eq.5.5, hardening with respect to suction increase is given by:

$$\frac{ds_o}{s_o} = \frac{v}{\lambda_s - \kappa_s} d\varepsilon_{vs}^p = \frac{(1+e)}{\lambda_s - \kappa_s} d\varepsilon_{vs}^p \tag{5.11}$$

Applying the same for triaxial stress states, the BBM yield surface is expressed in (*p, q, s*) coordinate system (Figure 5.5) with stress, $\boldsymbol{\sigma} = \boldsymbol{\sigma}_t - \boldsymbol{I}p_g$; and suction, $\boldsymbol{s} = \boldsymbol{\sigma} - p\boldsymbol{I}$. With the modified Cam clay as boundary condition (at s=0), the size of yield surface increases with suction and the trace on the isotropic p-s plane giving back the loading-collapse (LC) yield curve.

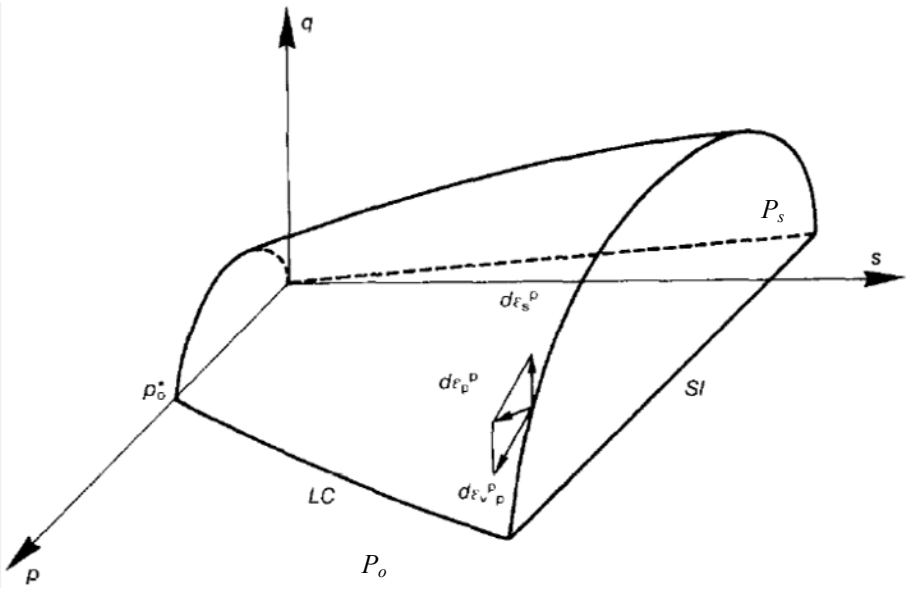

Figure 5.5. 3D representation of BBM yield surface in (*p,q,s*) space.

The increase in strength induced by suction is represented by increase in cohesion (p_s), maintaining the characteristics of critical state line of slope M, for saturated condition. It is given as expression:

$$-p_s = -ks \tag{5.12}$$

The yield surface thus can be expressed as:

$$F_{LC}=3J^2-\left[\frac{g(\theta)}{g(-30°)}\right]^2 M^2(p+p_s)(p_o-p)=0 \tag{5.13}$$

where, M is slope of critical state; g is a function of Lode's angle; p is the net mean stress; J and θ are given by expressions:

$$J^2=\frac{1}{2}\text{trace}(\mathbf{s}^2) \tag{5.14}$$

$$\theta=-\frac{1}{3}\sin^{-1}\left(1.5\sqrt{3}\det s/\mathbf{J}^3\right) \tag{5.15}$$

The volumetric strain in the elastic zone is given by Eq.5.16, while the elastic shear strain are computed through shear modulus G as in Eq.5.17.

$$d\varepsilon_{vp}^e=\frac{\kappa}{(1+e)}\frac{dp}{p}+\frac{\kappa_s}{(1+e)}\frac{ds}{(s+p_{atm})} \tag{5.16}$$

$$d\varepsilon_s^e=\frac{1}{3}G\,dq \tag{5.17}$$

A non-associated flow rule in plane of constant s is considered for the plastic flow of the volumetric strains and the plastic potential (G_{LC}) adopted is given by Eq.5.18, with α determining the condition that the flow rule predicts zero lateral strains in K_o stress path.

$$G_{LC}=\alpha 3J^2-\left[\frac{g(\theta)}{g(-30°)}\right]^2 M^2(p+p_s)(p_o-p)=0 \tag{5.18}$$

The temperature has its role on affecting the mechanical behavior and is included as per the thermo-mechanical law proposed by Gens (1995). It not only assist in drying the sample, thereby, increasing the suction, but it also induce strains, although it is assumed that only volumetric strains are affected.

The elastic component of strain induced by thermal effect is given as:

$$d\varepsilon_{vT}^{e}=(\alpha_0+\alpha_2\Delta T)dT \tag{5.19}$$

The increment in temperature decreases the size of yield surface making it soft at higher temperature. The effect of temperature on yield can be computed from its effect on p_o* and p_s as shown in equation below. The yield surface in (p,q,T) space is show in Figure 5.6.

$$p_{oT}^{*}=p_{co}^{*}+2(\alpha_1\Delta T+\alpha_3\Delta T|\Delta T|) \tag{5.20}$$

$$p_s=kse^{-\rho\Delta T} \tag{5.21}$$

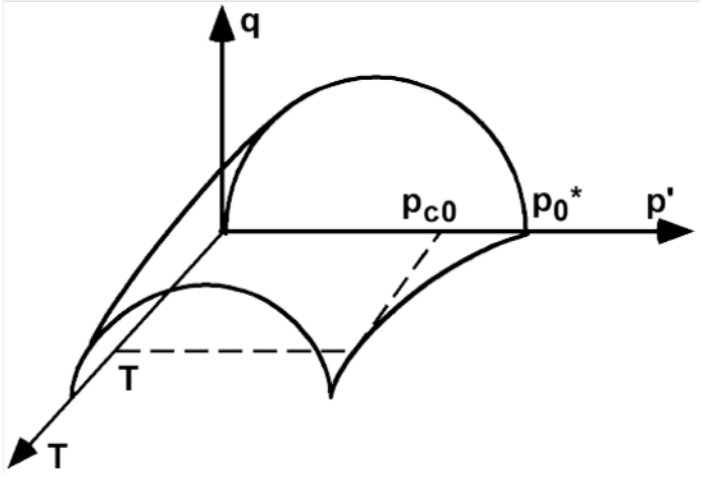

Figure 5.6. 3D representation of BBM yield surface in (p,q,T) space.

5.2 Micro Structural Model

Gens and Alonso (1992) described the micro structural behavior and accordingly, the physical-chemical phenomena occurring at the micro structural level form the basic phenomena behind the behavior of expansive clay soils. They are attributed the swelling

of clay minerals and their interaction with the macro structure is what that makes the clay soften/harden. Because of the random orientation of the clay particles, the deformations are considered to be volumetric and elastic. Although, the changes at this level influence the skeleton of the mineral thus the macro structure, the vice-versa is considered to be not true. The main feature of the micro structure is that it always remains saturated regardless of the suction of the bulk soil. So, whenever there is decrease or increase of suction, then the micro pores contract and expand respectively to accommodate the available micro pore water. And in accordance to the effective stress principle, the effects due to changes in suction or application of external stress are likely to be equivalent. Therefore, the effective micro structural stress ($\hat{p}$) is given by:

$$\hat{p} = p + \chi\,(s+s_o) \tag{5.22}$$

where, χ is constant given as S_r^n (Alonso, 1998), S_r degree of saturation; p is net mean stress; s is the matrix suction and s_o is the osmotic suction.

So, there is no micro structural deformation due to changes in p or s_t, as long as $\hat{p}$ remains constant and the situation is called neutral loading. There will be expansion or contraction depending on decrease or increase of $\hat{p}$ due changes in p or s_t. These loading and microstructural changes are represented in Figure 5.7, which shows the neutral loading (NL) line of constant $\hat{p}$ separates stress paths, causing swelling and compression.

$d\hat{p} > 0 \Rightarrow$ Contraction in microstructure,

$d\hat{p} < 0 \Rightarrow$ Swelling in microstructure.

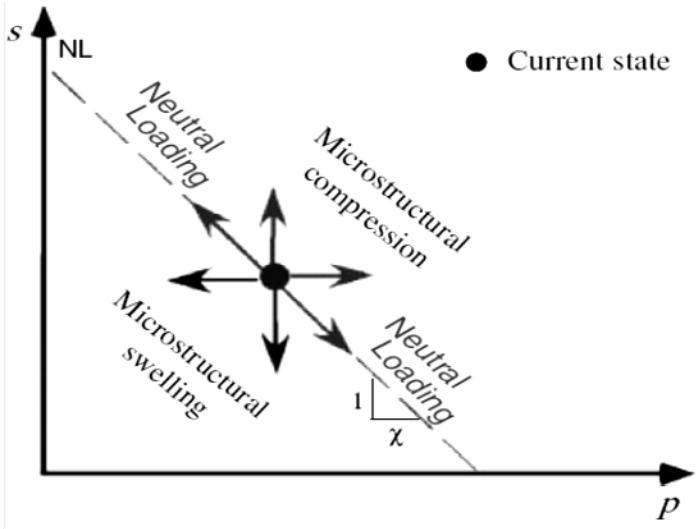

Figure 5.7. Directions of swelling and compression of microstructure (Sanchez et al., 2005).

The volumetric strains caused by the above effective stress are assumed to be elastic and are given as:

$$d\varepsilon_{vm} = \frac{d\hat{p}}{K_m} = \frac{dp}{K_m} + \chi \frac{ds_t}{K_m} \tag{5.23}$$

Where K_m is the microstructure bulk modulus and by considering the inter particle distance a function of effective stress as in double layer theory. The modulus is expressed as an exponential model with the material parameters, α_m and β_m as:

$$K_m = \frac{e^{-\alpha_m \hat{p}}}{\beta_m} \tag{5.24}$$

5.3 Interaction Between Micro and Macro Structures

The interaction between the micro and macro structures forms the base for the expansive behavior of the clays. If the soil is wetted, the micro structure of soil swells and this will

affect the macro structural void ratio. It may happen that the increase in micro void ratio may force the macro void ratio to increase, thus opening the macro structure and making the soil soften. The same concept is shown in Figure 5.9 and represented graphically in Figure 5.9. In (a), the micro structure swells more intruding into macro pores; (b) micro structure swell less when compared to that of macro, opening the macro pores; (c) micro structure contraction is less when compared to that of macro, where macro pores are closed more; (d) opens macro pores as the micro structure contract more than that of macro.

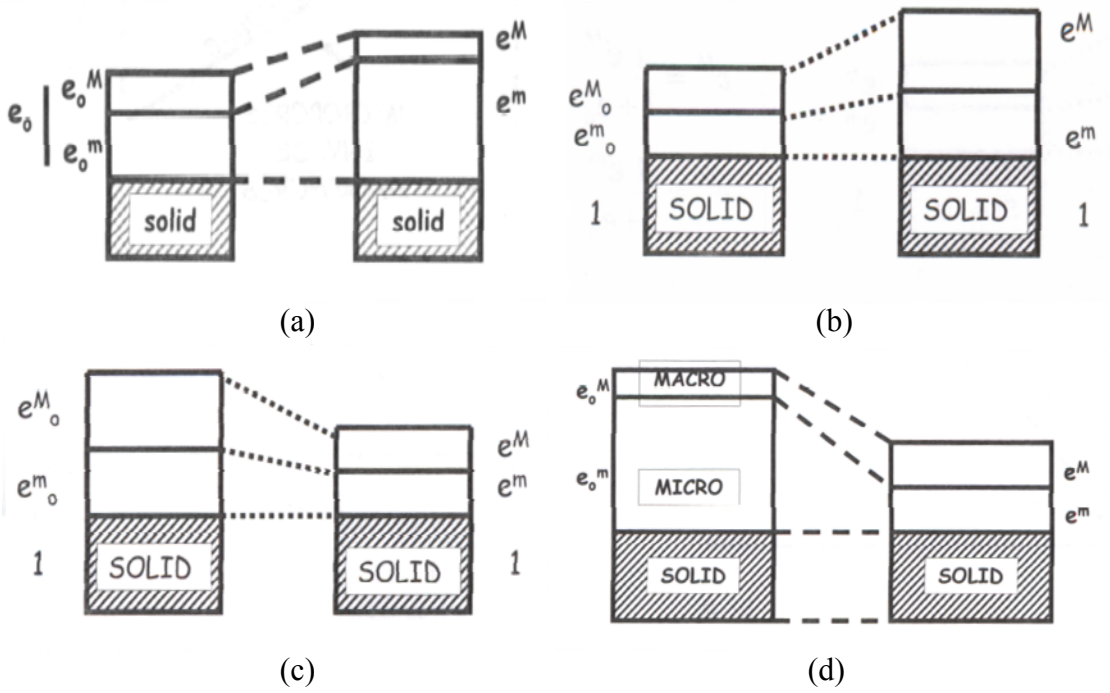

Figure 5.8 Swelling and Contraction of micro and macro voids.

When the soil is wetted from the current state A to B, as per the above description, when $\hat{p}$ is decreases, the micro structure expands, influencing the LC, shown to the right, by moving it to the left indicating the decrease of preconsolidation. And when it is dried

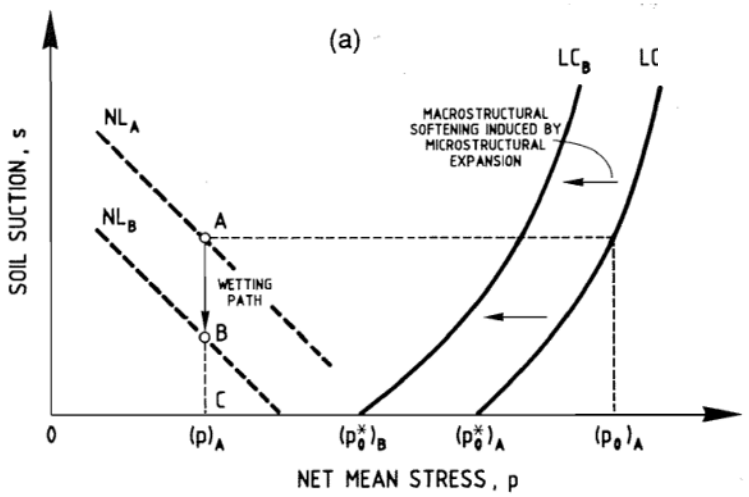

Figure 5.9. Coupling between micro structural deformation and macrostructural LC yield curve.

from B to A, LC doesn't move back to the right, leaving the macro structural deformation irreversible. In the same manner, the shrinkage in micro structure may induce decrease of macro pores closing the soil skeleton and making the soil harden. However, the amount to which this interaction takes place depends on the current state of the soil. It is also possible that the macro voids do not change in accordance to micro structure, in which case, the macro pores could be intruded by the micro structure in case of wetting the soil, thus closing the structure; or micro pore may contract more than the macro pores, thus opening the soil structure (Figure 5.10). Thus, the irreversible macro structural deformations are considered to be proportional to micro deformations and dependent through the interaction functions (Alonso et al., 1999).

$$\dot{\varepsilon}^{p}_{v\beta}=f(\dot{\varepsilon}^{e}_{vm}) \tag{5.25}$$

Where, $\dot{\varepsilon}^{p}_{v\beta}$ represent the plastic macro strain caused by elastic micro strain ($\dot{\varepsilon}^{e}_{vm}$).

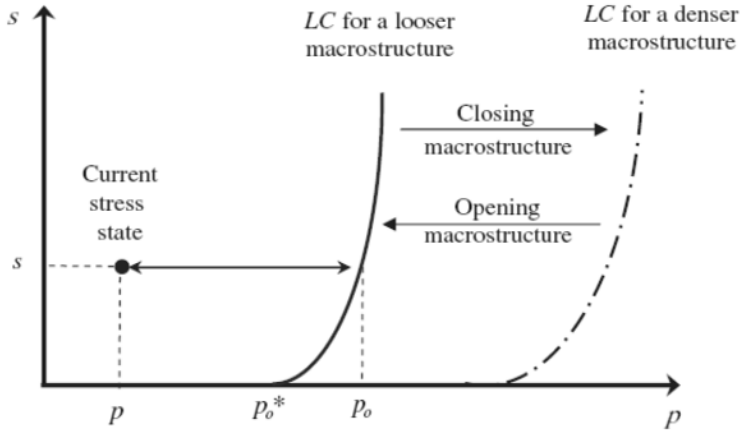

Figure 5.10. Movement of LC yield curve due to opening and closing of macro structure.

From the discussion earlier, there are two possible interaction functions *f*: f_c one for microstructure contraction (MC) and f_s for microstructure swelling (MS) (Figure 5.11). As the amount of interaction depends on the current stress states, the interaction function depend on the degree of openness given by the ratio p/p_o, where, p is the current state of mean applied stress and the p_o is the apparent preconsolidation pressure (Figure 5.11).

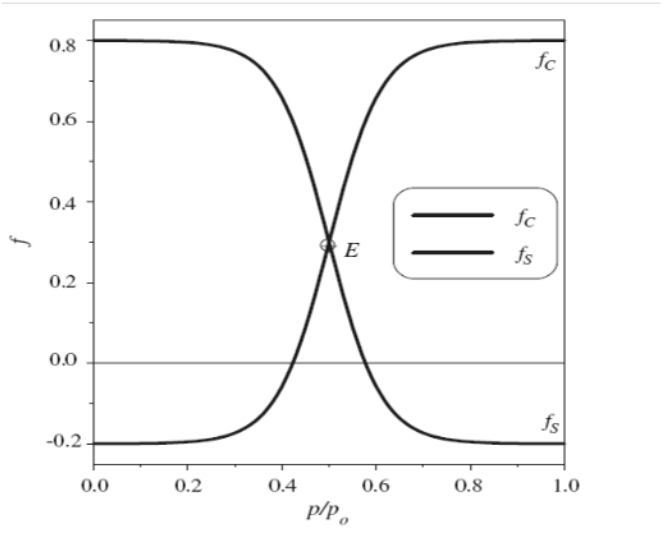

Figure 5.11. Interaction functions.

The lower value of the ratio means p_o is large when compared to p. Under this condition, if the macro structure is dense, then plastic strain will follow f_s during wetting, where the swelling of microstructure has huge impact on macro structure or it will follow f_c during drying, where the shrinking of microstructure has little impact on macro. Similarly, at higher value of p/p_o means the macro structure is loose, then when drying, the plastic strain following f_c indicating that the shrinkage of micro structure has huge impact on closing of macro structure or on wetting it will follow f_s where the swelling of micro has very less effect on further opening of macro pores. The function that the interacting plastic strain follows depends on the microscopic stress path relative to NL, caused by either applied external stress or suction and direction of the impact depends on the positive or negative value of the function.

The hardening of the soil depends on the total volumetric plastic strains ($\dot{\varepsilon}_v^p$) given sum of macro plastic strains ($\dot{\varepsilon}_{vM}^p$) and interactive plastic strains ($\dot{\varepsilon}_{v\beta}^p$) as:

$$\dot{\varepsilon}_v^p=\dot{\varepsilon}_{vM}^p+\dot{\varepsilon}_{v\beta}^p \tag{5.26}$$

In this way, the model is able to predict both hardening and expanding or softening of the soil. Further, to complete the description of model, the other elasto-plastic laws needs to be defined for each of the stress paths, which include loading and unloading direction; a plastic flow direction; and plastic modulus. And the governing strain-stress equations for multi-dissipative materials are also to be obtained. These are explained in detail in Sanchez (2004) and Sanchez et al., (2005). Thus the model is able to explain the overall mechanical behavior of the soil. It is also able to explain the concepts that BBM

was unable to explain, which include the plastic strain within the yield limits, invasion of macro pores by micro structure; dependence of amount of softening on the current stress state, cyclic wetting and drying (Sanchez et al., 2005) etc.

Finally, the numerical implementation of the general plasticity model is developed and incorporated into the finite element program, CODE_BRIGHT (UPC, 2004). This is further implemented in the coupled THM to check its capability to simulate actual behavior of bentonite clay in the nuclear waste disposal (Sanchez et al., 2008). Sanchez et al. (2011) used the same model to analyze the THM behavior of a mockup heating test. In the present study, the model is implanted to reproduce the same for the in situ testing performed in the underground tunnel as part of FEBEX project.

6. MODELING OF FULL SCALE FEBEX INSITU HEATING TEST

6.1 Description of FEBEX In situ Test

The study of clay mineral and the application of theoretical model give us an idea of possible phenomena that occur inside the barrier. But, the performance of full scale test under similar conditions encountered during the actual nuclear waste disposal should be framed for successful design of the barrier. The test performed under the repository conditions for reasonable time and providing a model that can represent the same phenomena for the given time, helps to provide long term predictions with reasonable accuracy. In view of attaining this objective, ENRESA (a Spanish agency for the management and storage of radioactive waste) carried a full-scale heating test in an underground laboratory of Grimsel test site (Switzerland).

The FEBEX in situ test is designed based on the Spanish reference disposal concept (Figure 6.1), where the horizontal drifts are excavated at some depth and long canisters are placed along the axis of gallery surrounded by buffer bentonite between the canister and the host rock. For the test, a tunnel of about 2.28m diameter and 70.4 m long is excavated and then about 17.4m of the tunnel is used to install the barrier prototype (Figure 6.3). Two heaters of 4300W capacity, designed to supply constant heat until the bentonite reaches the maximum allowable temperature of 100°C, are placed as replacement of canister to simulate the heat generation. The heaters are about 4.54m long, 0.90m diameter and are separated at a distance of 1.0m.

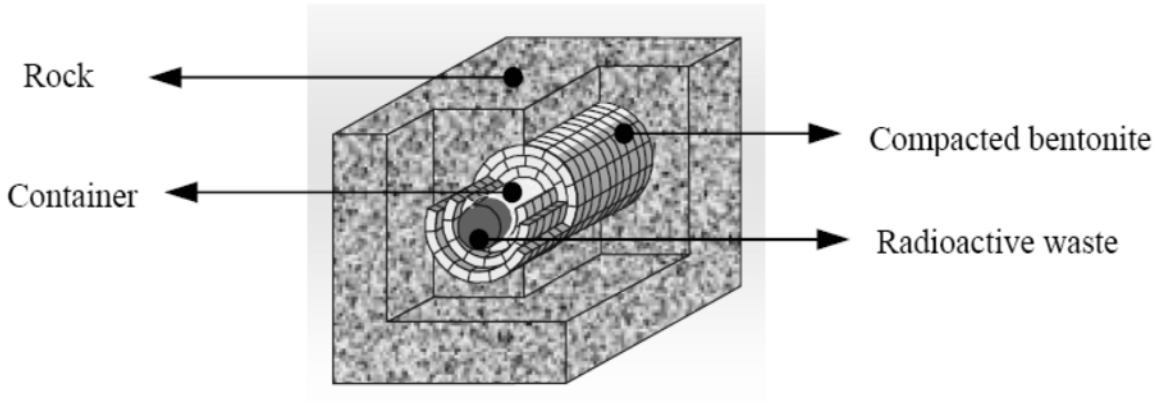

Figure 6.1. Layout showing the Spanish concept of engineered barrier (Sanchez et al., 2004).

The space between the canister and the rock, which is in shape of 0.69m thick semicircle, is filled with arc shaped compacted bentonite blocks. A liner is placed in the middle in the bentonite, which later assists in insertion of heater (Figure 6.2). Finally, the installation is sealed with a 2.7m long concrete plug.

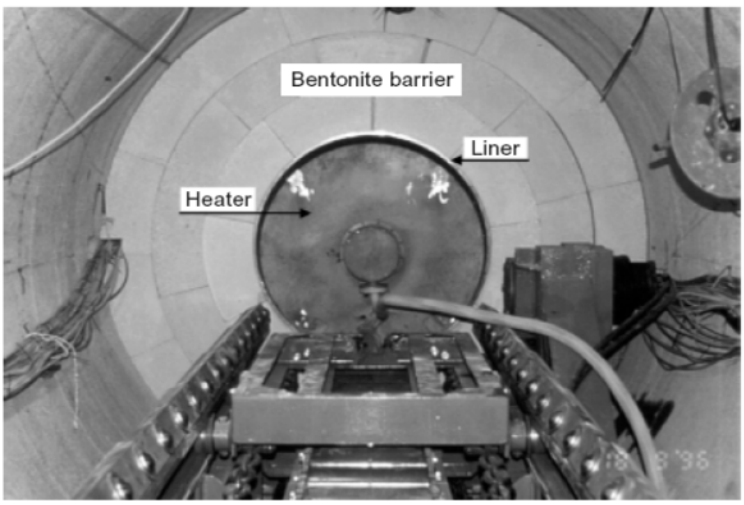

Figure 6.2. Layout of the barrier prototype installation inside the tunnel with heater surrounded by engineered barrier made up of compacted bentonite blocks. (Gens et al., 2009).

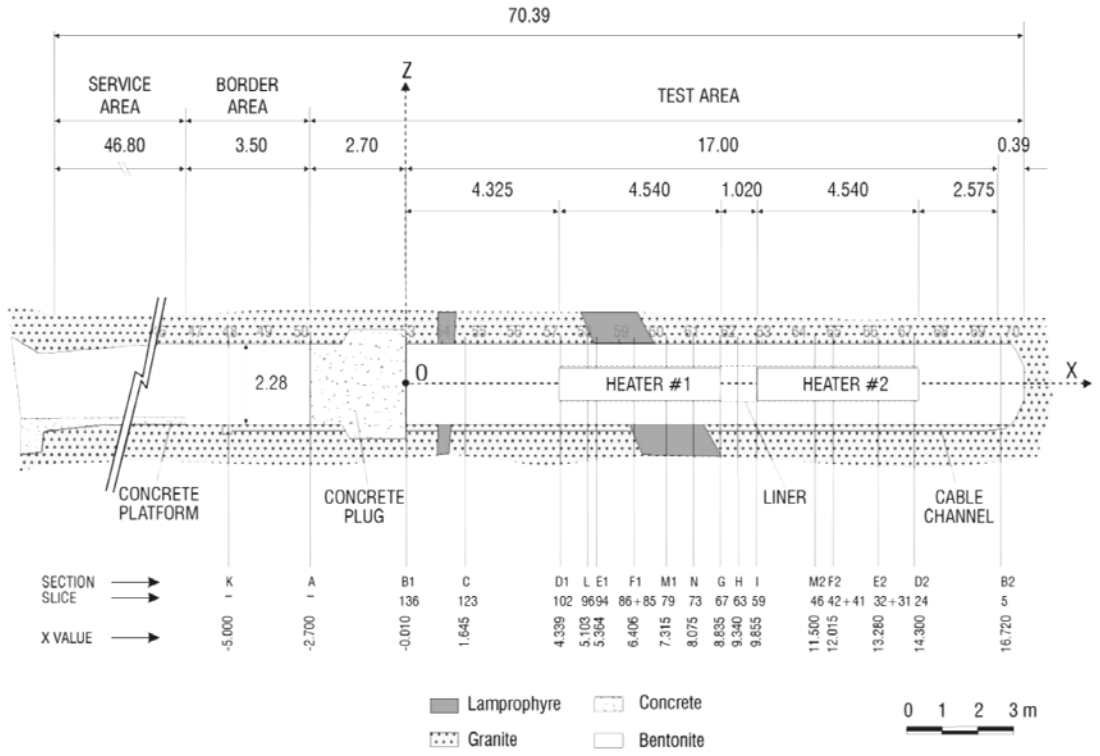

Figure 6.3. Layout and principal elements of FEBEX (ENRESA, 2006).

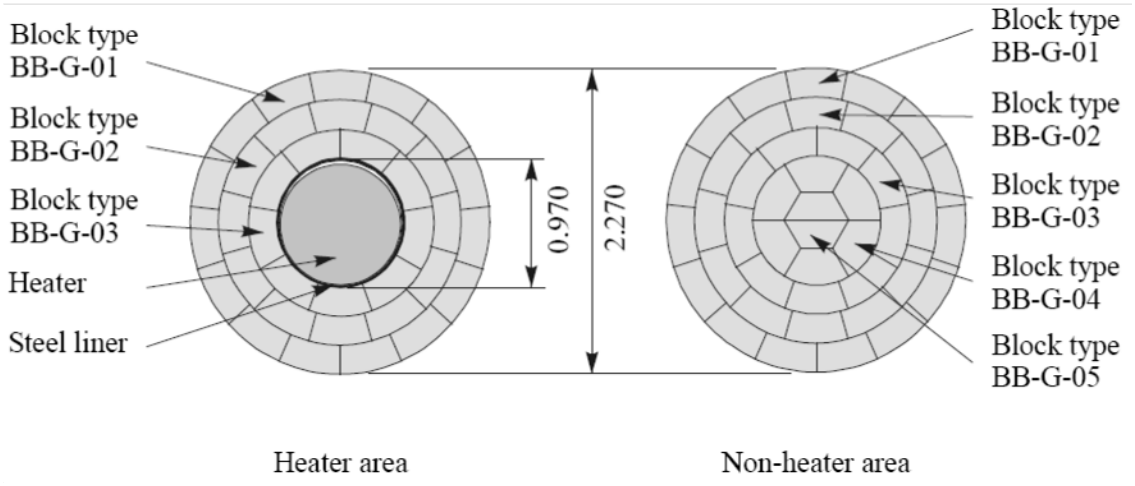

Figure 6.4. Geometry of the clay barrier inside the drift. (ENRESA, 2000).

The bentonite clay is obtained from La Serrata bentonite quarried from volcanic zone in south-east Spain. It is uniaxially compacted at pressures of (40 - 45) MPa, to produce 12 cm thick circular crown shaped blocks. These blocks are arranged in vertical slices to fit in to the circular drift giving the geometry of the barrier shown in Figure 6.4 for the heater and non-heater areas. In both areas, the three exterior rings are equal; in the heater area the interior ring is in contact with the steel liner. The hygroscopic water content of the compacted blocks is about 14.4% and has density of 1.70g/cm^3. During the construction, there is some gap left at the top of the barrier as shown in Figure 6.4. It is assumed that when the test operation is started, the expansion of the blocks during hydration will fill out this gap and the joints between the blocks and the dry density of the filled block will be around 1.60g/cm^3 (ENRESA, 2000).

The in situ host rock is of granite belonging to the Central Arae formation. The formation has very few discontinuities, but is crossed with lamprophyre dykes. Further information on the test site geology is given in Keusen et al. (1989). The pore water pressure at the depth of the experiment before the excavation is determined to be in range of (0.5 – 0.7) MPa. Although the initial water flow pattern is changed due to the tunnel excavation, same pressure is considered as the boundary liquid pressure for further analysis.

As mentioned earlier, the test is conducted to study the performance of the barrier for certain period of time. Thus the test is followed through a sequence of steps and the

actual disposal environment is created in subsequent time. Before the turning on the heater and starting the process, about four months are allowed for the barrier to hydrate and expand to fill up the gaps. Later, the two heaters are turned on for the thermal loading. The amount of heating is controlled so as to maintain a maximum temperature of 100°C at the contact between the liner and the bentonite. The sequence of steps followed during the test is stated below:

1. In order to determine the amount of heat required to maintain the temperature, the heaters are initially switched on at a constant power of 1200W for about 20 days. In these days, the thermal response of the barrier is recorded and the quantity of heat required is adjusted.
2. Using the thermal response from above, the power of each heater is increased to 2000W, so as to attain the temperature to 100°C, which occurred in 33 days.
3. Then the amount of heating is controlled time to time in order to maintain the temperature of 100°C at the liner contact. This is continued for five years during which the thermal-hydraulic-mechanical responses are monitored with respective sensors stationed at different locations.

   The power of heater is monitored regularly to control heating. But during the test, accidentally, there occurred a moment of overheating which has been discussed in Sanchez, 2005.
4. After about 1850 days, the heater I near the open end of drift is turned off and the bentonite at that part is allowed to cool for about 33 days.

5. Then after 1883 days, the concrete plug is taken out to accelerate cooling and after 1962 days, the barrier is dismantled within a month and heater is extracted. The bentonite samples were collected and postmortem test are performed for their actual state, both on site and in the laboratory for further investigations.

During the process of testing, various sensors are used to monitor temperature, relative humidity, pore pressures, total pressure and displacements. These are analyzed on the regular basis to characterize behavior (Gens et al., 1998; Alonso et al., 2005). During the partial dismantling of the barrier, onsite tests are conducted to determine the immediate response of the barrier. These onsite determinations include water content and dry density determination along the radius of the barrier with respect to the distance from heater. The in process monitoring and onsite determinations are summarized by Daucasse and Lloret, 2003; and Villar et al., 2005.

As part of postmortem analysis, various laboratory tests are performed with aim to characterize the actual state and determine the changes in THM properties of the bentonite. These laboratory investigations include variation of thermal conductivity; water retention capacity, hydraulic conductivity; swelling capacity and preconsolidation pressure. These experimental results are summarized along with the procedure in Villar and Lloret, 2007. Further, the Grimsel test is modeled using the THM framework mentioned in the section 2.3, using the Barcelona basic model as mechanical framework (Gens et al. 2009) and compared with the experimental results.

In the present thesis work, the same test is analyzed for the mechanical response, using the double structure model as mechanical framework. And then, the samples are collected at the same locations as collected during the dismantling. As the preconsolidation pressures of the samples are determined through consolidation test under oedometric conditions and controlled suction, the samples from the numerical model analysis are also further modeled for numerical consolidation tests under the same conditions. The results are then compared with the experimental results presented by Villar et al. (2007).

6.2 Numerical Modeling of In situ Experiment

A coupled thermo-hydro-mechanical analysis has been carried out numerically, using the finite element code CODE_BRIGHT (UPC, 2004). The program uses same THM framework presented in chapter 2, except the mechanical model is now based on the double structure theory explained in chapter 5. As the length of heater is relatively long when compared to the radius of the barrier, a one dimensional axis symmetric radial discretization is adopted with linear elements.

6.2.1 Discretization

When the bentonite blocks at dry density of 1.7 g/cm^3, there is some gap created at the top portion of the barrier which can be seen from heater section of Figure 6.4. Also, before the insertion of heater and bentonite blocks, a cylindrical liner is laid, around which the bentonite blocks are filled. This liner is made of steel mesh type structure thus

not allowing the block to collapse before insertion of heater. This mesh has some gap in between them. These two gaps are also modeled into the finite element program to represent the barrier from radius r=0.47m (first node) to r=1.12m (last node). So, initially an axisymmetric 1D finite element mesh is created using 21 elements and 22 nodes. Following the test sequence no.1 (as stated in previous section), the model is also allowed to hydrate from the rock end. The bentonite expands at both rock end and at the heater end. This mesh after expansion is then fully built with the other elements of the repository which include heater, air, liner and the rock.

The discretization of the various zones of the barrier into linear elements and location of particular nodes and elements are figuratively shown in Figure 6.5. The figure (a) shows the full in situ design with radial coordinates, while figure (b) enlarge the bentonite barrier (elements from #5 to #25). The bentonite is first allowed to expand to fill up the gap at the node #26. The main purpose for the allowance of the expansion is to track the changes in the mechanical behavior in terms of saturated preconsolidation pressure (p_o*). The mesh is then completed to represent preliminary design of the heating test. The figure also shows six reference elements which are further collected for the consolidation model. The barrier extends from 0.46m to about 1.12m before expansion and about 1.135 after expansion, giving total thickness of 0.66m and 0.675m before and after expansion, respectively. Further, the boundary of the host rock domain is located 50m away from the heater.

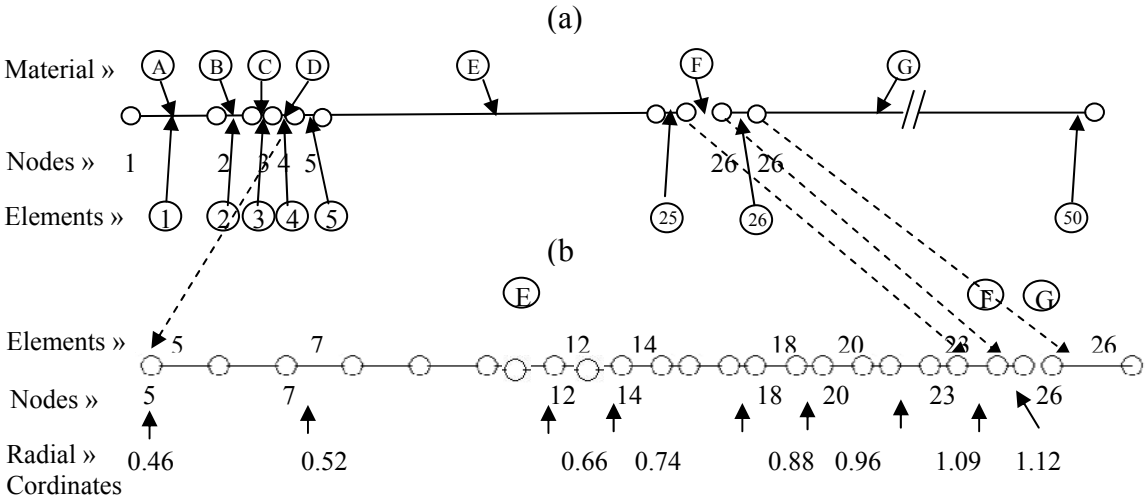

Element No.	Materials
# 1	A – Air
# 2	B – Steel with heater inside
# 3	C – Air gap
# 4	D – Steel liner
# 5 to # 25	E – Bentonite blocks
	F – Gap between the buffer and host rock
# 26 to # 50	G – Host rock (granite)

Figure 6.5. Linear discretization of the engineered barrier showing nodes, elements and their coordinates.

6.2.2 Material Parameters

A number of laboratory and in situ tests were performed to determine the properties of bentonite and the host rock and to define the material parameters required by the formulations. The specific properties and their parameters of the bentonite relating to thermal and hydraulic phenomena are described and summarized in section 2.4. The double structure mechanical parameters of the bentonite are extracted from Lloret et al. (2003) and are summarized in Table 6.1.

Table 6.1. Parameters used to define the elasto-plastic double structure model.

Parameters defining the Barcelona Basic Model (BBM) for macrostructural behavior			
κ	0.005	κ_s	0.001
$\lambda(0)$	0.080	p_c	0.50 MPa
r	0.90	β	0.2
p_o^*	12 MPa	α_o	1.0×10^{-5} °C^{-1}
Parameters defining the elastic behavior for macrostructural behaviour			
α_m	2.1×10^{-2} MPa^{-1}	β_m	2.3×10^{-3} MPa^{-1}
Interaction functions			
$f_c=1+0.9 \tanh[20(p/p_o -0.25)]$		$f_s=0.8-1.1 \tanh\left[20\left(p/p_o -0.25\right)\right]$	

From the observations of the clay fabric, the microstructural and macro structural void ratios are observed to be 0.45 and 0.11 respectively. The static compaction stress of 18MPa is assumed and from the LC (Eq.5.6), the saturated preconsolidation pressure (p_o*) is obtained to be 12 MPa and is used as the initial value for hardening parameter. It is assumed that p_o* is independent of thermal variation and so, thermal parameters (α_1, α_3 and ρ) from Eq.5.20 and Eq.5.21 are assumed to be zero.

The material properties of the granite host rock are obtained from the experimental investigations by Keusen et al. (1989) and Frieg and Vomvoris, 1994 and are summarized in Table 6.2. The granite is characterized with the presence of very few fractures but a lamprophyre dyke, which does not affect the behavior of barrier. The water pressure before excavation is obtained to be about 0.7MPa and the granite is assumed to be saturated throughout the test.

Table 6.2. Granite rock properties used in the THM model.

Thermal Parameters	
Thermal conductivity (λ_T)	3.6 W/m °C
Specific energy (E_s/T)	793 J/kg °C
Coefficient of linear expansion (α_o)	7.8 x 10^{-6} $°C^{-1}$
Hydraulic Parameters	
Intrinsic Permeability (k)	8.0 x 10^{-18} m^2
Retention curve, p_o	2.1 MPa
σ_o	0.072
λ_o	0.70
Mechanical Parameters	
Bulk Modulus (K)	2.92 x 10^4 MPa
Shear Modulus (G)	1.35 x 10^4 MPa

6.2.3 Initial and Boundary Conditions

The initial conditions of the bentonite during installation into the drifts are measured. The dry density of bentonite blocks is found to be 1.7 g/cm^3 and from the specific gravity of 2.65, the total void ratio is found to be 0.56. From the structure of clay fabric, the initial micro and macro void ratio are taken as 0.45 and 0.11, respectively. The water content is determined to be 14.4%. The initial suction is found to be about 138 MPa and from the retention cure, the degree of saturation is found to be about 0.55. Based on the insitu rock investigations, the temperature is found to be about 12 °C and same is assumed for the barrier also. The initial stresses inside the bentonite barrier are assumed isotropic and equal to 0.2 MPa. Regarding the rock, the porosity is about 0.01 and is assumed to be saturated throughout the test with the excess liquid pressure of 0.7 MPa.

The initial stresses in the rock are also assumed to be isotropic and uniform with stress value of 28 MPa.

As of boundary conditions, the outer boundary of rock which is at 50m radius from the axis of drift, is assumed to be having no effect from the heating of the barrier. Hence a constant temperature of 12°C; excess liquid pressure of 0.7 MPa; and constant radial stress of 28 MPa (corresponding a radial force of 8796 MN) is induced at the node # 51. Since, there some gap at the intersection of bentonite and rock, the excess liquid pressure is assumed to be 0.1 MPa. The heating elements are placed at the radial coordinates of 0.3m at node #3 which is the inner boundary of heaters. First a constant flux of 440 W/m is passed for 21 days and then increased to 525 W/m at this point, so as to attain a temperature of 100 °C at the node #4 (r=0.44m) i.e. outer boundary of heater. As the gas phase is not confined, gas phase calculations are not done and a constant gas pressure equal to atmospheric pressure (0.1MPa) is assumed. But, the vapour diffusion calculations are taken into account considering the unsaturated state of bentonite influencing the diffusion flow of fluids.

After initial four months of isothermal stagnation, the time of switching the heaters on is taken as starting time (t=0) and the simulations are run up to five years. The initial porosity of 0.358 ($n_o = e_o/(1+e_o)$; e_o= 0.56) increases to about 0.385 due to hydration during the four months of stagnation.

6.2.4 Results of Thermo-Hydro-Mechanical Analysis

Thermal Interpretation

The Figure 6.6 presents the evolution of temperature by the two frameworks (one that uses BBM and the other that uses double structure) for the representative section S19. In the figure the temperatures at different radial distances from the axis of the tunnel are plotted. The experimental observations are presented from more than one sensors which are placed along several radial lines. It can be seen that the results from both the models are in good agreement with the observations. This indicates that even under coupled phenomena, the models are able to reproduce the actual thermal condition of the test.

Hydraulic Interpretation

The hydraulic changes in the barrier are interpreted in term of the changes in relative humidity. In the test, the relative humidity (RH) is monitored using capacitive sensors installed at different locations. In the model, the relative humidity is calculated obtaining the total suction *s* obtained and using the Kelvin's psychometric equation:

$$RH = \exp\left[\frac{sM_w}{R\,(273+T)\rho_l}\right] \tag{6.1}$$

Figure 6.7 presents the evolution of relative humidity again from both the frameworks. Similar to the thermal observations, the results from both the models are able to reproduce the observations. As the observations, the relative humidity increase at high rate initially because of the reason that the increase temperature at heater end generates more vapour which are further transported to outer boundaries. But, gradually as the

pore water flows, the increase in relative humidity decreases. There can be also be seen that at radial distance of r=107cm, the RH reaches 100% earlier in case of the double structure model when compared to that of BBM. Perhaps this might be due to the fact that in double structure model, we assumed a gap at the junction of barrier and rock which leads to outer layer to absorb more water to get saturated faster. However when we go closer to the heater, no significant differences are observed between the models. It should be noted that it is not possible to measure the total amount of water flow in the in situ test. But in reference to modeling, the amount of water intake in the double structure modeling is matched with that in modeling with BBM.

Mechanical Interpretations

The changes in total stresses are considered as main parameter since, the barrier undergo mechanical changes under the confined conditions from the rock. Figure 6.8 shows the evolution of normal stresses, at the reference locations. It can be seen that the swelling pressures at beginning of the test are developed at faster rate in case of BBM modeling, when compared to double structure model. In fact the stresses produced by the double structure match closely with the experimental observations than that of BBM. It can be attributed to the same fact that a gap in between the barrier and rock is modeled in case of double structure. Also, it can also be seen that the stress near the heater, that is, at r=48 cm, the stresses are lower when compared to at r=88 cm. Again, during the double structure modeling, a small gap is assumed in between the heater and bentonite attributing to the liner mesh.

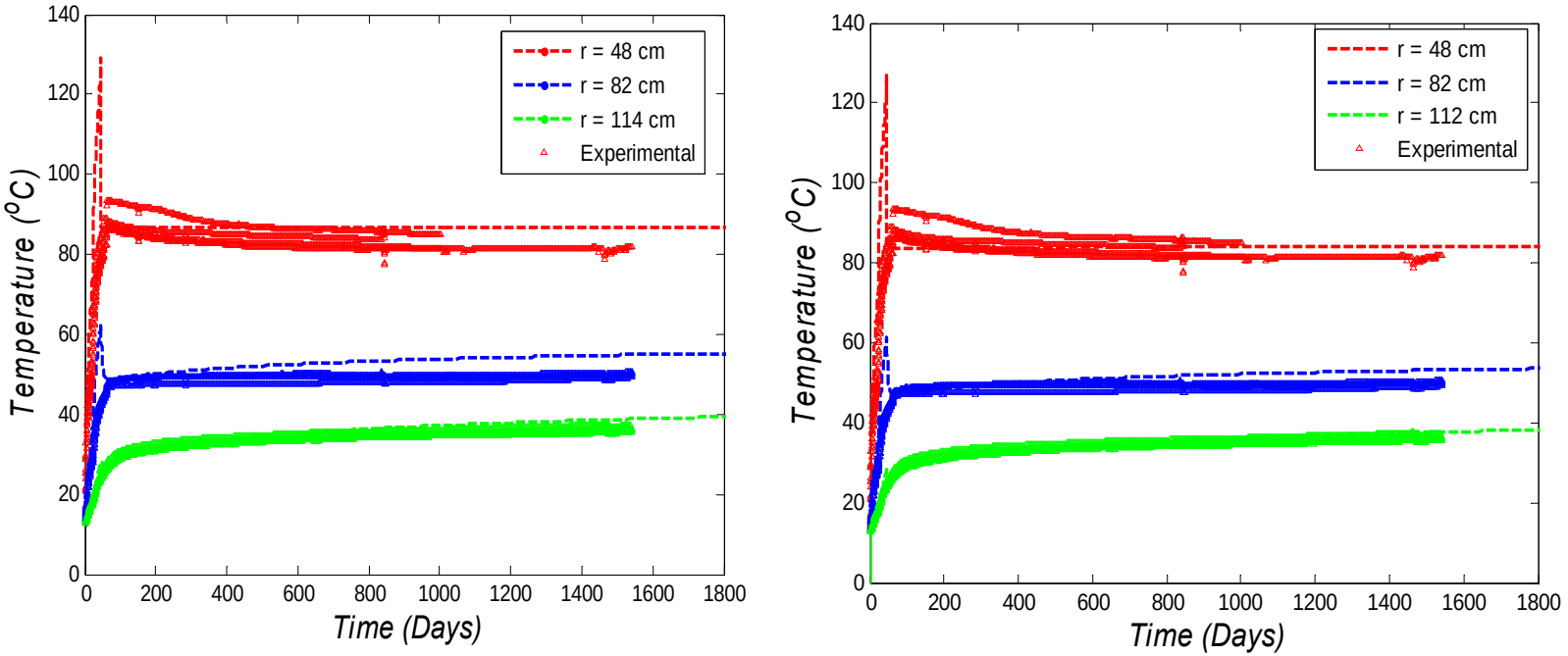

Figure 6.6. Evolution of temperature in bentonite barrier, observations and computed results from (a) BBM (b) Double structure, at distance of r=48 cm, r=82 cm and r=114 cm.

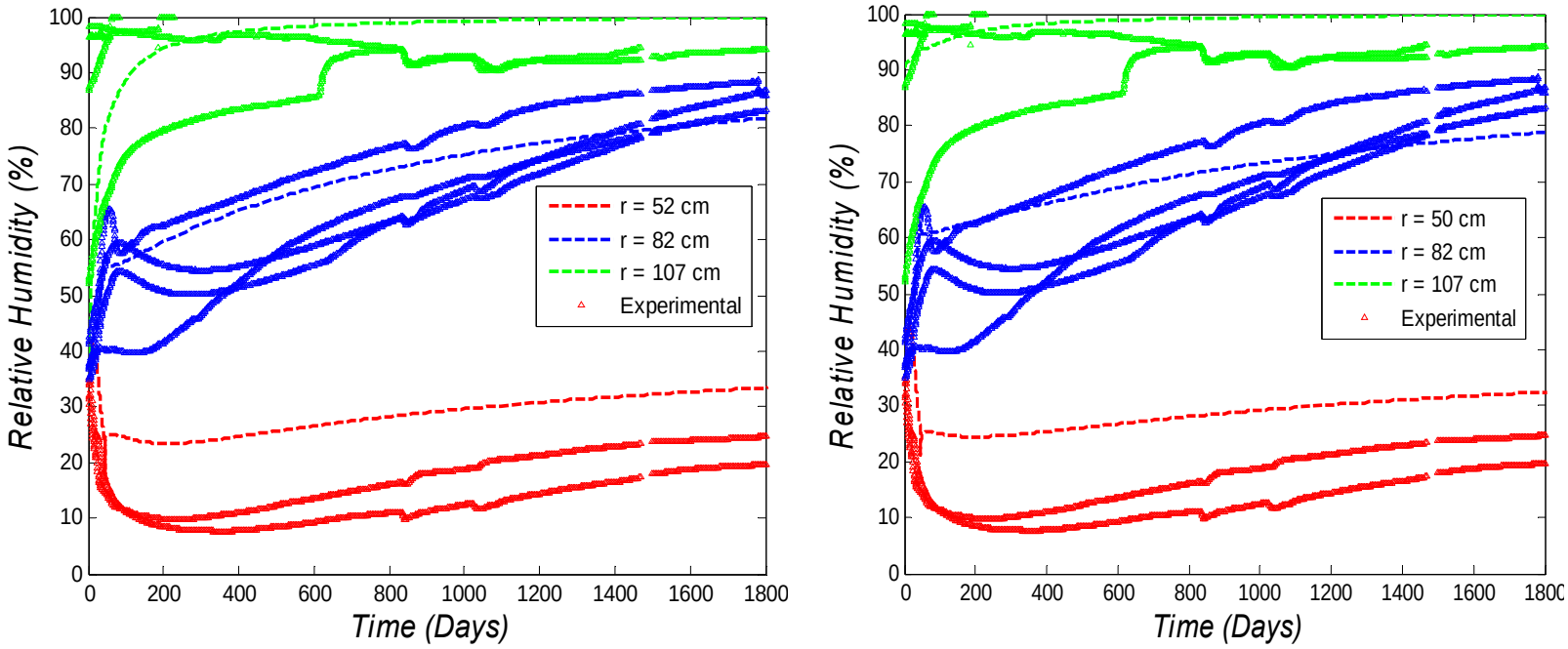

Figure 6.7 Evolution of relative humidity in bentonite barrier, observations and computed results from (a) BBM (b) Double structure, at distance of r=48 cm, r=82 cm and r=114 cm.

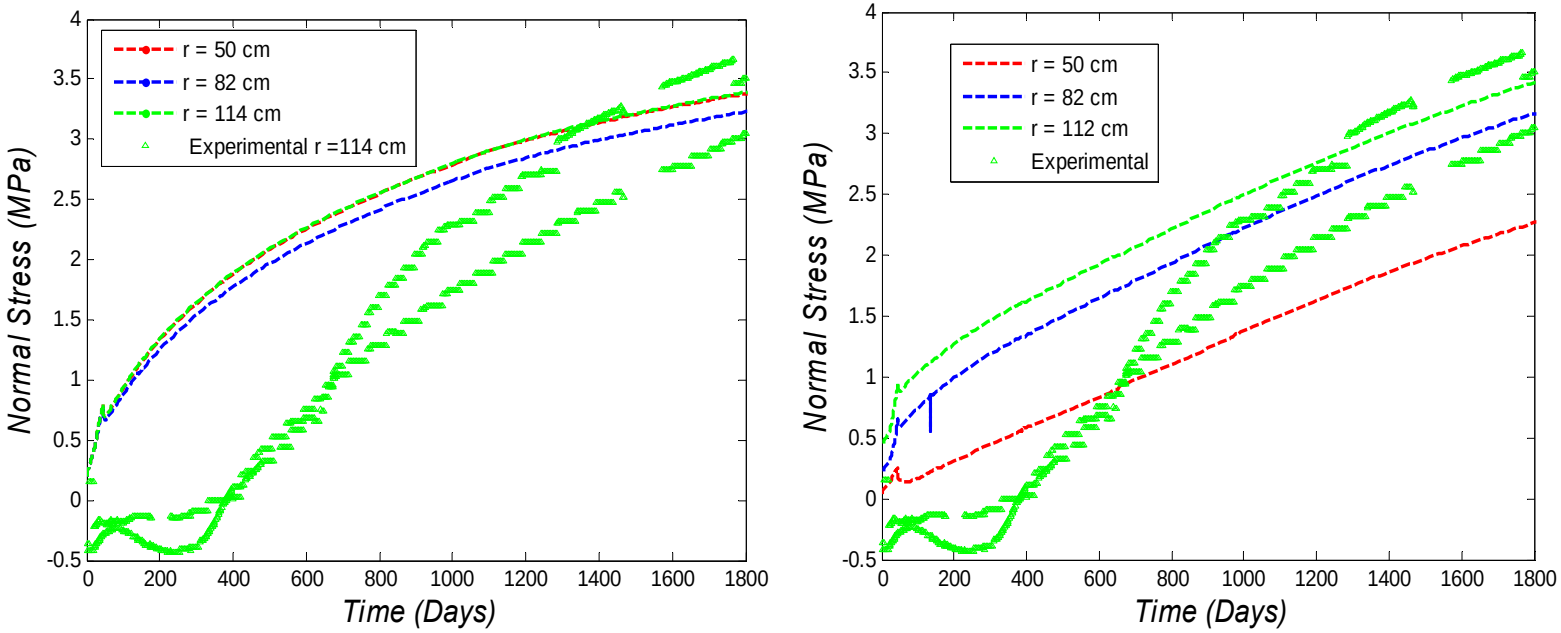

Figure 6.8. Evolution of normal stress in bentonite barrier, observations and computed results from (a) BBM (b) Double structure, at distance of r=48 cm, r=82 cm and r=114 cm.

6.2.5 Analysis of Mechanical Behavior

In this section, the changes in the mechanical properties of the bentonite barrier are observed. The representative section of the barrier is simulated using the BBM model and analyzed for the stress paths and the changes in the hardening parameter (p_o^*) at three reference locations (r=52cm, r=88cm, r=109 cm).

Figure 6.9 show the stress path followed by the bentonite and the variation of apparent preconsolidation pressure, p_o at three different locations during the heating and dismantling process. It is observed that the since the stress are far less that the p_o there is no change in the hardening parameter keeping the LC curve stationary. Figure 6.10 shows that the variation of void ratio depending on distance from the heater.

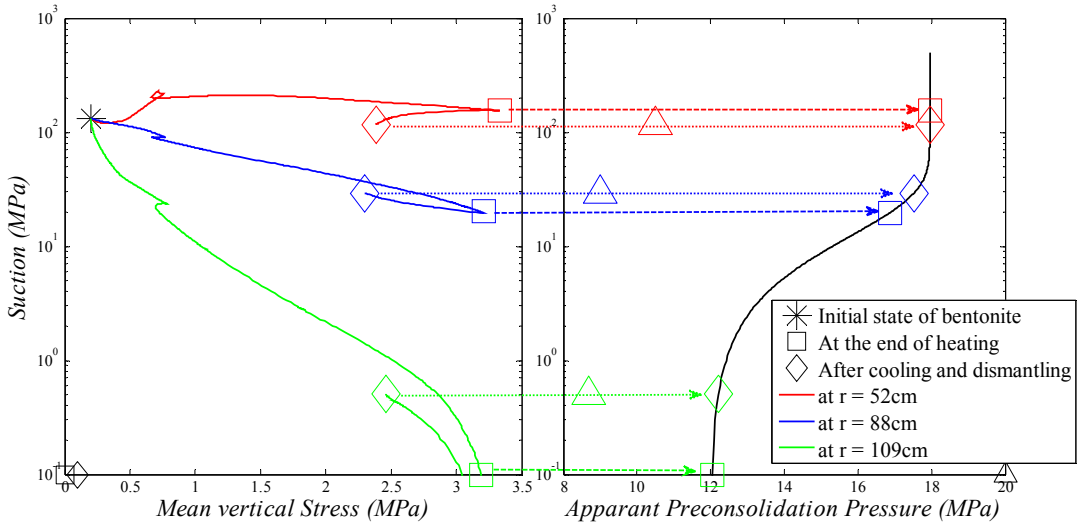

Figure 6.9. Stress path followed by bentonite clay in the BBM during the heating test and the variation of apparent preconsolidation pressure.

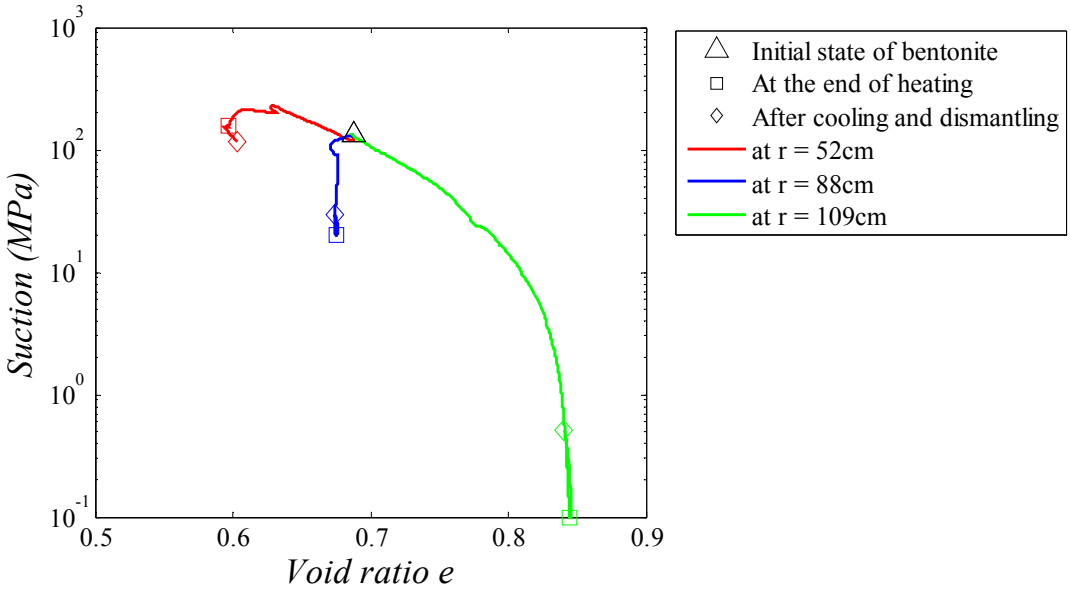

Figure 6.10. Variation of void ratio during the heating test.

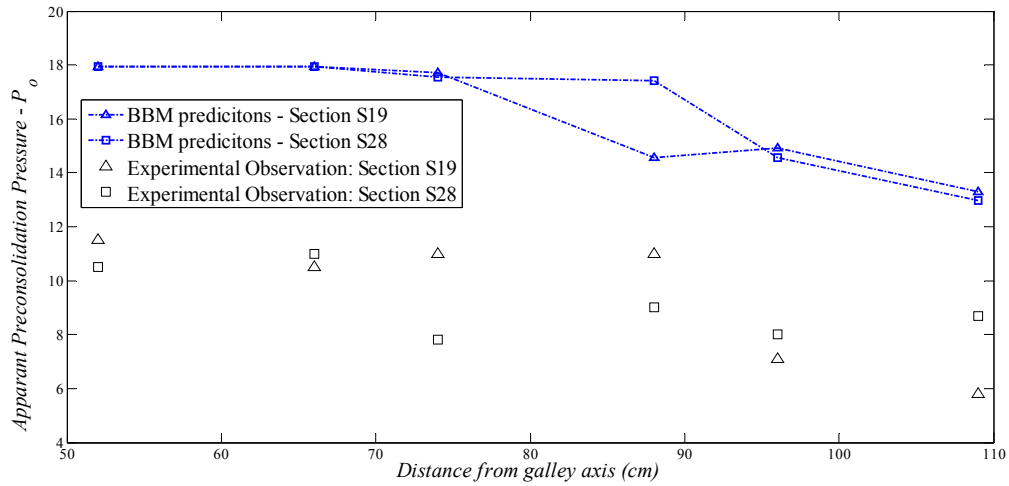

Figure 6.11. Comparison of BBM model predictions of apparent preconsolidation pressures of bentonite with the experimental observations after cooling.

Due to these changes in void ratio, we would expect some changes in p_o^* leading to the movement of LC. But, the BBM model fails to describe the complete variation of the plasticity of the clay. Figure 6.11 shows the BBM prediction of apparent

preconsolidation pressure. The reason is that the BBM assumes any changes with the yield zone to be elastic and in our case; the stresses are always less than the yield stress. As the BBM fails to explain this expansive behavior, the same in situ test is now analyzed by the double structure model. The analysis is done in total four stages: (1) The barrier is allowed to hydrate with in situ pore water from the host rock; (2) Then the operational stage is started by turning on the heater; (3) Turning off the heater and allowing the barrier to cool and then bentonite is excavated; (4) These samples are finally collected and prepared for oedometer tests. When the samples from the in situ tests are collected and sent for laboratory tests, they undergo disturbances in terms of both suction and stresses. So, in order to model the sample for these oedometric conditions, the model is subjected to the linear stress paths from stage 3 to stage 4, where the stress are changed under constant suction and then suction is changed under constant stress (Figure 6.21). In this way, the samples numerically collected and prepared to model the oedometer analysis. The stress paths followed by bentonite barrier during the four stages at reference locations are shown in Figure 6.12, Figure 6.13, and Figure 6.14. The variation of total, micro and macro void ratio during the stage 2, stage 3, and stage 4 are shown in the Figure 6.15, Figure 6.16, and Figure 6.17. The interaction function followed at the reference location is shown in Figure 6.19.

The movements of LC curve at different stages are also shown in the respective figures. The sample at r=52 cm from the heater doesn't under go much changes in the hardening behavior during the hydration and heating test, but when they are reduced to oedometric

condition, then there is huge movement of LC curve. As can be seen from the change in void ratio is very less in stage 2-3, and large stage 4, it can be so judged that the variation in the hardening parameter.

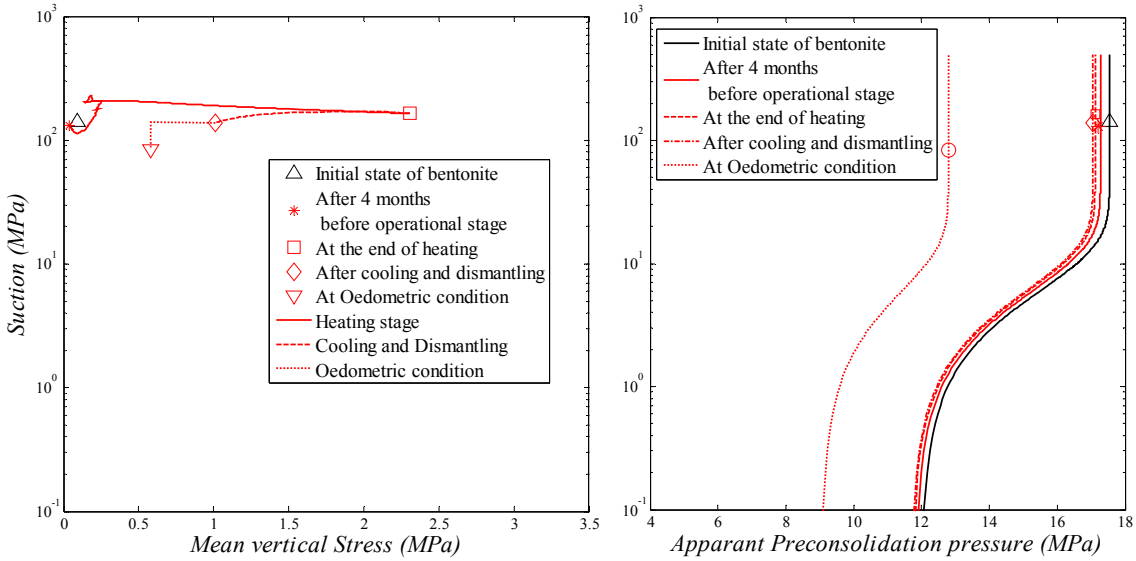

Figure 6.12. Stress path followed by the bentonite at every stage at r=52cm and movement of LC accordingly.

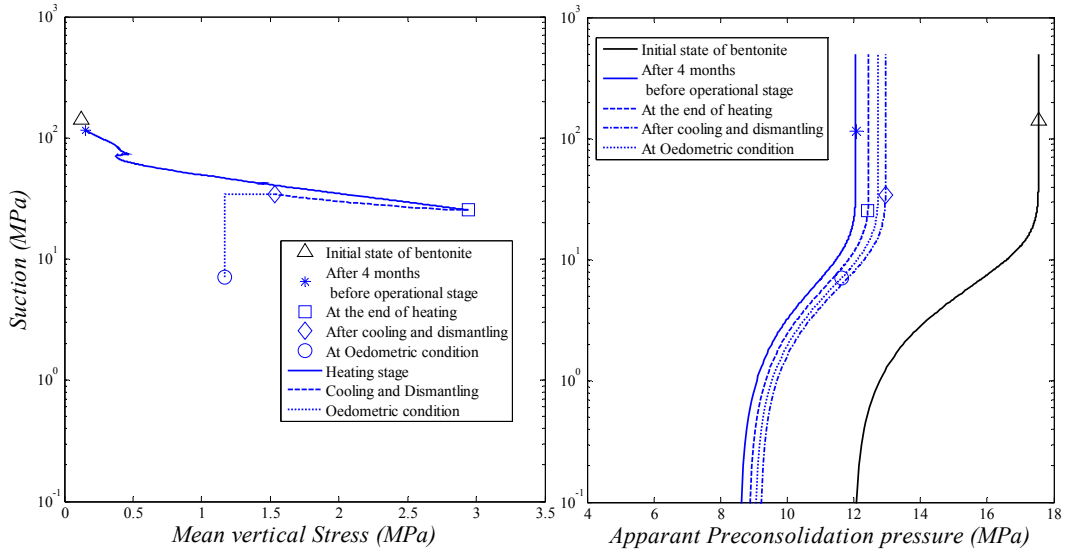

Figure 6.13. Stress path followed by the bentonite at every stage at r=88cm and movement of LC accordingly.

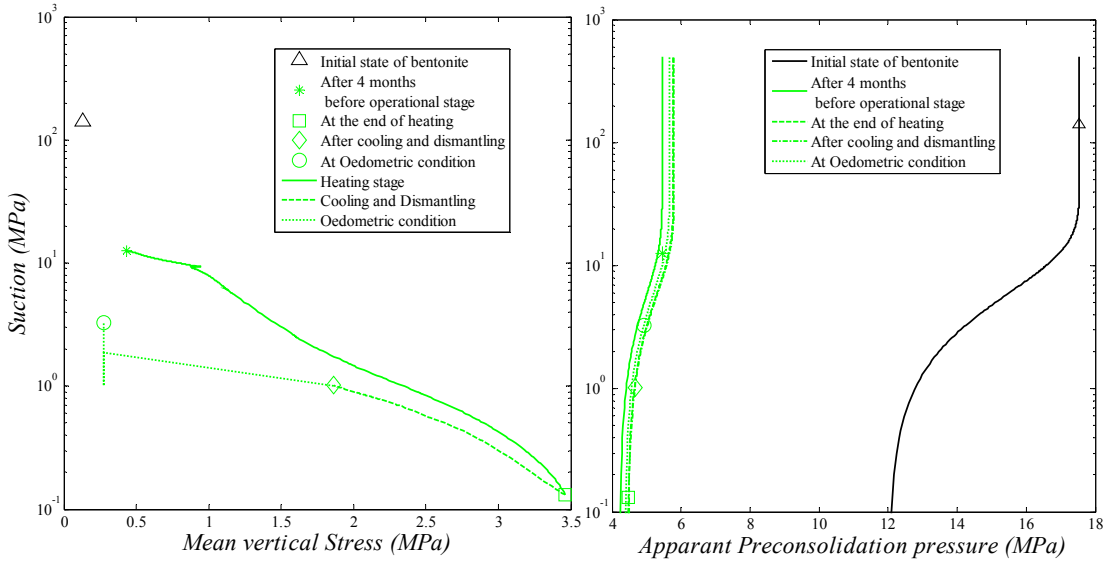

Figure 6.14. Stress path followed by the bentonite at every stage at r=109 cm and movement of LC accordingly.

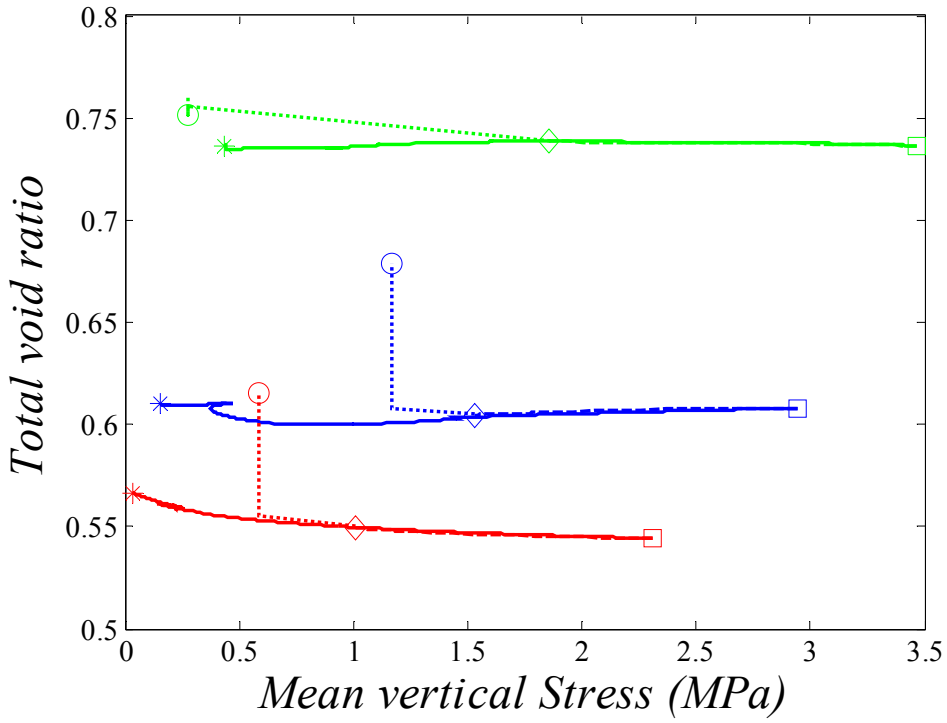

Figure 6.15. Variation of Total void ratio during stages 2-4.

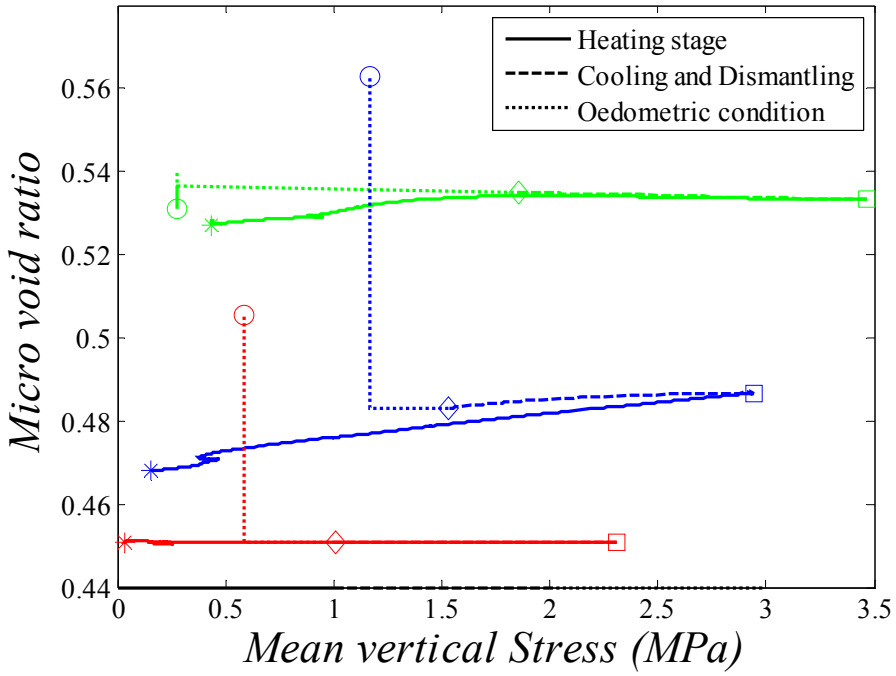

Figure 6.16. Variation of Micro void ratio during stages 2-4.

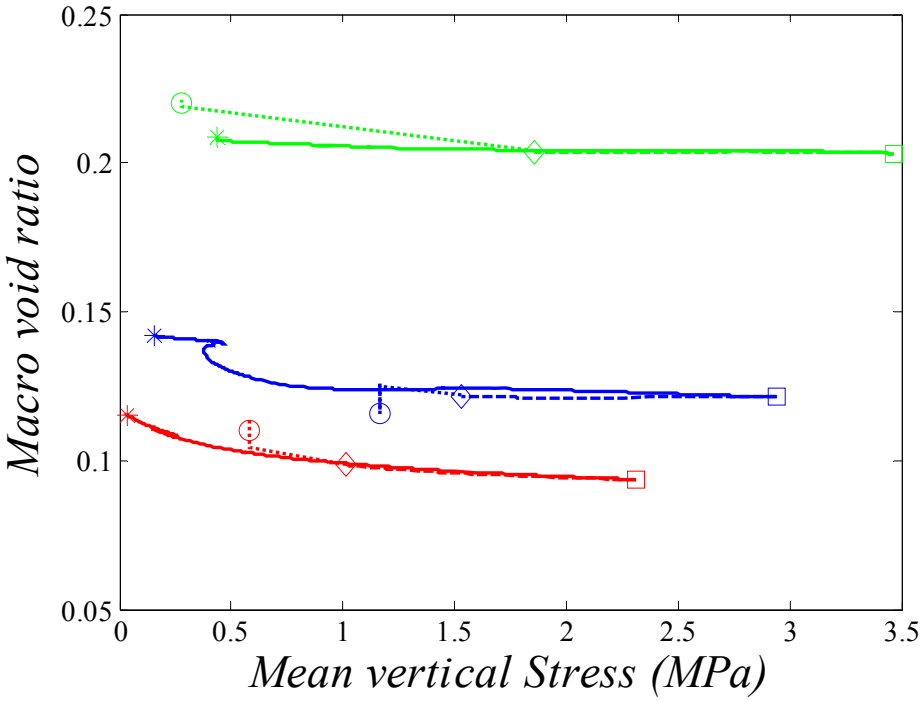

Figure 6.17. Variation of macro void ratio during stages 2-4.

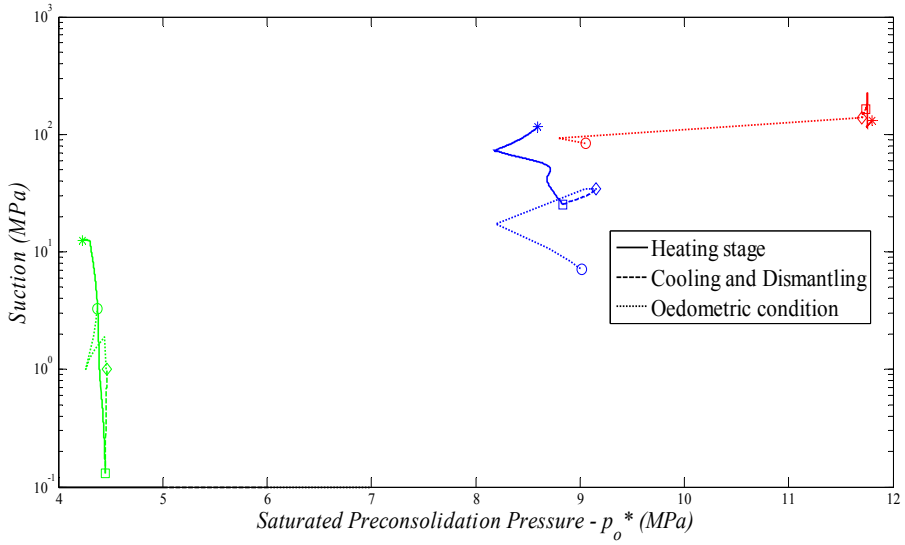

Figure 6.18. Evolution of hardening parameter p_o^* during the stages 2-3.

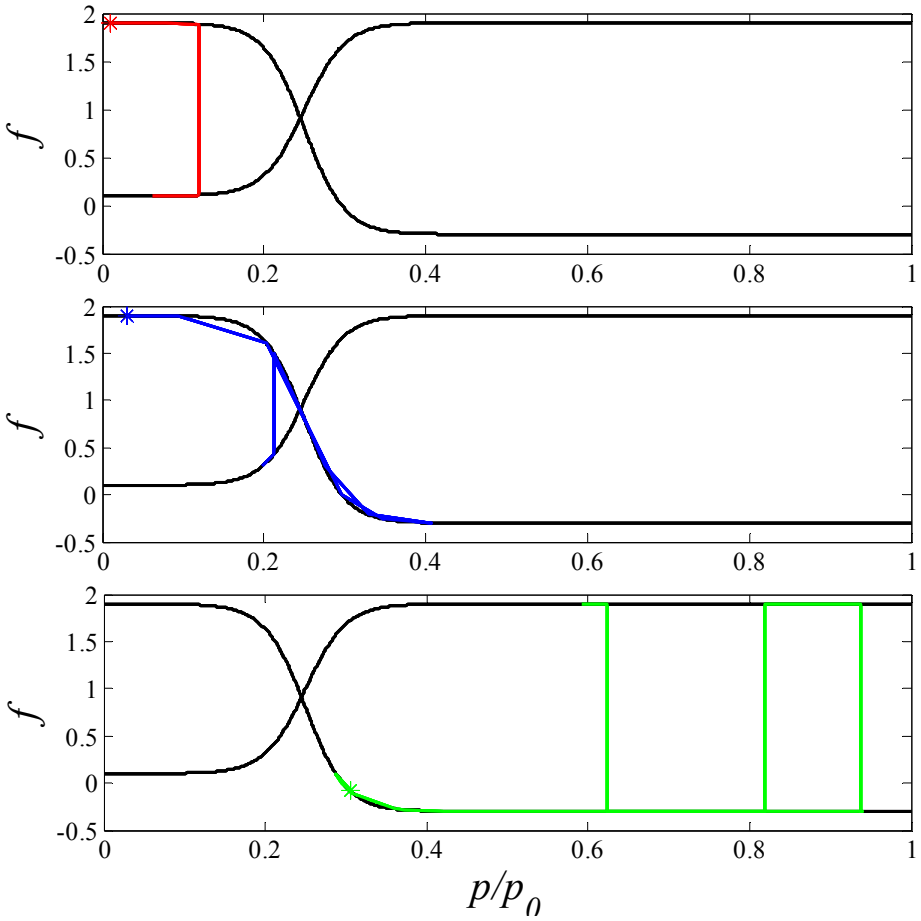

Figure 6.19. Interaction function followed by the bentonite clay at radial distance of r=52cm, 88cm and 109cm from the gallery axis.

At r=88 cm during the heating stage, although the macro void ratio doesn't change much, the micro changes to significant level and it mostly undergoes swelling and thus follow the f_s causing swelling and intruding into the macro pores thus the p_o^* increases as seen from Figure 6.18. During the hydration, the p_o^* reduces to about 8.5 MPa indicating it undergoes softening. But, during the heating stage, the p_o^* slightly increase indicating it undergoes hardening. Similarly at r=109cm, the p_o^* reduces significantly during the hydration stage and during heating the increase is very less.

6.3 Oedometer Tests

After dismantling the heater #1, the bentonite samples are collected at different sections and postmortem tests are performed to characterize the actual state of bentonite. As a part of these tests, samples are tested for preconsolidation pressures through consolidation test performed using suction controlled oedometric cells. The suction is controlled indirectly by checking the water content and dry density through the means of sulphuric acid solutions. When the targeted suction value is obtained, then the samples are loaded progressively with a time gap of 7 days per each load. In this section, these tests performed by Villar and Lloret (2007) are summarized and discussed.

Twelve samples are collected from two sections: S19 and S28 (Figure 6.20), taken at different locations along the radius of the barrier. The location at which the samples are collected can be seen from the Figure 6.5. The bentonite blocks are collected and transported to the laboratory as carefully so as to cause minimum disturbance.

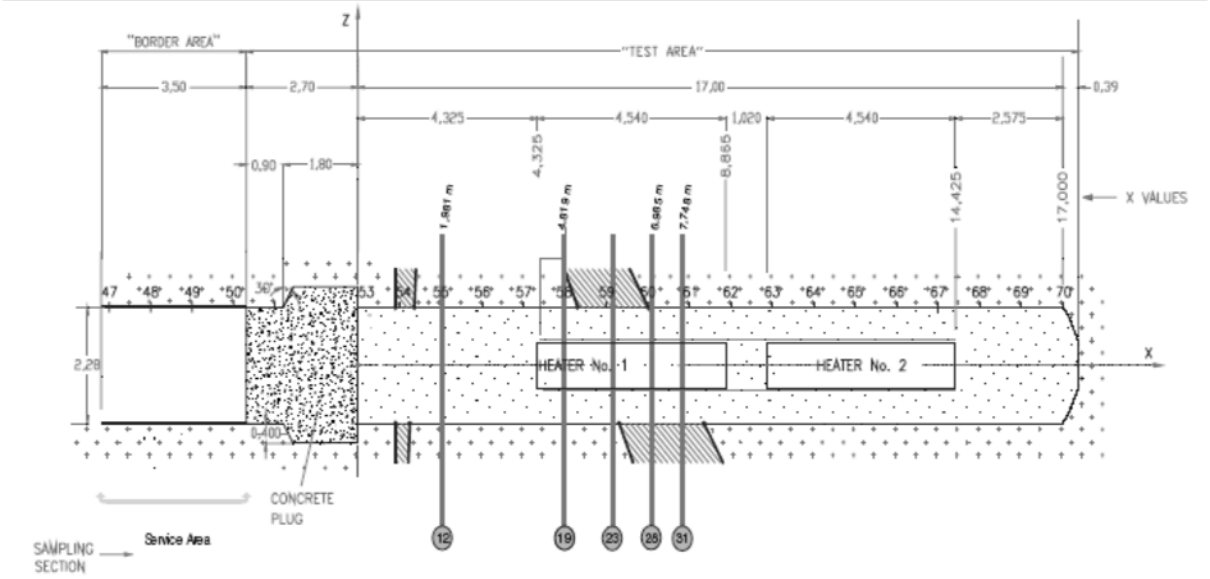

Figure 6.20. Location of sampling section for postmortem analysis.

But, since the samples collected after cooling, do not represent those exactly during the heating. They are unloaded from their original stress and the suction value may also be changed. Thus, in the oedometer test, before loading, the samples are taken back to their original stress and suction values.

The path followed by the samples is shown in Figure 6.21. At stage 1, the bentonite blocks are compacted at specific water content. Path 2 shows hydration under confined swelling followed during the barrier operation. The unloading stress during the dismantling stage is given by path 3. Finally, the samples are loaded back at the suction same as that during testing and consolidation tests are performed at stage 4. The

oedometric curves thus obtained are presented in Figure 6.22 and Figure 6.23 and the preconsolidation pressure obtained are given in Table 6.3.

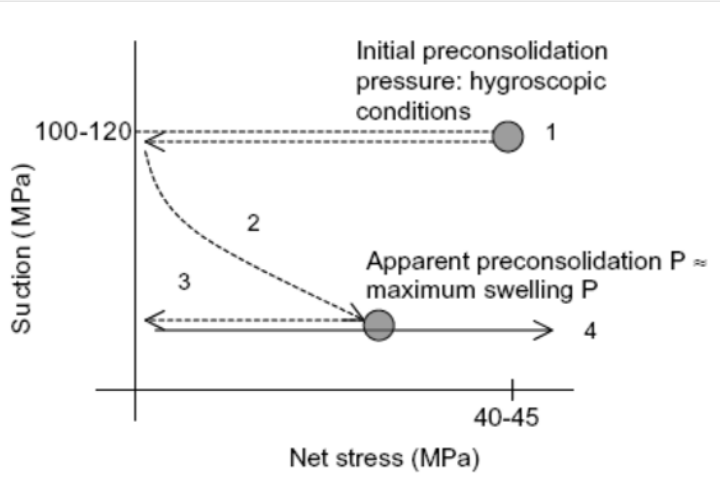

Figure 6.21. Stress path followed by the bentonite samples during the heating test.

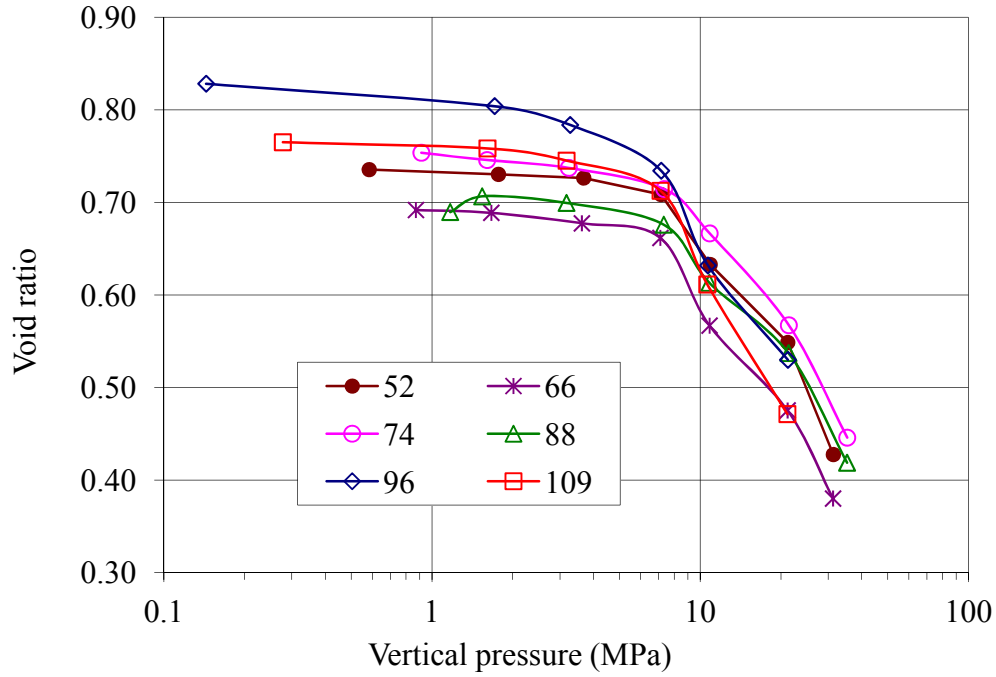

Figure 6.22. Consolidation curves of the tests performed on samples from section S19 taken at different distances from the axis of the gallery (indicated in cm).

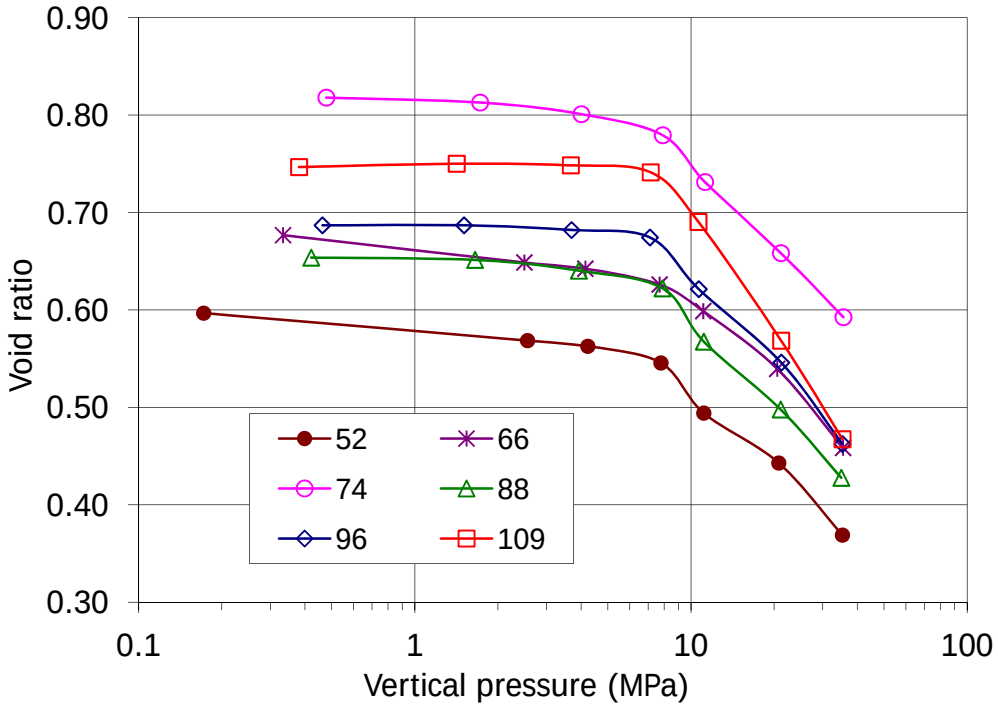

Figure 6.23. Consolidation curves of the tests performed on samples from section S28 taken at different distances from the axis of the gallery (indicated in cm).

Table 6.3. Apparent preconsolidation pressure obtained from the consolidation curves.

Distance from the heater (cm)	Apparent Preconsolidation Pressure (MPa) (appx.)	
	Section S19	Section S28
52	11.5	12.0
66	11.0	12.5
74	12.0	8.8
88	11.0	9.0
96	7.4	8.0
109	5.8	6.7

6.4 Numerical Modeling of Oedometer Tests

The oedometer tests from the previous section are numerically modeled using the double structure mechanical model. As said earlier, when the in situ samples are transported to laboratory for further test, there may have occurred some disturbance in terms of liquid pressure and stresses. Therefore, before analyzing the oedometer numerically, the samples obtained through the numerical program are also subjected to same conditions so as to achieve the state at which actual consolidation tests are performed. For this the stress are first decreased under constant suction and then suction is varied under constant stress. The path other way could also be taken, that is, first decrease suction and then stress. But, for our case the former case is considered.

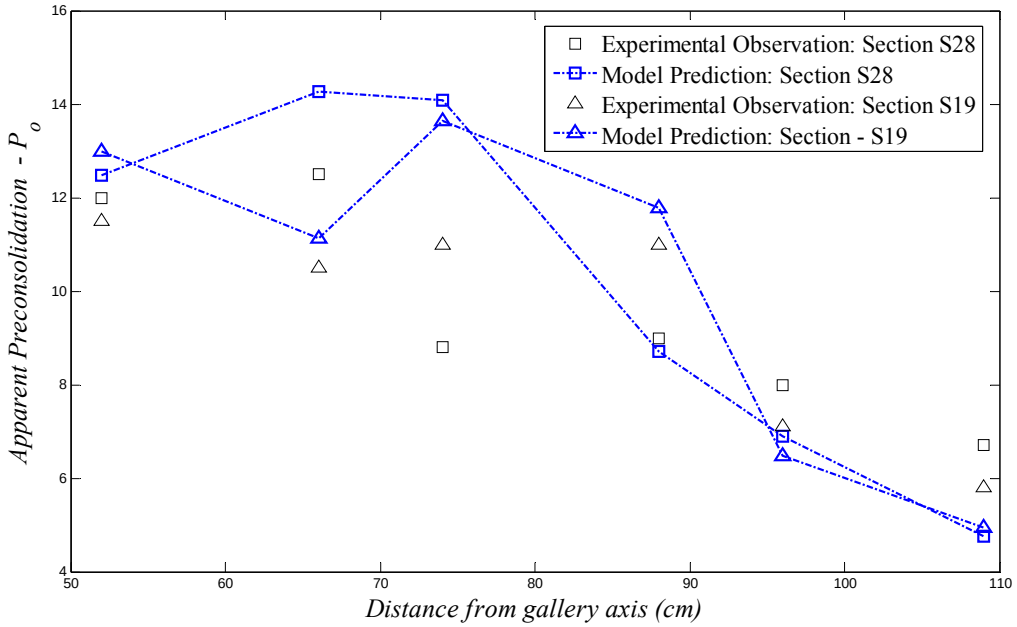

Figure 6.24. Comparison of model predictions of apparent preconsolidation pressures of bentonite with the experimental observations after Stage 5.

The samples are collected from both sections: S19 and S28 at six different locations in each section. They are subjected to sequential increase in the load and their change is void ratio in term of ($\Delta e/(1+e)$) is recorded. They are plotted against the experimental compression curve and are shown in Appendix B.

Finally, the preconsolidation pressures (P_o) predicted by the model in the both the sections are compared with the experimentally obtained values and shown in Figure 6.24. It can be observed that the model is able to able to predict the variation in P_o at almost every location. Thus, from all the predictions, it can be said that the double structure model can successfully explains the mechanical behavior of the unsaturated expansive soils

7. CONCLUSIONS

7.1 Summary

The two objectives of the study are: (1) to determine the possible source of parametric uncertainty and to quantify amount of variability of the THM response due to thermal and hydraulic parameters; (2) to study the mechanical behavior of engineered barrier using an advanced mechanical model.

One of the main sources of uncertainty in the THM response of the model is from the variability in the input parameters which could be due to many reasons: measurable and non-measurable. To capture the random distribution of these parameters, a simple random model was developed. The randomly generated parameter samples are used in a finite element program to study the effect of thermal conductivity; retention curve and hydraulic conductivity on temperature, dry density and water content were found. The study has allowed us the better understanding of uncertainties in the THM behavior of clay barrier.

The structural integrity of a nuclear barrier is based on the mechanical behavior of the material used, which is effected by heating and hydration process. The suction and temperature has their effect on stress-strain behavior of material under restricted swelling conditions. An elasto-plastic hardening model was used to describe the clay behavior, but it fails to explain the plastic deformations within the yield zone. An

advanced double structure model is used in which deformations at micro particle level influence the deformations at macroscopic level of the clay, which may lead to plastic strains within the yield zone. Thus, a model was developed for better understanding of the strain hardening-softening of the soil, which the previously applied BBM model fails to explain.

7.2 Conclusions

Some of the conclusions that can be deducted from the uncertainty quantification of the THM analysis are stated as following.

1. Calibration of the parameters shows the large variation from the values that were used for deterministic analysis. The mean values of the parameters obtain from the calibration are far different from the experimental observed showing great degree of uncertainty.
2. The assessment of THM response show that:
    - The predictions near the heater are more uncertain and it decreases as we move away from heater. It means at higher temperatures, the prediction show large variations when compared to lower temperatures.
    - The model predictions show huge variation with respect to the actual response observed. Although this variation decreases with time and as closing towards heater, the predictions themselves show large variations. In short, when the predictions are certain, they far different from observation and when the predictions are more uncertain, it is able to reproduce the observations.

- The individual thermal conductivities show no influence on the THM response, but when combined with the variation in hydrological parameters, its influence increases.

- Similarly, retention curve parameters and permeability parameters individually show lower variation when compared to the case where their variation is combined with that of other parameters.

3. The correlation between the response variable and the material parameters gives us the influence of each input parameter on the output response. It also gives us the parametric variability depending on the observed THM response.
4. The auto and cross correlation functions gives the idea of how one response variable vary with changes in the other in space and time. They can be used to predict the variation of a response at any time and at any location using the observed values of any response at particular location and time.
5. The auto and cross correlation functions also reveal the consistency of the THM response with time.

From the advanced modeling of in situ heating test, it can be concluded that

1. The Numerical analysis of the in situ heating test shows that the double structure model can effectively describe the mechanical behavior of the unsaturated soil.
2. The consideration of the two structural levels provides the opportunity to define the constitutive laws and properties of the two pore levels that exist in the bentonite clay material.

3. According to the model results, as the barrier hydration progresses, the macro pores are increased due to availability of the gaps, but, subsequently the macro pores are reduced during the operational stage. This is due mainly to microstructural swelling under confined conditions. As a consequence, the full saturation of the barrier is delayed and the barrier near heater does not get saturated soon.
4. As the time lapses, due to increase in temperature and formation of vapor, the liquid pressure decrease due to which there is compression of micro pores. This opens up the macro pores and thus making the barrier softer.
5. In summary, the model has contributed to a better understanding of the complex behavior observed in this large-scale heating test and has provided a physically based explanation for the very slow hydration of the barrier.

7.3 Scope of Future Work

1. The applicability of probabilistic calibration method is so efficient, that it can be extended further to various other THM properties, whose parameter values are generally decided by fitting the experimental observations, rather than conceptually derived.
2. The model uncertainty can be introduced in the calibration for better predictions. For instance, even after the parametric calibration, the intrinsic permeability is not well defined by kozeney's law. To eliminate such uncertainty, exponential law can be introduced.

3. The spatial-temporal statistical inferences from the numerical predictions can be used in computation of Functional Bayesian (FB) solution to inverse problem.
4. The posteriors obtained in the study can be used as the prior for future analysis in any other case studies.
5. In advanced mechanical modeling of the clay, the assumption of micro deformation to elastic can dissolute and extend to plastic micro deformations.
6. During modeling the barrier cross section, the gaps between the blocks are neglected which can be modeled using joint elements for better capture of hydraulic response. It can also be modeled in 2D to enhance the predictions and analyze the section no heater.
7. The double structure model can further be extended THG formulation to include the geochemical interaction of nuclear waste with the barrier.

REFERENCES

AECB (1985), "Deep Geological disposal of nuclear fuel waste: Background information and Regulatory requirement regarding the concept assessment phase." *Regulatory Document*, R-71.

Alonso, E.E., Gens, A., and Hight, D.W. (1987). "Special problem soils - General report." *Proc. 9th European Conf. on Soil Mechanics and Foundation Engineering*, Dublin, **3**, 1087-1146.

Alonso, E.E., Gens, A., and Josa, A. (1990). "A constitutive model for partially saturated soils." *Geotechnique*, **40**, 405-430.

Alonso, E.E. (1998). "Modelling expansive soil behaviour. Keynote lecture." *Proc. of II Int. Conf. on Unsaturated Soils*, UNSAT '98, Beijing, **2**, 37–70.

Alonso, E.E., Vaunat, J., and Gens, A. (1999). "Modelling the mechanical behaviour of expansive clays." *Engineering Geology*, **54**,173 – 183.

Alonso, E.E., Romero, E., Hoffmann, C., Garcı´a-Escudero, E. (2005). "Expansive bentonite–sand mixtures in cyclic controlled-suction drying and wetting." *Engineering Geology,* **81**, 213–226

Brooks, R.H., and Corey, A.T. (1966). "Properties of porous media affecting fluid flow", *J. of Irrigation and Drainage Divsion*, 61-87.

Casagrande, A. (1936). "The determination of the pre-consolidation load and its practical significance." *Proc. of the first Int. Conf. on Soil Mechanics and Foundation Engineering, Cambridge*, **3**, 60-64.

Corey, A.T., (1954). "The interrelation between gas and oil relative permeability". *Prod. Monthly*, **19**, No.1, 38–41.

Cui, Y.J., Delage, P., Sultan, N. (1995). "An elasto-plastic model for compacted soils." *Proc. of the 1st Int. Conf. on Unsaturated Soils*, *Paris*, **2**, 703–709

Cui, Y.J., Sultan, N., and Delage P. (2000). "A thermomechanical model for saturated clays." *Canadian Geotechnical J.*, **37**, No.3, 607–620.

Cui, Y.J., Loiseau, C., and Delage, P. (2001). "Water transfer through a heavily compacted swelling soil. " *6th Int. workshop on key issues in waste isolation Research (KIWIR)*, *Paris*, 43-60.

Cui, Y.J., Yahia-Aissa, M., and Delage, P. (2002). "A model for the volume change behaviour of heavily compacted swelling clays. " *Engineering Geology*, **64**, 233–250.

Cui, Y.J., Tang, A.M., and Loiseau, C. (2008). "Determining the unsaturated hydraulic conductivity of a compacted sand-bentonite under constant volume and free-swell conditions." *Physics and Chemistry of the Earth - A/B/C*, **33**, No.1, 462–471.

Daucausse, D., and Lloret, A., (2003). "*Results of in situ measurements of water content and dry density*." FEBEX report 70-UPC-L-5-012, Barcelona.

Delage, P. (2007). "Microstructure features in the behaviour of engineered barriers for nuclear waste disposal." *Proc. on Int. Conf. on Mechanics of Unsaturated Soils. Germany*, 11–32.

Delage, P., Cui, Y.J., and Tang, A.M. (2010). "Clays in radioactive waste disposal." *J. of Rock Mechanics and Geotechnical Engineering*, **2**, No.2, 111-123.

DOE (2008). "Data from the department of energy draft global nuclear energy partnership programmatic environmental impact statement" *DOE/EIS-0396*, Tables 4.8-5 and 4.8-6, 4-138 and 4-139.

ENRESA, (2000). "*Full-scale Engineered Barriers EXperiment for a deep geological repository for high level radioactive waste in crystalline host rock.*" Final Report. Publicación Técnica, ENRESA 1/2000: 354.

ENRESA, (2006). "*Full-scale Engineered Barriers EXperiment, Updated Final Report 1994–2004*." Publicación Técnica, ENRESA 05/2006: 590.

Fredlund, D.G., and Xing, A. (1994). "Equations for the soil-water characteristic curve." *Canadian Geotechnical J.*, **31**, 521-532.

Frieg, B., and Vomvoris, S. (1994). "*Investigation of hydraulic parameters in the saturated and unsaturated zone of the ventilation drift.*" Technical Report 93-10, Baden, Nagra.

Gardner, W. (1958). "Some steady-state solutions of the unsaturated moisture flow equation with application to evaporation from a water table." *Soil Science*, **85**, 228–232.

Gens, A., and Alonso, E.E. (1992). "A framework for the behaviour of unsaturated expansive clays. " *Canadian Geotechnical J.*, **29**, 1013–1032.

Gens, A. (1995). "*Constitutive laws. Modern Issues in Non-saturated Soils*." Springer: Berlin, 129–158.

Gens, A., Garcia-Molina, A.J., Olivella, S., Alonso, E.E., and Huertas, F. (1998). "Analysis of a full scale in situ test simulating repository conditions." *Int. J. Numerical and Analytical Methods in Geomechanics*, **22**, No.7, 515–548.

Gens, A., Sanchez, M., Guimaraes, L., Alonso, E.E., Lloret, A., Olivella, S., Villar, M.Y., and Huertas, F. (2009). "A full scale in situ heating test for high level nuclear waste disposal - Observations, analysis and interpretation. " *Géotechnique*, **59**, No. 4, 377–399.

Gilks, W.R., Richardson, S., and Spiegelhalter, D.J., (1996). "Introducing Markov chain Monte Carlo." *Markov Chain Monte Carlo in Practice*, 1-19, Chapman and Hall.

Harrison., T. (2000). "*Vertical deep borehole: Deutag's opinion on boring, canister emplacement and retrievability.*" SKB Report R-00-35, Swedish Nuclear Fuel and Waste Management Co., Stockholm.

Hassanizadeh, S.M., and Gray, W.G. (1993). "Thermodynamic basis of capillary pressure in porous media." *Water Resource Research*, **29**, 3389-3405

Helton, C.J. (1993). "Uncertainty and sensitivity analysis techniques for use in performance assessment for radioactive waste disposal." *Reliability Engineering and System Safety,* **42**, Nos.2-3, 327-367.

Josa, A., Balmaceda, A., Gens, A., Alonso, E.E. (1992). "An elastoplastic model for partially saturated soils exhibiting a maximum of collapse." *Proc. of the 3rd International Conf. on Computational Plasticity*, *Barcelona*, **1**, 815–826.

Keusen, H.R., Ganguin, J., Schuler, P., and Buletti, M. (1989). "*Grimsel test site. Geology.*" Technical Report 87-14E, Switzerland.

Kline, S.J. (1985). "The purpose of uncertainty analysis" *J. of Fluid Engineering*, **107**, 153-160.

Kohgo, Y., Nakano, M., and Mayazaki, T. (1993). "Theoretical aspects of constitutive modelling of unsaturated soils." *Soils and Foundations*, **33**, No.4, 49-63.

Kueper, B.H., and McWhorter, D.B. (1992). "The use of macroscopic percolation theory to construct large-scale capillary pressure curves." *Water Resource Research,* **28**, No.9, 2425–2436

Lloret, A., Villar, M.V., Sanchez, M., Gens, A., Pintado, X., and Alonso, E.E. (2003). "Mechanical behaviour of heavily compacted bentonite under high suction changes." *Geotechnique*, **53**, No.1, 27–40.

Lubliner, J. (1991). "A simple model of generalized plasticity." *Int. J. of Solids and Structures*, **28**, No. 6,769–778.

Martinez, W.L., and Martinez, A.R. (2001). "Computational statistics handbook with MATLAB." Chapman & Hall/CRC, Boca Raton.

Medina-Cetina, Z., (2006). "*Probabilistic calibration of soil model.*" Ph.D. Dissertation, Johns Hopkins University.

Metropolis, N., Rosenbluth, A.W., Rosenbluth, M.N., Teller, A.H., and Teller, E. (1953). "Equations of state calculations by fast computing machine." *J. of Chemistry and Physics*, **21**, 1087-1091.

Moffat, R.J. (1988). "Describing the uncertainties in experimental results." *Experimental Thermal and Fluid Science*, **1**, 3-7

NRC (2010) "Data from report by Nuclear Regulatory Commission 2010: 78 adjusted to January 2011."

Olivella, S., Gens, A., Carrera, J., and Alonso, E.E. (1994). "Nonisothermal multiphase flow of brine and gas through saline media. " *Transport in Porous Media*, **15**, 271–293.

Olivella, S., Gens, A., Carrera, J., and Alonso, E.E. (1996). "Numerical formulation for a simulator (CODE-BRIGHT) for the coupled analysis of saline media." *Engineering Computations*, **13**, No.7, 87–112.

Pusch, R. (1980). "*Swelling pressure of highly compacted bentonite.*" Technical Report, SKBF KBF 90-13.

Pusch, R. (1982). "Mineral water-interaction and their influence on the physcial behavior of highly compacted Na bentonite." *Canadian Geotechnical J.*, **19**, 381–387.

Romero, E. (1999). "*Characterisation and thermal-hydro-mechanical behaviour of unsaturated Boom clay: an experimental study*" Ph.D. Dissertation, Technical University of Catalonia.

Roscoe, K.H., Schofiled, A.N., and Thurairajah, A. (1963)."Yielding of clays in states wetter than critical. " *Geotéchnique*, **13**, 211–240.

Roscoe, K.H., and Burland, J.B. (1968). "On the generalized stress–strain behavior of wet clay.", In *Engineering Plasticity*, (Eds. Heyman, J., Leckie, F.A.), Cambridge University Press, 535-609.

Russo, D. (1988). "Determining soil hydraulic properties by parameter estimation: On the selection of a model for the hydraulic properties." *Water Resource Research*, **28**, 1911-1925.

Sanchez, M. (2004). "*Thermo-hydro-mechanical coupled analyses in low permeability media.*" Ph.D. Dissertation, Universitat Politecnica de Catalunya.

Sanchez, M., Gens, A., Guimaraes, L., and Olivella, S. (2005). "A double structure generalized plasticity model for expansive materials." *Int. J. Numerical and Analytical Methods in Geomechanics*, **29**, 751–787.

Sanchez, M., and Gens, A. (2006). "*FEBEX project: Final report on thermo-hydro-mechanical modelling.*" Technical Publication, ENRESA, 05-2/2006.

Sanchez, M., Gens, A., Guimaraes, L., and Olivella, S. (2008). "Implementation algorithm of a generalised plasticity model for swelling clays." *Computers and Geotechnics,* **35**, 860–871.

Sanchez, M., Gens, A., and Olivella, S. (2011). "THM analysis of a large scale heating test incorporating material fabric changes." *Int. J. of Numerical and Analytical methods in Geomechanics*, http://dx.doi.org/10.1002/nag.1011.

Thomas, F., Anne, C., Hanspeter, W., Lawrence, J., Olivier, L. (2008). "The swiss concept for the disposal of spent fuel and vitrified HLW." *Int. Conf. Underground Disposal Unit Design & Emplacement Processes for a Deep Geological Repository*, *Prague*.

Tiktinsky, D.H. (1988). "Numerical Parametric sensitivity study of thermal and mechanical properties for a high level nuclear waste repository." *29th US Symp. of Rock Mechanics (USRMS)*.

Tsang, C.F., Stephansson, O., and Hudson, J.A. (2000). "A discussion of thermo-hydro-mechanical (THM) processes associated with nuclear waste repositoris." *Int. J. of Rock Mechancis and Mining Science*, **37**, 397-402.

UPC (2004). "CODE_BRIGHT - User Manual." *Geo-mechanical Group*.

Van Genuchten, M.T. (1980). "A closed-form equation for predicting the hydraulic conductivity of unsaturated soils." *Soil Science Society of America J.*, **44**, 892-898.

Villar, M.V. (2002). "*Thermo-hydro-mechanical characterisation of a bentonite from Cabo de Gata: A study applied to the use of bentonite as sealing material in high-level radioactive waste repositories.* " Technical Publication, ENRESA, 01/2002.

Villar, M.V., Martín, P.L., Barcala, J.M., (2005). "Modification of physical, mechanical and hydraulic properties of bentonite by thermo-hydraulic gradients." *Engineering Geology*, **81**, 284–297.

Villar, M.V., and Lloret, A. (2007). "Dismantling of the first section of the FEBEX in situ test: THM laboratory tests on the bentonite blocks retrieved." *Physics and Chemistry of the Earth*, **32**, 716–729.

Villar, M., Sánchez, M., and Gens, A. (2008). "Behaviour of a bentonite barrier in the laboratory: Experimental results up to 8 years and numerical simulation." *Physics and Chemistry of the Earth A/B/C*, **33**, S476-S485.

Wheeler, S.J., Sivakumar, V. (1995). "An elasto-plastic critical state framework for unsaturated soil." *Géotechnique*, **45**, No. 1, 35-53.

Wheeler, S.J., Naatanen, A., Karstunen, M., Lojander, M. (2003). "An anisotropic elastoplastic model for soft clays." *Canadian Geotechnical J.*, **40**, 403-418.

Young, R.N., (1999). "Overview of modeling of clay microstructure and interactions for prediction of waste isolation barrier performance." *Engineering Geology*, **54**, 83 – 91.

Zimmerman, D.A., Wahl, K.K., Gutjahr, A.L,. and Davis, P.A. (1990). "*A review of techniques for propagating data and parameter uncertainties in high-level radioactive waste repository performance assessment models.*" Technical Publication, NUREG/CR-5393, SAND89-1432.

APPENDIX A

Case 1: Variation of thermal properties i.e. λ_{dry} and λ_{sat}

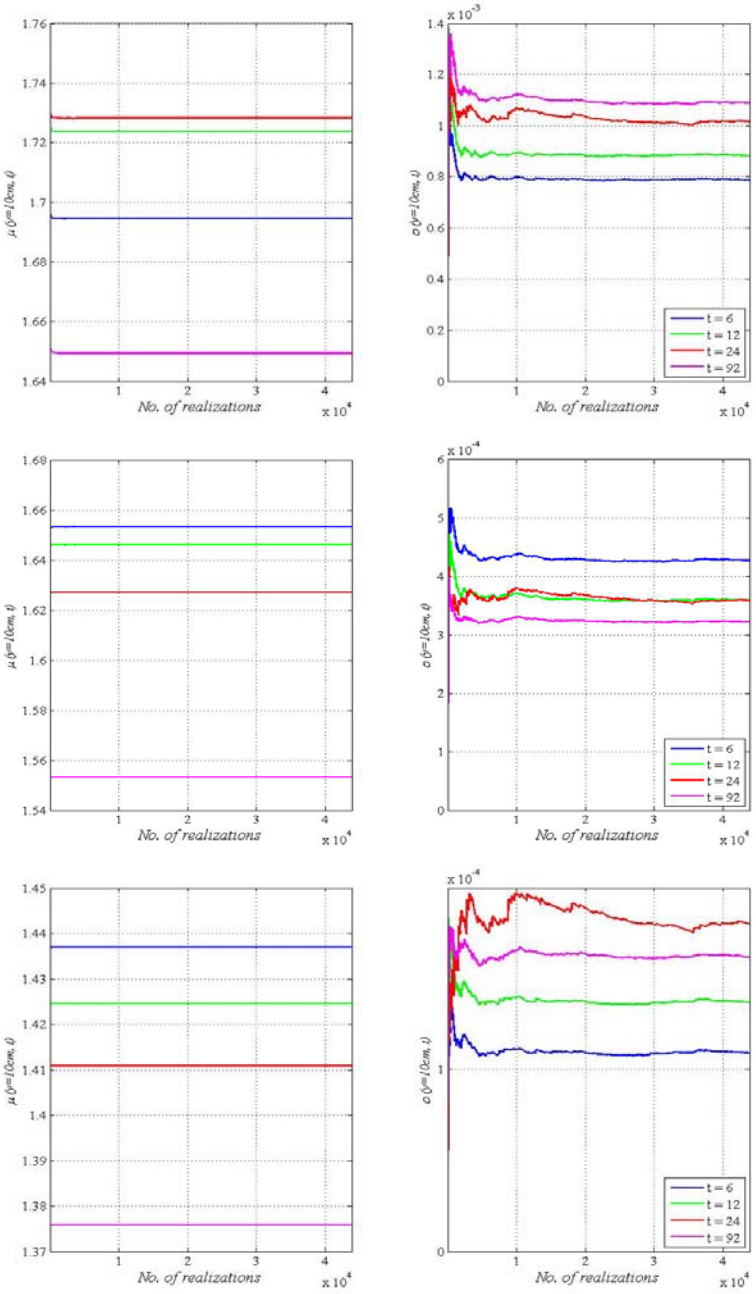

Figure A-1. Cumulative mean and standard deviation of Dry Density at A, B, C (10 cm, 30cm and 50 cm from heater).

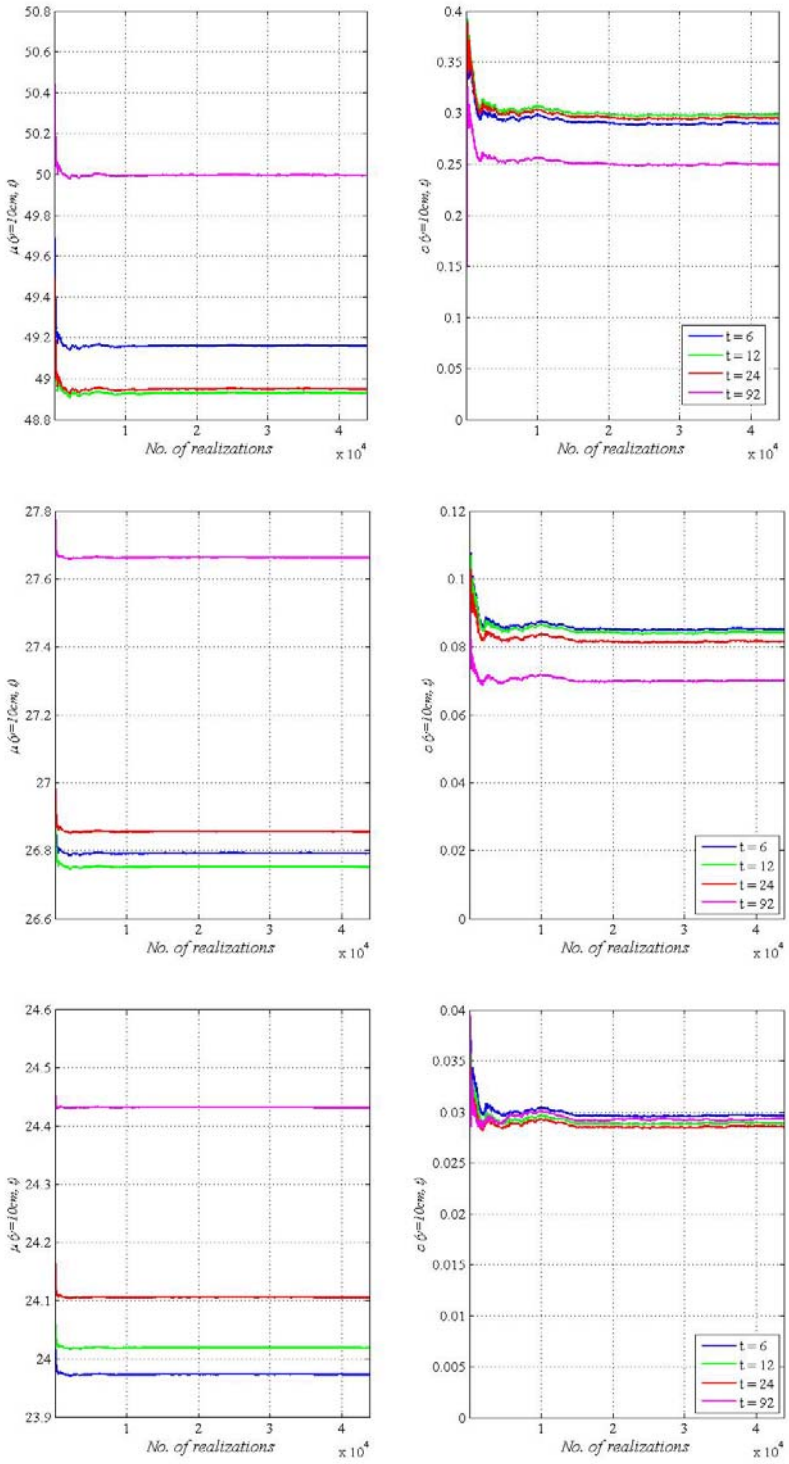

Figure A-2. Cumulative mean and standard deviation of Temperature at A, B, C.

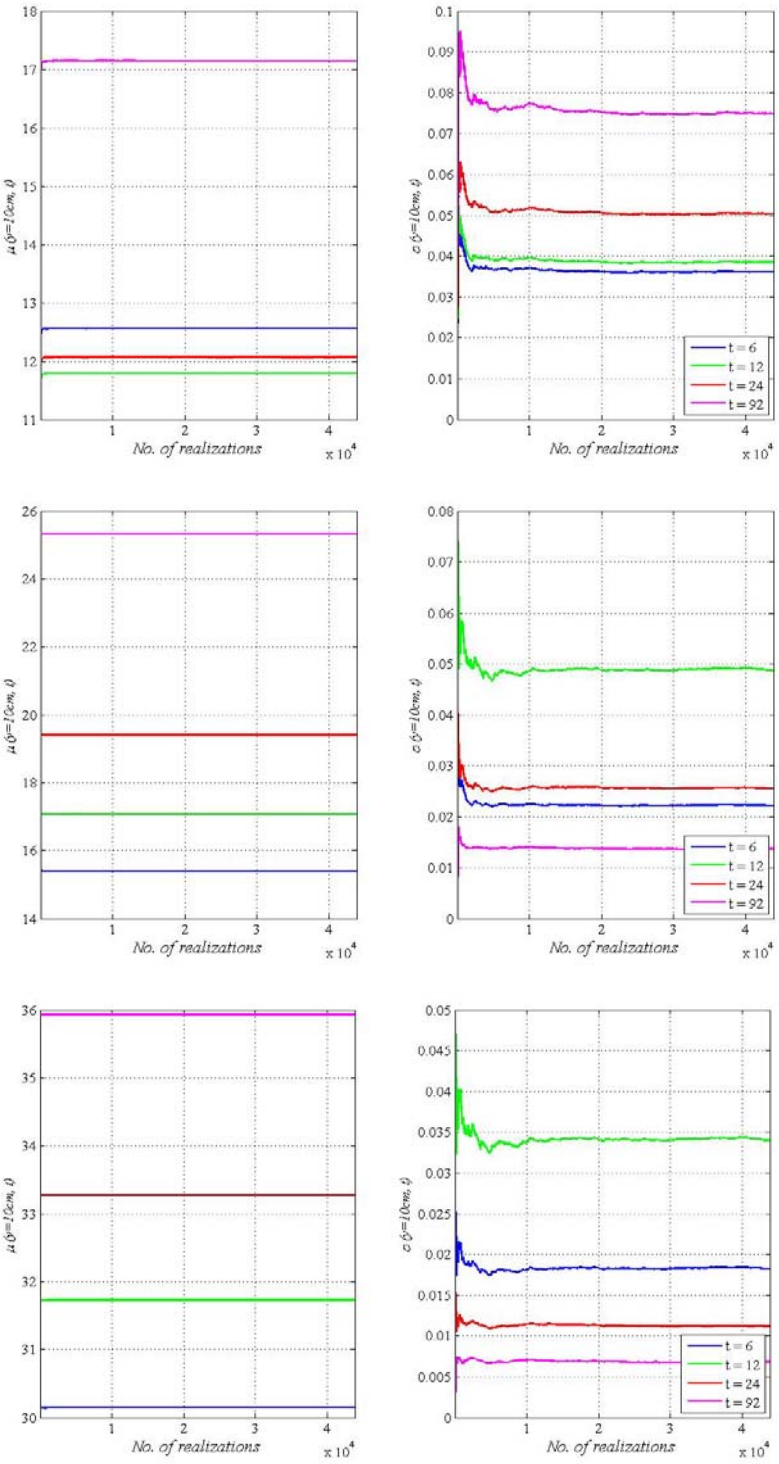

Figure A-3. Cumulative mean and standard deviation of Water Content at A, B, C.

Case 2: Variation of retention parameters of hydral properties i.e. P_0, λ_0 and λ_d

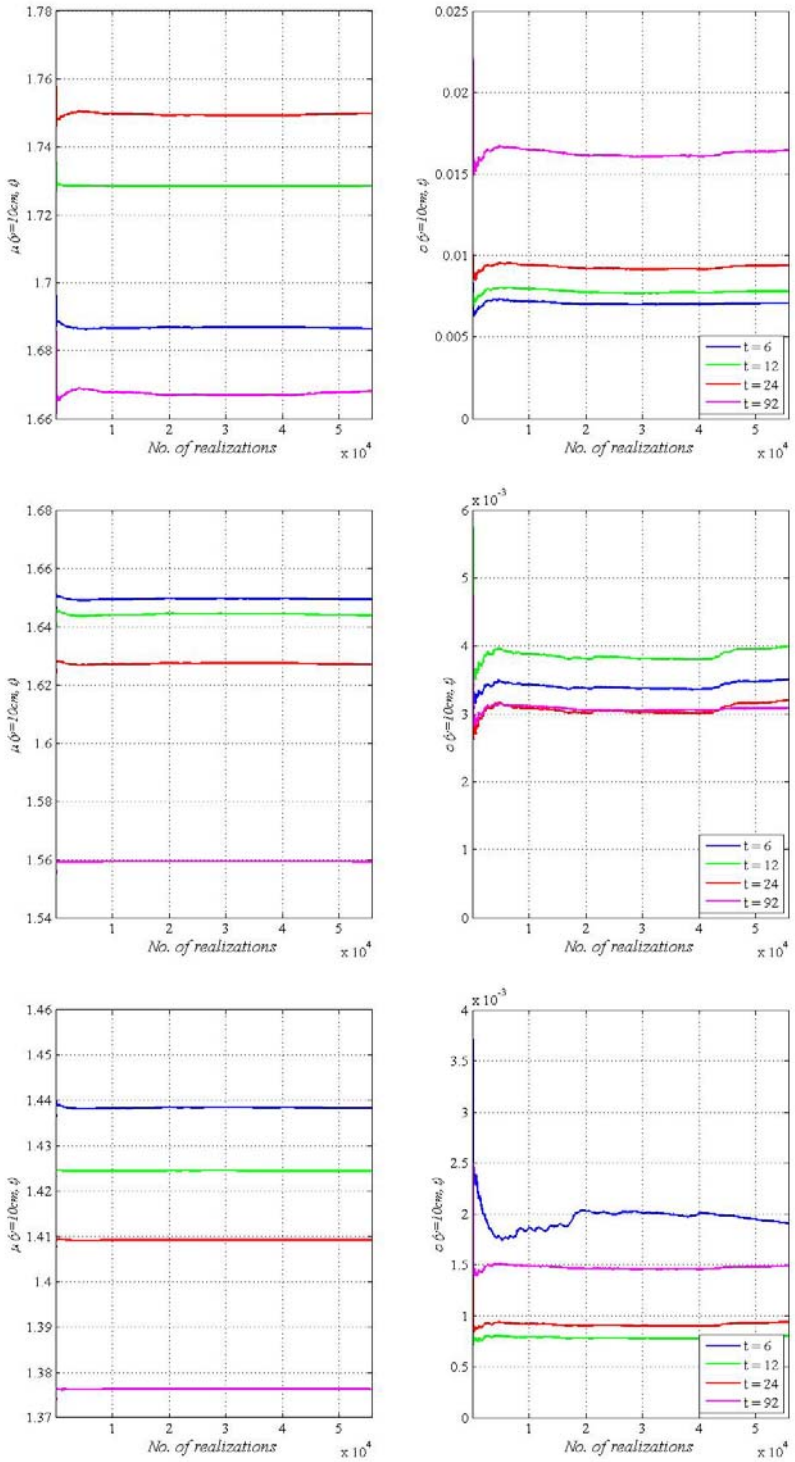

Figure A-4. Cumulative mean and standard deviation of Dry Density at A, B, C.

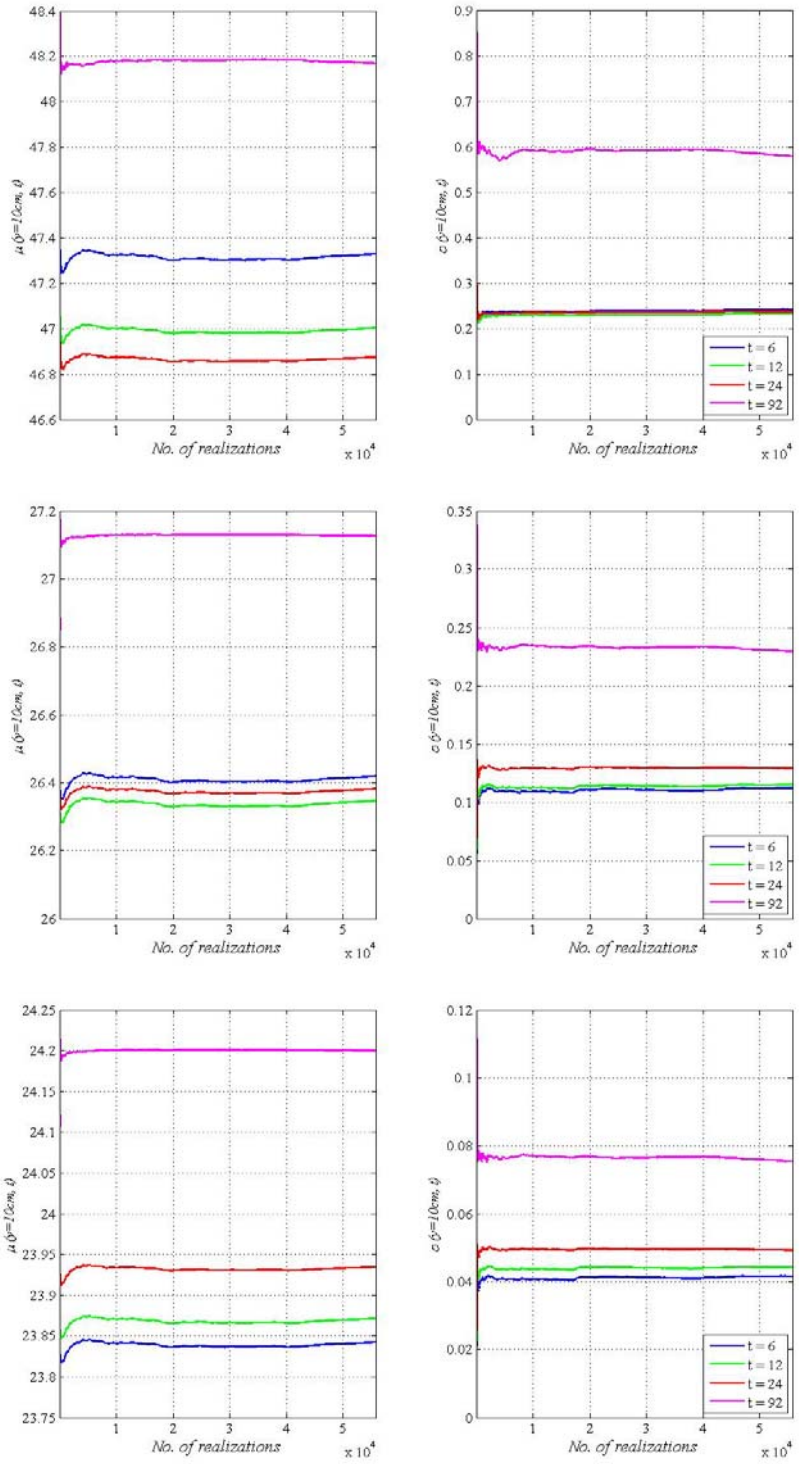

Figure A-5. Cumulative mean and standard deviation of Temperature at A, B, C.

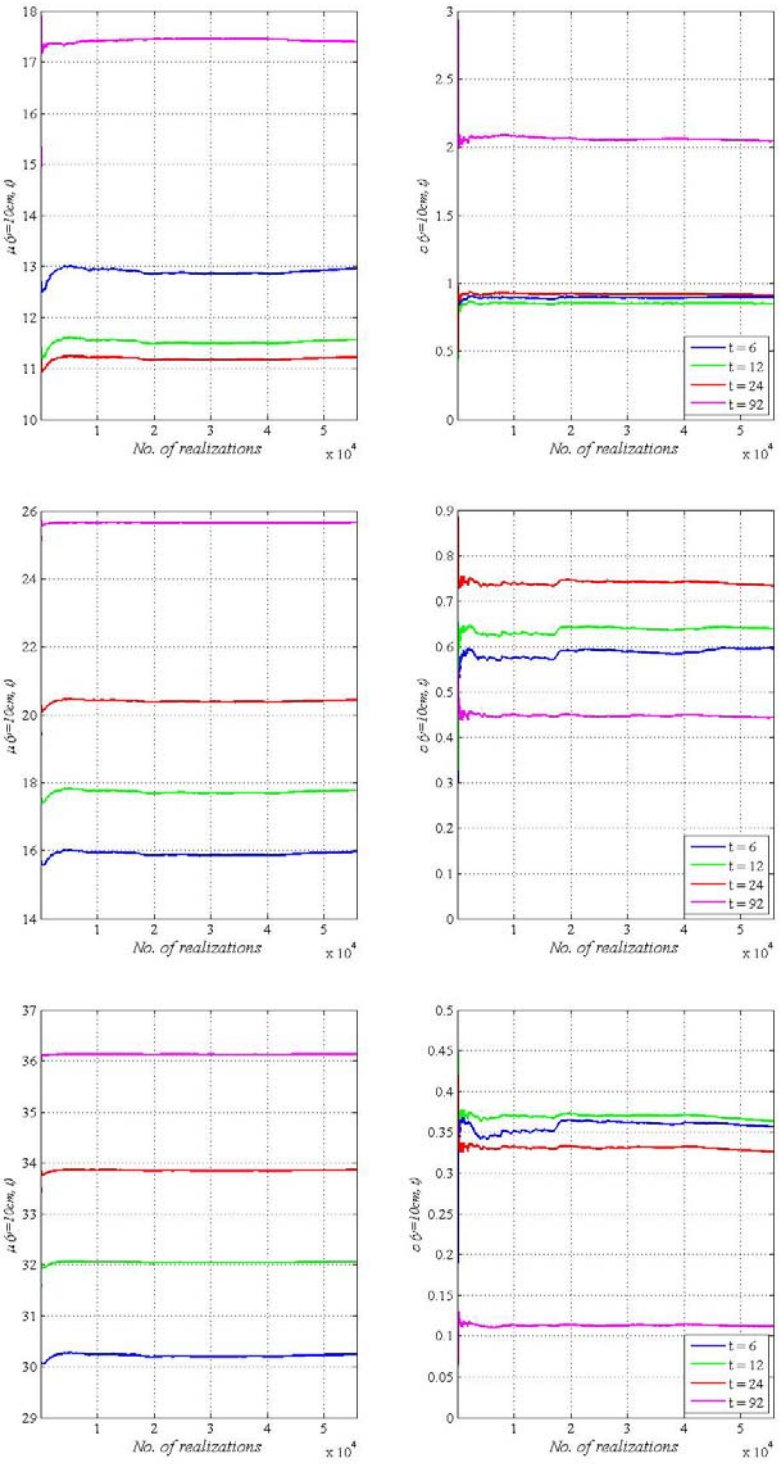

Figure A-6. Cumulative mean and standard deviation of Water Content at A, B, C.

Case 3: Variation of permeability parameters of hydral properties i.e. k_0

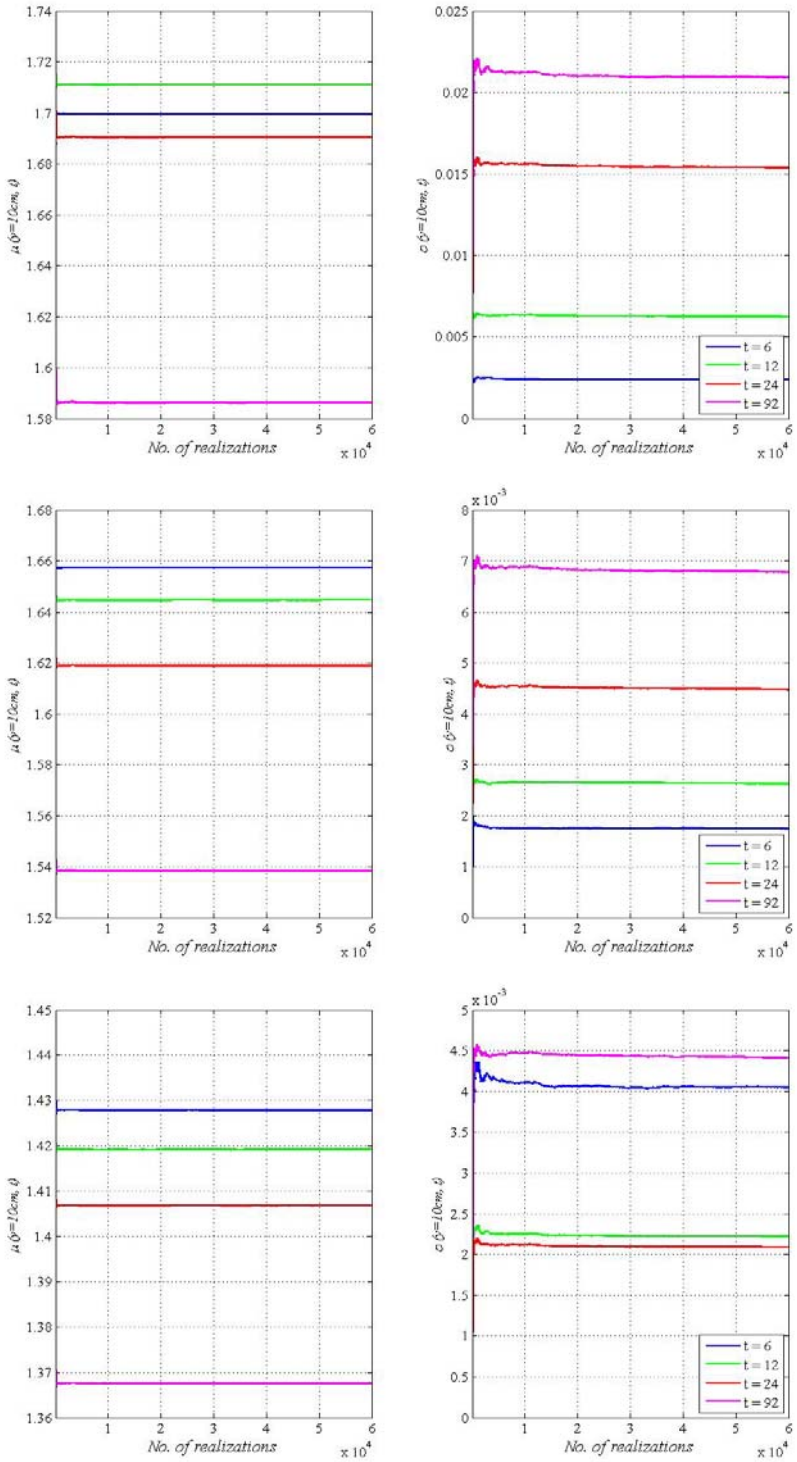

Figure A-7. Cumulative mean and standard deviation of Dry Density at A, B, C.

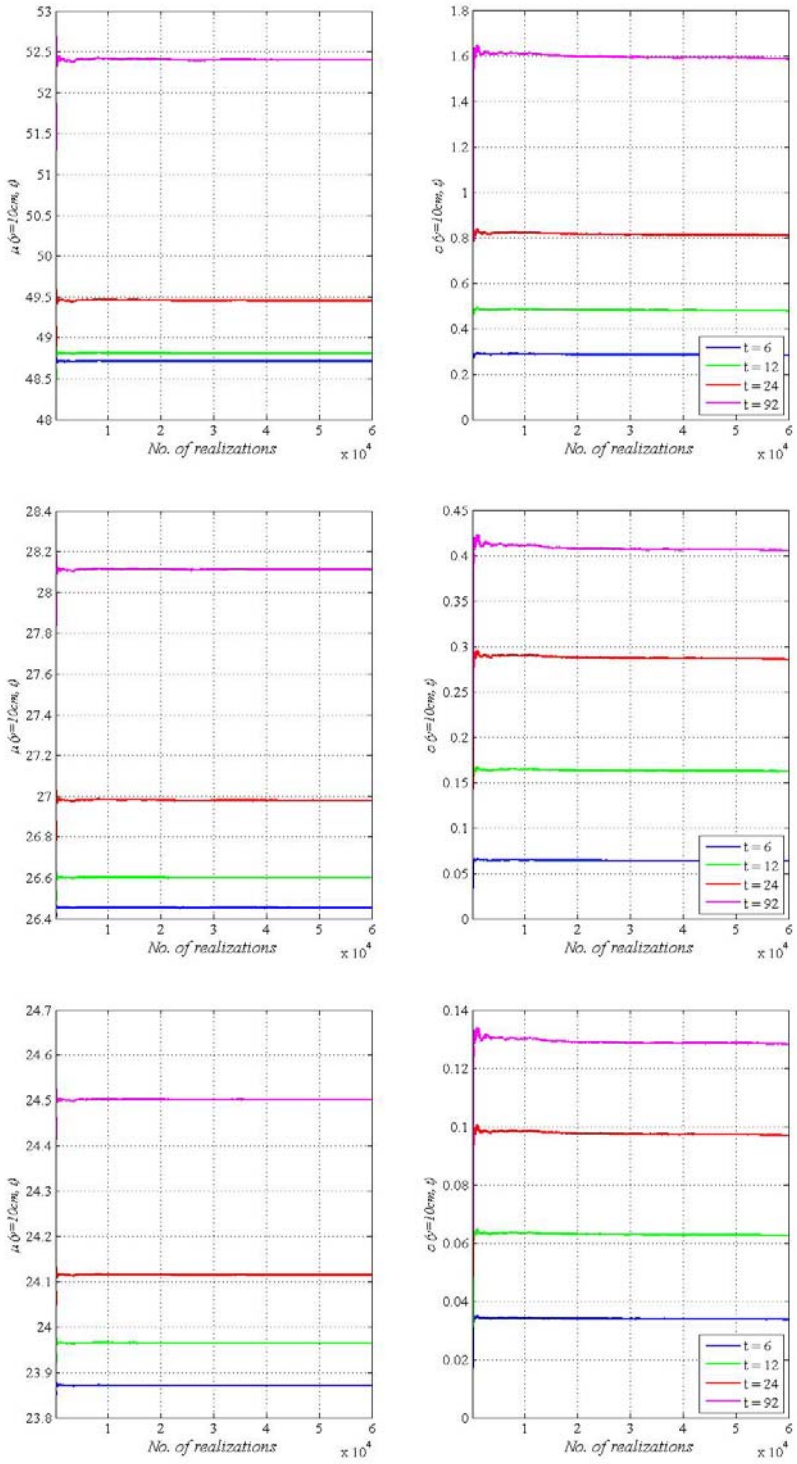

Figure A-8. Cumulative mean and standard deviation of Temperature at A, B, C.

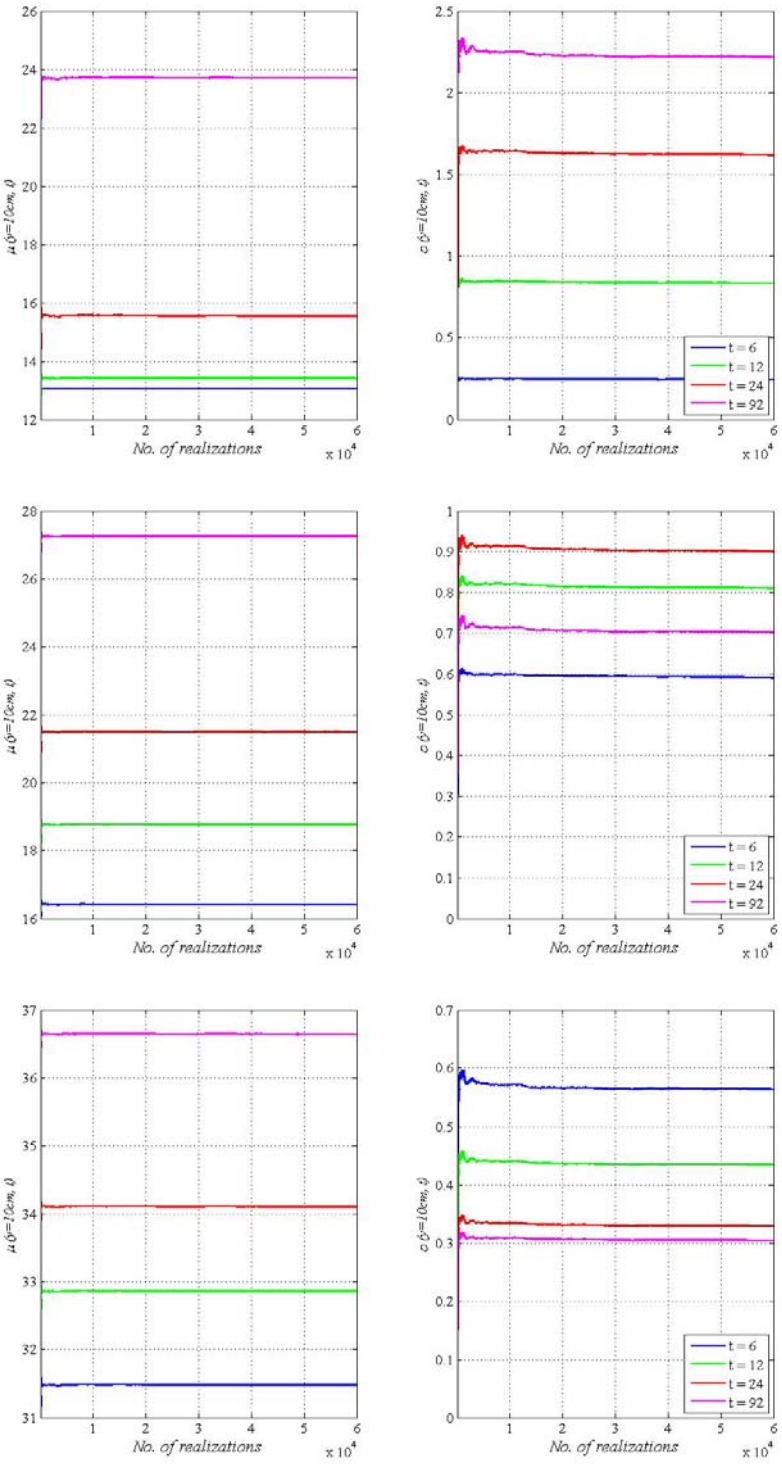

Figure A-9. Cumulative mean and standard deviation of Water Content at A, B, C.

Case 4: Variation of both of hydral properties i.e. P_0, λ_0, λ_d and k_0

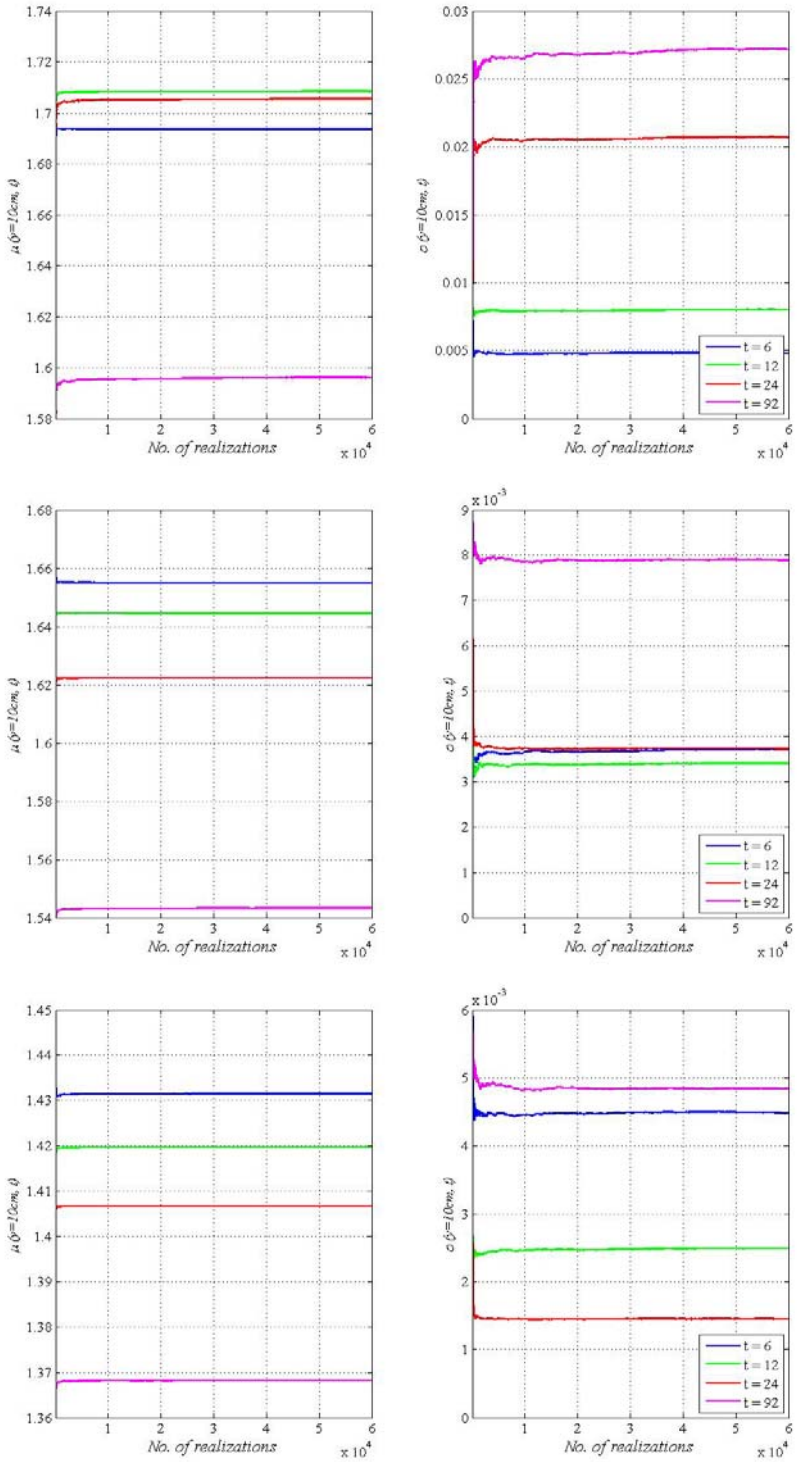

Figure A-10. Cumulative mean and standard deviation of Dry Density at A, B, C.

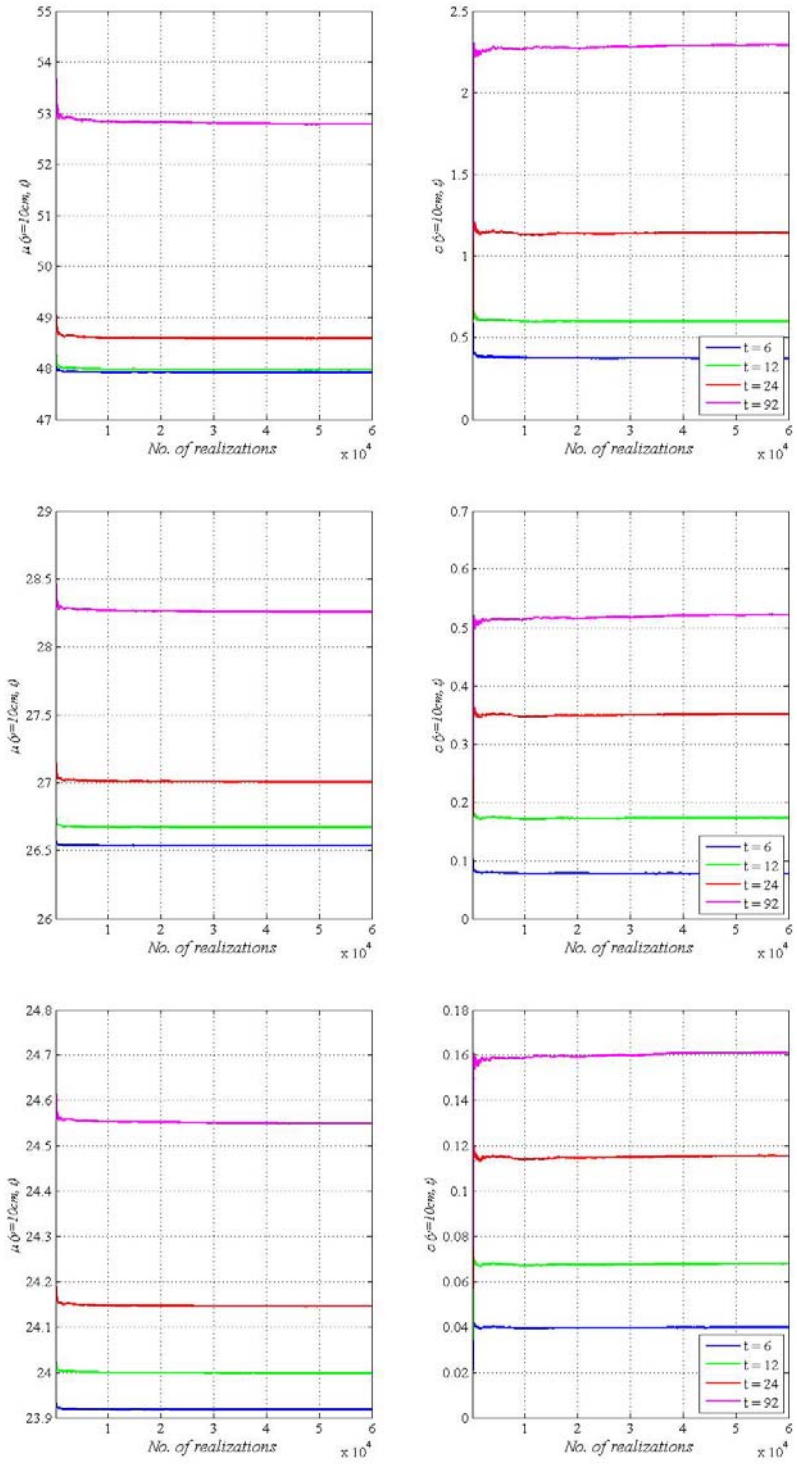

Figure A-11. Cumulative mean and standard deviation of Temperature at A, B, C.

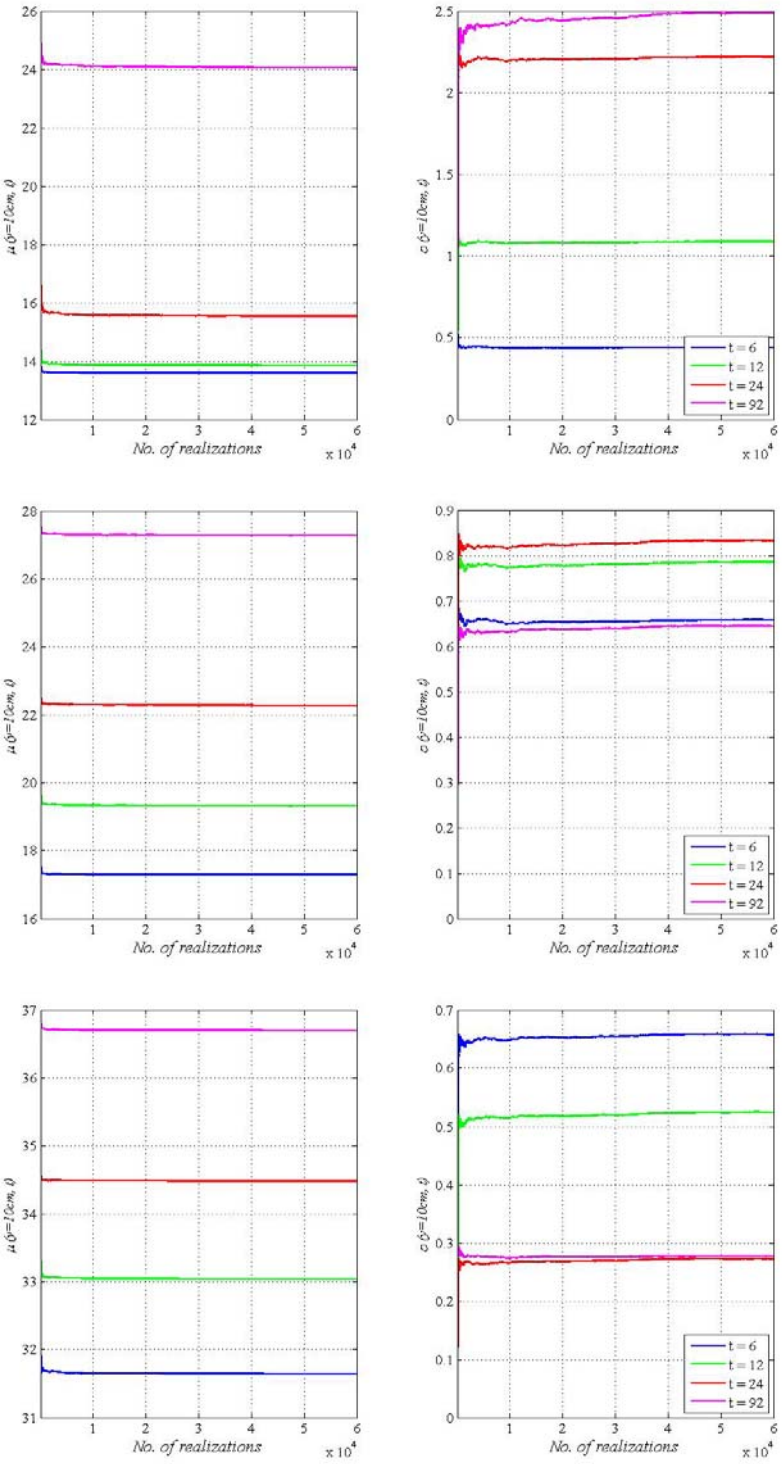

Figure A-12. Cumulative mean and standard deviation of Water content at A, B, C.

Case 5: Variation of both of thermal and hydral properties i.e. λ_{dry}, λ_{sat}, P_0, λ_0, λ_d and k_0

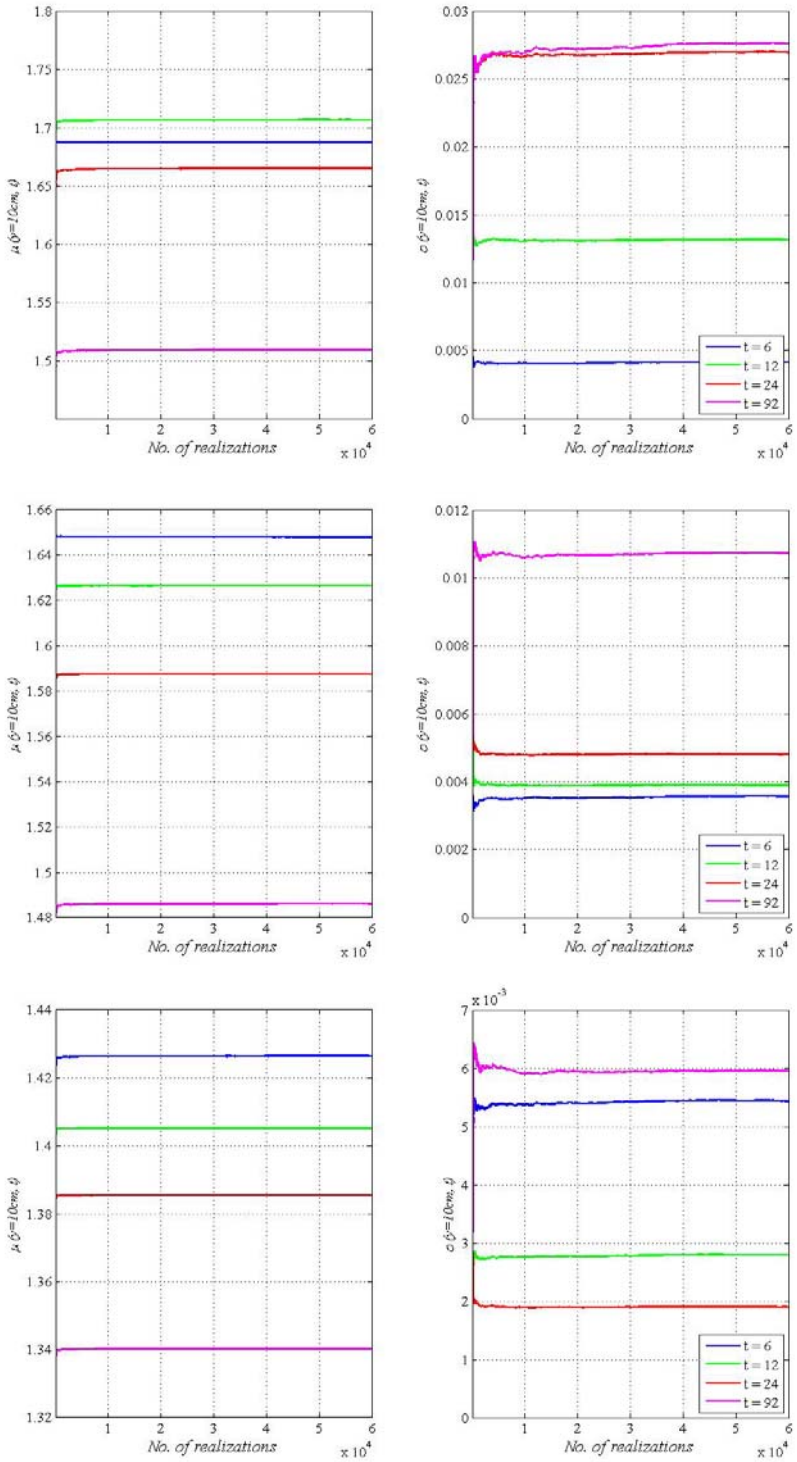

Figure A-13. Cumulative mean and standard deviation of Dry Density at A, B, C.

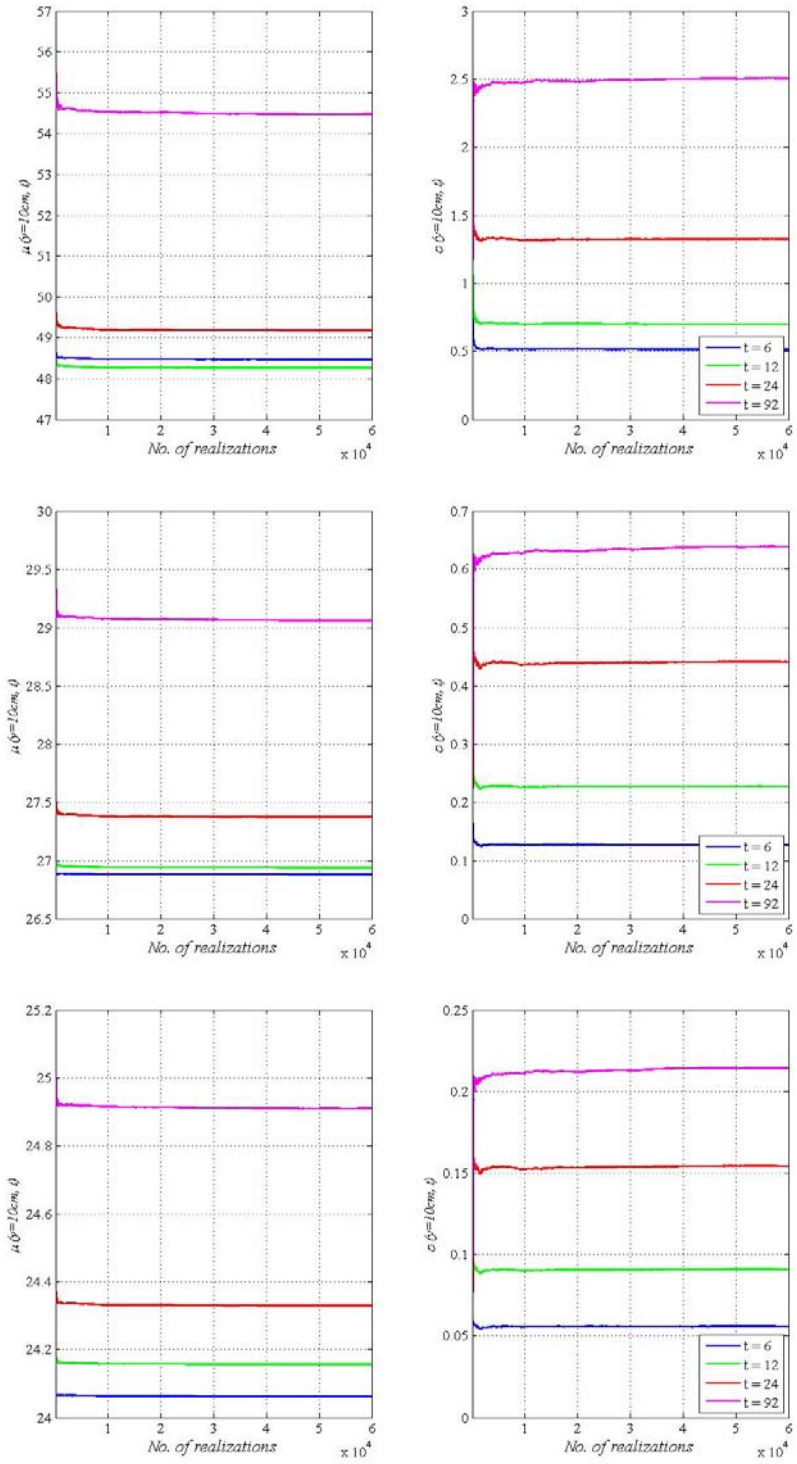

Figure A-14. Cumulative mean and standard deviation of Temperature at A, B, C.

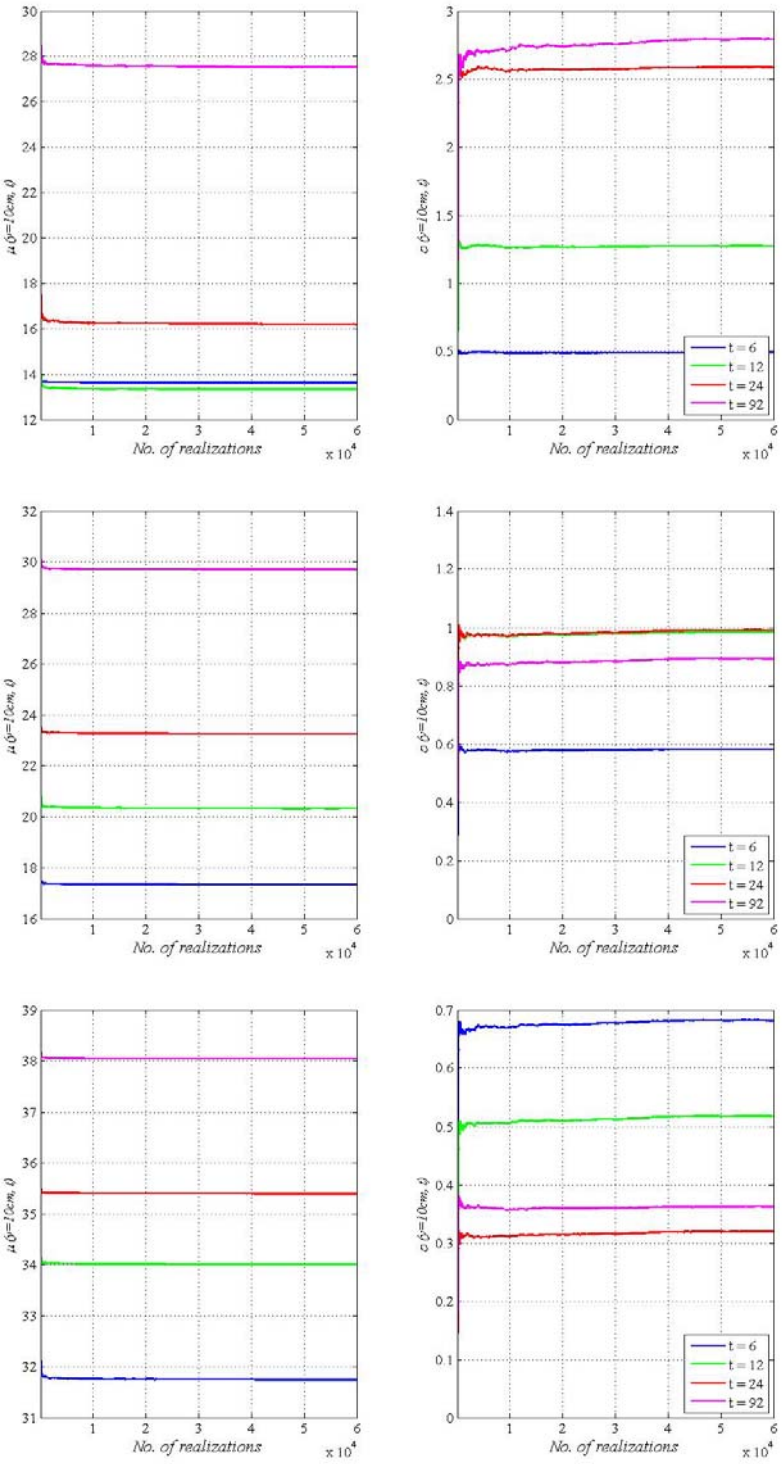

Figure A-15. Cumulative mean and standard deviation of Water Content at A, B, C.

APPENDIX B

Elastic Model used in the Double Structure

For a general case, the elastic stress is given by a matric (UPC, 2004) as:

$$D_e = \begin{bmatrix} K+\frac{4}{3}G_t & K-\frac{2}{3}G_t & K-\frac{2}{3}G_t & 0 & 0 & 0 \\ & K+\frac{4}{3}G_t & K-\frac{2}{3}G_t & 0 & 0 & 0 \\ & & K+\frac{4}{3}G_t & 0 & 0 & 0 \\ & & & G_t & 0 & 0 \\ & & & & G_t & 0 \\ & & & & & G_t \end{bmatrix} \quad \text{(B1)}$$

where, K is global bulk modulus, G_t is shear modulus. In the double structure of the material, the K is computed from the elastic modulus of both the pore structures as:

$$\frac{1}{K} = \frac{1}{K_m} + \frac{1}{K_M} \quad \text{(B2)}$$

where, microstructural bulk modulus, K_m is given from Eq.5.24. and macrostructural bulk modulus, K_M is given as:

$$K_M = \frac{(1+e_M)}{\kappa} p \quad \text{(B3)}$$

The macrostructural bulk modulus for changes in suction is given by:

$$K_s = \frac{(1+e_M)}{\kappa_s}(s+p_{atm}) \quad \text{(B4)}$$

Similarly, the macrostructural bulk modulus for changes in suction is given by:

$$K_T = \frac{1}{(\alpha_0+\alpha_2\Delta T)} \quad \text{(B5)}$$

APPENDIX C

The observations from the consolidation of the samples through oedometer tests are used to calculate the preconsolidation pressure of the sample. For this purpose, the most common Casagrande's method (Casagrande, 1936) method is used. Following are the figures showing the compression curves.

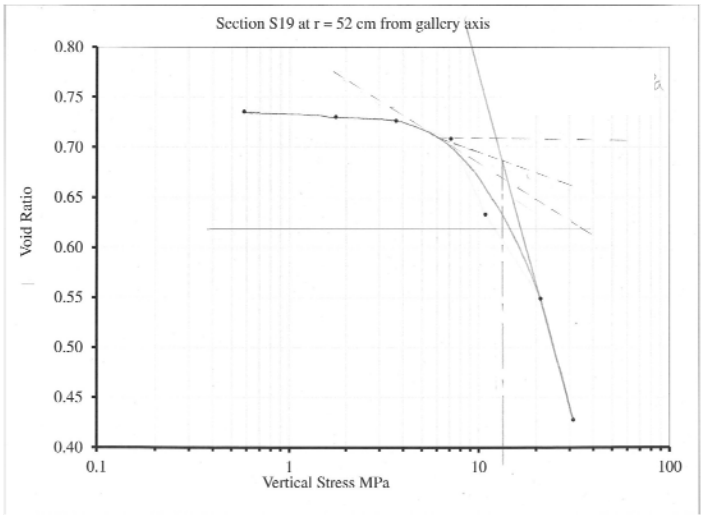

Figure C.1 Calculation of P_0 for sample collected at r=52cm at section S19.

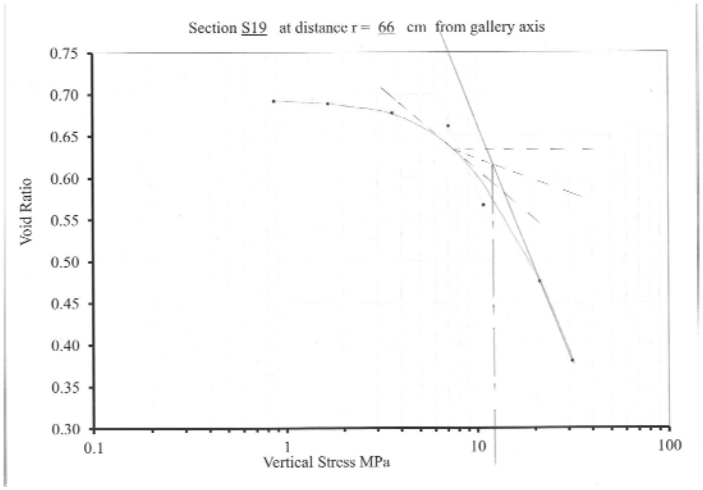

Figure C.2 Calculation of P_0 for sample collected at r=66 cm at section S19.

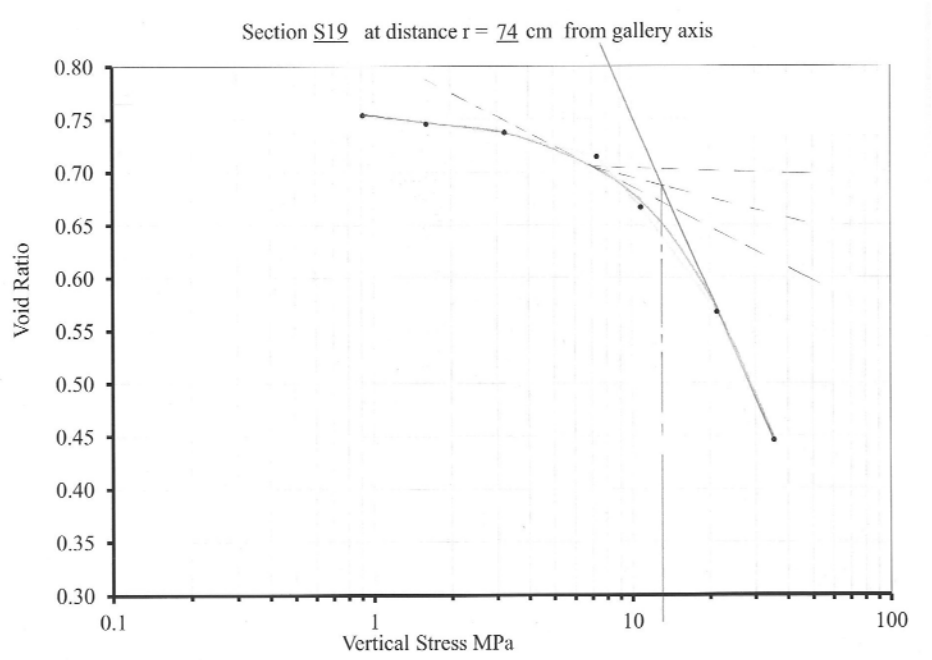

Figure C.3. Calculation of P_0 for sample collected at r=74cm at section S19.

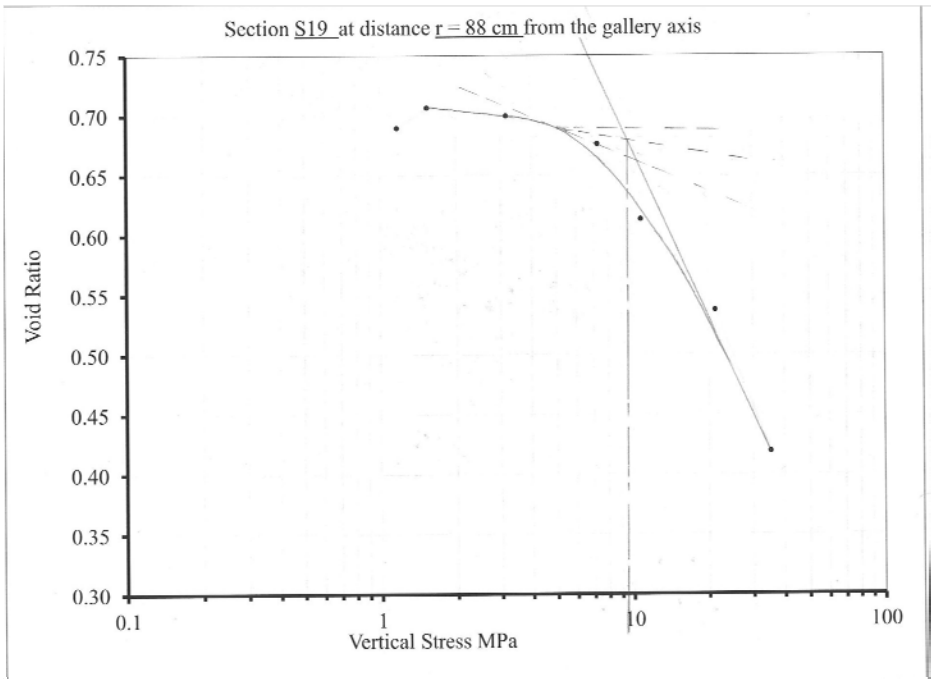

Figure C.4. Calculation of P_0 for sample collected at r=88 cm at section S19.

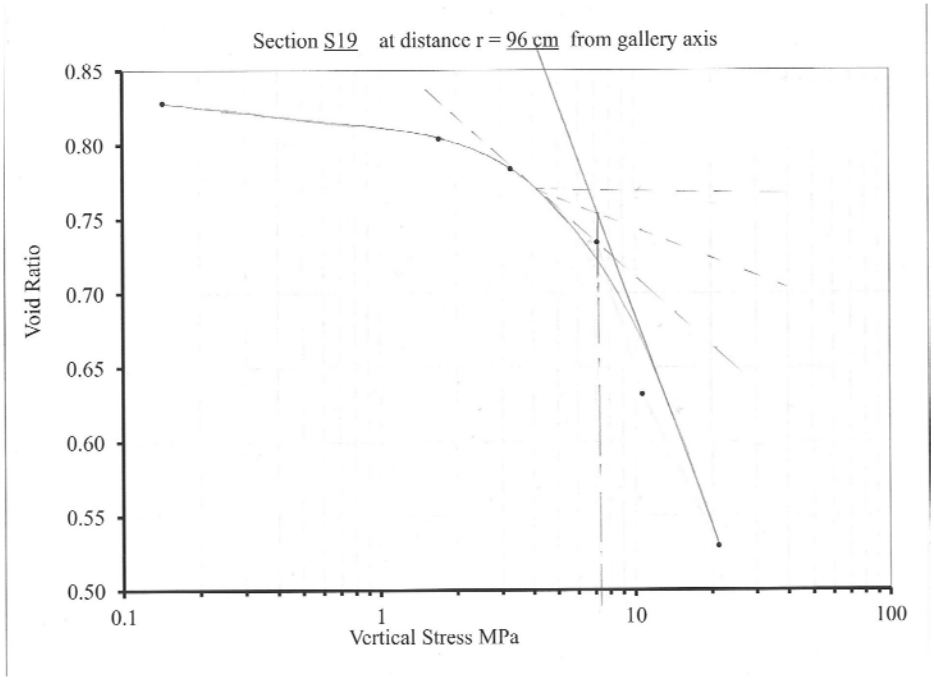

Figure C.5. Calculation of P_0 for sample collected at r=96 cm at section S19.

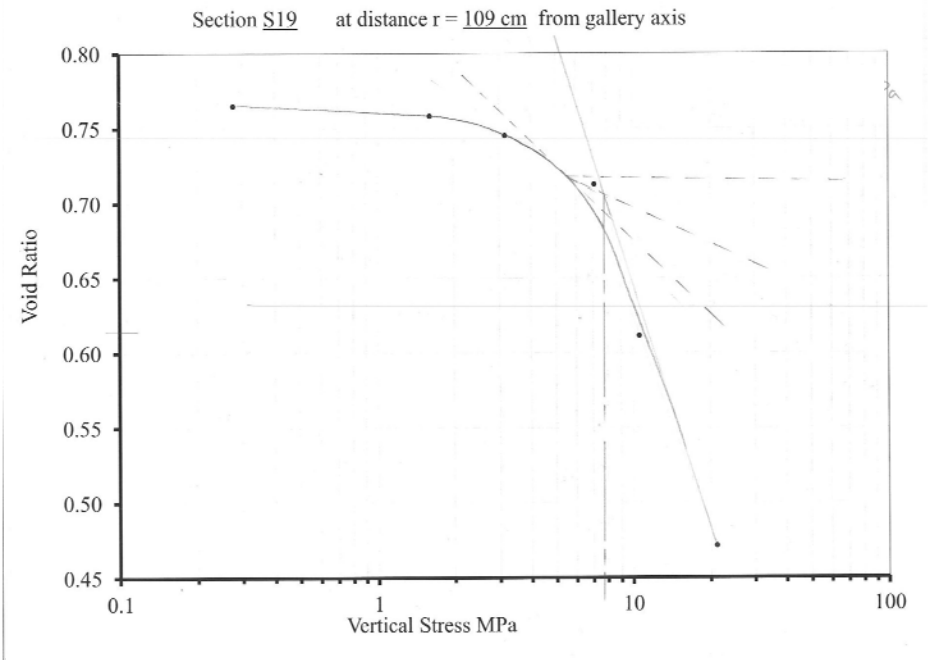

Figure C. 6. Calculation of P_0 for sample collected at r=109 cm at section S19.

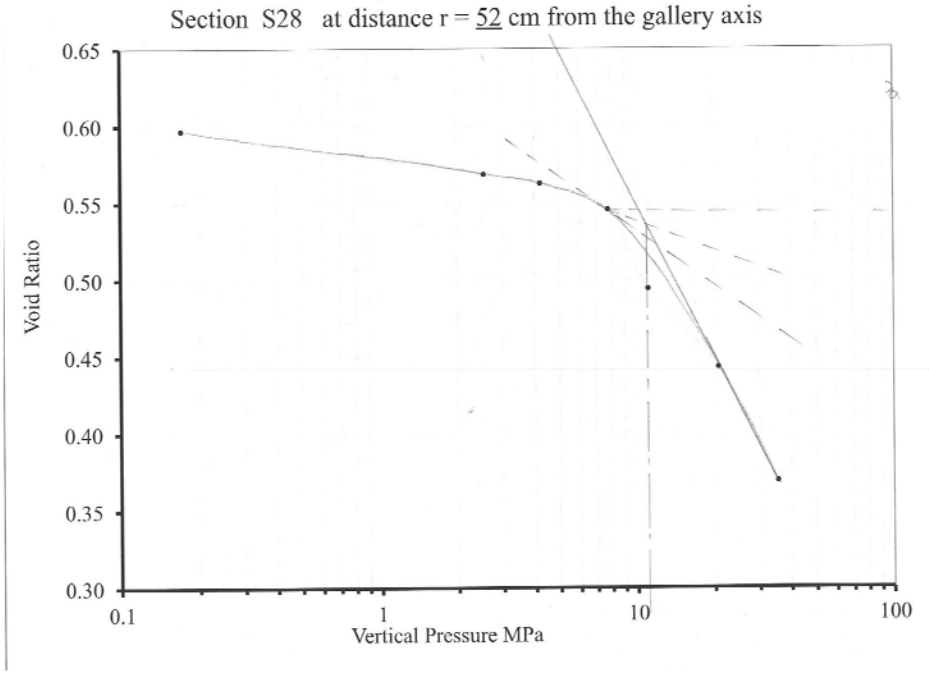

Figure C.7 Calculation of P_0 for sample collected at r=52cm at section S28.

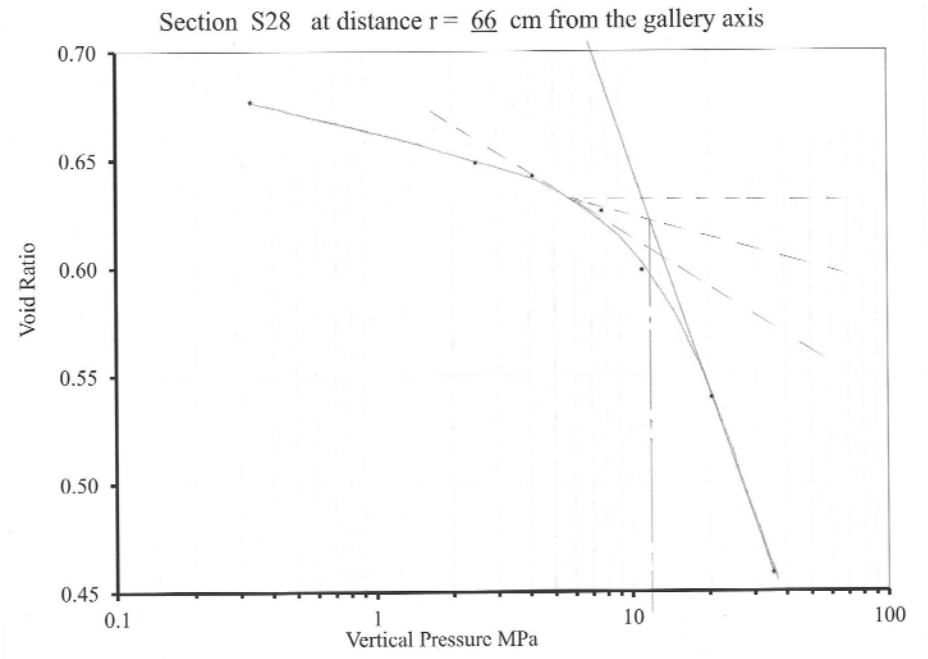

Figure C.8. Calculation of P_0 for sample collected at r=66 cm at section S28.

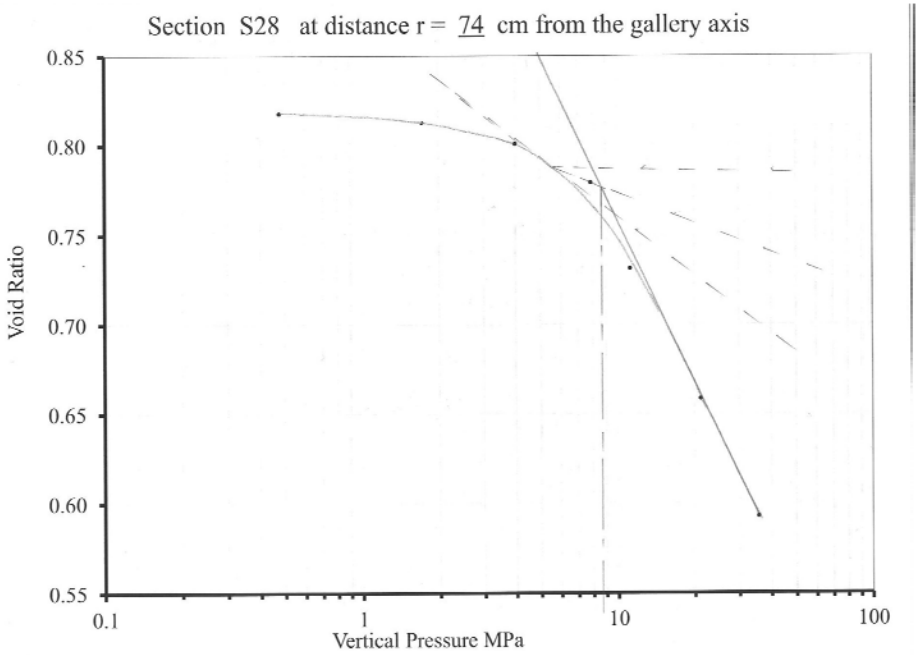

Figure C.9. Calculation of P_0 for sample collected at r=74 cm at section S28.

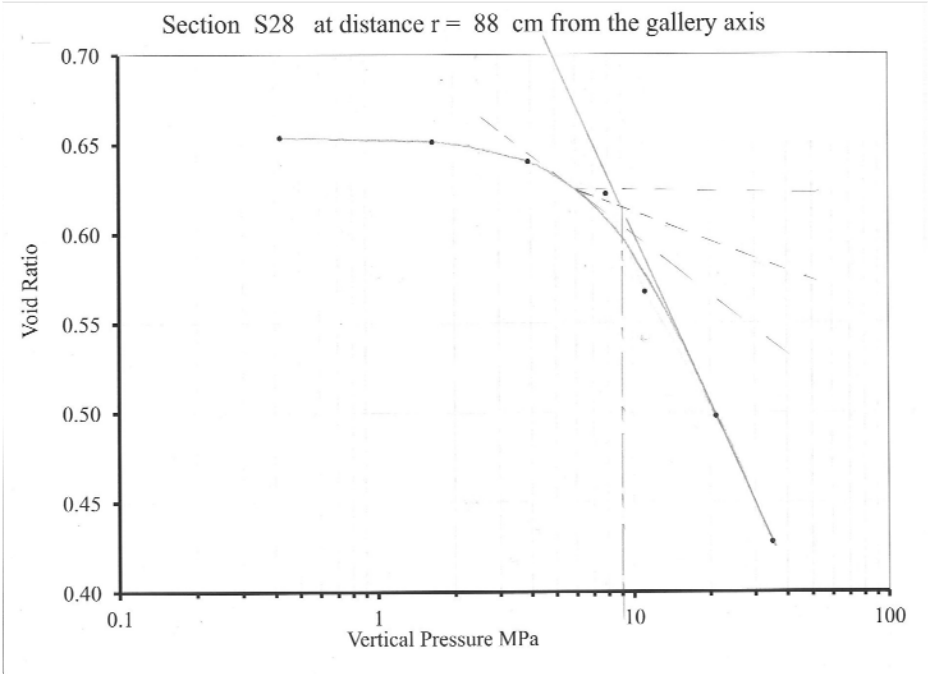

Figure C.10. Calculation of P_0 for sample collected at r=88 cm at section S28.

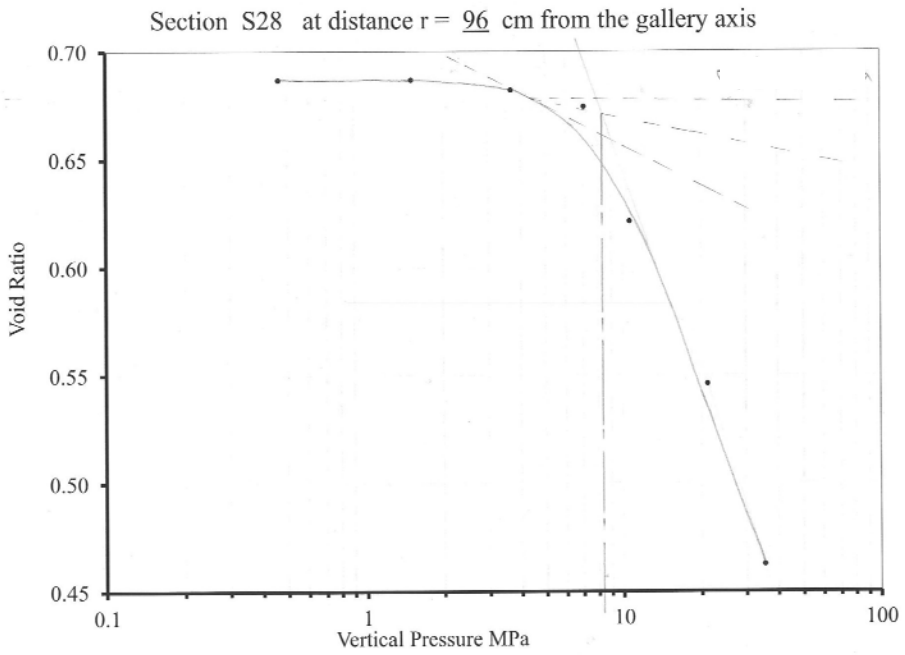

Figure C.11. Calculation of P_0 for sample collected at r=96 cm at section S28.

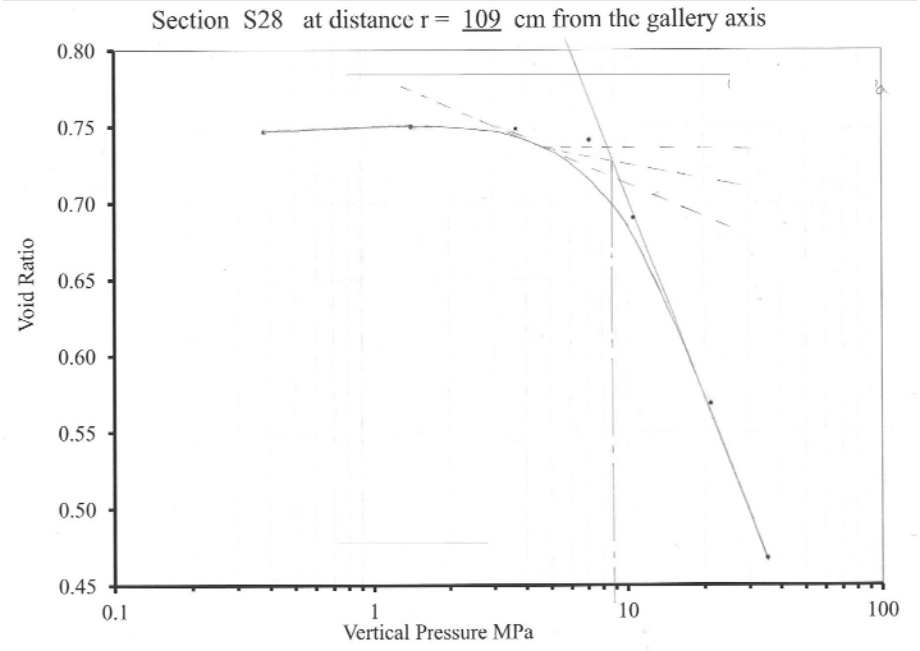

Figure C.12. Calculation of P_0 for sample collected at r=109 cm at section S28.

APPENDIX D

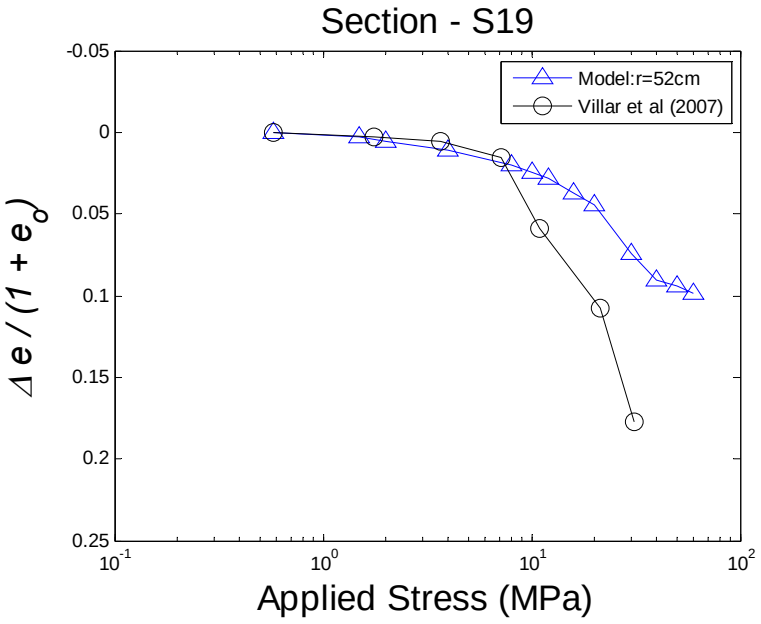

Figure D.1. Experimental and model consolidation curves at r=52 cm of section S19.

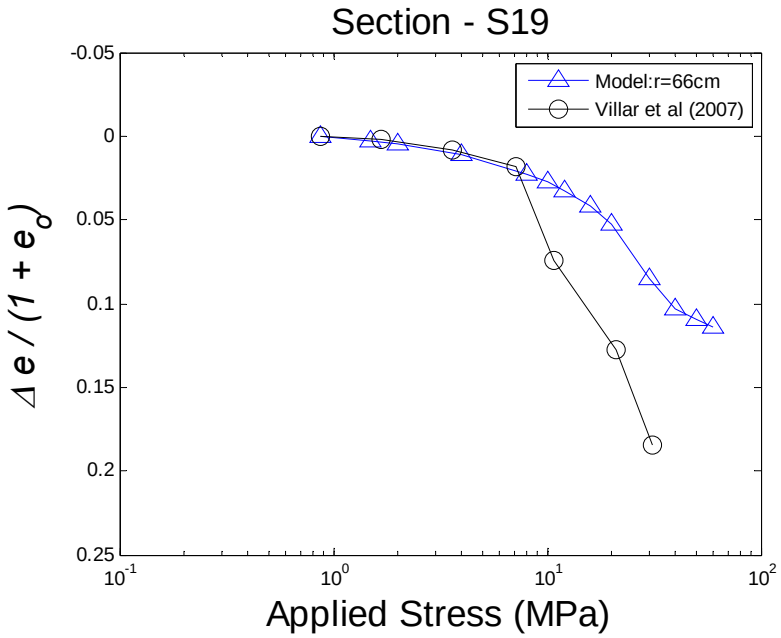

Figure D.2 Experimental and model consolidation curves at r=66 cm of section S19.

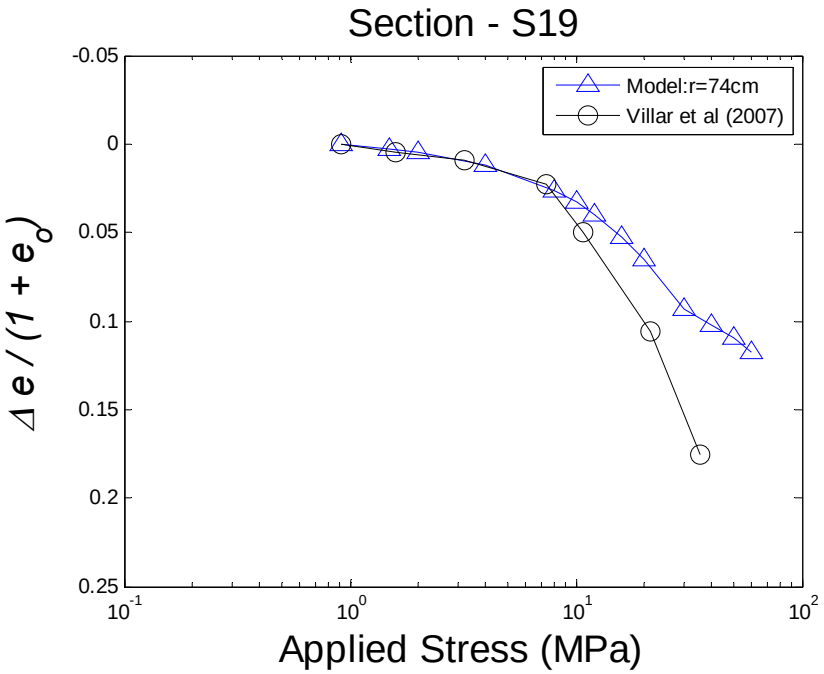

Figure D.3. Experimental and model consolidation curves at r=74 cm of section S19.

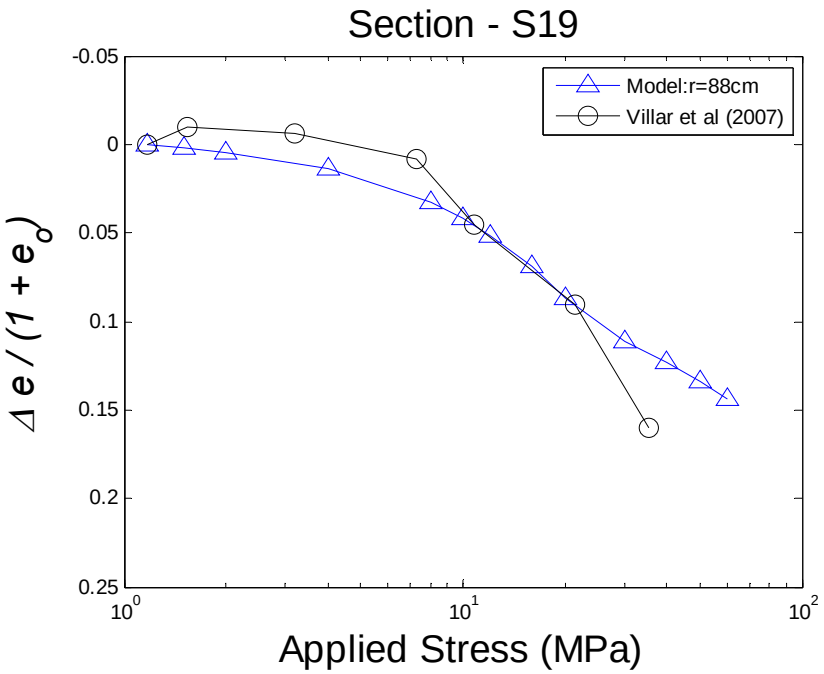

Figure D. 4. Experimental and model consolidation curves at r=88 cm of section S19.

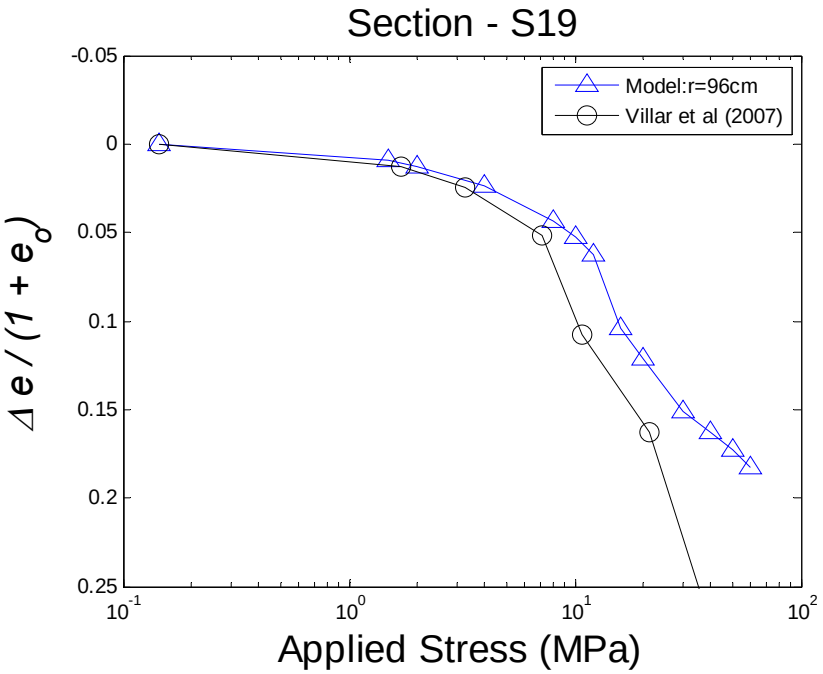

Figure D.5. Experimental and model consolidation curves at r=96 cm of section S19.

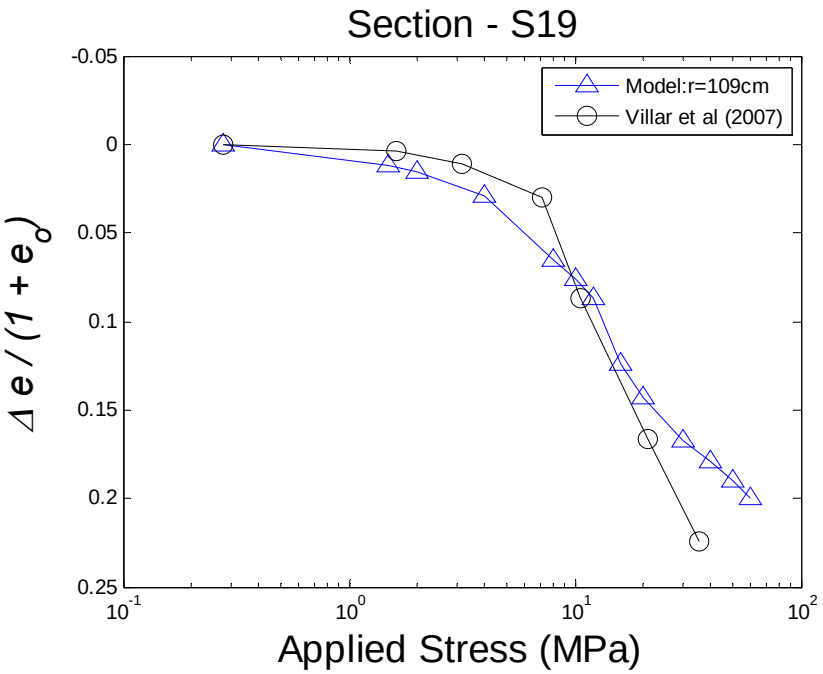

Figure D. 6. Experimental and model consolidation curves at r=109 cm of section S19.

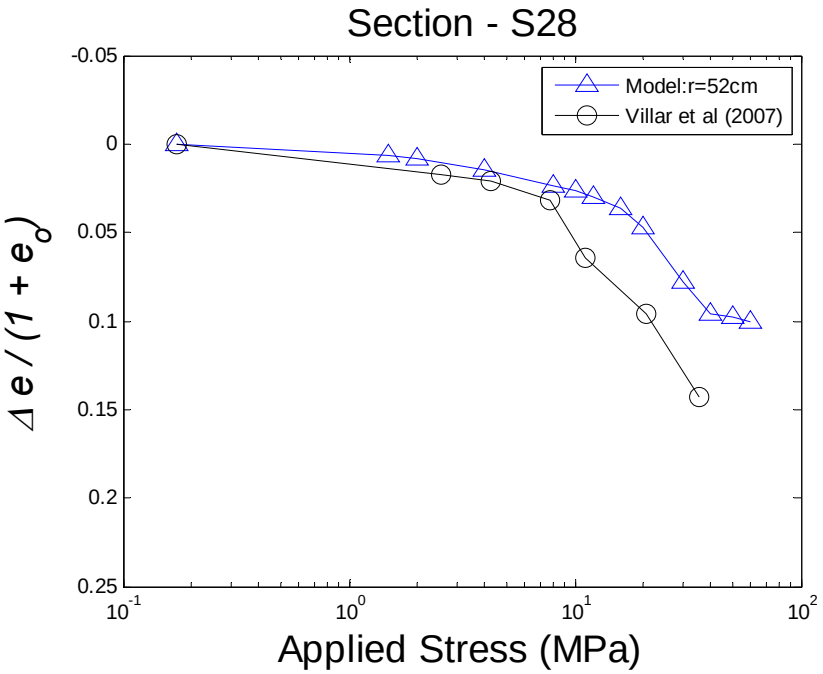

Figure D.7. Experimental and model consolidation curves at r=52 cm of section S28.

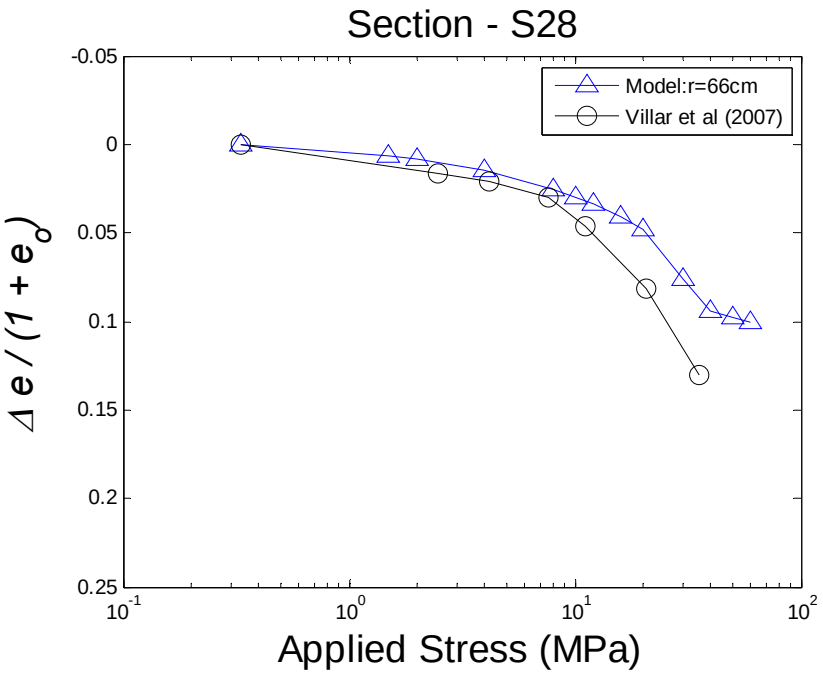

Figure D.8. Experimental and model consolidation curves at r=66 cm of section S28.

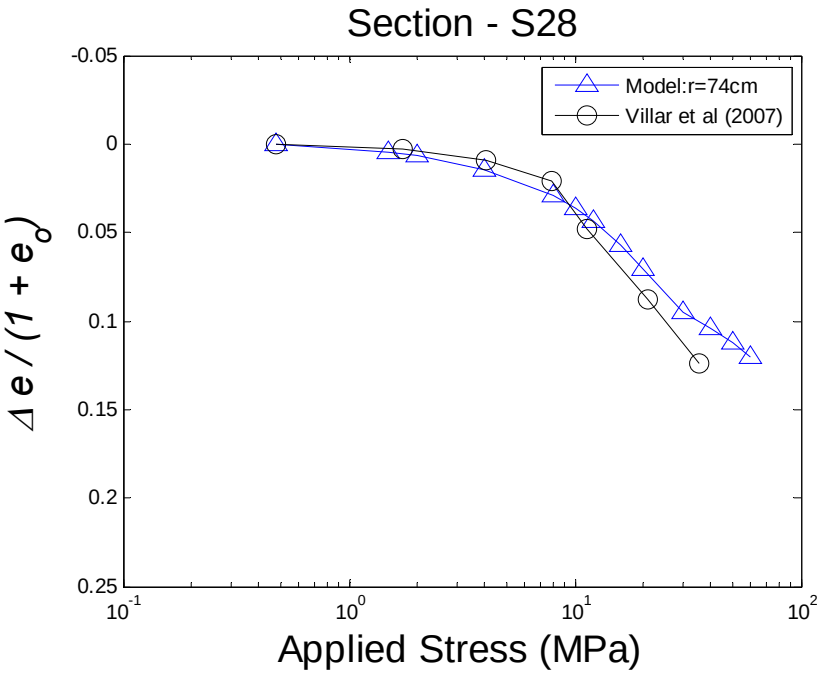

Figure D.9. Experimental and model consolidation curves at r=74cm of section S28.

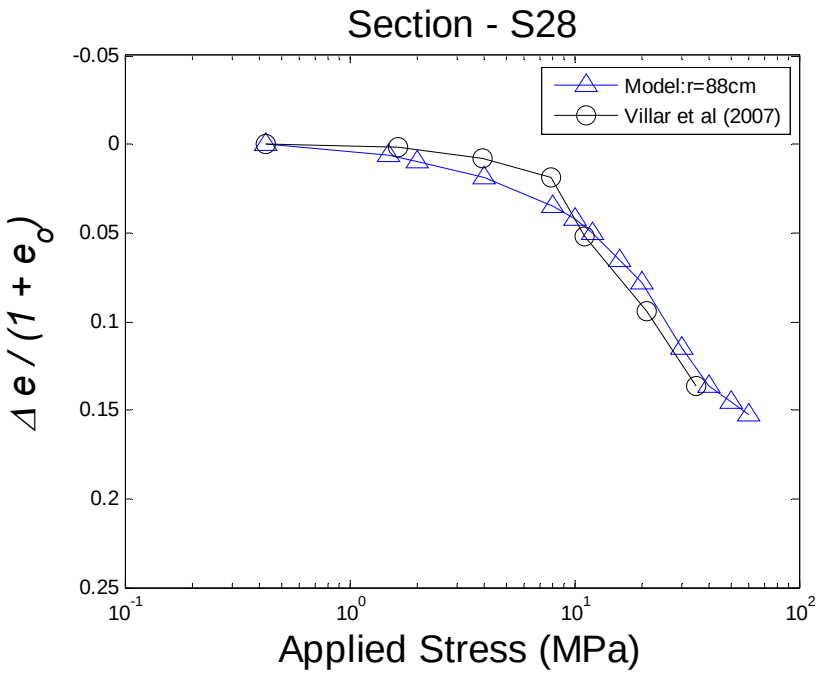

Figure D.10. Experimental and model consolidation curves at r=88 cm of section S28.

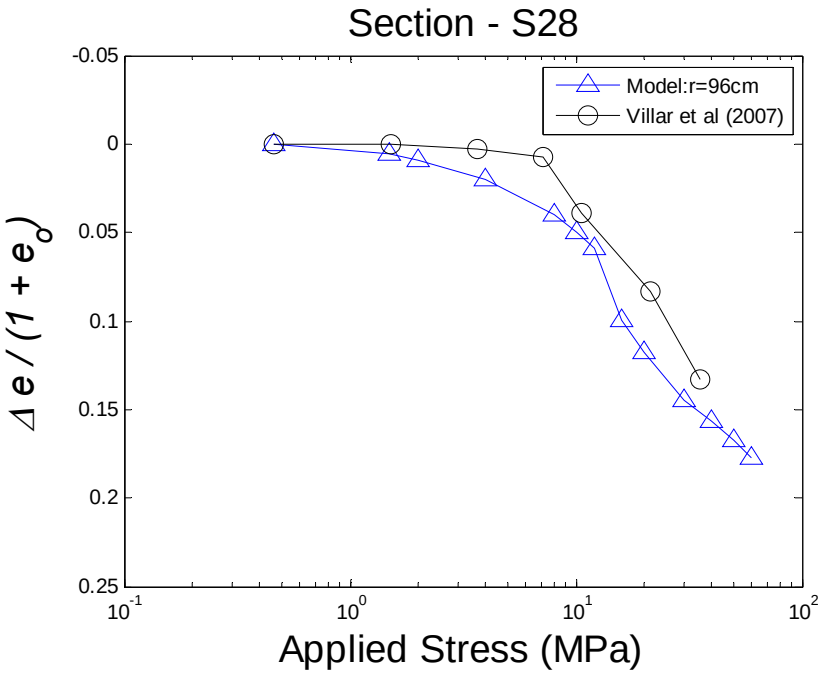

Figure D.11. Experimental and model consolidation curves at r=96 cm of section S28.

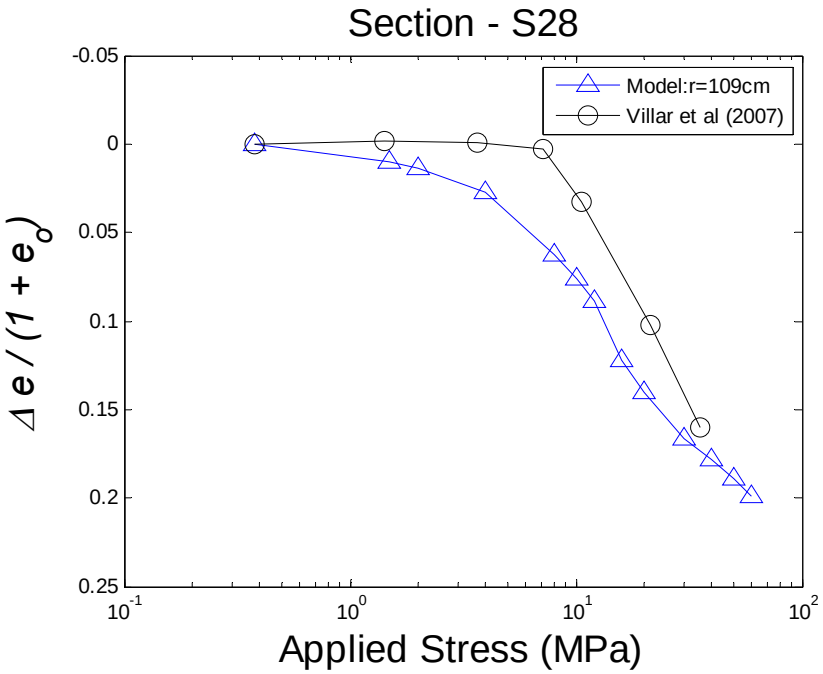

Figure D.12 Experimental and model consolidation curves at r=109 cm of section S28.

VITA

Lakshman Kumar Dontha received his Bachelor of Technology degree in mining engineering from Banaras Hindu University in 2008. He then joined Reliance Power Limited, a private power company and assisted in building the green power plant. He entered the civil engineering program at Texas A&M University in August 2010 and received his Master of Science degree in May 2012. His research interests include unsaturated soil mechanics, numerical modeling and uncertainty quantification. He plans to publish peer reviewed journal papers on these topics, focusing on the phenomena of coupled thermo-hydrological-mechanical phenomena.

Mr. Dontha may be reached at Department of Civil Engineering, Texas A&M University, 3136 TAMU, College Station, Texas 77843-3136, USA. His email is lakshman.851@gmail.com.